

Polymer Melt Rheology and the Rheotens Test

von
Anka Bernnat

Institut für Kunststofftechnologie
Universität Stuttgart

2001

Polymer Melt Rheology and the Rheotens Test

Von der Fakultät Verfahrenstechnik und Technische Kybernetik
der Universität Stuttgart zur Erlangung des akademischen Grades
eines Doktors der Ingenieurwissenschaften (Dr.-Ing.)
genehmigte Abhandlung

von
Anka Bernnat
aus Stuttgart

Hauptberichter: Prof. Dr.-Ing. M.H. Wagner
Mitberichter: Prof. Dr.-Ing. habil. M. Piesche
Tag der mündlichen Prüfung: 18.10.2001

Institut für Kunststofftechnologie
Universität Stuttgart
2001

Abstract

The Rheotens experiment is a quasi-isothermal fibre spinning experiment. A polymer melt presheared in a capillary die is stretched under the action of a constant drawdown force until rupture of the filament. The experiment results in an extension diagram which describes the elongational behaviour of a polymer melt and therefore is relevant for many polymer processes like blow moulding, film blowing, and fibre spinning. Also, the rupture stress of a polymer melt can be calculated, which is of importance for these industrial applications.

As an extension of the experiment, the local velocity distribution along the fibre can be measured with a Laser-Doppler Velocimeter (LDA). From this, the shape of the deformed filament as well as local elongation rates can be derived.

In general, melt strength and drawability depend on the material properties of the melt and on the processing conditions of the experiment. The existence of Rheotens mastercurves allows to separate the polymer melt properties from the processing conditions and thus simplifies the description of elongational behaviour under constant force deformation. The Rheotens mastercurve reflects structural differences of polymer melts.

Two models to extract the apparent elongational viscosity from a Rheotens experiment are developed: the analytical model and the similarity model. The apparent elongational viscosity calculated from Rheotens curves strongly depends on the rheological prehistory in the extrusion die. The viscosity curve is shifted to lower viscosities and higher extension rates with increasing extrusion velocity. A large amount of preshear lowers the apparent elongational viscosity to the level of three times the shear viscosity. Low preshear on the other hand results in an apparent elongational viscosity, which is of the same order of magnitude as the steady-state elongational viscosity.

The detailed results of Rheotens experiments including the LDA spinline velocity measurements are used to benchmark the results of numerical simulation. The integral Wagner constitutive equation describes viscoelastic flow behaviour and is suitable for this type of analysis. However, the prediction of the correct amount of extrudate swell is a critical task. While the numerical simulation matches the experimental results qualitatively, the amount of extrudate swell, and hence the instantaneous elastic response predicted by the model is overpredicted, as shown for the example of a HDPE melt.

Rheotens experiments, Rheotens mastercurves, and apparent elongational viscosities calculated from Rheotens experiments are reported for LDPE, LLDPE, HDPE, PP, PS, and PC melts. The elongational behaviour of the melts is characterised under conditions which are relevant for typical industrial processing applications.

Zur Rheologie des Schmelzespinnprozesses

Das Rheotensexperiment

Die Spinnbarkeit von Polymerschmelzen ist von großer Bedeutung für viele Prozesse der Kunststoffverarbeitung. Die Beurteilung des Verstreckverhaltens erfolgt in der Praxis häufig auf Basis eines technischen Dehnungsdiagramms, bei dem mit Hilfe des von Meissner (1971) entwickelten Dehnungstesters (Rheotens) die Abzugskraft eines extrudierten Stranges als Funktion der Abzugsgeschwindigkeit ermittelt wird. Es ist bekannt, daß u.U. schon geringe Chargenunterschiede eines Polymers zu deutlich verschiedenen Rheotenskurven führen. Weitere Vorteile der Methode sind einfache Versuchsdurchführung, gute Reproduzierbarkeit und Praxisnähe.

Der Rheotensversuch wurde experimentell weiterentwickelt, indem die lokale Geschwindigkeit der Polymerschmelze entlang der Spinnstrecke zwischen Düse und Abzugseinrichtung per Laser-Doppler-Velocimeter (LDA) direkt gemessen wurde. Damit kann zum einen die durch die Drehgeschwindigkeit der Abzugsräder hervorgerufene Abzugsgeschwindigkeit der Schmelzestranges überprüft werden, zum anderen läßt sich so die Geschwindigkeitsverteilung entlang der Spinnstrecke und damit die lokale Dehngeschwindigkeit ermitteln. Diese wurden für die Modellbildung zur Berechnung von Dehnviskositäten herangezogen und außerdem für die Überprüfung von Simulationsergebnissen benötigt.

Rheotens Grandmasterkurven

Wegen der komplizierten rheologischen Vorgeschichte der Schmelze vor Austritt aus der Düse war bisher nur eine qualitative Interpretation unterschiedlichen Dehnverhaltens möglich, etwa durch Angabe der Schmelzefestigkeit und der maximalen Dehnbarkeit. Bei diesen Untersuchungen erfolgte der Vergleich verschiedener Polymerschmelzen bei konstantem Durchsatz. Im Rahmen dieser Arbeit konnte basierend auf Untersuchungen von Wagner et. al. (1996) gezeigt werden, daß sich bei Fahrweise mit konstantem Extrusionsdruck in einfacher Weise temperatur- und molmassen-invariante Rheotens-Masterkurven ergeben. Ausnahmen von der Temperaturinvarianz, die auf Wandgleiteneffekte bzw. Spannungskristallisation zurückzuführen sind, wurden experimentell gefunden.

Rheotens-Masterkurven erlauben einen direkten, quantitativen Vergleich des Dehnverhaltens verschiedener Polymerschmelzen bei Beanspruchung mit konstanter Kraft. Damit kann der Einfluß von Strukturunterschieden der Polymere untersucht werden. Zum Beispiel zeigen verzweigte Polyethylenschmelzen ein deutlich unterschiedliches Kraft-Dehnverhalten abhängig vom Herstellungsprozeß (Autoklav- oder Rohrreaktor). Auch die Bruchspannung des Schmelzen, die aus Kraft und Verstreckung am Abrißpunkt der Rheotenskurve berechnet werden kann, ist vom Aufbau des Netzwerkes aus Molekülketten abhängig und liegt bei linearen Polymeren niedriger als bei verzweigten. Die im Rheotensversuch gemessene Bruchspannung läßt sich auf Verarbeitungsprozesse übertragen.

Im allgemeinen ist die im Rheotensversuch gemessene Abzugskraft eine komplexe Funktion der Polymereigenschaften, der Geometrie von Extrusionsdüse und Spinnstrecke sowie der Prozeßbedingungen (Durchsatz und Abzugsgeschwindigkeit). Die Existenz eines einfachen Verschiebungsgesetzes ließ sich nachweisen, das den Einfluß von Geometrie- und Durchsatzänderungen

auf die Rheotenskurven berücksichtigt. Mit diesem ist es gelungen, Stoff- und Prozeßabhängigkeit der Rheotenskurven zu trennen. Während die Rheotens-Grandmasterkurve das Stoffverhalten im quasi-isothermen Spinnprozeß beschreibt, enthält der Skalierungsfaktor die Information über die Prozeßabhängigkeit der Rheotenskurve. Umfangreiche Rheotensmessungen an linearen und verzweigten Polyethylen-Schmelzen sowie an Polypropylen, Polystyrol und Polycarbonat belegen die Richtigkeit dieser Überlegungen. Damit besteht die Möglichkeit, die Ausziehfähigkeit verschiedener Polymerschmelzen unter Praxisbedingungen quantitativ zu vergleichen und zu werten.

Ableitung der effektiven Dehnviskosität aus dem Rheotensversuch

Ein wichtiges Ziel dieser Arbeit war es, aus den Rheotenskurven effektive Dehnviskositäten abzuleiten, da die Messung der Dehnviskosität mit einem Dehnrheometer experimentell sehr aufwendig ist. Dazu wurden zwei Modelle entwickelt: Zum einen ein analytisches Modell von Wagner et. al. (1996) und zum anderen eine Ähnlichkeitslösung basierend auf der Annahme, daß die Dehnviskosität im Rheotensversuch einzig eine Funktion der Verstreckung ist. Die Gültigkeit der Annahmen, auf denen analytisches Modell und Ähnlichkeitsgesetz basieren, konnten durch die LDA-Messungen experimentell belegt werden.

Die so berechnete effektive Dehnviskosität wird ganz wesentlich durch die rheologische Vorgeschichte in der Extrusionsdüse beeinflusst, und zwar so, daß der gesamte Viskositätsverlauf mit zunehmender Extrusionsgeschwindigkeit zu kleineren Dehnviskositäten und größeren Dehngeschwindigkeiten verschoben wird. Bei großer Vorscherung wird die scheinbare effektive Dehnviskosität bis auf das Niveau der dreifachen Scherviskosität herabgesetzt. Bei geringer Vorscherung kann der Rheotensversuch dagegen Anhaltswerte für die Größenordnung der stationären Dehnviskosität liefern.

Der Vergleich der effektiven Dehnviskosität, die aufgrund der rheologischen Vorgeschichte prozeßabhängig ist, mit der uniaxialen Dehnviskosität, die an isotropen Proben gemessen wird, zeigt klar, daß durch Vorscherung die gemessene Dehnverfestigung reduziert wird. Dies ist von Bedeutung für viele Verarbeitungsprozesse, die von Dehnströmungen dominiert werden, womit ein Zusammenhang zur industriellen Praxis hergestellt werden konnte.

Numerische Simulation mit integraler Zustandsgleichung

Der Schmelzespinnprozeß ist ein prototypisches Beispiel eines Kunststoffverarbeitungsprozesses: die Polymerschmelze unterliegt zunächst einer einfachen Scherung in der Extrusionsdüse und anschließend einer uniaxialen Verstreckung unter Beanspruchung mit konstanter Abzugskraft. Diese gekoppelte Scher- und Dehnströmung in Verbindung mit der a priori unbekanntem freien Oberfläche des Schmelzestranges macht diesen einfachen Laborversuch zu einem anspruchsvollen Testfall für die numerische Simulation. Dabei ist der Einsatz einer geeigneten rheologischen Zustandsgleichung für viskoelastische Fluide zur Beschreibung des Rheotensversuches notwendig.

Eingesetzt wurde eine rheologische Zustandsgleichung vom Integraltyp nach Wagner (1978) unter Berücksichtigung der Irreversibilität von Netzwerkentschlauungen. Das verwendete Simulationsprogramm *filage* von Fulchiron et.al. (1998) für isothermes Schmelzespinnen berücksichtigt

die Deformationsgeschichte in der Extrusionsdüse. Vereinfachende Annahmen über das Geschwindigkeitsprofil in der Düse (Potenzgesetz) und entlang der Spinnstrecke (eindimensional) werden getroffen. Damit lassen sich Simulationsrechnungen schnell und mit guter Konvergenz durchführen. Die Parameter der Zustandsgleichung wurden an rheologische Grundexperimente in Scherung und Dehnung angepaßt.

Der Vergleich berechneter und gemessener Rheotenskurven zeigt qualitative Übereinstimmung des Kraft-Dehnverhaltens. Quantitativ ergeben sich allerdings deutliche Abweichungen zwischen Simulation und Experiment, vor allem im Anfangsbereich der Kurven, das heißt die Strangaufweitung läßt sich nicht korrekt vorhersagen, sondern wird von der Simulationsrechnung überschätzt.

Dies läßt sich folgendermaßen interpretieren: das Simulationsmodell beschreibt eine zu starke Elastizität der Schmelze direkt nach der Düse, was zu einer Überschätzung der Strangaufweitung führt. Bei starker Verstreckung wird das Material dagegen zu viskos (und zu wenig elastisch) beschrieben. Dieses Verhalten liegt in der verwendeten Form des Integralmodelles begründet, das zwar einfache Scherung und uniaxiale Dehnung beschreibt, aber nicht die biaxiale Dehnung, die bei der Strangaufweitung auftritt. Außerdem bestehen Zweifel daran, ob das Modell die Irreversibilität der Netzwerkentschlaufung korrekt wiedergibt.

Zusammenfassung

Im Rahmen dieser Arbeit ist es gelungen, den Rheotensversuch, der industriell häufig zum qualitativen Vergleich verschiedener Polymerschmelzen eingesetzt wird, auf eine neue wissenschaftliche Basis zu stellen. Die Analyse des Kraft-Dehnungsverhaltens beim Schmelzespinnen wird durch die Existenz von Rheotens-Grandmasterkurven vereinfacht, die es erlauben, das Materialverhalten des Polymers von der Prozeßabhängigkeit des Experiments zu trennen. Zusätzliche Informationen lassen sich aus der vorgestellten Berechnung der effektiven Dehnviskosität bei konstanter Kraft gewinnen. Damit wurden die theoretischen Grundlagen der Rheologie des Schmelzespinnprozesses wesentlich erweitert.

Vorwort

Die vorliegende Arbeit entstand während meiner Tätigkeit als wissenschaftliche Mitarbeiterin des Instituts für Kunststofftechnologie der Universität Stuttgart von 1996 bis 2000.

Mein herzlicher Dank gilt Herrn Prof. Dr.-Ing. M.H. Wagner für die interessante Aufgabenstellung, die intensive Betreuung und Förderung der Arbeit und viele Gelegenheiten zur Diskussion.

Ich danke Herrn Prof. Dr.-Ing. H.G. Fritz, dem Leiter des Instituts, für die Unterstützung meiner wissenschaftlichen Arbeit und das mir zur Verfügung stehende Arbeitsumfeld am IKT.

Danken möchte ich auch Herrn Prof. Dr.-Ing. habil. M. Piesche für die Übernahme des Mitberichts.

Für die Möglichkeit, die Experimente zum Wandgleiten im Rheologielabor der BASF AG durchzuführen, danke ich Herrn Dr. H.M. Laun, und dem Laborteam für die gute Zusammenarbeit.

Ich danke allen Kolleginnen und Kollegen am IKT für die gute Zusammenarbeit und der Arbeitsgruppe Rheologie für viele interessante Diskussionen. Steffi, Kathrin und Frauke haben im Rheologielabor zu dieser Arbeit beigetragen. Bedanken möchte ich mich außerdem für die Mitarbeit meiner wissenschaftlichen Hilfskräfte, vor allem bei Zeynep, die so engagiert an den Experimenten mitgearbeitet hat.

Diese Arbeit wurde durch Mittel der Deutschen Forschungsgemeinschaft, der Europäischen Gemeinschaft und von BP Chemicals gefördert.

Zum Schluß gilt mein herzlicher Dank meinem Mann Helmut für seine große Unterstützung, und ihm und unserer Tochter Helen für Geduld und Verständnis für meine Arbeit. Meine und seine Familie haben mich in vieler Hinsicht unterstützt und damit mein Studium und diese Arbeit ermöglicht. Danke.

Contents

| | | |
|----------|---|------------|
| 1 | Introduction | 1 |
| 2 | The Rheotens Experiment | 3 |
| 2.1 | Experimental Set-up | 3 |
| 2.2 | Evaluation of spinline profiles by means of Laser-Doppler velocimetry (LDV) . . . | 7 |
| 2.3 | Material Characterisation | 12 |
| 3 | Rheotens Mastercurves | 16 |
| 3.1 | Temperature Invariant Mastercurves | 16 |
| 3.2 | Molar Mass Invariant Mastercurves | 22 |
| 3.3 | Rheotens Supermastercurves | 24 |
| 3.4 | Concept of Grandmastercurves | 28 |
| 3.5 | Critical Rupture Stress | 35 |
| 4 | Elongational Viscosity from Constant Force Deformation Experiments | 40 |
| 4.1 | Analytical model | 40 |
| 4.2 | Similarity model | 44 |
| 4.3 | Comparison of apparent and true elongational viscosity | 54 |
| 4.4 | Relevant Processing Conditions for the Approximation of Elongational Viscosities | 59 |
| 5 | Numerical Simulation of the Rheotens Test | 64 |
| 5.1 | Integral Constitutive Equation | 64 |
| 5.2 | The Simulation Program | 68 |
| 5.3 | Modelling Results | 69 |
| 6 | Conclusions | 75 |
| A | Linear Material Characterisation | 82 |
| B | LDV measurements and the similarity model | 92 |
| C | Results of the analytical model and the similarity model | 103 |

Nomenclature

| | | |
|----------------------------------|---|-------------------|
| a_M | Molar mass shift factor | |
| a_T | Temperature shift factor | |
| a_1, a_2 | Fitting parameters of the similarity model | |
| acc | Acceleration of the drawdown velocity | mm/s ² |
| A | Cross section of the strand | mm ² |
| A_0 | Cross section of the extrusion die | mm ² |
| b | Shift factor | |
| $\underline{\underline{C}}^{-1}$ | Finger strain tensor | |
| \overline{D}_0 | Diameter of the extrusion die | mm |
| D_Z | Diameter of barrel before extrusion die | mm |
| De | Deborah number | |
| E_0 | Activation energy | kJ/mol |
| $\underline{\underline{E}}$ | Unit tensor | |
| f | Parameter of the double exponential damping function | |
| F | Drawdown force of the Rheotens | cN |
| F_p | Critical force of analytical model | cN |
| g_i | Relaxation strength of the discrete relaxation spectrum | Pa |
| $G(t)$ | Relaxation modulus | Pa |
| $G^0(t, t')$ | Linear viscoelastic relaxation modulus | Pa |
| G' | Storage modulus | Pa |
| G'' | Loss modulus | Pa |
| h | Damping function | |
| $H(t, t')$ | Damping functional | |
| I | Generalised invariant of the Finger strain tensor | |
| I_1 | First invariant of the Finger strain tensor | |
| I_2 | Second invariant of the Finger strain tensor | |
| L | Spinline length | mm |
| L_0 | Die length | mm |
| \dot{m} | Mass flow rate | g/min |
| $m_0(t, t')$ | Linear viscoelastic memory function | Pa/s |
| M | Average molar mass | g/mol |
| MS | Melt strength | cN |
| MWD | Molar mass distribution | |
| n | Power law index | |
| n_1, n_2 | Parameters of the double exponential damping function | |
| p | Extrusion pressure | bar |
| r | Strand radius | mm |
| R | General gas constant | J/mol K |
| SR | Swell ratio | |
| t | time | s |
| t_m | Characteristic material time | s |
| t_{pz} | Characteristic processing time | s |
| T | Temperature | °C |
| v | Drawdown velocity of the Rheotens | mm/s |
| v_0 | Extrusion velocity in the die | mm/s |

| | | |
|----------------------------------|--|----------|
| v_g | Wall slip velocity | mm/s |
| v_s | Start velocity of the Rheotens experiment | mm/s |
| V | Draw ratio | |
| V_p | Critical draw ratio of the analytical model | |
| V_s | Relative start velocity | |
| x | Distance from die along the spinline | mm |
| α | Parameter of the PSM damping function | |
| β | Parameter for description of the generalised invariant | |
| η | Viscosity | Pas |
| η_0 | Zero shear viscosity | Pas |
| η^* | Complex viscosity | Pas |
| ε | Extensional deformation | |
| $\dot{\varepsilon}$ | Elongation rate | s^{-1} |
| γ | Shear deformation | |
| $\dot{\gamma}$ | Shear rate | s^{-1} |
| $\dot{\gamma}_{ap}$ | Apparent wall shear rate | s^{-1} |
| λ | Stretch ratio | |
| λ_i | Relaxation time of the discrete relaxation spectrum | s |
| ω | Frequency | s^{-1} |
| ρ | Density | g/cm^3 |
| σ | Tensile stress at the end of the spinline | Pa |
| σ_B | Rupture stress | Pa |
| σ_p | Critical stress of the analytical model | Pa |
| $\underline{\underline{\sigma}}$ | Extra stress tensor | |
| τ | Shear stress | MPa |
| τ_{ap} | Apparent wall shear stress | MPa |
| τ_{crit} | Critical wall shear stress | MPa |

1 Introduction

The Rheotens experiment was developed by Meissner simultaneously with the uniaxial elongational rheometer [35]. Both instruments are based on the principle of two rotating wheels, which draw down a polymer melt sample with defined velocity and thereby produce an elongational deformation. While the elongational rheometer realises a time dependent uniaxial extension with constant elongation rate starting from a homogeneous, stress-free polymer sample, the Rheotens performs an elongational experiment under constant force on a melt pre-sheared in a capillary die.

The Rheotens test results in an extension diagram which describes the elongational behaviour of a polymer melt and therefore is relevant for many polymer processes like blow moulding, film blowing, and fibre spinning. The measurement is fast and easy to perform with good reproducibility. In contrast to experiments with the elongational rheometer, it does not reach steady-state conditions and realises higher deformation rates, both indicating that this laboratory experiment is close to processing conditions.

Literature Review

Experiments in elongation are more sensitive to structural differences of polymer materials than those in shear, which was shown by investigations of the IUPAC Working Party on Structure and Properties of Commercial Polymers [36]. Therefore, the Rheotens is widely used for quality control purposes [61]. Also, the force needed to elongate a filament can be correlated to processing parameters like minimum film thickness and bubble stability in film blowing [17], [10], [48] and extrusion [60]. From force and draw ratio at the break of the filament the rupture stress can be calculated, which is a vital parameter for spinning processes and is of importance in understanding melt fracture phenomena [15], [34].

Even small modifications of the molecular structure of a polymer can be detected by the Rheotens test. Correlations between melt strength and average molar mass were reported [26]. The reactor technology for the production of polymer samples can be identified by differences in melt strength [17]. Also the influence of different molecular weight distributions, for example produced by blending, is reflected in the melt strength [18], [16].

Different attempts were made to convert the tensile force/drawdown speed diagram into a relation between elongational viscosity and elongation rate, for which a rheological model is needed. Such analysis was for example presented by Laun and Schuch [32] and later Wagner et. al. [53]. Also algorithms have been presented using an integral constitutive equation to link the Rheotens test with steady-state elongational viscosity [30], [14].

Apart from the long known practical applications of the Rheotens test mentioned, a more fundamental understanding of the experiment has been achieved in recent years. The concept of Rheotens mastercurves was suggested by Wagner [53], [56], [55], proving that Rheotens curves are invariant with respect to temperature and average molar mass if compared at constant wall shear stress in the extrusion die. Moreover, the influence of different die and spinline geometries can be taken into account by simple scaling laws, separating material behaviour from processing conditions [51], [52]. This allows comparison of material properties independent of experimental conditions and enables to correlate the extension diagram to the molecular structure of the melt [9].

Objective of this work

The objective of this work is to investigate Rheotens curves of various polymer melts and to show the differences in melt strength, extensibility, and critical rupture stress. The existence of various mastercurves will be proven. The experimental data will be correlated with the molecular structure of the materials, focusing on the difference between linear and branched polymers, and the effect of molecular weight distribution and long-chain branching. Also, the relevance of the results for processing will be investigated.

The Rheotens test is a rather simple, isothermal experiment with an axissymmetrical geometry of the spinline and well defined boundary conditions. Therefore it will be used as a prototype industrial flow for benchmarking different enhanced constitutive equations and numerical simulation codes. The critical task, as it turns out, is the correct prediction of extrudate swell from a given die geometry.

To obtain a more fundamental understanding of the conditions in the spinline, the local velocity distribution needs to be measured. Based on this information, a more detailed analysis of the Rheotens test will be used to develop a model which allows to extract the elongational viscosity from Rheotens measurements.

2 The Rheotens Experiment

2.1 Experimental Set-up

The following experimental set-up (fig. 2.1) is used for all the experiments described. An extruder (manufacturer Extrudex, screw diameter 25 mm, screw length 20 D) serves as a melt feeder, operated in pressure controlled mode. After a cross head (with a channel diameter D_Z of 8 mm) several capillary dies (tab. 2.1) can be assembled. The pressure regulating the feedback loop is measured in front of the die entry. The flow rate can be kept steady in this mode without using a gear pump, the deviation is less than $\pm 1 \%$ during half an hour. The flow rate and hence the extrusion velocity v_0 ,

$$v_0 = \frac{\dot{m}}{\rho A_0}, \quad (2.1)$$

with \dot{m} being the mass flow rate, ρ the melt density, and A_0 the cross section of the die, is measured by weighting the extruder output for at least two minutes.

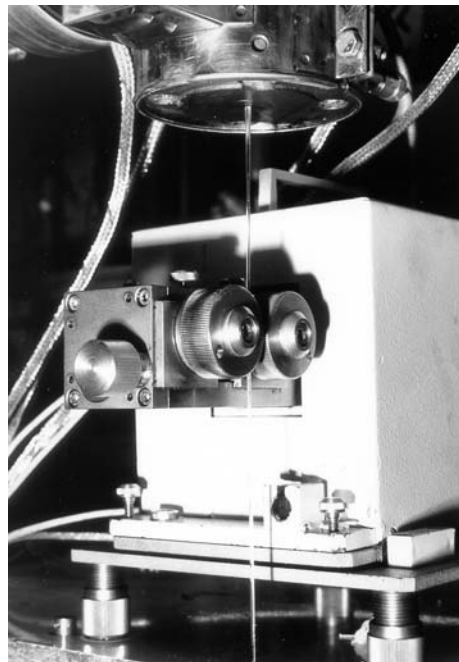
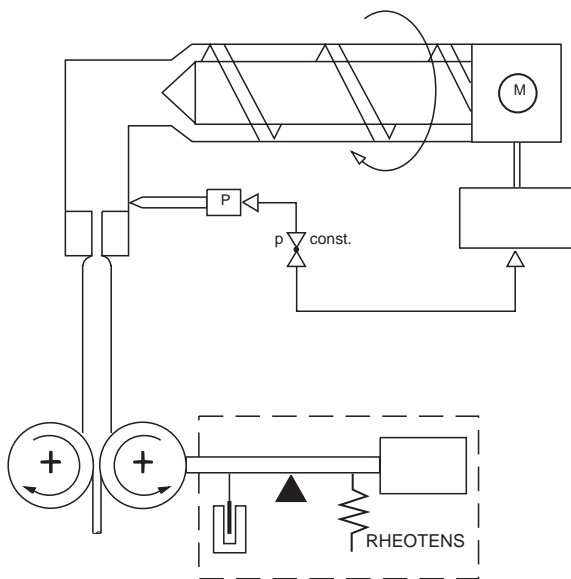


Figure 2.1: Experimental set-up for Rheotens measurements.

The polymer strand is extruded continuously and after a spinline length L is taken up by the wheels of the Rheotens. In a Rheotens test, these wheels turn with a slowly increasing velocity v and draw down the polymer strand. The resistance of the material against this drawdown is then measured by a force balance in the arm onto which the wheels are fixed. This results in an extension diagram, force F as a function of drawdown velocity v (fig. 2.2). At the start of the experiment, the velocity of the Rheotens wheels is adjusted in such a way that it is equal to the actual velocity v_s of the strand. Therefore, if a material exhibits extrudate swell at the die exit, v_s is smaller than the extrusion velocity v_0 calculated from eq. (2.1). The signal of

| die diameter D_0 | die length L_0 | entrance cone |
|--------------------|------------------|---------------|
| 2 mm | 60 mm | 180° |
| 2 mm | 20 mm | 180° |
| 2 mm | 2 mm | 180° |
| 2 mm | 60 mm | 50° |
| 2 mm | 30 mm | 50° |
| 2 mm | 2 mm | 50° |

Table 2.1: Capillary dies used for Rheotens experiments.

the force balance is equal to zero at the starting point, as the material is not yet elongated. The force signal can be calibrated with defined weights. During the experiment the velocity of the Rheotens wheels is accelerated slowly, and thereby a drawdown velocity v is applied to the polymer strand. The resulting force signal F is measured until rupture of the strand. The maximum force at rupture is also referred to as melt strength (MS), while the maximum velocity is called drawability of the melt.

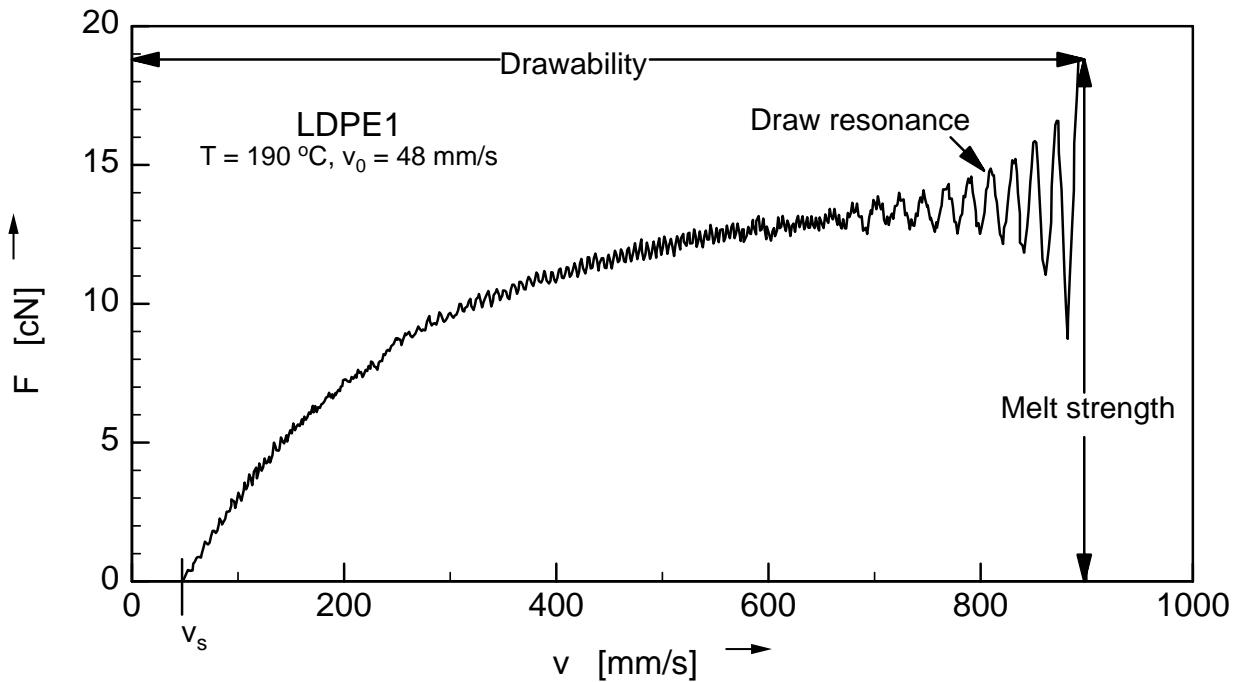


Figure 2.2: Rheotens curve: Melt strength as a function of drawdown velocity.

At higher draw ratios, the experimental curves start to oscillate, an effect which is called draw resonance. It is a fluctuation of the fibre diameter in the spinline, which is explained in detail in [12]. The onset of draw resonance is of practical importance for fibre spinning processes, where a uniform fibre diameter is required, but will not be considered in the following.

The acceleration of the drawdown velocity can be varied over a broad range. As can be seen in fig. 2.3, the acceleration factor acc has an influence on the onset of draw resonance and the maximum drawability. High acceleration results in higher drawability and later onset of draw resonance than low acceleration. The curves are compared to a measurement at stationary condition, where the drawdown velocity is increased manually and a steady state value of the force signal is obtained after a short time. It is not possible to obtain steady-state values in the region of draw resonance. Slow acceleration leads to a maximum drawability smaller than values obtained in steady state, and also is disadvantageous because it increases the measurement time considerably. High acceleration leads to an increased drawability but difficulties arise due to the very fast experiment. The intermediate value of $acc = 24 \text{ mm/s}^2$ was therefore used for all experiments. The comparison with the stepwise increase of the drawdown velocity demonstrates that the Rheotens is operated in quasi stationary condition.

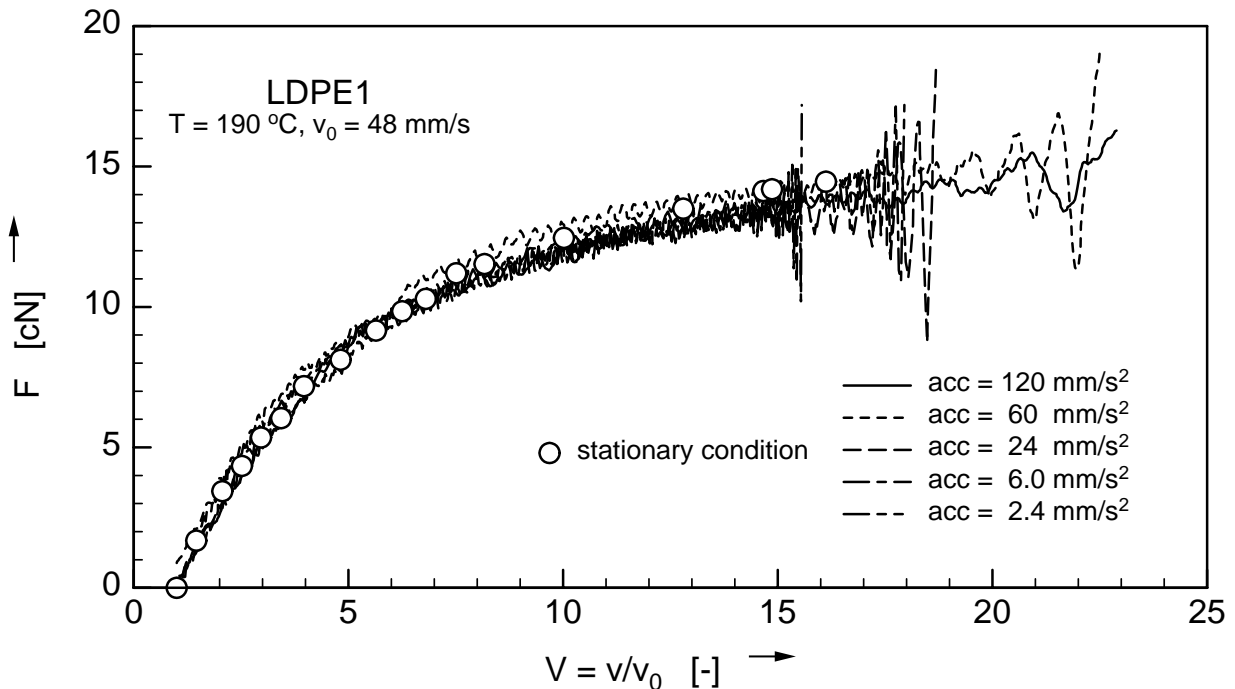


Figure 2.3: Rheotens curves measured at different accelerations acc of the drawdown velocity, and by a stepwise increase of the drawdown velocity (stationary condition).

The experiment can be considered to be isothermal, even without a heating chamber around the polymer strand, if the following conditions are fulfilled: the spinline length L is less than 150 mm, the die diameter D_0 is at least 2 mm, and the extrusion velocity v_0 is higher than 50 mm/s. For such conditions, the local temperature has been measured by Laun and Reuther [29] with a mini-thermocouple especially developed for this purpose, confirming a temperature decrease of less than 15 K. For lower flow rates, strong cooling effects can be observed. This often is a problem if the Rheotens is used in combination with a capillary rheometer where the piston length limits the flow rate and duration of the experiment. Dies with a small diameters also cause cooling problems. To overcome these, a heating chamber would need to be assembled. Dies with larger diameter are not recommended as a thick polymer strand will be squeezed strongly in the gap between the Rheotens wheels, causing flow disturbances.

The general reproducibility of the experiment is high, as shown in fig. 2.4, where an experiment has been repeated several times. The starting velocity v_s might vary depending on the strand length below the wheels, which should either be extremely short to avoid an influence of gravity, or always have the same length. As cutting the strand often results in the strand turning around the wheels, a defined strand length of around 0.5 m below the wheels is recommended. Here the influence of the weight of the strand is up to 3 g, certainly depending on the material, and getting less in the course of the experiment as the fibre is elongated. The main influence of this weight is on the value of the starting velocity v_s , which therefore, and due to the fact that it is adjusted manually, is not a good reference to characterise the experiment.

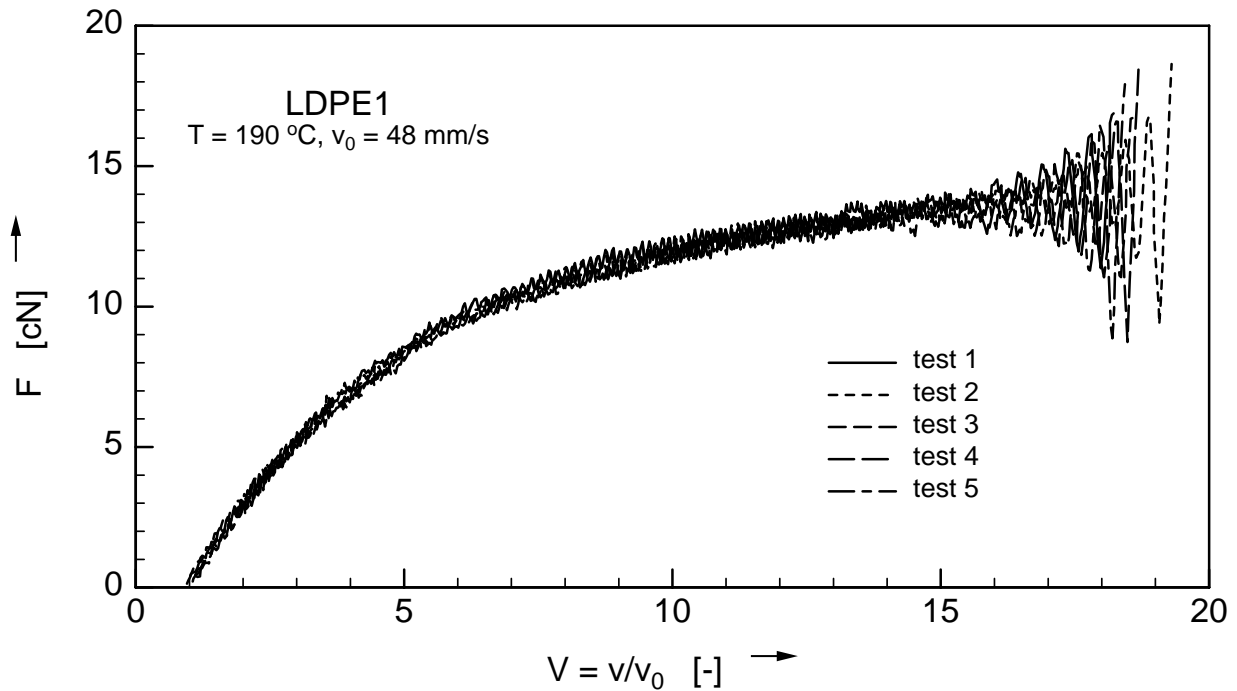


Figure 2.4: Reproducibility of Rheotens measurements.

A major source of error can arise from pressure transducers which are not (well) calibrated. The pressure transducer needs to be calibrated at the temperature of the experiment, and the calibration needs to be checked at regular intervals. This is necessary to ensure that for the same material, same die and same spinline configuration, the mass flow rate can be reproduced at constant pressure. Otherwise a direct comparison at constant extrusion pressure leads to misleading results.

The Rheotens originally was developed to test polyolefine melts. This indicates that it is not necessarily suitable for testing all types of polymeric materials. Resolution and accuracy of the force signal is limited to ± 0.1 cN. Typical spinning materials, and also injection moulding grades, have a melt strength less than 2 cN, and therefore can not be measured accurately. Also, low viscosity materials have a tendency to stick to the wheels of the Rheotens disabling the measurement. Different wheels, for example with a smooth metal surface, can be tried to overcome this problem, also a solvent or coolant can be applied to avoid sticking. On the other hand, most film blowing or extrusion grades can be measured without greater difficulties.

The advantages of this experimental set-up, Rheotens plus extruder, can be summarised as

follows: the extruder provides a continuous process, in which high flow rates and short residence times can be realised. It can be operated at constant pressure as well as at constant flow rate. However, it is not suitable for probing small amounts of material. For this purpose, the combination of a Rheotens with a capillary rheometer is recommended.

There are two types of Rheotens testers available, the design shown in fig. 2.1 with two turning wheels and the data acquisition program Extens, and the new design with a second pair of wheels below the first one. This lower pair of wheels does not influence the measurement but directs the strand downwards to avoid sticking. This can be advantageous for low viscosity materials, but causes problems for materials with high extrudate swell because then the gap between the second pair of wheels is too narrow. The maximum velocity of the new Rheotens was extended to 1800 mm/s compared to the old one which is limited to 1200 mm/s. The new data acquisition program Rheotens.97 has a higher resolution of force and velocity signal than Extens. Most of the experiments reported here were measured with the old Rheotens as the new one was only available from 1999 onwards.

2.2 Evaluation of spinline profiles by means of Laser-Doppler velocimetry (LDV)

If one wants to derive elongational viscosity values from Rheotens curves, the local elongation rate $\dot{\epsilon}(x)$ at each point of the spinline needs to be known. This information does not result from the Rheotens curve directly but can be measured contact-free by optical methods. The procedure used was to keep the velocity of the Rheotens wheels constant, measure the force at steady-state condition, and evaluate the velocity of the strand along the spinline with a Laser-Doppler velocimeter (fig 2.5). The instrument used is a LSV-065 manufactured by Polytec [43].

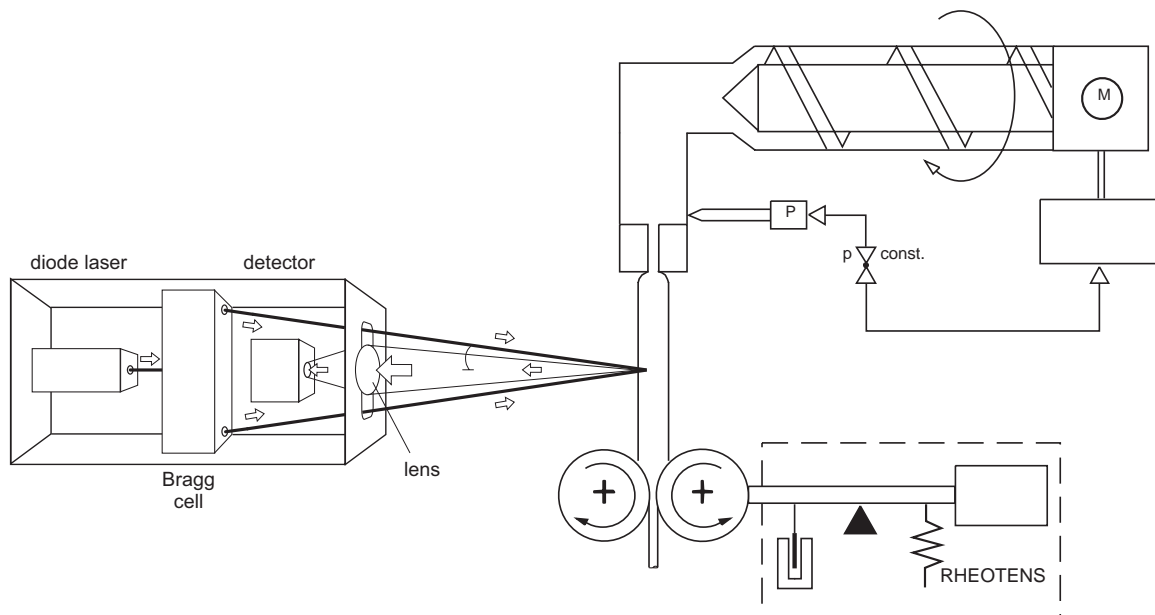


Figure 2.5: Experimental set-up including Laser-Doppler velocimeter.

A laser beam (wavelength 760 nm, power 10 mW) is splitted into two parts which are focused on the surface of the flowing polymer melt. The reflected signal is detected by an optical system.

It is transmitted to the control unit LSV-200 and evaluated by Fast Fourier Transformation, resulting in an absolute velocity value. The distance between laser and polymer strand is approximately 100 mm and needs to be focused in such a way that the two laser beams meet exactly at the centre of the strand surface. With accurate adjustment of the beam it is possible to measure even colourless polymer melts without adding tracer particles.

The laser is mounted onto a tripod with a scale, so it can be moved up and down along the spinline. Usually, for a spinline length of 100 mm, measurement points were taken in 5 mm steps from the die exit downwards to the wheels. The tripod used for the experiments was adjusted manually with an accuracy of ± 1 mm. This could be increased considerably by positioning the laser with a computer controlled step motor.

Fig. 2.6 gives a typical example of velocity profiles along the spinline for different draw ratios, while the corresponding Rheotens curve is given in fig. 2.7. It can be seen that close to the die, the velocity in the spinline is lower than the extrusion velocity v_0 due to extrudate swell, but with higher drawdown velocity swelling is prevented by a higher pulling force. For moderate draw ratios, the velocity increases nearly linear with the distance from the die, which has been described as constant strain rate spinning by Shridhar [47]. For higher draw ratios, this increase is overproportional, resulting in the thinning of the strand radius r , which is shown in fig. 2.8. The local spinline radius $r(x)$ is calculated from the local velocity $v(x)$ by

$$r(x) = \frac{D_0}{2} \sqrt{\frac{v_0}{v(x)}} \quad (2.2)$$

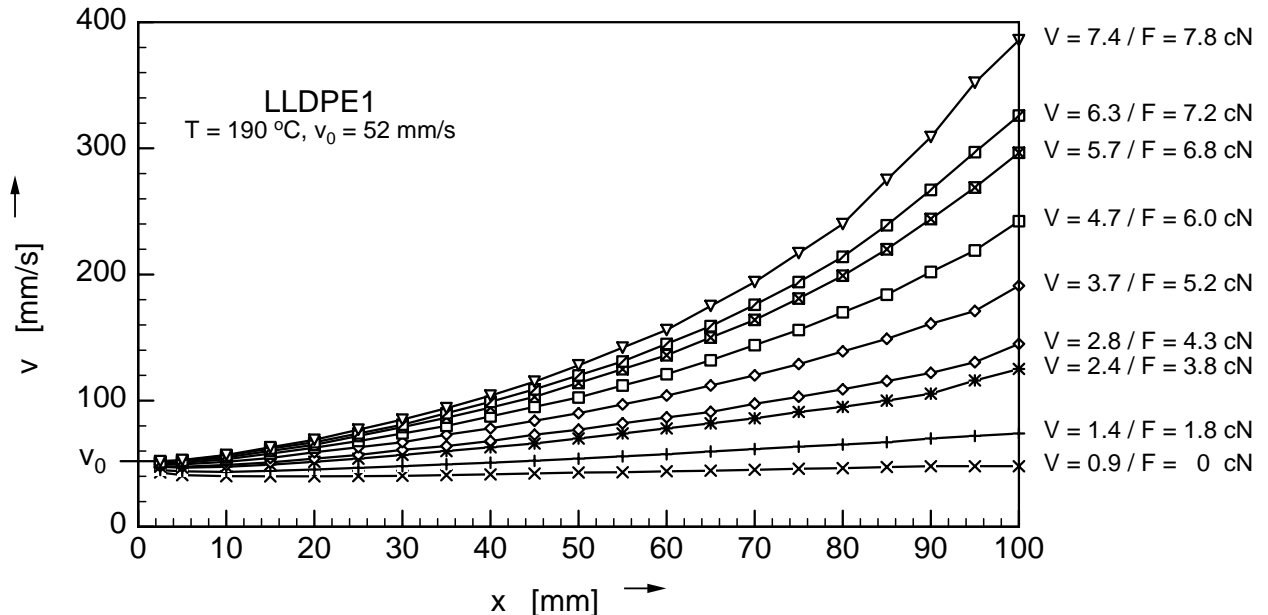


Figure 2.6: Velocity profile along spinline length x for different draw ratios.

As velocity measurements are taken under stationary conditions, no data can be obtained for the draw resonance region because of velocity and force fluctuations. The velocity at the Rheotens wheels is measured by two independent methods: (1) by the speed of rotation of the Rheotens

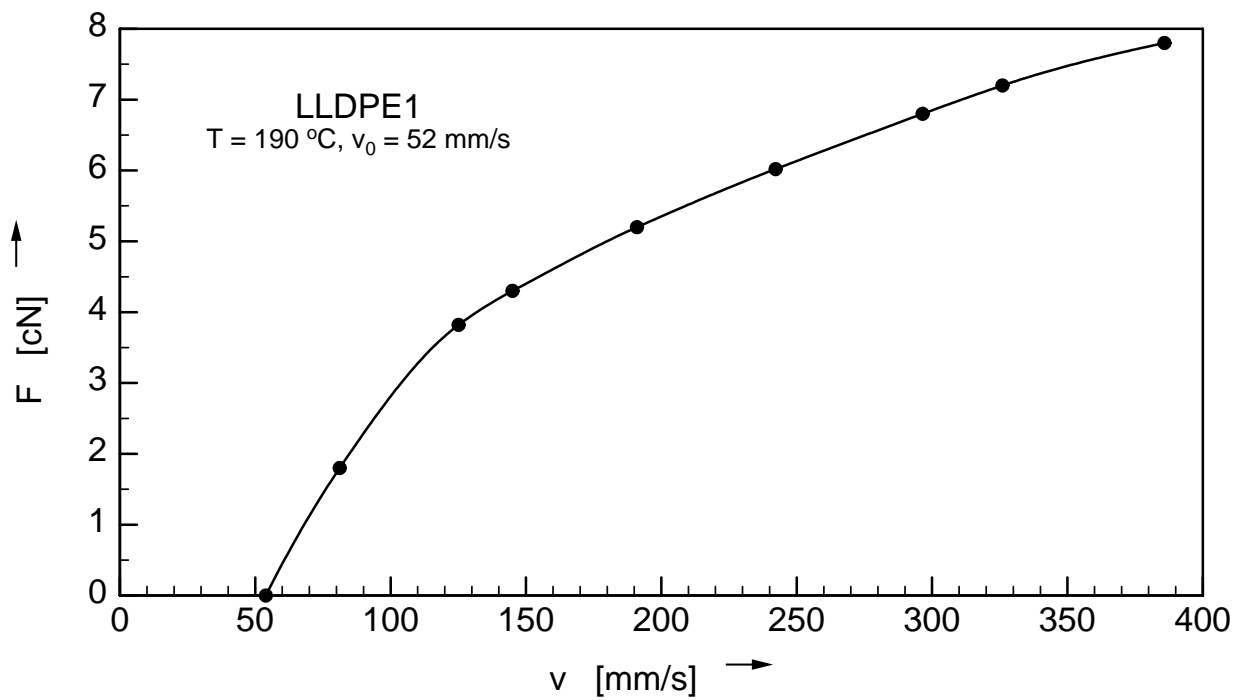


Figure 2.7: Rheotens curve (stationary condition) derived from fig. 2.6.

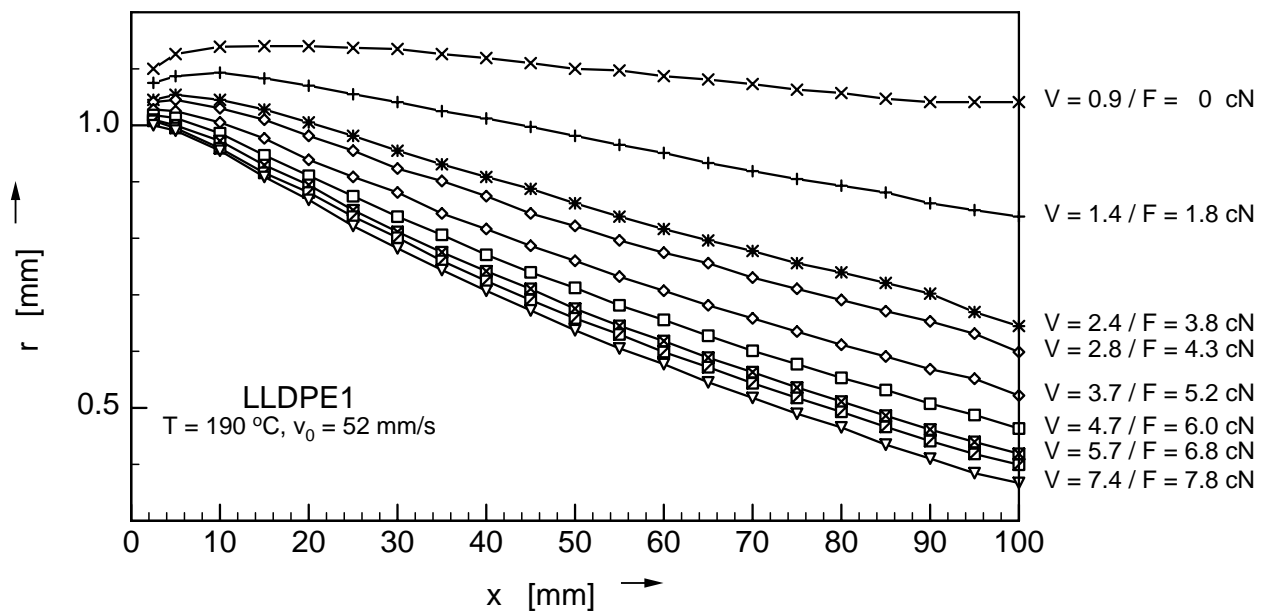


Figure 2.8: Filament radius r along spinline length x derived from velocity profiles of fig. 2.6.

wheels, which is measured together with the pulling force, and (2) by the optical system. In the example given in fig. 2.6 and 2.7, the two velocity values agree very well. Still, as can best be seen in fig. 2.8, the measured velocity values close to the wheels lead to small discontinuities in the fibre radius, which must be attributed to experimental error. Possible sources of error, for example slip at the Rheotens wheels, are discussed in the following paragraphs.

Depending on the gap between the Rheotens wheels, it might be impossible to measure the actual velocity of the polymer between the wheels, as the laser beam has a diameter of around 1.5 mm. If the gap is smaller, for example for materials which do not exhibit extrudate swell or at high draw ratios, the velocity of the metal wheels is measured instead of the velocity of the polymer, or no valid signal can be obtained at all. But under constant force extension, the velocity at a certain distance from the die is independent of the overall spinline length, which is illustrated in fig. 2.9. It needs to be noted that experiments under constant force conditions are difficult to perform, as already small variations of the force signal can lead to considerable changes of the corresponding velocity, which explains the small deviations visible.

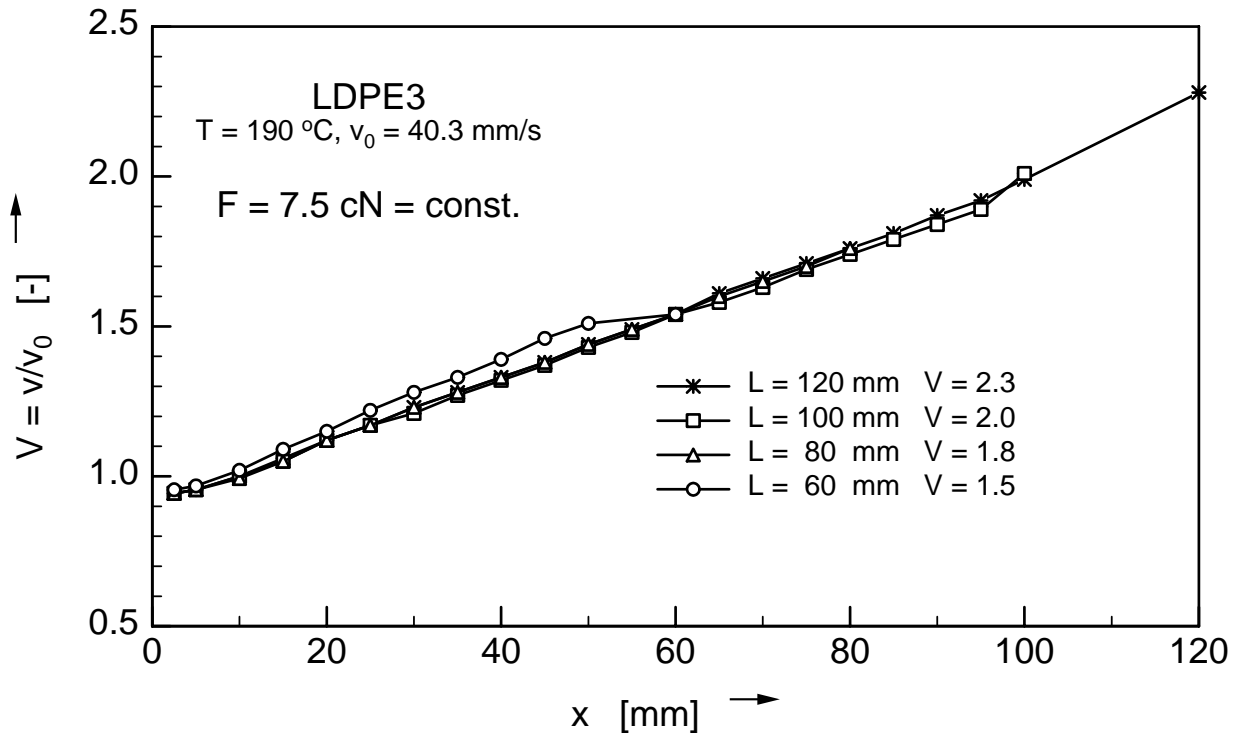


Figure 2.9: Velocity profile for different spinline length L under constant force extension.

The result of fig. 2.9 can be used to overcome the experimental problem of measuring end effects at the wheels: Only the spinline up to a certain distance from the wheels is taken into account. The draw ratio corresponding to this reduced spinline length is calculated from the velocity measurement of the LDA. This spinline length and the corresponding draw ratio are then used to recalculate the whole Rheotens curve. Uncertainties originating for example from slip at the wheels are thus eliminated.

If slip is present between the polymer melt and the Rheotens wheels, this alters the shape of the Rheotens curve considerably. For a material with high extrudate swell, fig. 2.10 shows the discrepancy between the laser measurement and the real Rheotens wheel velocity at the end of the spinline, which cannot be attributed to measurement errors only. It indicates that

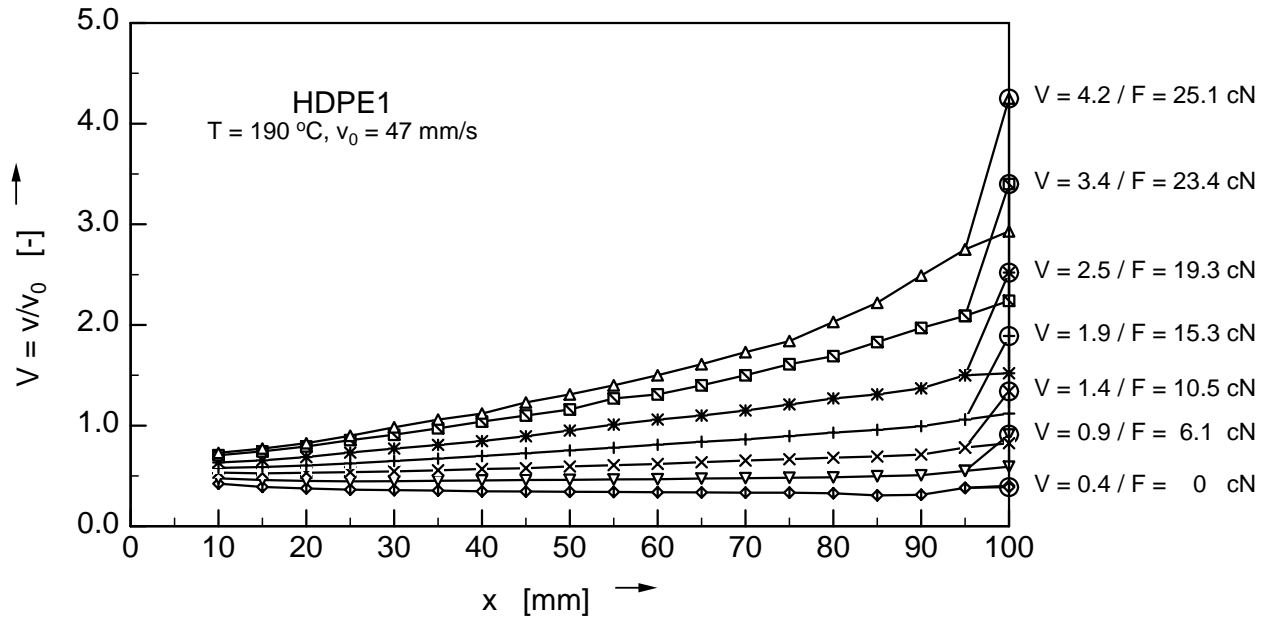


Figure 2.10: Velocity profile along spinline. Imposed velocity of the Rheotens wheels is indicated by open circles. Constant gap between the wheels.

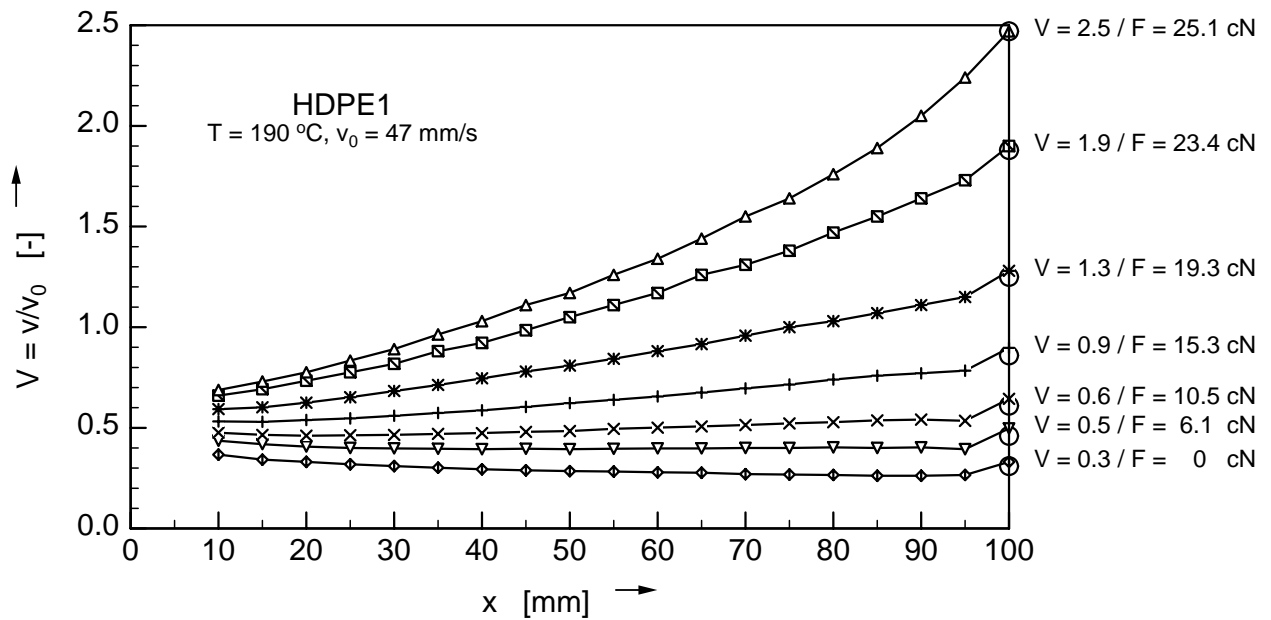


Figure 2.11: Velocity profile along spinline. Imposed velocity of the Rheotens wheels is indicated by open circles. The gap between the wheels is narrowed down with increasing drawdown.

slip is present between the strand and the wheels. The gap between the Rheotens wheels was set to 2 mm for all draw ratios. On the other hand, as illustrated in fig. 2.11 for the same extrusion conditions, the problem of slip at the wheels can be reduced by narrowing the gap with increasing drawdown. During this experiment the gap was reduced to 1.2 mm for the highest drawdown force. However, this is only possible if the velocity is increased stepwise, and not in the automatic acceleration mode.

If Rheotens curves are measured to obtain technological information, quite often it will be sufficient to do without the time consuming evaluation of the spinline velocity. As high extrudate swell increases the problem of slip, it is advantageous to reduce swell by using long extrusion dies and a smooth entry cone for the measurements. Also, measurements with constant acceleration should be reproduced with a stepwise increase of velocity to probe if slip influences the result.

However, if more detailed information is demanded, for example to compare the measurements to simulation results, the velocity distribution along the spinline is an important information to quantify the predictability of constitutive equations and numerical schemes. Experimental difficulties with end effects at the wheels should then be overcome by evaluating the draw ratio at a reduced spinline length and relying on the accuracy of the velocity measurement with the Laser-Doppler velocimeter rather than the nominal velocity data indicated by the Rheotens.

2.3 Material Characterisation

In the following section, the material properties of the polymers investigated are listed. The emphasis of the experimental work is on branched low density polyethylene melts (LDPE1 - LDPE9), but also linear low (LLDPE1 - LLDPE2) and high density polyethylene (HDPE1 - HDPE2) was investigated. A linear polypropylene (PP1) was compared to a branched one (PP2). In addition to the semi-crystalline polymers mentioned so far, the amorphous materials polystyrene (PS1) and polycarbonate (PC1 - PC3) were investigated.

Tabs. 2.2 - 2.7 give an overview of the material properties as given by the material suppliers. Not all product names and suppliers of the resins can be mentioned due to confidentiality. In addition, measurements of storage and loss modulus and the complex viscosity of the polymers are documented in Appendix A. The linear relaxation time spectrum at a reference temperature of 260 °C for polycarbonate and 190 °C for all other materials is also included into figs A.1 - A.17.

The material selection was influenced by the shear viscosity level of the melts, as a low viscosity would cause experimental problems for the Rheotens test, like sticking of the polymer strand to the wheels of the Rheotens, or a too small force signal. Therefore suitable resins are extrusion, film blowing, or blow moulding grades, and not injection moulding or spinning materials.

Low Density Polyethylene (LDPE)

The LDPE melts selected differ in the production process. While LDPE1-LDPE6 were produced in a tubular reactor, LDPE7-LDPE9 originate from an autoclave reactor, which causes a different branching structure [23]. LDPE1 was the standard material for the Rheotens test, as it was used for many basic investigations, like the reproducibility of the experiment. This

melt is similar to the well known Melt I from the investigations of the IUPAC Working Party on Structure and Properties of Commercial Polymers [36]. Melts LDPE4 - LDPE9 have the same density at room temperature. Therefore all differences the materials exhibit can be related to differences in average molar mass, molar mass distribution, or branching structure.

| Name | Resin | $MFI_{190/2.16}$ [g/10min] | $\eta_{0190^{\circ}C}$ [Pas] | $\rho_{23^{\circ}C}$ [kg/m ³] | M_w [g/mol] | M_w/M_n | T_m [°C] |
|-------|--------------------|-------------------------------|---------------------------------|--|------------------|-----------|---------------|
| LDPE1 | Lupolen 1800H/BASF | 1.46 | 17000 | 919 | 300000 | 17.6 | 108 |
| LDPE2 | Lupolen 3020D/BASF | 0.25 | 72400 | 926 | 248000 | 13.4 | 114 |
| LDPE3 | Lupolen 3040D/BASF | 0.25 | 69700 | 927 | 215000 | 11.3 | 115 |
| LDPE4 | | 0.95 | 21700 | 924 | 119000 | 4.85 | |
| LDPE5 | | 2.1 | 8240 | 923 | 113000 | 5.82 | |
| LDPE6 | Lupolen 2410F/BASF | 0.7 | 28800 | 924 | 144000 | 6.7 | 130 |
| LDPE7 | | 0.3 | 59100 | 921 | 175000 | 12 | |
| LDPE8 | | 0.93 | 15600 | 921 | 130000 | 5.95 | |
| LDPE9 | | 2.1 | 5740 | 921 | 115000 | 6.8 | |

Table 2.2: Material properties of LDPE melts.

Linear Low Density Polyethylene (LLDPE)

The two LLDPE melts have the same MFI, but were produced with different catalysts and therefore exhibit a different branching structure. Affinity PL1880 is a polyolefine plastomer (POP), produced by a metallocene catalyst, while the ethylene octene copolymer Dowlex NG5056E was produced by a conventional Ziegler-Natta catalyst.

| Name | Resin | $MFI_{190/2.16}$ [g/10min] | $\eta_{0190^{\circ}C}$ [Pas] | $\rho_{23^{\circ}C}$ [kg/m ³] | M_w [g/mol] | M_w/M_n | T_m [°C] |
|--------|-------------|-------------------------------|---------------------------------|--|------------------|-----------|---------------|
| LLDPE1 | PL1880/DOW | 1.04 | 7950 | 902 | 116400 | 2.1 | 103 |
| LLDPE2 | NG5056E/DOW | 1.04 | 12650 | 920 | 105000 | 3 | 119 |

Table 2.3: Material properties of LLDPE melts.

High Density Polyethylene (HDPE)

Both high density polyethylene melts have a broad molecular weight distribution and no measurable amount of long-chain branching. They show similar molecular characteristics but differ in processing behaviour.

| Name | Resin | $MFI_{190/5}$ [g/10min] | $\eta_{0190^{\circ}C}$ [Pas] | $\rho_{23^{\circ}C}$ [kg/m ³] | M_w [g/mol] | M_w/M_n | T_m [$^{\circ}C$] |
|-------------|--------------------|----------------------------|---------------------------------|--|------------------|-----------|--------------------------|
| HDPE1 | Stamylan 8621/DSM | 0.98 | 275000 | 958 | 205000 | 34 | 131 |
| HDPE2 | Stamylan X1010/DSM | 1.15 | 71700 | 957 | 195000 | 35 | 131 |

Table 2.4: Material properties of HDPE melts.

Polypropylene (PP)

PP1 is a linear polypropylene homopolymer, while PP2 was treated with irradiation and therefore has long-chain branches. PP2 was thoroughly investigated by Kurzbeck [24], [25]. The material was provided from the University of Erlangen.

| Name | Resin | $MFI_{230/2.16}$ [g/10min] | $\eta_{0190^{\circ}C}$ [Pas] | $\rho_{23^{\circ}C}$ [kg/m ³] | M_w [g/mol] | M_w/M_n | T_m [$^{\circ}C$] |
|-------------|--------------------|-------------------------------|---------------------------------|--|------------------|-----------|--------------------------|
| PP1 | Novolen 1100H/BASF | 2.4 | 24600 | 910 | | | 163 |
| PP2 | | 3.9 | 23700 | 909 | 586600 | 9.5 | 162 |

Table 2.5: Material properties of PP melts.

Polystyrene (PS)

PS1 is a standard polystyrene and was used as an example for an amorphous material.

| Name | Resin | $MFI_{200/5}$ [cm ³ /10min] | $\eta_{0190^{\circ}C}$ [Pas] | $\rho_{23^{\circ}C}$ [kg/m ³] | T_g [$^{\circ}C$] |
|-------------|--------------|---|---------------------------------|--|--------------------------|
| PS1 | PS 168N/BASF | 1.15 | 97000 | 1050 | 100 |

Table 2.6: Material properties of melt PS1.

Polycarbonate (PC)

The polycarbonate melts have been investigated in order to correlate their rheological properties with the results of extrusion experiments by Krohmer [21], [22].

| Name | Resin | <i>MFI</i> [g/10min] | $\eta_{0260^{\circ}C}$ [Pas] | $\rho_{23^{\circ}C}$ [kg/m ³] | T_m [$^{\circ}C$] |
|-------------|----------------|---------------------------------|---------------------------------|--|--------------------------|
| PC1 | Lexan/GE | 8.7 (300 $^{\circ}C$, 2.16 kg) | 5810 | 1200 | |
| PC2 | Makrolon/Bayer | 10.4 (300 $^{\circ}C$, 1.2 kg) | 1800 | 1200 | 148 |
| PC3 | Makrolon/Bayer | 2.2 (300 $^{\circ}C$, 1.2 kg) | 14400 | 1200 | 148 |

Table 2.7: Material properties of PC melts.

3 Rheotens Mastercurves

In the original contribution introducing the Rheotens test [35], Meissner suggested to compare different materials on the basis of a constant mass flow rate through the extrusion die. This procedure was followed by many investigators [17], [18], [16], [32], and can be used for a qualitative comparison of different materials. Effects of branching structure as well as viscosity differences of the materials can be observed by this method, but they cannot be separated from each other.

In the following section a concept of mastercurves suggested by Wagner et. al. [53], [56], [52] is introduced, which is based on comparison of Rheotens curves at constant extrusion pressure and consequently constant wall shear stress. Using the extrusion pressure as a reference is derived from investigations e.g. of Han [20], who showed that extrudate swell of a polymer is temperature dependent if measured as a function of the wall shear rate, and is temperature independent, if measured as a function of the wall shear stress.

3.1 Temperature Invariant Mastercurves

Verification of Temperature Invariance

Fig. 3.1 shows Rheotens curves $F(v)$ of melt HDPE1 at an extrusion pressure of 95 bar at five different temperatures. From these, the stress curves $\sigma(v)$ in fig. 3.2 can be derived. σ is the real stress at the end of the spinline between the Rheotens wheels,

$$\sigma = \frac{F}{A} = \frac{FV}{A_0}, \quad (3.1)$$

where A is the cross section of the strand at the end of the spinline, A_0 the cross section of the die and V the drawdown ratio,

$$V = \frac{v}{v_0}. \quad (3.2)$$

For thermo-rheologically simple materials, the time-temperature superposition principle is valid [46]. For semi-crystalline polymers, it can be described by the Arrhenius equation with a shift factor a_T ,

$$a_T = \exp \left[\frac{E}{R} \left(\frac{1}{T} - \frac{1}{T_{ref}} \right) \right], \quad (3.3)$$

with E being the activation energy, R the gas constant, and T and T_{ref} absolute values of the temperature in Kelvin.

The flow rate at different temperatures and at constant extrusion pressure is inverse proportional to a_T ,

$$v_0(T) = a_T^{-1} v_0(T_{ref}). \quad (3.4)$$

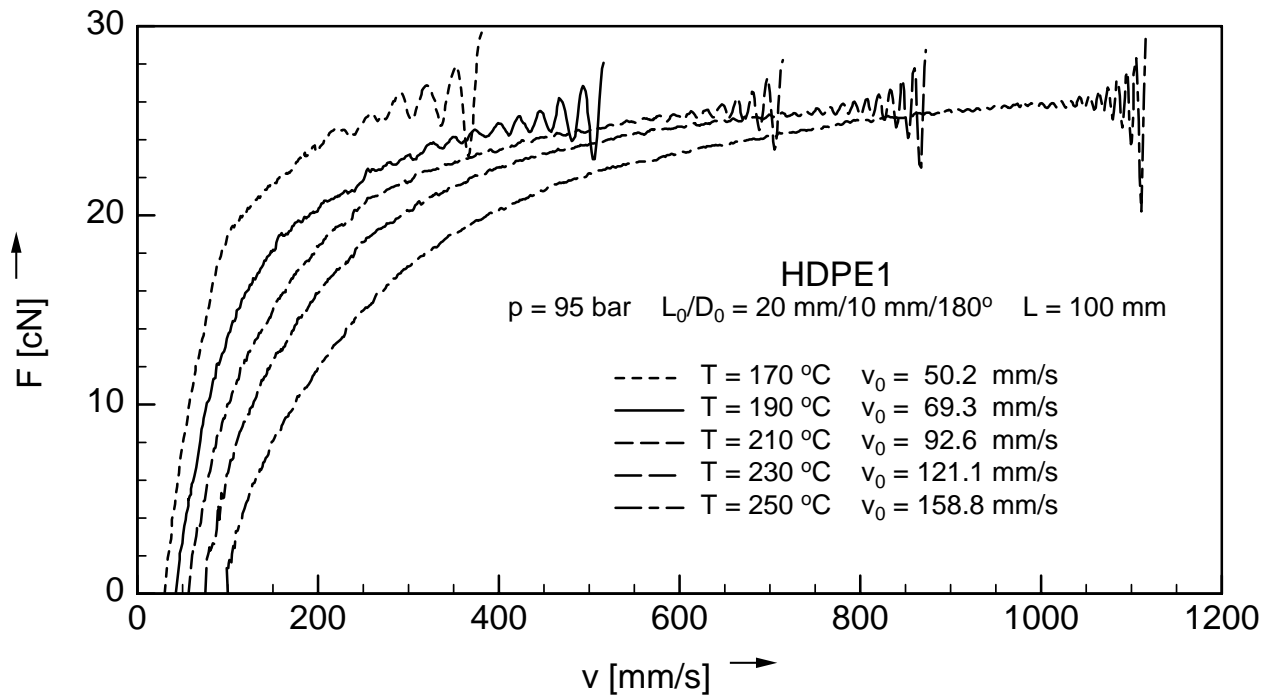


Figure 3.1: Rheotens curves $F(v)$ for melt HDPE1. $p = 95 \text{ bar}$, $T = 170 \text{ }^\circ\text{C} - 250 \text{ }^\circ\text{C}$.

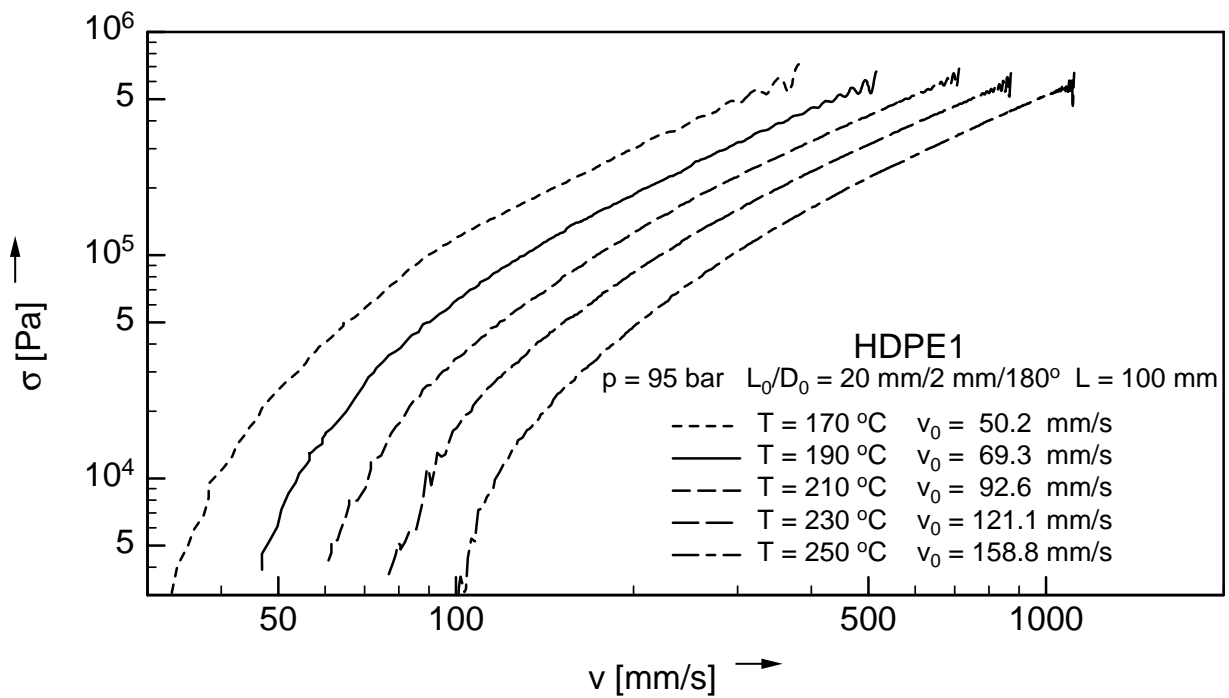


Figure 3.2: Rheotens curves $\sigma(v)$ for melt HDPE1. $p = 95 \text{ bar}$, $T = 170 \text{ }^\circ\text{C} - 250 \text{ }^\circ\text{C}$.

Investigations of Han [20] prove that extrudate swell at the exit of a capillary die is constant at constant wall shear stress independent of temperature. A swell ratio SR can be defined as

$$SR = \sqrt{\frac{v_0}{v_s}}, \quad (3.5)$$

with v_0 being the extrusion velocity and v_s the real strand velocity at $F = 0$, where swelling occurs undisturbed of the drawdown force. Tab. 3.1 gives the swell ratios for melt HDPE1 corresponding to the Rheotens curves shown in fig. 3.1:

| T [$^{\circ}\text{C}$] | v_0 [mm/s] | v_s [mm/s] | SR |
|----------------------------|-------------------------|-------------------------|------|
| 170 | 50.2 | 30.1 | 1.29 |
| 190 | 69.3 | 42.5 | 1.28 |
| 210 | 92.6 | 57.1 | 1.27 |
| 230 | 121.1 | 73.2 | 1.29 |
| 250 | 158.8 | 95.2 | 1.29 |

Table 3.1: Extrudate swell of melt HDPE1 at $p = 95$ bar and $T = 170$ $^{\circ}\text{C}$ - 250 $^{\circ}\text{C}$.

It can be seen that the swell ratio is indeed the same for all temperatures within experimental error. So the differences of the Rheotens curves at different temperatures result not from their swelling behaviour but are caused by the dependence of flow rate on extrusion temperature. As this is described by the shift factor a_T , a mastercurve can be obtained by a shifting procedure. Dividing the velocity of the Rheotens wheels v by the extrusion velocity v_0 causes all experimental curves to fall together onto a mastercurve, which is given in fig. 3.3 as a function of the drawdown force $F(V)$, and in fig. 3.4 as a function of the stress $\sigma(V)$ at the Rheotens wheels.

Temperature invariant Rheotens mastercurves can also be reported for other linear polymers like PP (fig. 3.5). Exceptions at temperatures close to the melting point are found, which have been explained as flow-induced crystallisation for example by Ghijssels [16]. Temperature invariant Rheotens mastercurves exist for long-chain branched polymers like LDPE [56] (fig. 3.6) as well.

The existence of Rheotens mastercurves has certain experimental advantages: homopolymers with strongly different melting points or melt indices are directly comparable irrespective of the melt temperature if investigated at constant pressure, thus avoiding problems with a very low force signal caused by a low viscosity at high temperatures. Also, the temperature can be selected in such a way, that no melt fracture is visible on the polymer strand. Melt strength differences of different homopolymers investigated at constant pressure can directly be attributed to structural differences of the materials considered.

Exceptions from Temperature Invariance Caused by Wall Slip

In fig. 3.3, a demonstration of temperature invariant Rheotens mastercurves is given for melt HDPE1 at a pressure of 95 bar. For the same material, Rheotens curves at various temperatures have been measured at 125 bar (fig. 3.7). Surprisingly, extrusion at 170 $^{\circ}\text{C}$ results in a

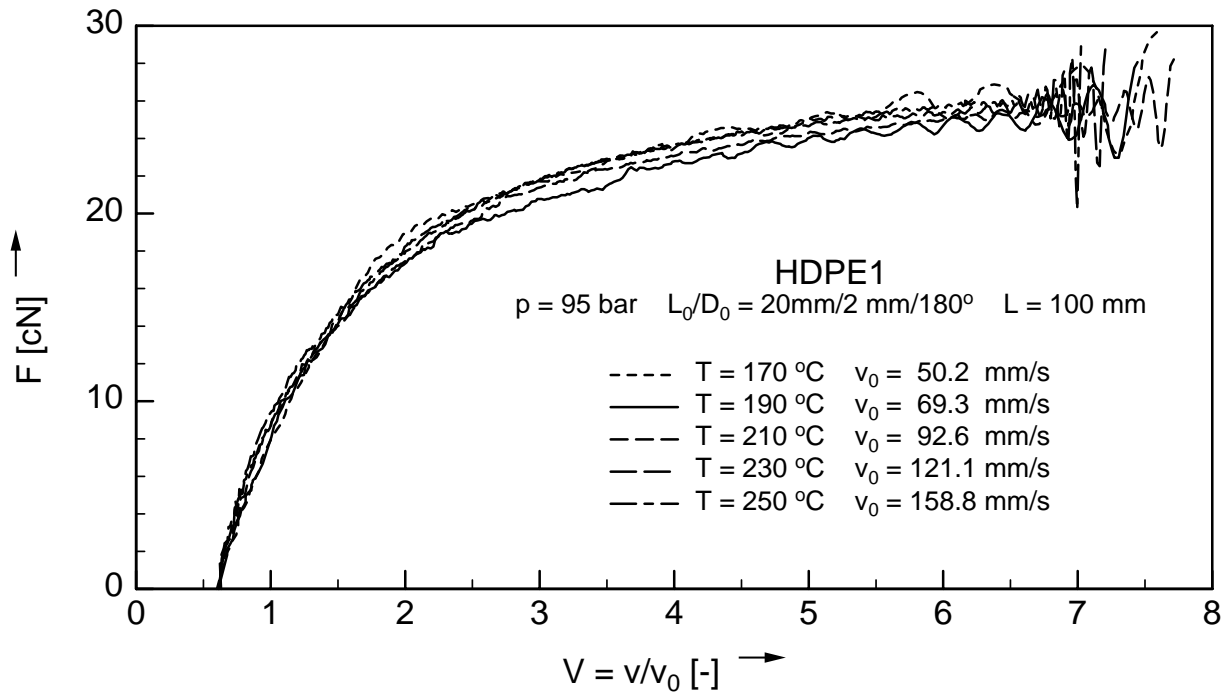


Figure 3.3: Temperature invariant Rheotens mastercurve $F(V)$ for melt HDPE1. $p = 95 \text{ bar}$.

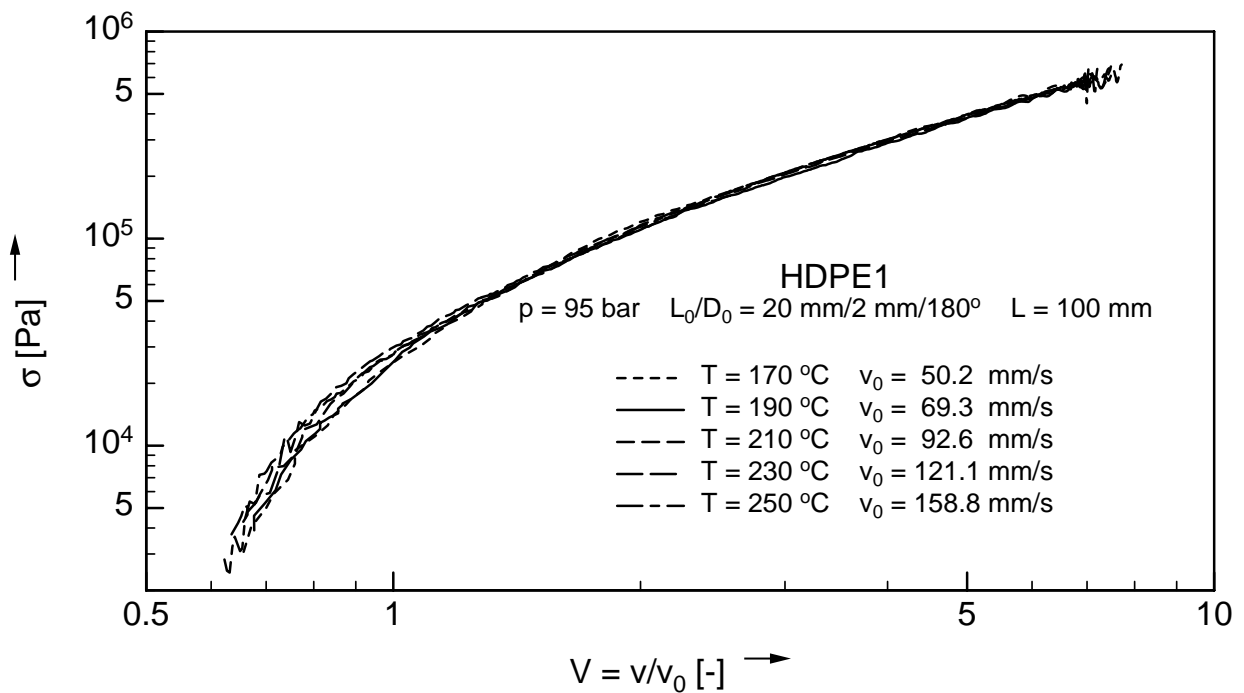


Figure 3.4: Temperature invariant Rheotens mastercurve $\sigma(V)$ for melt HDPE1. $p = 95 \text{ bar}$.

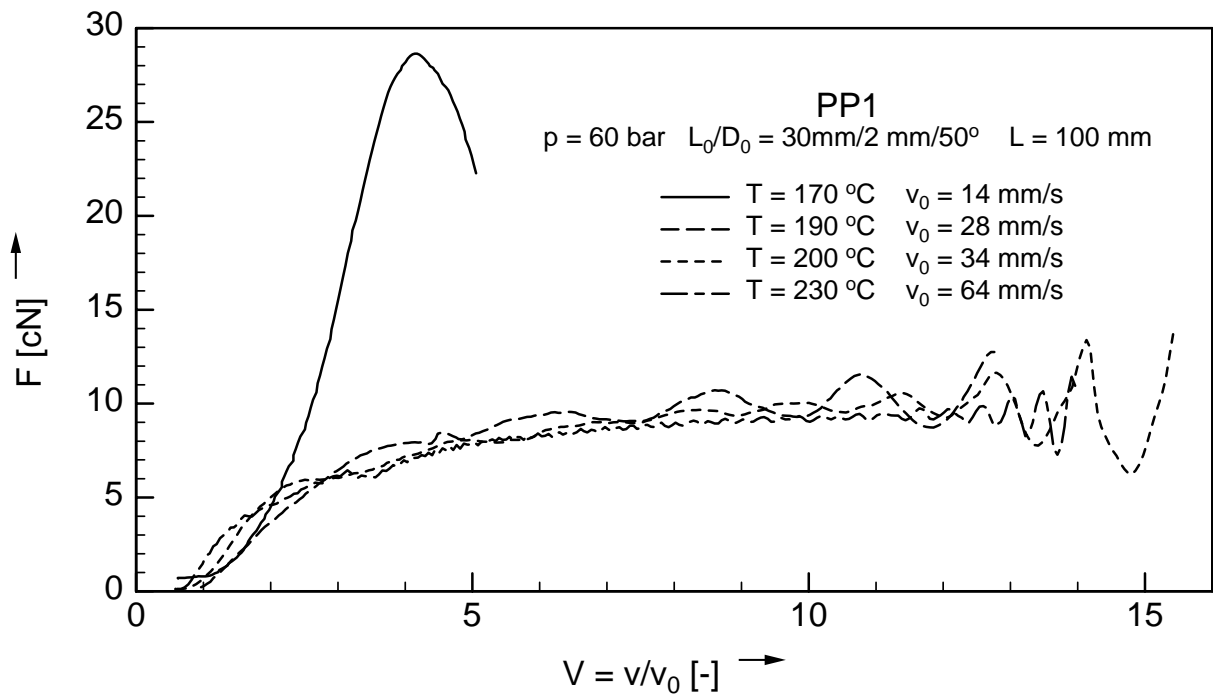


Figure 3.5: Temperature invariant Rheotens mastercurve for melt PP1. Exception from temperature invariance at $T = 170\text{ °C}$ due to stress induced crystallisation.

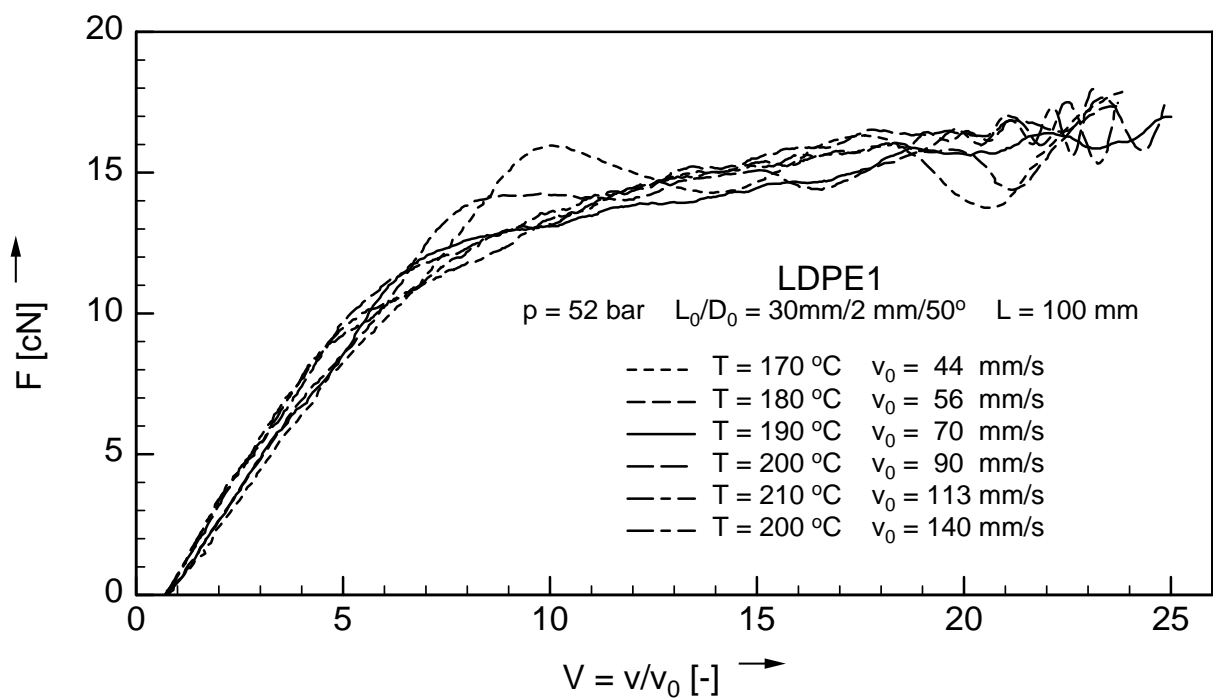


Figure 3.6: Temperature invariant Rheotens mastercurve for melt LDPE1.

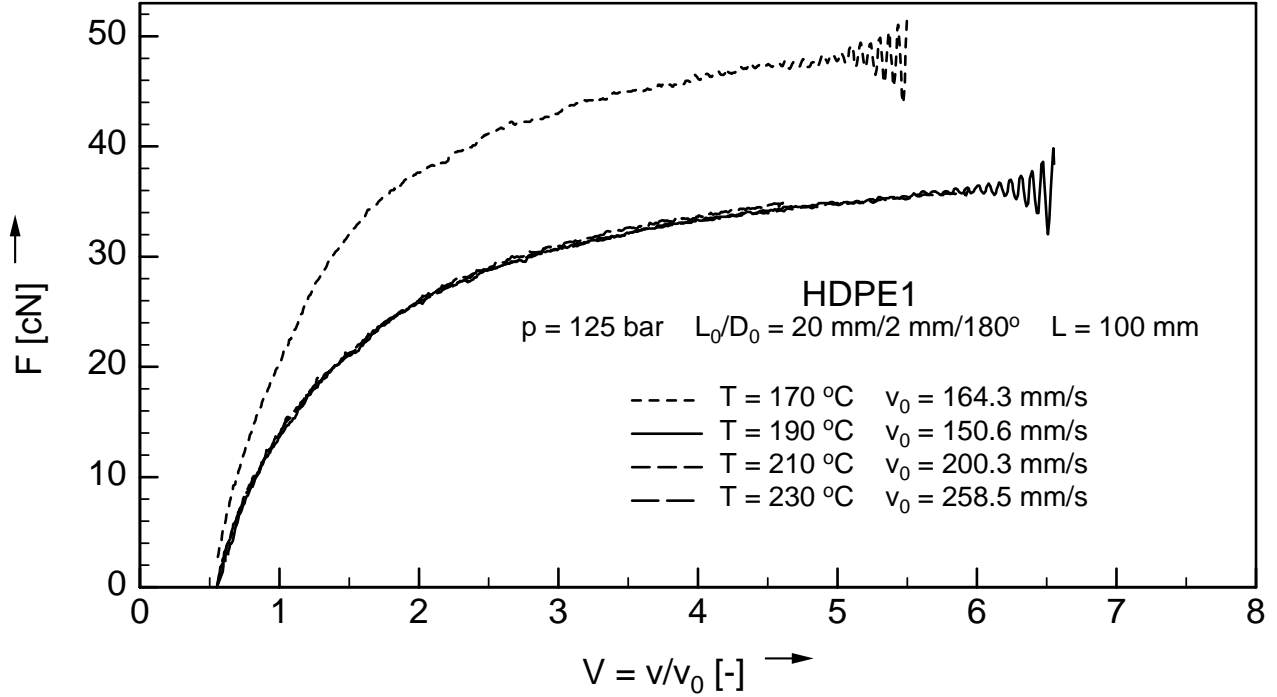


Figure 3.7: Rheotens curves $F(V)$ for melt HDPE1. $p = 125$ bar, $T = 170$ °C - 230 °C.

significantly higher force level than observed at higher temperatures, for which invariance is found again. In addition, it can be seen that the flowrate for the experiment at 170 °C is higher than the flowrate at 190 °C. Measuring the output characteristic of the extruder at 170 °C shows that at a pressure of 114 bar, corresponding to an apparent wall shear stress τ_{ap} of approximately 0.29 MPa, a sudden change towards wall slip conditions (stick-slip transition) is visible as the flowrate increases at approximately constant pressure. At higher pressures, the output characteristic at an extrusion temperature of 170 °C stays above the one at 190 °C. This indicates that at 170 °C a stick-slip transition occurs at 114 bar.

To investigate wall slip in more detail, additional capillary rheometry was carried out. An automatic nitrogen pressure driven capillary rheometer (AKVM), which was developed by the Polymer Laboratory of BASF AG [28], [31] was used for this purpose. The extrusion pressure for this type of capillary rheometer is imposed by nitrogen gas. Hence the pressure can be measured and controlled accurately. The mass flow rate is measured directly by the displacement of a floating piston on top of the polymer melt. Flow curves with imposed pressure can be measured with high precision.

Following the method of Mooney [40], wall slip is analysed as follows: as long as the material sticks to the wall, the shear stress/shear rate relation is unique and independent of die radius. As soon as the material starts to slip at the wall, a dependence of the apparent shear rate on the die radius R is observed. To calculate the effective wall shear rate, a slip component has to be subtracted from the apparent shear rate. Stick-slip transition is indicated by an increase of shear rate at constant shear stress.

For melt HDPE1, capillary rheometry with four different dies was carried out and is reported in [8]. As a result the critical stress at which the stick-slip transition occurs is confirmed. It

can be seen in fig. 3.8 that for 170 °C, stick-slip transition is found at a pronounced lower wall shear stress (approximately 0.29 MPa as in the output characteristic of the extruder) than for higher temperatures, explaining the deviation of the 170 °C Rheotens curve in fig. 3.7. This particular wall slip phenomenon has already been described by Wang [59], [58] as low temperature anomaly for linear polyethylene melts.

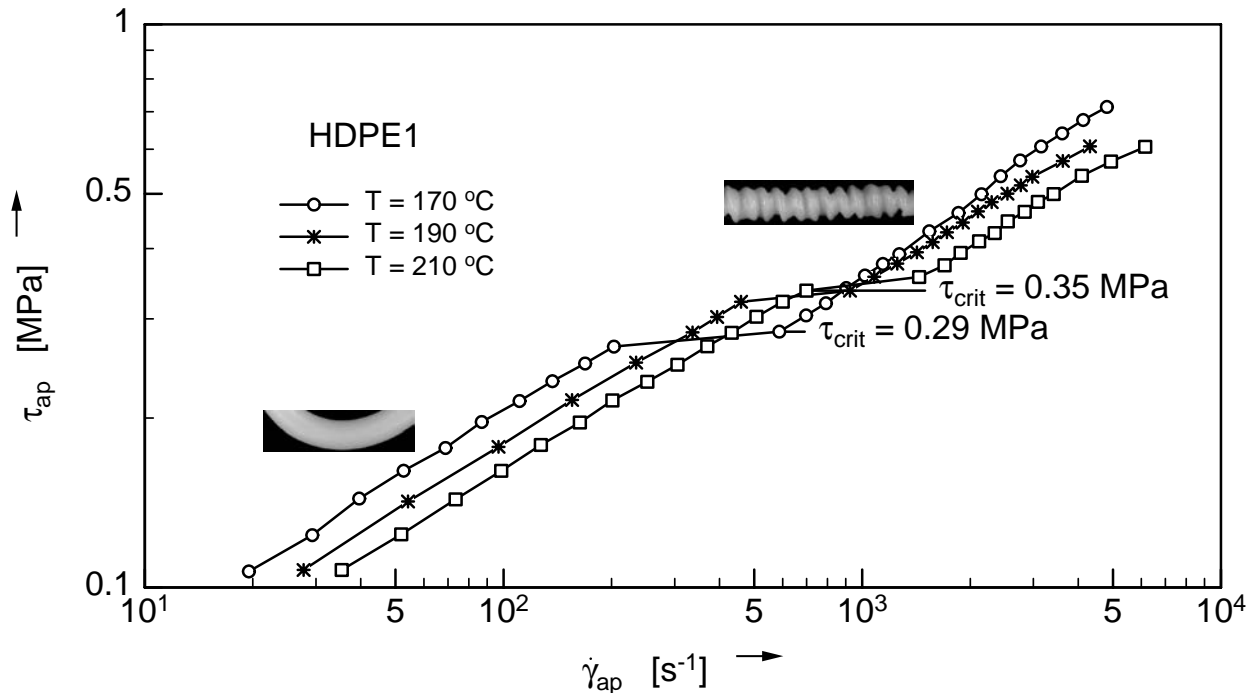


Figure 3.8: Apparent wall shear stress as a function of apparent shear rate for melt HDPE1 at 170 °C, 190 °C, and 210 °C. Surface distortions visible above the stick-slip transition.

A similar effect can be reported for another linear Polyethylene melt, LLDPE2 [8]: again stick-slip transition causes a sudden deviation of Rheotens curves to higher force levels. But already at shear stresses below the stick-slip transition this material exhibits partial wall slip (fig. 3.9), resulting in a gradual deviation of the Rheotens curve from the mastercurve (fig. 3.10). The effect is temperature dependent, at lower temperatures higher absolute wall slip velocities are found by Mooney’s method. For this particular material slip has also been reported by Lee and Mackley [33], who showed that a slip boundary condition is necessary to model extrusion of LLDPE2 correctly.

Summarising this section it can be said that while for branched polyethylene melts Rheotens mastercurves are found at constant wall shear stress independent of temperature, linear polyethylene melts can exhibit wall slip causing deviations from the mastercurve.

3.2 Molar Mass Invariant Mastercurves

A similar argument as above can be used to prove that Rheotens curves of polymer melts differing in molar mass are invariant with respect to the average molar mass M , if their relative molar mass distribution MWD is similar. The molar mass shift factor a_M is given by

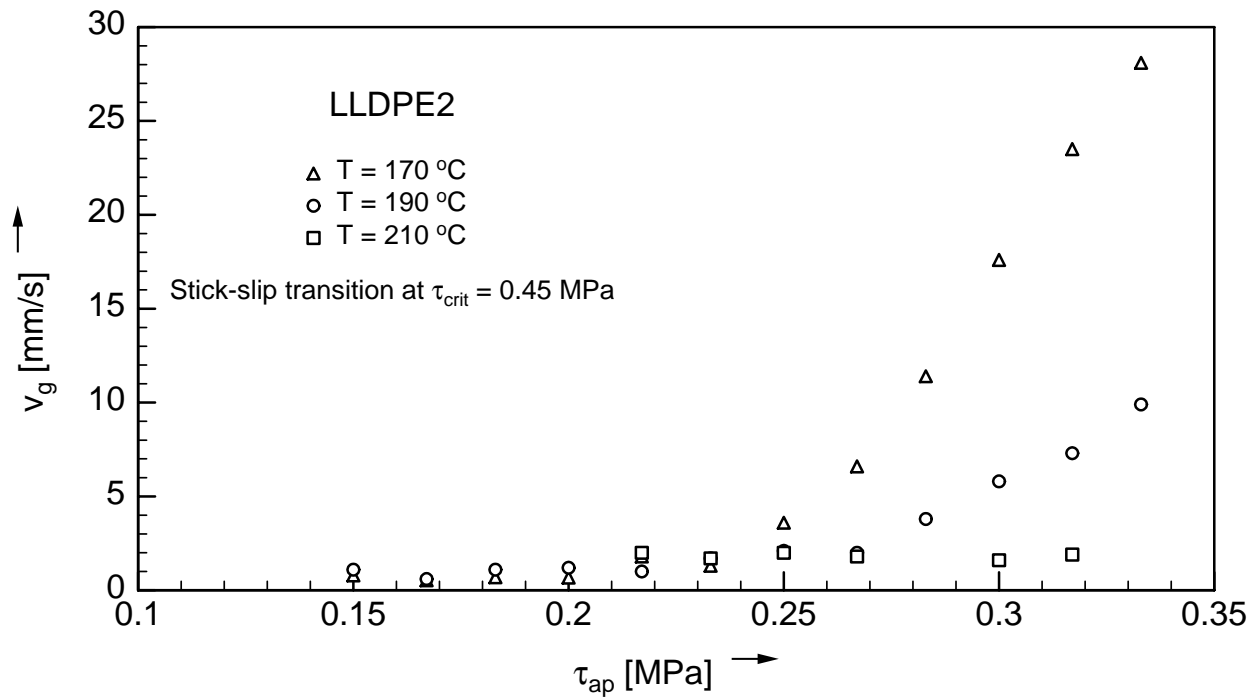


Figure 3.9: Temperature dependent wall slip velocity v_g at shear stresses below the stick-slip transition for melt LLDPE2.

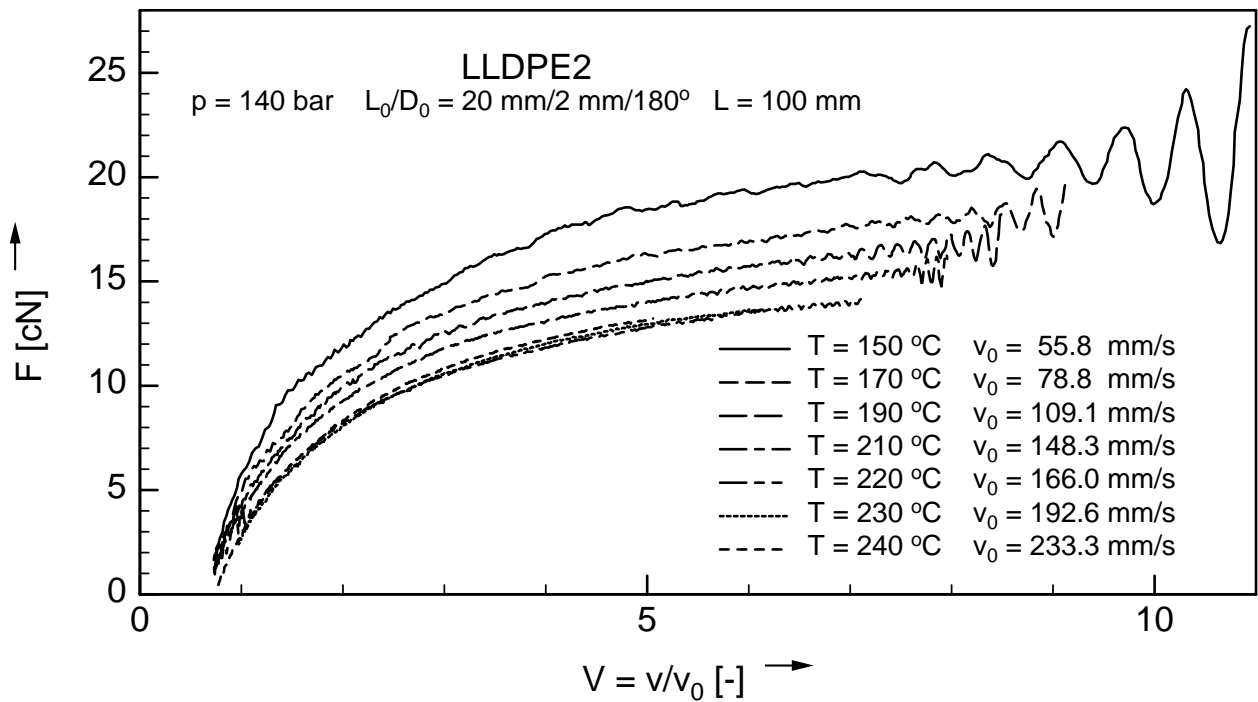


Figure 3.10: Rheotens curves $F(V)$ for melt LLDPE2. $p = 140$ bar, $T = 150$ °C - 240 °C.

$$a_M = \frac{\eta_0(M)}{\eta_0(M_{ref})} = \left(\frac{M}{M_{ref}} \right)^{3.4}, \quad (3.6)$$

where η_0 is the zero shear viscosity, which for homopolymers scales with the power 3.4 of the (weight average) molar mass M .

Again for constant extrusion pressure, the relation

$$v_0(M) = a_M^{-1} v_0(M_{ref}) \quad (3.7)$$

holds.

Therefore invariance of Rheotens mastercurves with respect to changes of the average molar mass (for similar molar mass distributions) exist if measurements are taken at constant extrusion pressure. This means that if Rheotens curves are compared at constant extrusion pressure and are plotted as tensile force vs. draw ratio, any influence of temperature and average molar mass drops out.

Differences of Rheotens mastercurves for different grades of the same homopolymer therefore are only related to differences of molar mass distribution and branching structure. As demonstrated by Wagner et al. [56], a higher degree of long-chain branching and a broader molar mass distribution cause a higher degree of strain hardening. This results in a higher drawdown force at higher draw ratios, which is in agreement with earlier results from measurements at constant elongation rate and constant tensile stress of Muenstedt and Laun [41], and Meissner and Hochstettler [37].

This is demonstrated in fig. 3.11, where a comparison of Rheotens curves for melts LLDPE1 (narrow MWD), LDPE6 (LCB) and HDPE1 (broad MWD) is given. The different amount of strain-hardening of such materials has been reported by Meissner and Hostettler [37].

To demonstrate the influence of structural differences on melt strength, LDPE grades produced by different reactor technologies are compared in fig. 3.12. LDPE4, LDPE5, and LDPE6 are tubular grades while LDPE7 and LDPE8 were produced in autoclave reactors, and therefore have a different branching structure. The MFR values of the materials differ, but by direct comparison at the same reference extrusion pressure, it is possible to detect a distinctive difference in melt strength, leading to the well known result that autoclave materials have higher melt strength than tubular grades [17], [26]. This can be explained by the difference in branching structure caused by the production process: Polymers produced in an autoclave reactor have a more tree-like structure and more long-chain branching, while tubular reactors produce a more comb-like structure [23].

3.3 Rheotens Supermastercurves

Rheotens experiments are very often performed in combination with a capillary rheometer as a melt feeder instead of the extruder set-up described in this work. With a capillary rheometer, one is usually forced to prescribe the flow rate, and not the extrusion pressure in front of the die. Therefore the concept of Rheotens supermastercurves [56] is now explained which allows

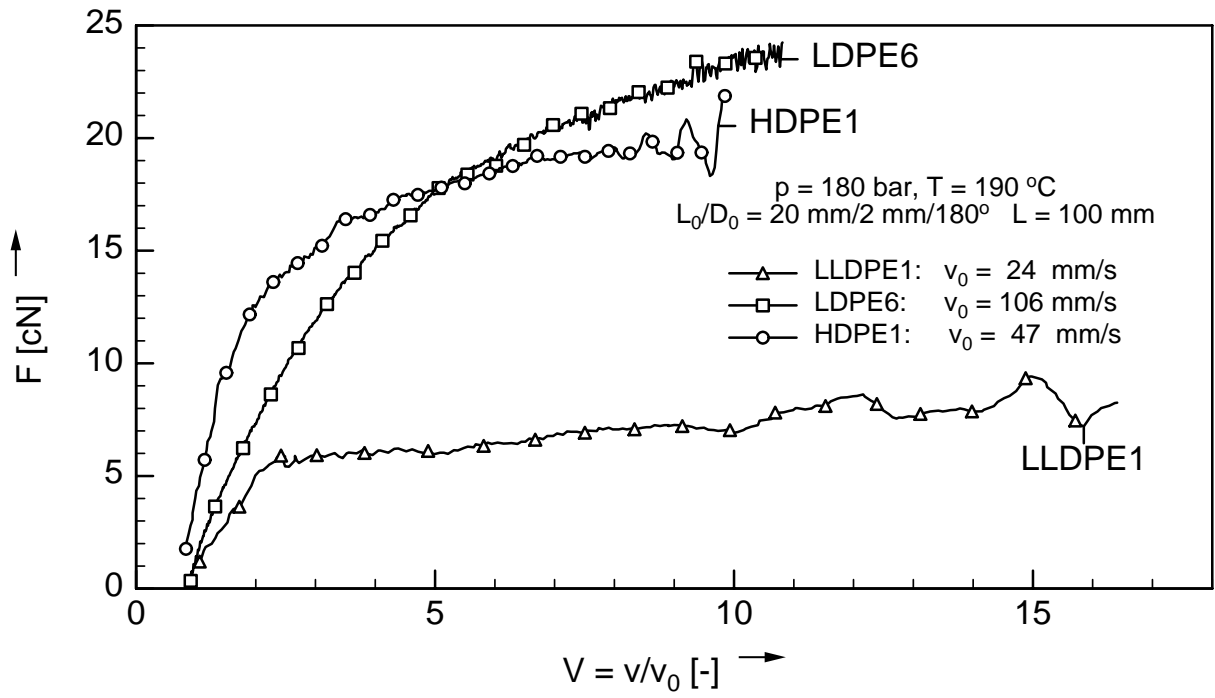


Figure 3.11: Comparison of Rheotens curves for melts LLDPE1, LDPE6, and HDPE1.

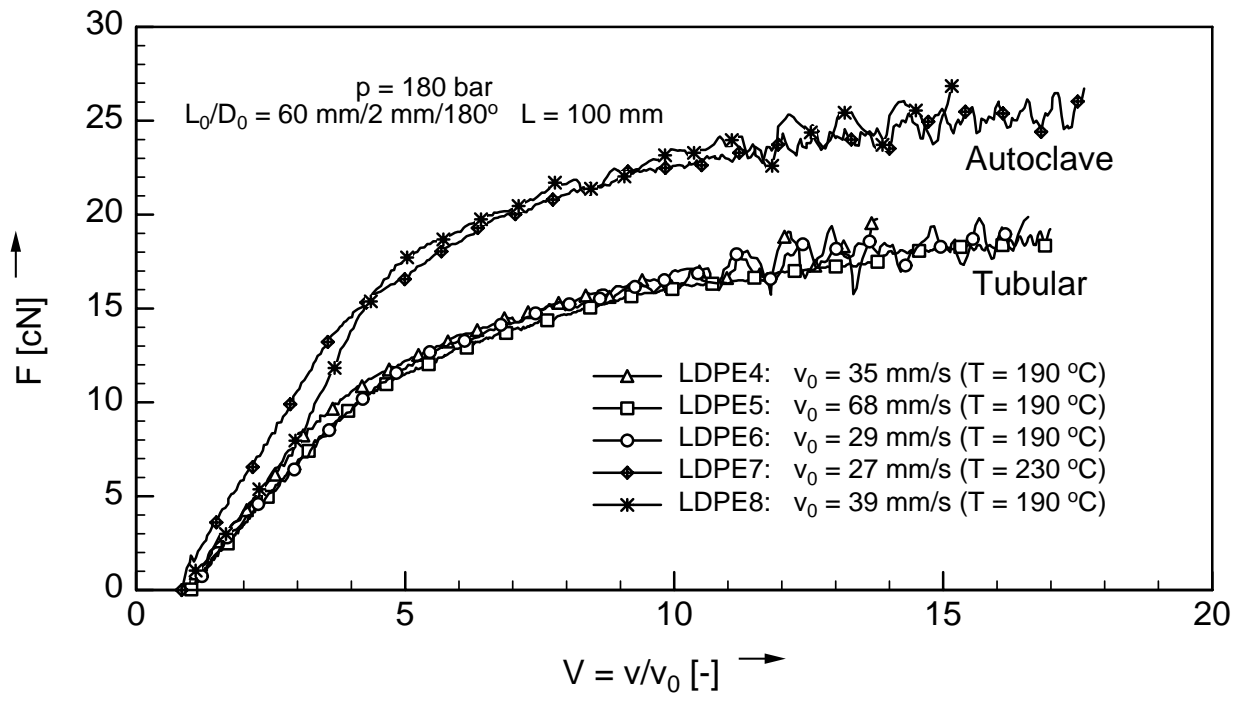


Figure 3.12: Structural differences of tubular and autoclave reactor grades reflected in Rheotens mastercurves.

interpolation of Rheotens diagrams measured at constant flow rate (and measured extrusion pressure) in such a way, that the Rheotens diagrams for any reference extrusion pressure can be obtained. A pre-condition for this procedure is, however, that the experiments are carried out quasi-isothermally, which is usually guaranteed at high enough flow rates.

If Rheotens curves measured at different extrusion pressures are compared, one cannot expect to find a mastercurve simply by plotting force as a function of draw ratio as in the case of constant extrusion pressure. One observes increasing melt strength and decreasing drawability with increasing flow rate (fig. 3.13). Mastercurves can only be found by an additional shifting procedure. As explained in [56], the stress curves can be shifted horizontally by dividing the draw ratio by an additional shift factor b . This corresponds to a Rheotens supermastercurve $b \cdot F = f(V/b)$ (fig. 3.14), where the shift factor b is a function of the flow rate and hence the extrusion pressure, as illustrated in fig. 3.15 for melt PC1.

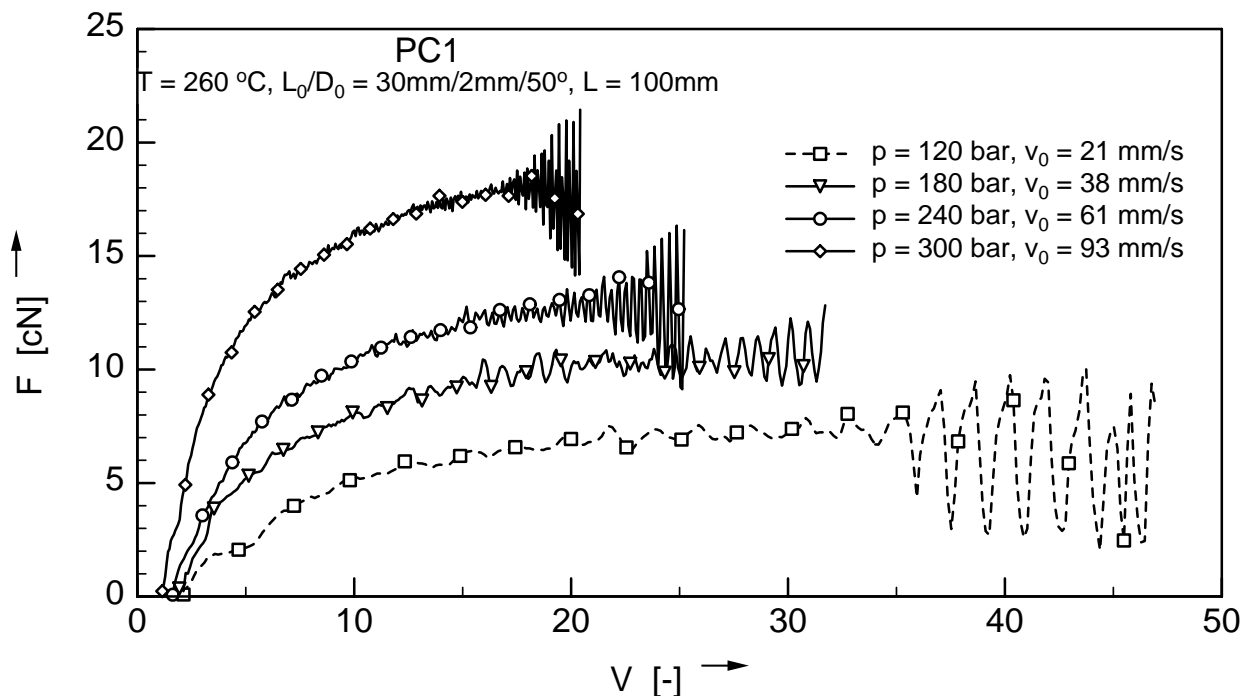


Figure 3.13: Rheotens experiments at constant temperature and various flow rates for melt PC1.

As can be seen in fig. 3.15, the shift factor b as a function of flow rate as well as of extrusion pressure can be fitted by a straight line in a log-log plot. Interpolation for all intermediate pressures is therefore possible. Melt PC1 can for example be compared to melt PC2 and melt PC3, at an extrusion pressure of 200 bar (fig. 3.16), which has not been measured for melt PC1. The shift factor b needed is (from fig. 3.15) $b = 0.92$. As a result one finds pronounced structural differences between the three PC types: PC3 has a very low melt strength, which causes it to be unsuitable for extrusion processes [21], [22], while PC1 as well as PC2 can successfully be used for profile extrusion.

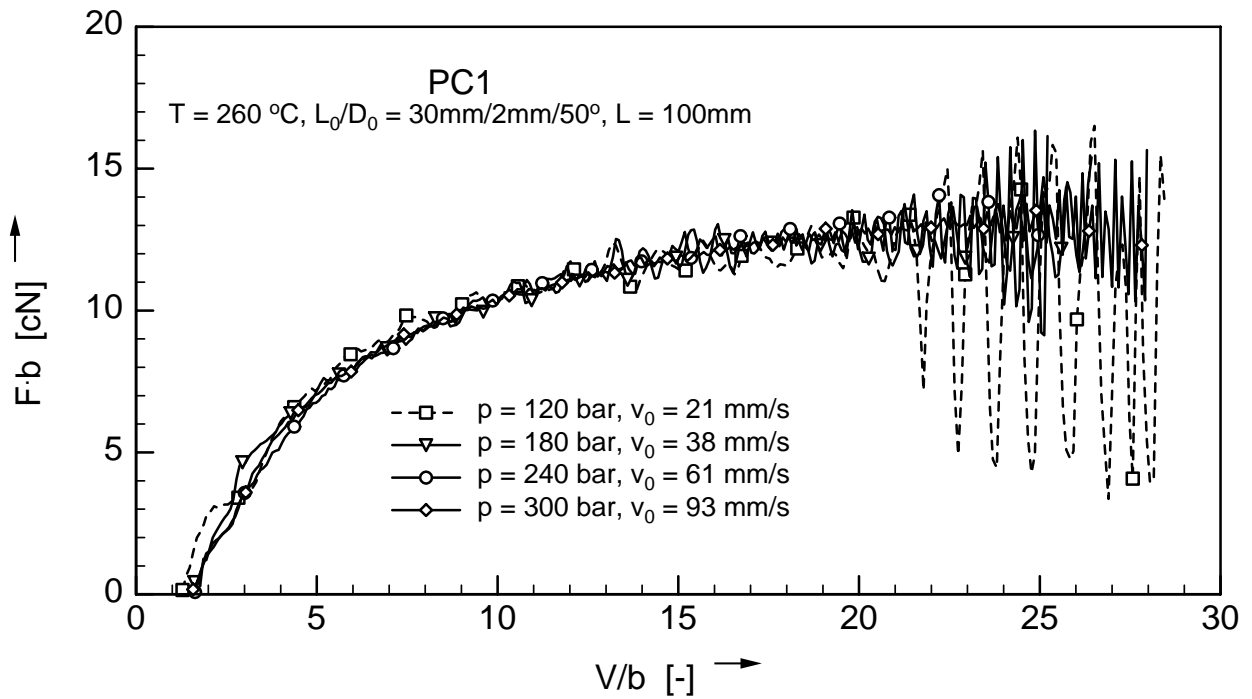


Figure 3.14: Rheotens supermastercurve $b \cdot F = f(V/b)$ for melt PC1.

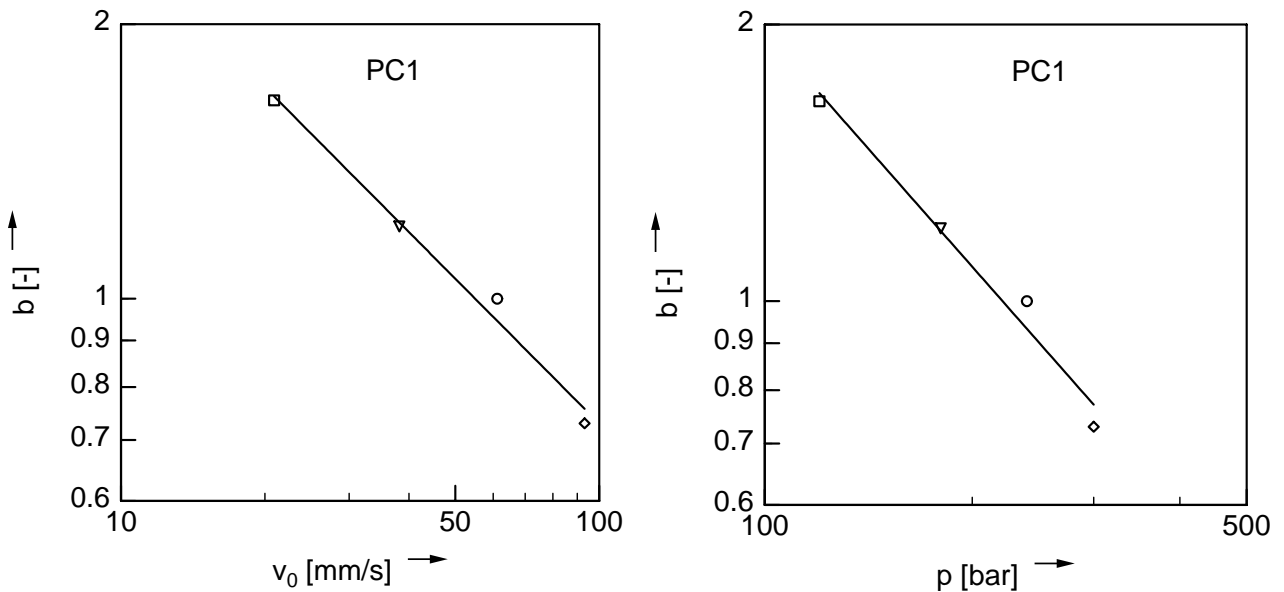


Figure 3.15: Shift factor b needed for the conversion of Rheotens experiments (fig. 3.13) into the supermastercurve (fig. 3.14), a) as a function of extrusion velocity v_0 , b) as a function of extrusion pressure p .

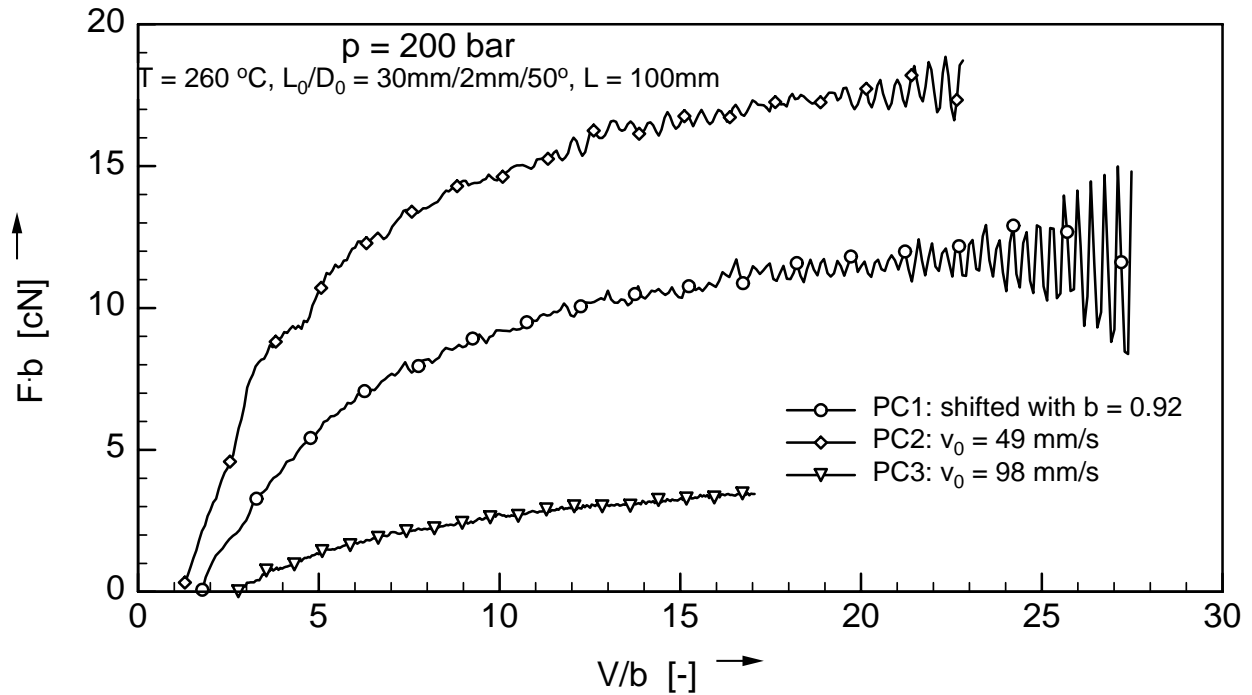


Figure 3.16: Comparison of supermastercurves of different polycarbonate melts.

3.4 Concept of Grandmastercurves

Experimental Evidence

Finally, the concept of mastercurves is extended to variations of die and spinline geometry as well as flow rate variation. In fig. 3.17, Rheotens curves for 4 different die and spinline geometries at 4 flowrates are reported [52]. Tab. 3.2 lists the processing conditions of the experiments. (These experiments were performed without pressure control, which explains the differences of flowrate at constant die geometries and pressure. However, all statements derived from these data remain valid.)

Plotted as a function of the draw ratio (fig. 3.18), all Rheotens curves show a similar shape and a certain ordering of the curves appears. Initially, the tensile force increases linearly with the draw ratio and reaches a nearly horizontal plateau at high draw ratios, with differently pronounced oscillations due to the draw resonance effect. Closer analysis of fig. 3.18 reveals that for higher extrusion velocities v_0 , higher drawdown forces (melt strength) and lower draw

| Die L_0/D_0 | Spinline L | $p = 50$ bar | $p = 70$ bar | $p = 90$ bar | $p = 120$ bar |
|---------------|--------------|--------------|--------------|--------------|---------------|
| 15 | 100 mm | 20.4 mm/s | 51.7 mm/s | 116 mm/s | 292 mm/s |
| 15 | 50 mm | 29.5 mm/s | 68.5 mm/s | 144 mm/s | 344 mm/s |
| 30 | 100 mm | 7.0 mm/s | 13.6 mm/s | 25.3 mm/s | 53.2 mm/s |
| 30 | 50 mm | 6.7 mm/s | 13.7 mm/s | 24.8 mm/s | 52.7 mm/s |

Table 3.2: Extrusion velocity v_0 for Rheotens experiments in fig. 3.17.

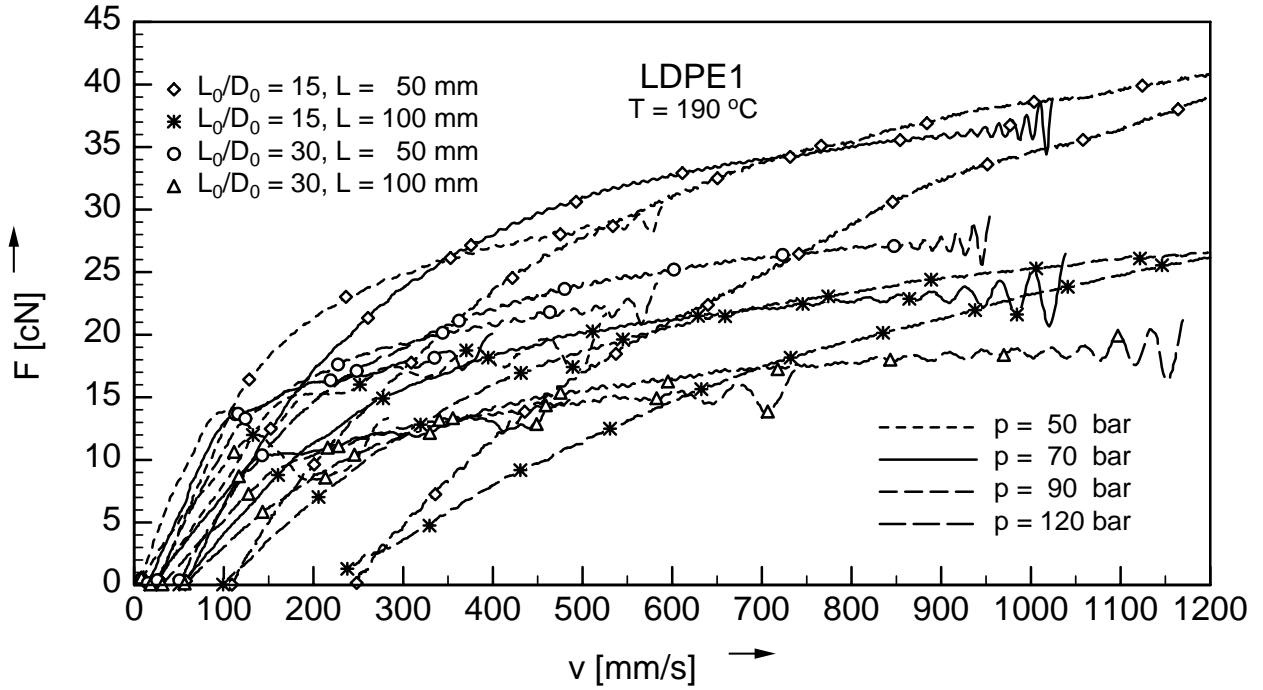


Figure 3.17: Drawdown force $F(v)$ for melt LDPE1, variation of flowrate, die and spinline geometry.

ratios to break (extensibility) are observed. At high values of v_0 , the filament can no longer be extended to break due to the maximum drawdown speed of the Rheotens. A shorter extrusion die or a shorter spinline length for the same v_0 , causes higher drawdown forces and lower draw ratios to break.

If the tensile stress σ instead of the force F is plotted vs. the draw ratio V (fig. 3.19), it is obvious that all experiments result in similar Rheotens curves, irrespective of the differences in die and spinline geometry or mass flow rate. As in the case of temperature invariance, a mastercurve can be found by a horizontal shift. However, the shifting is now done with respect to the drawdown ratio V , and not to the drawdown velocity v . A shift factor b is defined, by which all curves are shifted onto a reference curve with $b = 1$, hence

$$\sigma = \sigma\left(\frac{V}{b}\right). \quad (3.8)$$

The result of the shifting procedure is shown in fig 3.20 and leads to a mastercurve, which now is called grandmastercurve, as it includes flow rate variations as well as different die and spinline geometries. The shift provides a best fit of the curves between 0.1 and 1 MPa, as smaller stresses are severely influenced by the weight of the polymer strand below the wheels. The oscillations in the draw resonance region do not superimpose, as they are influenced not only by the draw ratio but also by the absolute drawdown velocity.

The grandmastercurve for the drawdown force can be obtained as

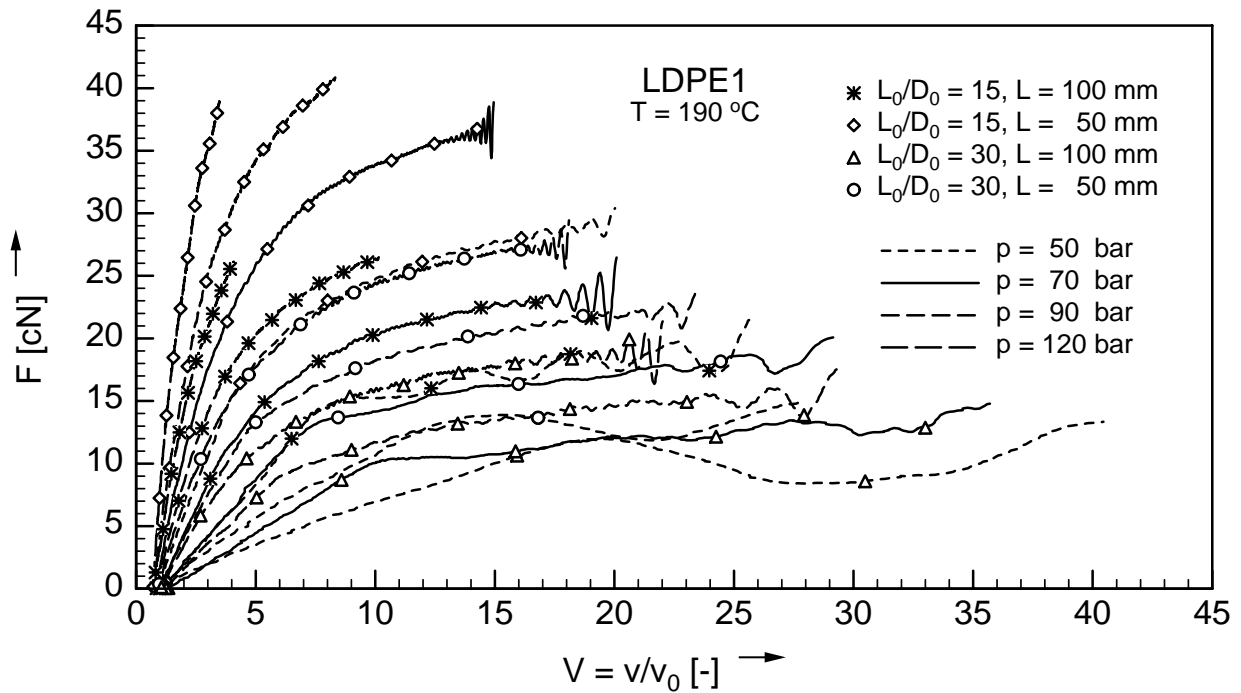


Figure 3.18: Drawdown force $F(V)$ for melt LDPE1. Variation of flowrate, die and spinline geometry.

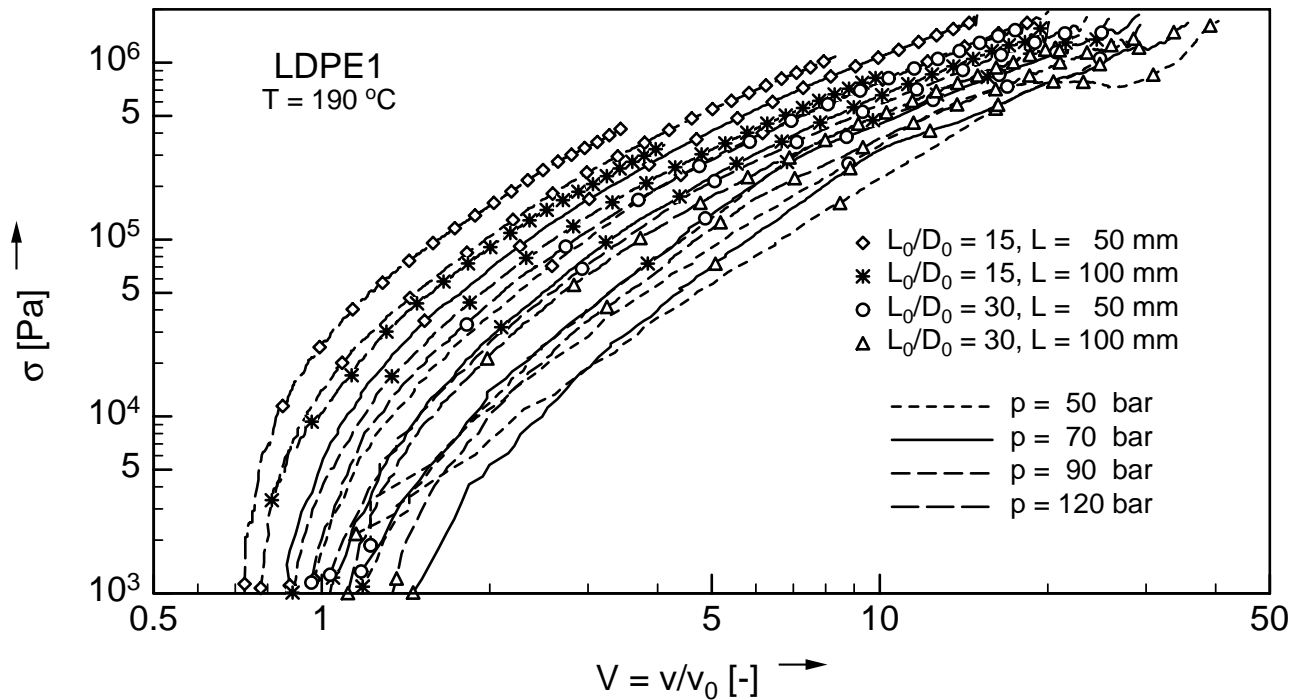


Figure 3.19: Drawdown stress $\sigma(V)$ for melt LDPE1. Variation of flowrate, die and spinline geometry.

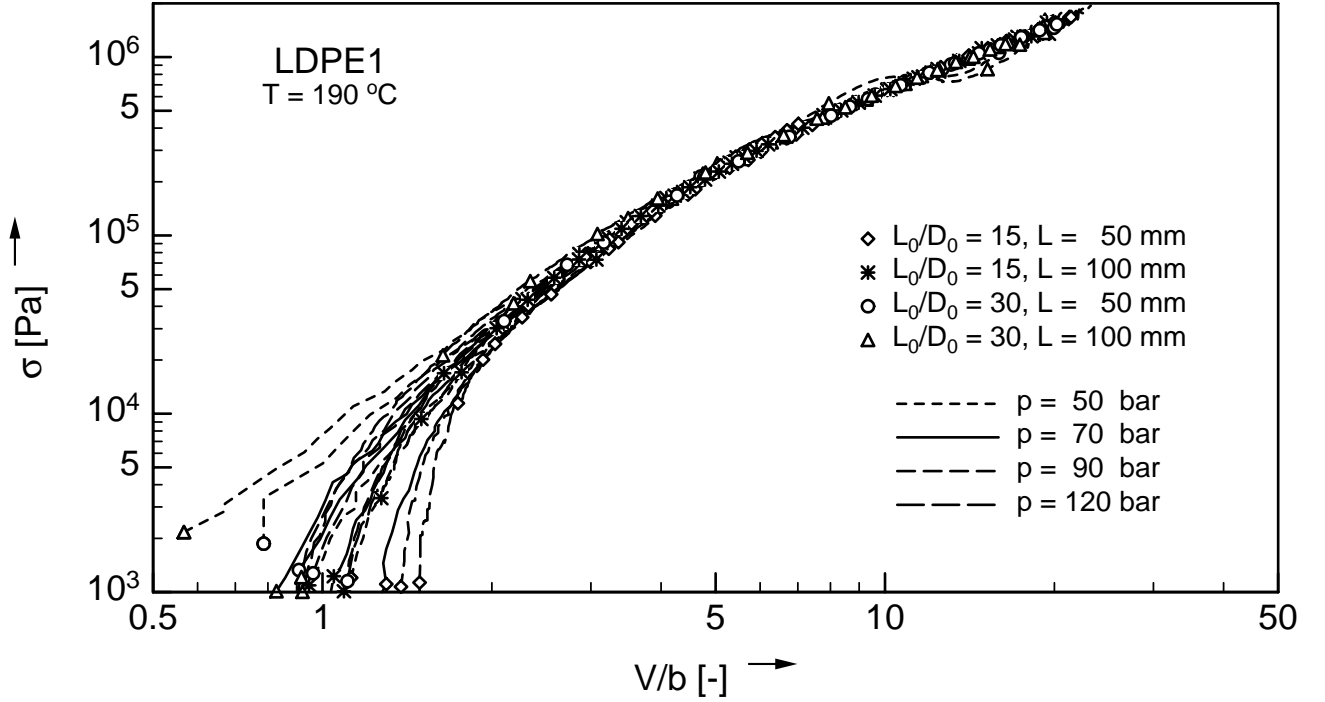


Figure 3.20: Rheotens grandmastercurve $\sigma(V/b)$ for melt LDPE1 (reference $L_0/D_0 = 15$, $L = 100$ mm, $v_0 = 51.7$ mm/s).

$$bF = \frac{\sigma(V/b) A_0}{(V/b)}, \quad (3.9)$$

which describes a shift of the force curves of fig. 3.18 under 45 °C in a log-log plot. The result is shown in fig. 3.21.

The corresponding shift factors b are presented in fig. 3.22 a) as a function of the extrusion velocity v_0 . A value of b greater than 1 means less preshear in the extrusion die compared to the reference, hence either a lower flow rate for the same die geometry or a longer die for the same flow rate. b greater than 1 corresponds also to a longer spinline length for the same die geometry and flow rate as the reference.

Furthermore, an attempt is made to establish a direct connection between b and the processing conditions. These are reflected by the extrudate swell and hence by V_s , the relative velocity at the start of a Rheotens curve (for $F = 0$). It should be noted that V_s does not represent the undisturbed swelling of the material after exiting the die but is influenced by the drawdown, hence it also changes with the spinline length. This means that V_s in the way as it is defined here, fully represents the processing conditions.

If the shift factor b is plotted as a function of V_s (fig. 3.22 b)), it can well be represented by a linear relationship, even though deviations from the grandmastercurve are significant around $F = 0$. (The deviation seen at a very small flow rate is caused by cooling effects.) The shift factor b can therefore be related directly to the processing conditions.

This result was confirmed by experiments of Laun [29], who reported that for a wide variation

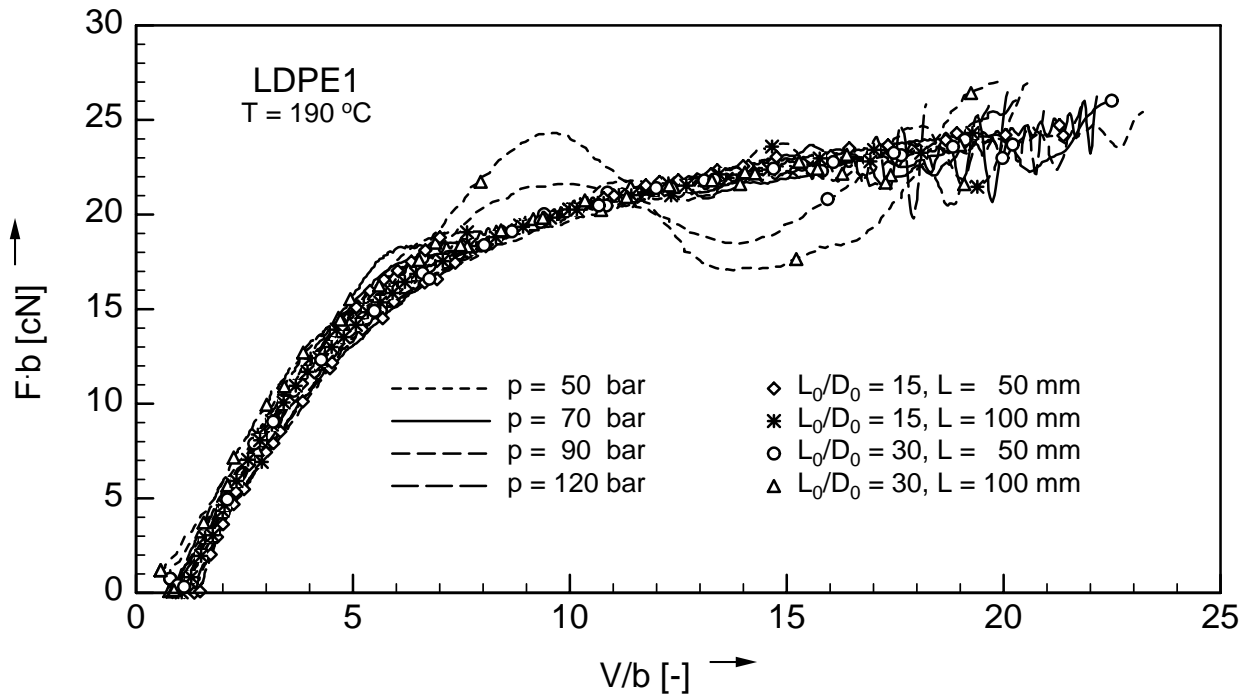


Figure 3.21: Rheotens grandmastercurve for melt LDPE1.

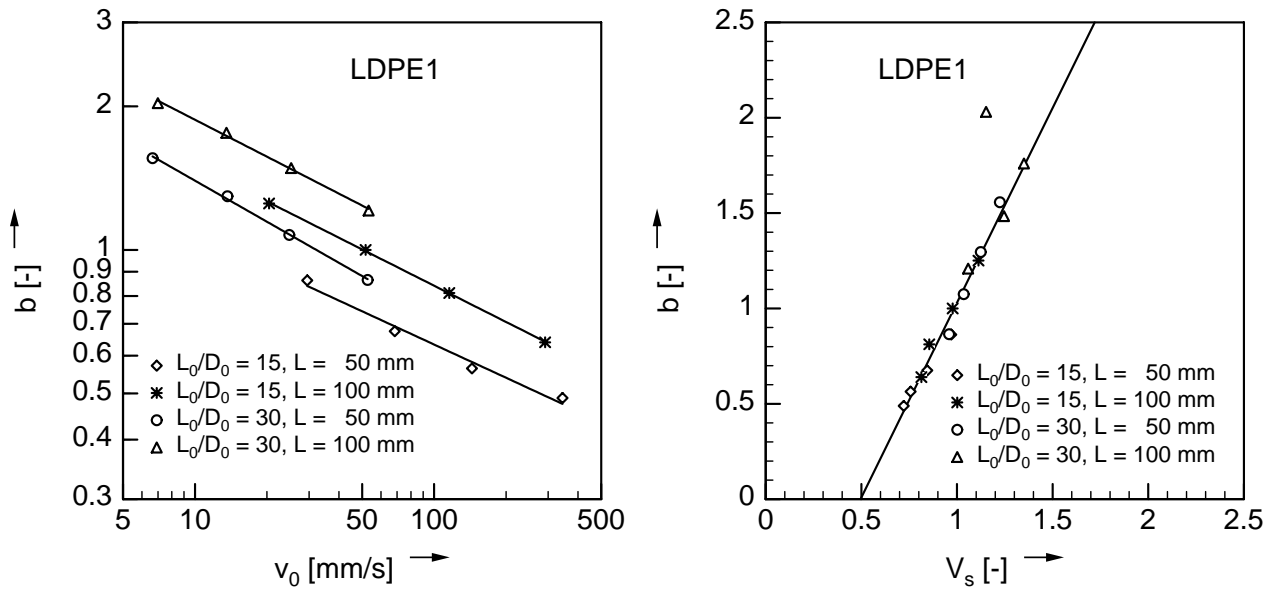


Figure 3.22: Shift factor b needed for the shifting of Rheotens curves (fig. 3.19) onto the grandmastercurve (fig. 3.20) a) as a function of v_0 , b) as a function of V_s .

of die geometries, Rheotens curves of a LDPE can be shifted onto a grandmastercurve. The shift factors, plotted as a function of the inverse extrudate swell, also fall onto a straight line.

The existence of Rheotens grandmastercurves allows to separate between material properties, which are reflected by the grandmastercurve, and processing conditions. The latter are represented by the shift factor b . Thus, for a given material, the knowledge of the grandmastercurve and the shift factor b allows prediction of Rheotens diagrams for all processing conditions. If Rheotens experiments are performed at constant mass flow rate, the shift factor b for an intermediate extrusion pressure can be obtained by interpolation.

Theoretical Argument

The existence of Rheotens grandmastercurves has been demonstrated experimentally, but can also be supported by a general theoretical argument suggested by Wagner et. al. [52]. It includes Rheotens grandmastercurves, supermastercurves, as well as mastercurves.

As seen from fig. 3.17, the measured tensile force F at the take-up is a complex function of the properties of the polymer melt on the one hand, and of the geometry of die and spinline, as well as the processing conditions (extrusion pressure p , extrusion velocity v_0 , melt temperature T , and drawdown velocity v) on the other hand:

$$F = F(\text{polymer, geometry, processing conditions}). \quad (3.10)$$

The temperature condition in the spinline is considered to be isothermal, and the effects of gravity, inertia, air drag, and surface tension are neglected. The tension $\sigma = \sigma(L)$ in the polymer melt at the end of the spinline between the wheels of the Rheotens, depends only on the rheological prehistory: it is assumed to be a function of the Deborah number De ,

$$\sigma = \sigma(De). \quad (3.11)$$

The Deborah number De is defined as the ratio of a characteristic material time t_m to a characteristic process time t_{pz} . As characteristic material time t_m a reference retardation time can be chosen. The characteristic process time t_{pz} is simply the residence time of a melt particle in the spinline of length L , i.e., $t_{pz} = L/v$. Hence,

$$De = \frac{t_m}{t_{pz}} = \frac{t_m}{L/v}, \quad (3.12)$$

or, in terms of the nondimensional draw ratio,

$$De = \frac{t_m v/v_0}{L/v_0} = \frac{V}{L/(v_0 t_m)}. \quad (3.13)$$

$L/(v_0 t_m)$ is equivalent to a draw ratio V_m , therefore

$$De = \frac{V}{V_m}. \quad (3.14)$$

V_m corresponds to the draw ratio necessary to extend the melt to a certain characteristic tension σ_m , which is used as a reference.

Inserting eq. (3.14) into eq. (3.11) leads to

$$\sigma = \sigma\left(\frac{V}{V_m}\right) = \sigma(V_r), \quad (3.15)$$

where V_r is the relative draw ratio

$$V_r = \frac{V}{V_m}. \quad (3.16)$$

Therefore, if the melt tension σ is plotted as a function of the relative draw ratio V_r , this results in a mastercurve, which is invariant with respect to changes in the rheological prehistory (melt temperature, extrusion pressure or mass flow rate, die geometry, and spinline length).

As the drawdown force F is the product of tension σ and cross section $A(L) = A_0/V$ at the take-up of the strand (with A_0 being the cross section of the die)

$$F = \frac{\sigma A_0}{V}, \quad (3.17)$$

invariance of the force-extension diagram is obtained as

$$V_m F(V) = \frac{\sigma(V_r) A_0}{V_r} = F_r(V_r), \quad (3.18)$$

from eqs. (3.15), (3.16), and (3.17), i.e., if $V_m F$ is plotted as a function of the reduced draw ratio V_r .

Instead of determining V_m explicitly for the reference tension σ_m , one experimental curve is chosen as a reference curve which is characterised by a specific reference draw ratio V_b . The measured $\sigma(V)$ curves are shifted onto this reference curve. Defining a shift factor b ,

$$b = \frac{V_m}{V_b}, \quad (3.19)$$

the mastercurve for melt tension σ , eq. (3.15), can be expressed as

$$\sigma = \sigma\left(\frac{V/b}{V_b}\right) = \sigma(V/b), \quad (3.20)$$

and the mastercurve for the drawdown force corresponding to eq. (3.18) by

$$b F(V) = \frac{\sigma(V/b) A_0}{V/b} = F_r(V/b). \quad (3.21)$$

Eqs. (3.20) and (3.21) are called Rheotens grandmastercurves [52]. They contain as special cases the Rheotens supermastercurves [56], [55], [51] (invariance with respect to changes in mass flow rate or extrusion pressure at constant geometry of die and spinline) and Rheotens mastercurves [53] (invariance with respect to changes of temperature and average molar mass of the polymer melt at constant extrusion pressure and constant geometry of die and spinline). Their existence has been demonstrated experimentally for several polymer melts in the preceding sections.

In general, i.e., in the case of Rheotens grandmastercurves, for a given polymer melt the shift factor b depends on the L_0/D_0 ratio of the die, the length L of the spinline, and either the die exit velocity v_0 and the melt temperature T or the wall shear stress τ in the die [52], respectively,

$$b = b(L_0/D_0, L, v_0, T) = b_\tau(L_0/D_0, L, \tau). \quad (3.22)$$

For supermastercurves (i.e., in the case of constant geometry), b depends only on the die exit velocity v_0 and the melt temperature T or the wall shear stress τ in the die, respectively [56], [55], [51],

$$b = b(v_0, T) = b_\tau(\tau). \quad (3.23)$$

In the case of mastercurves at constant extrusion pressure p or constant wall shear stress τ [53], the shift factor v reduces to

$$b = 1, \quad (3.24)$$

as under these process conditions the reference draw ratio V_m is invariant with respect to melt temperature changes, i.e., $V_m \equiv V_b$.

Hence, for thermo-rheologically simple materials, a theoretical background for the existence of Rheotens grandmastercurves, supermastercurves and mastercurves has been given. While the Rheotens grandmastercurve accounts for the material behaviour of a specific polymer, the shift factor b is related to the processing conditions of the experiment. Rheotens grandmastercurves therefore allow a direct and quantitative comparison of the drawability of polymer melts.

3.5 Critical Rupture Stress

The experimental findings reported in the previous sections can also be used to investigate the rupture stress of the fibres. To do so, a critical rupture stress needs to be defined. While other authors, e.g. [29], use a fitted, smooth Rheotens curve for the calculation of the rupture stress in order to overcome the influence of the draw resonance, the maximum stress reached before breaking of the fibre is defined in this work as the critical stress. An example is given in fig. 3.23 for melt HDPE2. The critical stress is reached at the smallest diameter of the fibre, where the material fails by brittle fracture [15].

It can be seen that the rupture stress σ_B is largely independent of extrusion velocity as well as die and spinline geometry. As shown in fig. 3.24 for HDPE1, σ_B is not temperature dependent. The values of σ_B in figs. 3.24 and 3.25 have been corrected with $\rho \cdot T$ according to investigations of Wang [59],

$$\sigma_B(T) = \sigma_B(T_0) \frac{\rho_0 T_0}{\rho T}, \quad (3.25)$$

with T_0 being the reference temperature of 463 K and ρ the melt density. The same result is found for LLDPE2 (fig. 3.25), except for the crystallisation effect which is visible at low temperatures.

On the other hand, as illustrated in fig. 3.26 for LDPE2, melt fracture lowers the stress level at which rupture occurs [7]. This means that the experimental window in which the critical rupture stress can be investigated by the Rheotens is limited: no surface defects must be visible, also the maximum velocity of the Rheotens must not be reached.

A comparison of the rupture stress σ_B of all branched polyethylene melts investigated is given in fig. 3.27. The autoclave LDPE melts (LDPE7 - LDPE10) show a tendency for a higher rupture stress than the tubular LDPE melts (LDPE1, LDPE4 - LDPE6) [9], which can be explained by a higher degree of long-chain branching produced in the autoclave [23]. A true rupture stress in the range between 1 and 2 MPa is found for all LDPE melts.

Tab. 3.3 lists the rupture stress found for other materials. Linear PE melts as well as linear PP show a considerably lower rupture stress in the range between 0.5 and 0.6 MPa. The amorphous materials PS and PC have a rupture stress above 1 MPa, similar to the branched LDPE melts.

| Material | σ_B |
|-----------------|------------|
| LLDPE2 | 0.6 Mpa |
| PP1 | 0.6 MPa |
| PS1 | 1.2 MPa |
| PC1 | 1.4 MPa |
| PC2 | 1.2 MPa |

Table 3.3: Rupture stress σ_B for various polymer melts.

In general, the Rheotens experiment provides a suitable means to evaluate rupture mechanisms and rupture stress. This is not only important for fibre spinning, but also relevant to other polymer processes. For example, the sharkskin phenomena can be explained by rupture of the polymer surface at the exit of the extrusion die, as investigated by Rutgers and Mackley [34], [45].

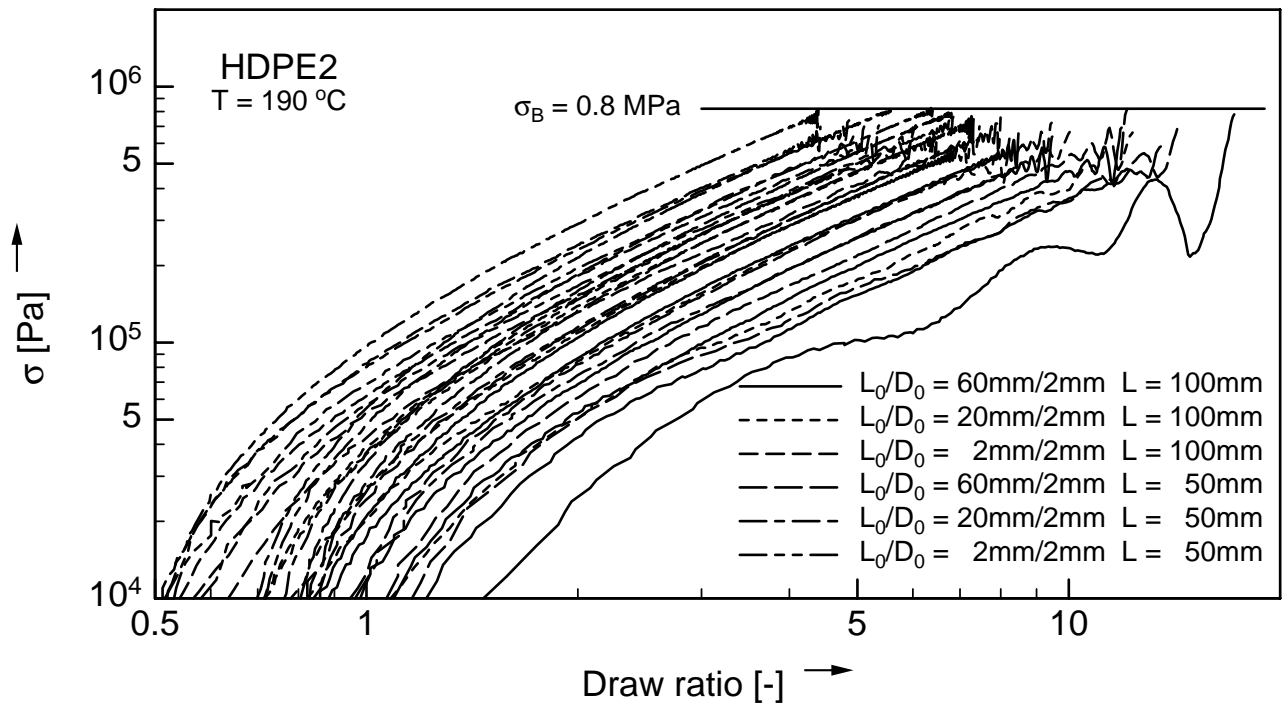


Figure 3.23: Rupture stress σ_B for melt HDPE2 extracted from Rheotens curves $\sigma(V)$.

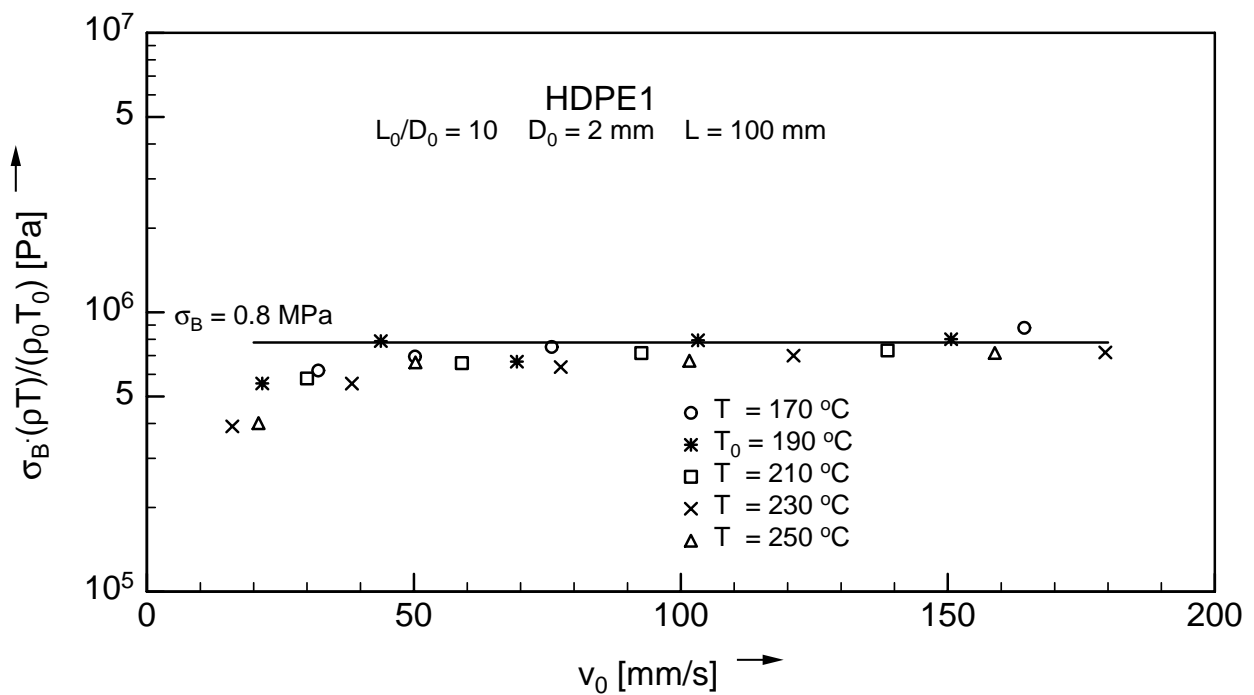


Figure 3.24: Rupture stress σ_B for melt HDPE1 as a function of temperature.

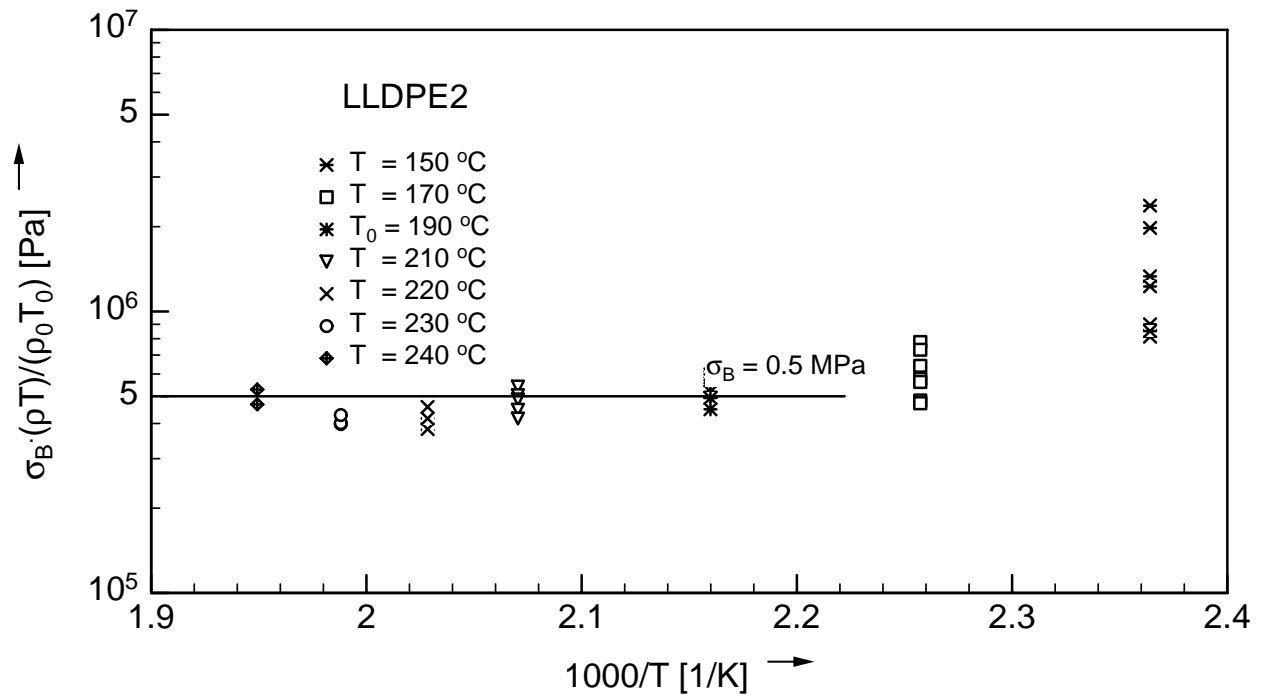


Figure 3.25: Rupture stress σ_B for melt LLDPE2 as a function of temperature. Crystallisation visible for low temperatures.

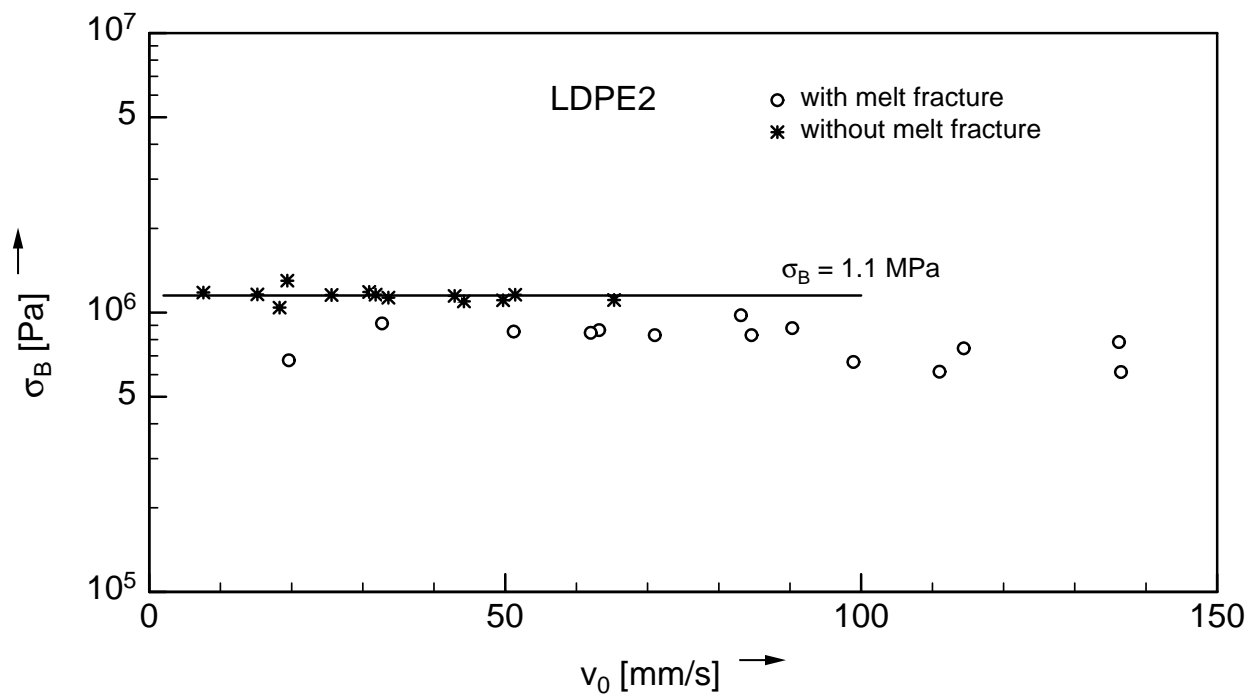


Figure 3.26: Influence of melt fracture on rupture stress σ_B for melt LDPE2.

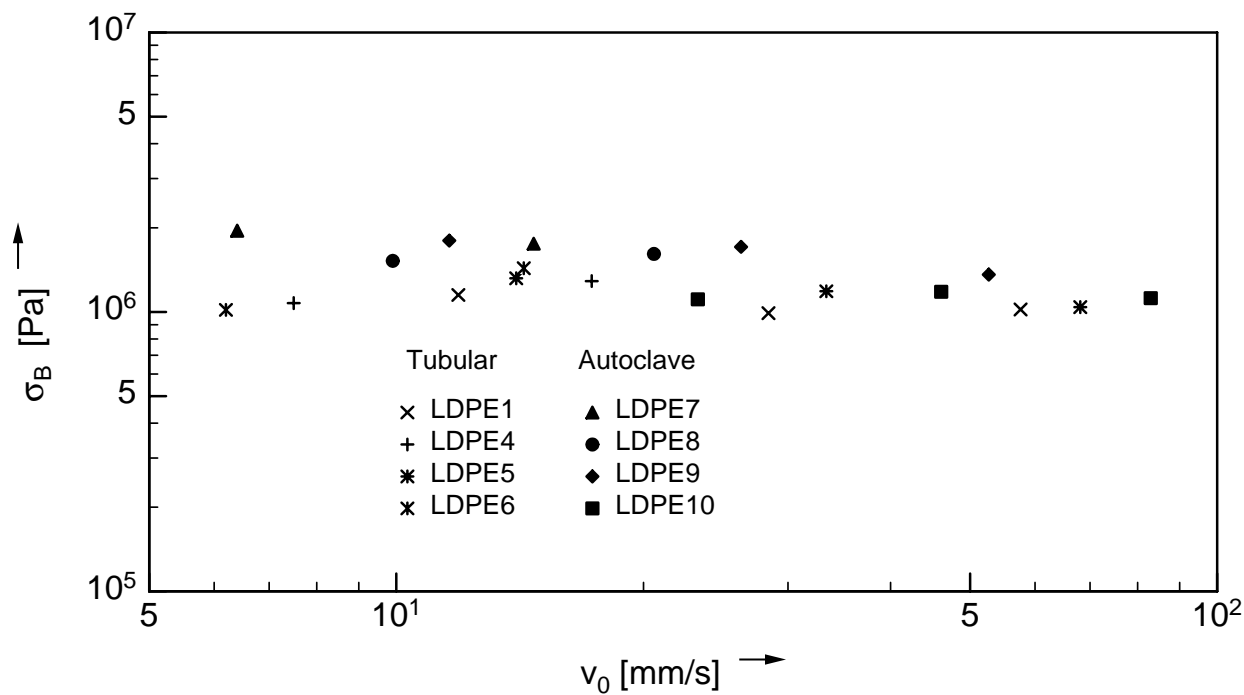


Figure 3.27: Rupture stress σ_B for LDPE melts. Comparison of tubular vs. autoclave reactor technology.

4 Elongational Viscosity from Constant Force Deformation Experiments

In a Rheotens experiment, elongation of the polymer melt is performed under the action of a tensile drawdown force, and not at a prescribed elongation rate. A direct conversion of the Rheotens diagram, where the tensile force is plotted as a function of the drawdown speed, into a relation between uniaxial elongational viscosity and elongation rate is not possible. For this, a rheological model is needed.

In the following, two concepts are introduced, which allow to extract the information on the elongational viscosity of a polymer melt from Rheotens curves either by use of an analytical model or by a more general solution. These apparent elongational viscosities calculated from Rheotens experiments are compared to steady-state viscosities derived from elongational experiments performed at constant elongation rate, and to shear viscosities.

4.1 Analytical model

The analytical model [52] is based on experimental evidence about the velocity distribution along the spinline. The data points were measured using the Laser-Doppler-Velocimeter (LDV), which gives more accurate results than the photographic method which was published in [52].

As can be seen in fig. 4.1, the local velocity increases approximately linearly with the spinline length x below a critical value of the draw ratio V_p . This linear regime was already reported by several reserchers, and Sridhar and Gupta [47] termed it "constant strain-rate spinning". For draw ratios higher than V_p , an overproportional increase of the velocity with x can be observed. Comparing the different spinline profiles in fig. 4.1 shows that the critical draw ratio V_p is largely independent of the drawdown force, and therefore is a constant in the analytical model.

Hence the model distinguishes between two regimes, a linear one (1) for $V \leq V_p$ and a nonlinear regime (2) for $V > V_p$, where V increases overproportionally with x .

(1) Linear regime: $V \leq V_p$

In the linear regime, the elongation rate $\dot{\epsilon}(x) = \partial v(x)/\partial x$ is constant and given by

$$\dot{\epsilon} = \frac{v_0}{L} (V - V_s) \quad (4.1)$$

$V_s = v(x=0)/v_0$ is the extrapolated starting point of the drawdown and describes the inverse of the effective extrudate swell of the filament, caused by the viscoelastic deformation of the polymer melt in the extrusion die. V_s is assumed to be constant and independent of the drawdown force F . F is then obtained from the kinematics as

$$F = F_p \frac{V - V_s}{V_p - V_s}. \quad (4.2)$$

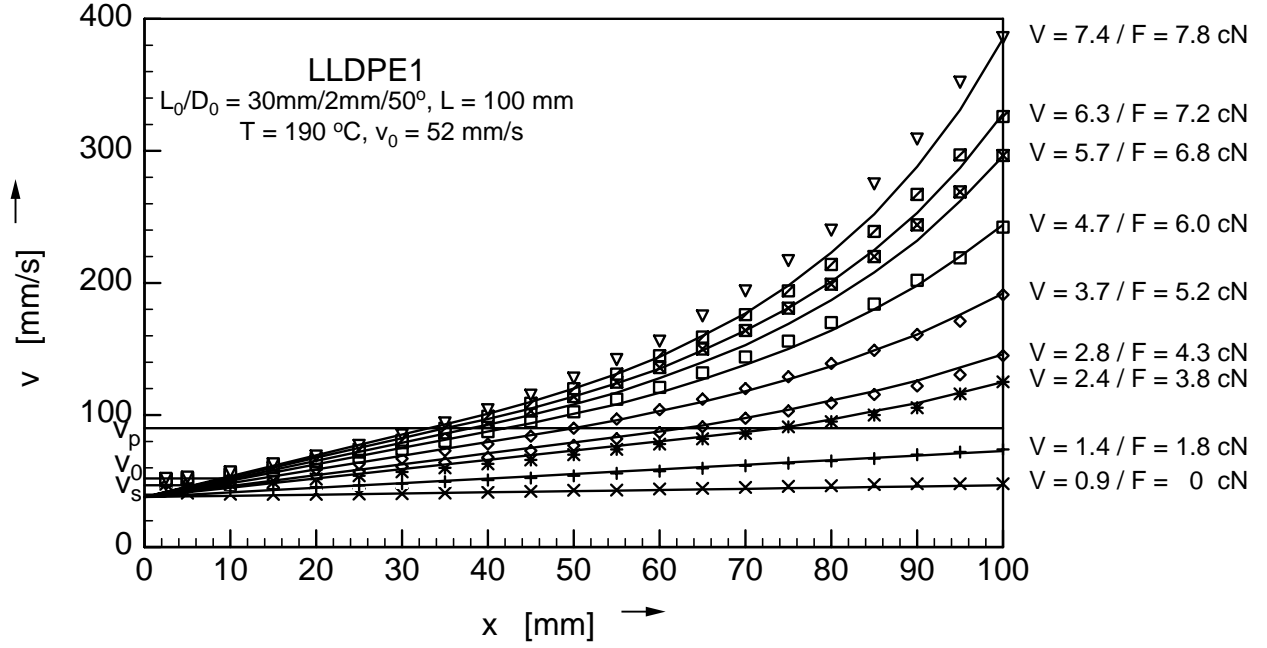


Figure 4.1: Filament velocity v along the length x of the spinline for LLDPE1. Measurements (symbols) by LDV, compared to the prediction of the analytical model (lines).

F_p is the drawdown force necessary to achieve the critical draw ratio V_p , and the critical tensile stress σ_p at the end of the spinline. This corresponds to a linear increase of the drawdown force F with increasing draw ratio V up to the critical force F_p , which is illustrated in fig. 4.2 for the Rheotens curve corresponding to the spinline profiles in fig. 4.1.

This linear increase is called the "viscoelastic startup" regime due to the fact that the elongational viscosity increases with increasing deformation, as in the case of constant strain rate extension. Here, the apparent elongational viscosity can be calculated as

$$\eta = \frac{\sigma_p}{(v_0/L)(V_p - V_s)} \left(\frac{V}{V_p} \right), \quad (4.3)$$

where σ_p is the melt tension at the critical draw ratio V_p ,

$$\sigma_p = \frac{F_p V_p}{A_0}. \quad (4.4)$$

(2) Nonlinear regime: $V > V_p$

The overproportional increase of the velocity for $V > V_p$ can be described by a power-law dependence of the tensile stress on the extension rate, with a power-law index $n < 1$:

$$\sigma(x) \sim \left(\frac{\partial v(x)}{\partial x} \right)^n \quad (4.5)$$

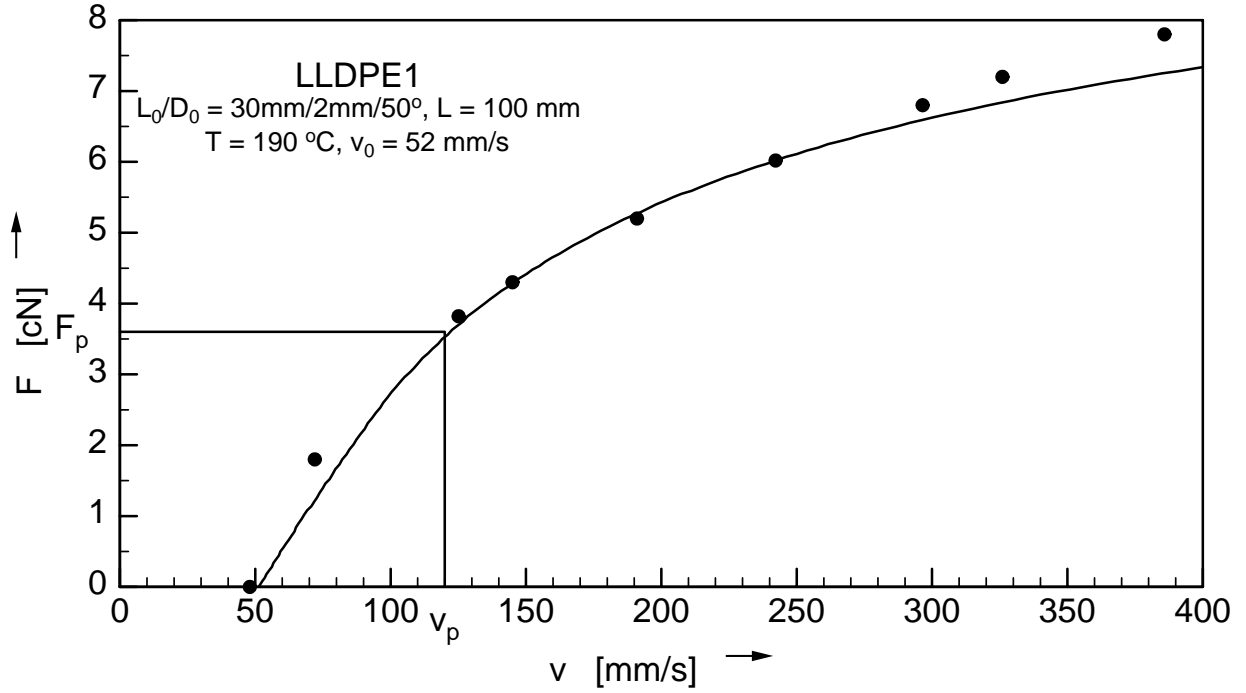


Figure 4.2: Rheotens curve corresponding to the experiments shown in fig. 4.1

As seen in fig. 4.1 this power-law does describe the experimental data quite well. It can also be supported theoretically: for $V > V_p$, the melt has reached a quasi steady-state and further deformation is purely viscous. Thus, the critical draw-ratio V_p indicates the amount of stretch necessary to reach the quasi steady-state.

Using Huyn and Ballman's solution for a power-law model [3], the drawdown force F is calculated as

$$F = F_p P(V) \quad (4.6)$$

with

$$P(V) = 1 + \frac{n}{(n-1)} \frac{V_p}{(V_p - V_s)} \left[\left(\frac{V}{V_p} \right)^{\frac{(n-1)}{n}} - 1 \right]. \quad (4.7)$$

The extension rate $\dot{\epsilon} = \dot{\epsilon}(L)$ at the end of the spinline can then be obtained as

$$\dot{\epsilon} = \frac{v_0}{L} (V_p - V_s) \left(\frac{V}{V_p} \right)^{\frac{1}{n}} P(V). \quad (4.8)$$

The apparent elongational viscosity $\eta = \eta(L)$ at the end of the spinline is found to be

$$\eta = \frac{\sigma_p}{(v_0/L)(V_p - V_s)} \left(\frac{V}{V_p} \right)^{\frac{(n-1)}{n}}. \quad (4.9)$$

Thus the analytical model has four free parameters: the effective extrudate swell described by V_s , the critical draw ratio V_p and the corresponding critical tensile force F_p , which indicate the quasi steady-state, and the power law index n . These parameters are obtained by the following procedure: Eq. (4.2) and (4.6) are fitted simultaneously to a reference Rheotens curve by use of a modified Levenberg-Marquardt procedure. The shift factors b for Rheotens curves measured at different processing conditions are fitted to this reference curve simultaneously. The quality of the fit is shown in fig. 4.3 for LLDPE1. The reference curve is the one shown in fig. 4.2, and the processing conditions are indicated in the figure. The following values of the parameters were found: $V_s = 0.77$, $V_p = 2.3$, $F_p = 3.6$ cN, and $n = 0.62$.

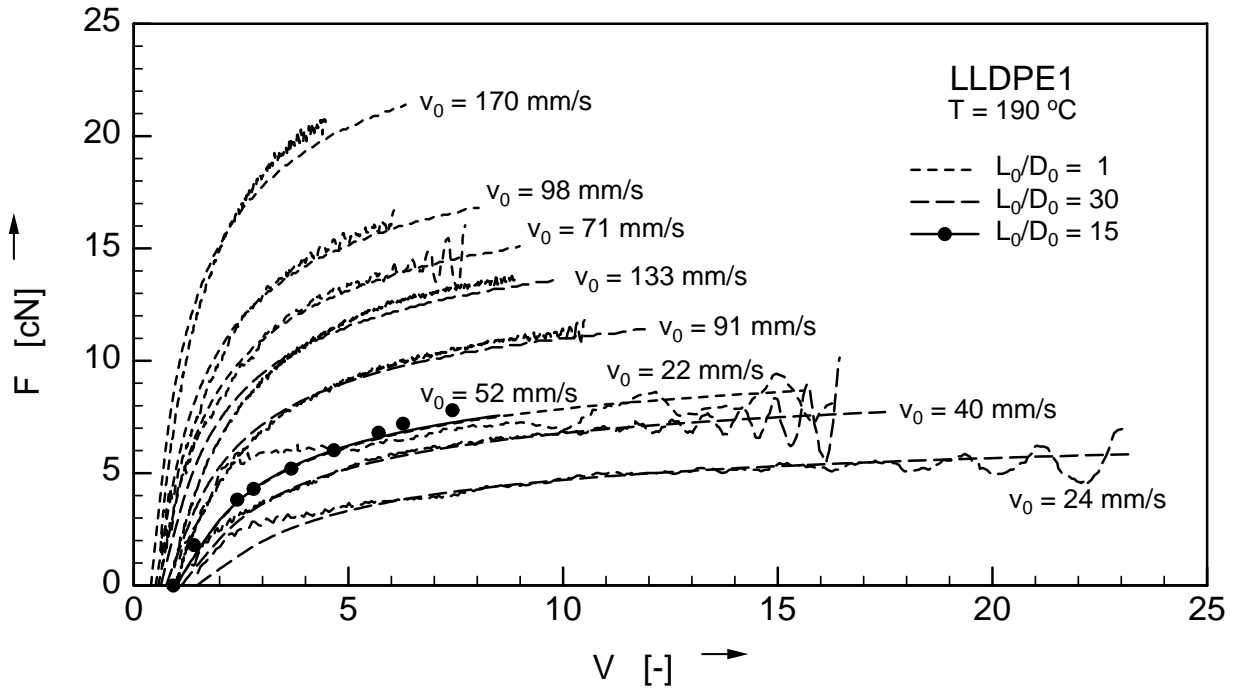


Figure 4.3: Comparison of experimental Rheotens curves for melt LLDPE1 and fit by the analytical model.

The apparent elongational viscosities calculated from the Rheotens curves are presented in fig. 4.4. The abrupt change of slope at the critical tension σ_p indicates the transition from the viscoelastic startup to viscous deformation, and is due to the simplifications of the model. The power law index n found by fitting the Rheotens data is similar to the one observed in shear. It can be seen that increasing the rate of preshear (corresponding to increasing the extrusion velocity v_0) leads to a lower level of the apparent elongational viscosity. This also is the key to the legend of fig. 4.4 and the following plots where apparent elongational viscosity values are shown: For each die length, the extrusion velocities of the experiments are given, the smallest v_0 corresponds to the highest apparent elongational viscosity curve.

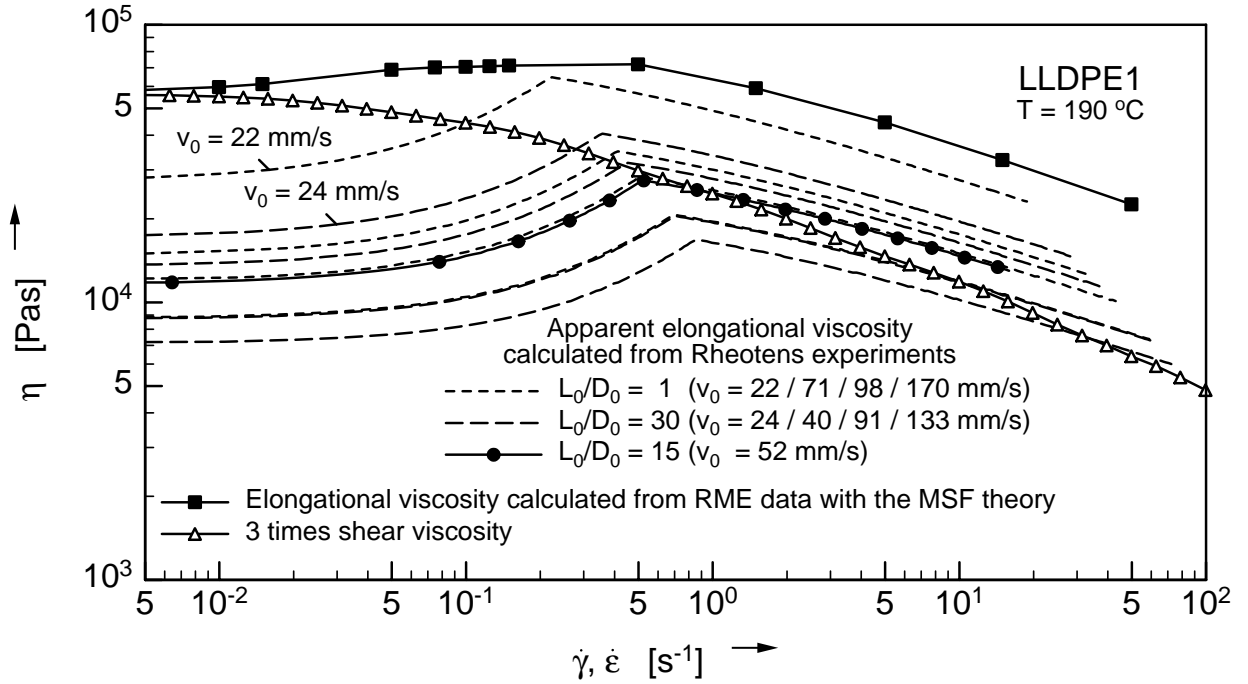


Figure 4.4: Apparent elongational viscosity for melt LLDPE1 calculated from Rheotens curves by use of the analytical model. Also shown is the elongational viscosity calculated from RME data [5] as well as 3 times the shear viscosity.

4.2 Similarity model

This model is based on the assumption that the elongational viscosity in the Rheotens test is a function of the draw ratio only, i.e. $\eta = \eta(V)$. This is plausible as the drawdown is the dominant deformation in the Rheotens experiment.

Like the analytical model, this model is based on a detailed knowledge of the velocity distribution along the spinline (with $x = 0$ at the exit of the extrusion die and $x = L$ at the wheels of the Rheotens). This information is mainly needed to calculate the elongation rate at the end of the spinline ($x = L$), while the corresponding tensile stress is calculated from the pulling force and the local diameter at $x = L$. In the following, we distinguish between two cases: V_s is independent (1) or dependent (2) on the drawdown force.

(1) V_s is independent of the drawdown force, i.e. $V_s = \phi$

Fig. 4.5 is a sketch of the velocity distribution along the spinline for two different drawdown forces F_x and F_L as a function of x .

Obviously, the following considerations are valid:

- (a) Drawdown force F_L results in draw ratio V_L at length L .
- (b) Drawdown force F_L results in draw ratio V_x on length x .
- (c) Drawdown force F_x results in draw ratio V_x on length L .

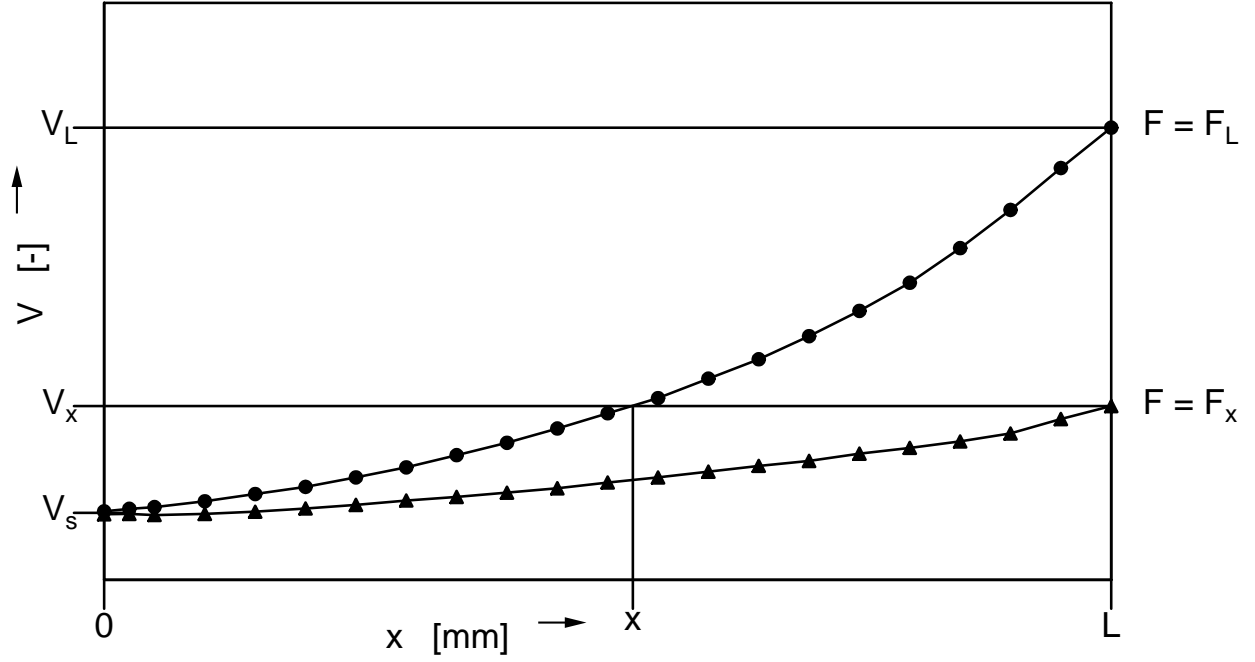


Figure 4.5: LDV measurement of the velocity distribution along the fiber in case $V_s = \phi$.

From the conservation of momentum for constant force along the spinline it follows that

$$F = \frac{A_0 v_0}{v(x)} \sigma(x) = \phi, \quad (4.10)$$

leading to

$$\sigma(x) = \frac{F}{A_0 v_0} v(x). \quad (4.11)$$

Assuming that the elongational viscosity is a function of the draw ratio only, the following constitutive equation is valid:

$$\sigma(x) = \eta(V) \dot{\epsilon}(x) = \eta(V) \frac{dv}{dx} \quad (4.12)$$

From (4.11) and (4.12) and subsequent integration the following expression for the force F is found:

$$F = A_0 \frac{v_0}{x} \int_{V_s}^{V(x)} \eta(V') d \ln V' \quad (4.13)$$

Eq. 4.13 is now applied to the considerations (a), (b), (c) above:

$$\text{from (a) follows } F_L = A_0 \frac{v_0}{L} \int_{V_s}^{V_L} \eta(V') d \ln V' \quad (4.14)$$

$$\text{from (b) follows } F_L = A_0 \frac{v_0}{x} \int_{V_s}^{V_x} \eta(V') d \ln V' \quad (4.15)$$

$$\text{from (c) follows } F_x = A_0 \frac{v_0}{L} \int_{V_s}^{V_x} \eta(V') d \ln V' \quad (4.16)$$

The integrals in eqs. (4.15) and (4.16) are equal, therefore

$$F_L x = F_x L \quad \text{or} \quad F_x = F_L \frac{x}{L} \quad \text{or} \quad x = L \frac{F_x}{F_L}, \quad (4.17)$$

which means that the coordinates x and corresponding forces F_x are simply proportional to each other. This allows to convert a velocity profile $V(x) = V(L \frac{F_x}{F_L})$ into a portion of the Rheotens curve $F = F(V)$ and vice versa. Therefore this model is called the similarity model.

For the LLDPE experiment shown in fig. 4.1 and 4.2, the resulting force curve calculated from the spinline velocity profiles according to eq. (4.17) is given in fig. 4.6. The resulting force curve agrees well with the original Rheotens curve, demonstrating the validity of the similarity model. Also, as shown in fig. 4.7, the local velocity distribution along the spinline as calculated from the model agrees with the experimental data. This result has been obtained by calculating F_x from eq. 4.17 and finding the corresponding V_x on the Rheotens curve fitted by the similarity model.

From the constitutive equation suggested in (4.12), the apparent elongational viscosity $\eta = \eta(V)$ can be calculated by differentiating eq. (4.13),

$$\boxed{\eta(V) = \frac{1}{A_0} \frac{L}{v_0} \frac{dF}{d \ln V}}. \quad (4.18)$$

On the other hand, the following relation for the force is valid,

$$F = \frac{A_0}{V} \sigma = \frac{A_0}{V} \eta \dot{\epsilon}, \quad (4.19)$$

and therefore the elongation rate $\dot{\epsilon}$ can be expressed as

$$\boxed{\dot{\epsilon} = \dot{\epsilon}(x = L) = \frac{v_0}{L} \left(\frac{d \ln F}{dV} \right)^{-1}}. \quad (4.20)$$

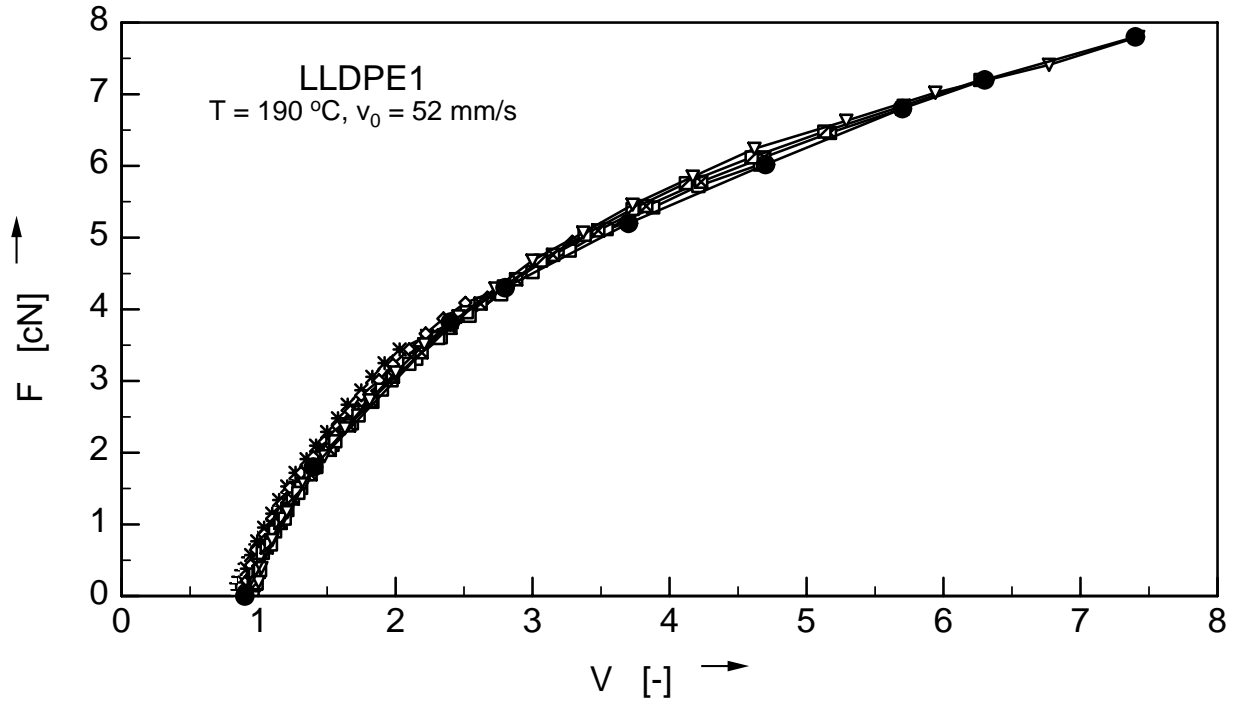


Figure 4.6: Force curve resulting from the conversion of velocity profiles according to the similarity solution (4.17) for melt LLDPE1.

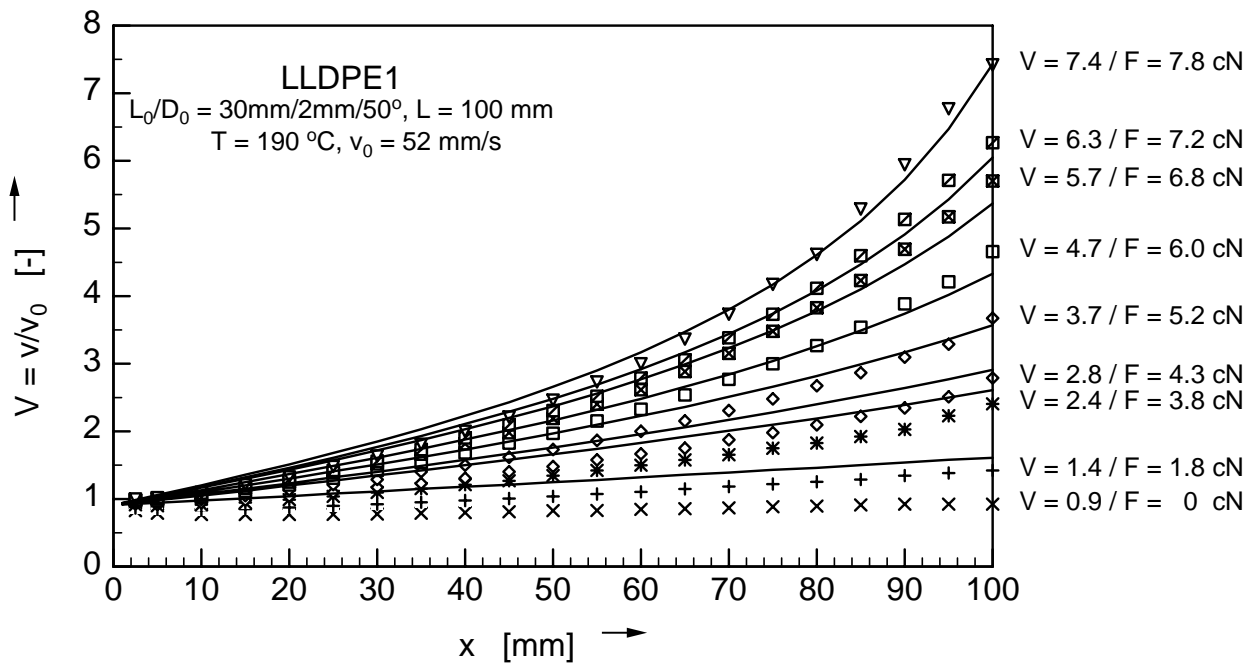


Figure 4.7: Filament velocity v along the length x of the spinline for melt LLDPE1. Measurements (symbols) by LDV, compared to the prediction of the similarity model (lines).

Eqs. (4.18) and (4.20) represent a general scheme to convert Rheotens curves into apparent elongational viscosities. Consistency with the analytical model can be checked in the following way. If eq. (4.2) for $V \leq V_p$ and eq. (4.6) for $V > V_p$ are differentiated and inserted into eqs. (4.18) and (4.20), the resulting expressions for elongation rate $\dot{\epsilon}$ and viscosity η are found to be identical to eqs. (4.1) and (4.3) for $V \leq V_p$, and eqs. (4.8) and (4.9) for $V > V_p$. Thus, the analytical solution is a special case of the similarity model.

The result of this conversion is finally given in fig. 4.8. Due to differentiation of the Rheotens curve, no discontinuity of the viscosity curve as in the analytical model is found, but in general the result remains the same. The fitting routine used is again a modified Levenberg-Marquardt procedure with 4 free parameters: V_s , n , and two fitting parameters a_1 and a_2 . The empirical relation between force and draw ratio which is used to fit the experimental Rheotens curves is the following:

$$F = a_1 \frac{\left(\frac{V}{V_s} - 1\right)}{\left[1 + a_2 \left(\frac{V}{V_s} - 1\right)^{\left(\frac{1-n}{n}\right)}\right]^{\left(\frac{n}{1-n}\right)}}. \quad (4.21)$$

The following fitting parameters were used to calculate the result in fig. 4.8: $a_1 = 2.47$, $a_2 = 0.13$, $V_s = 0.77$, and $n = 0.44$. The value of n is different than the one from the analytical model, which is caused by the slightly different shape which the equations for the force of the two models give.

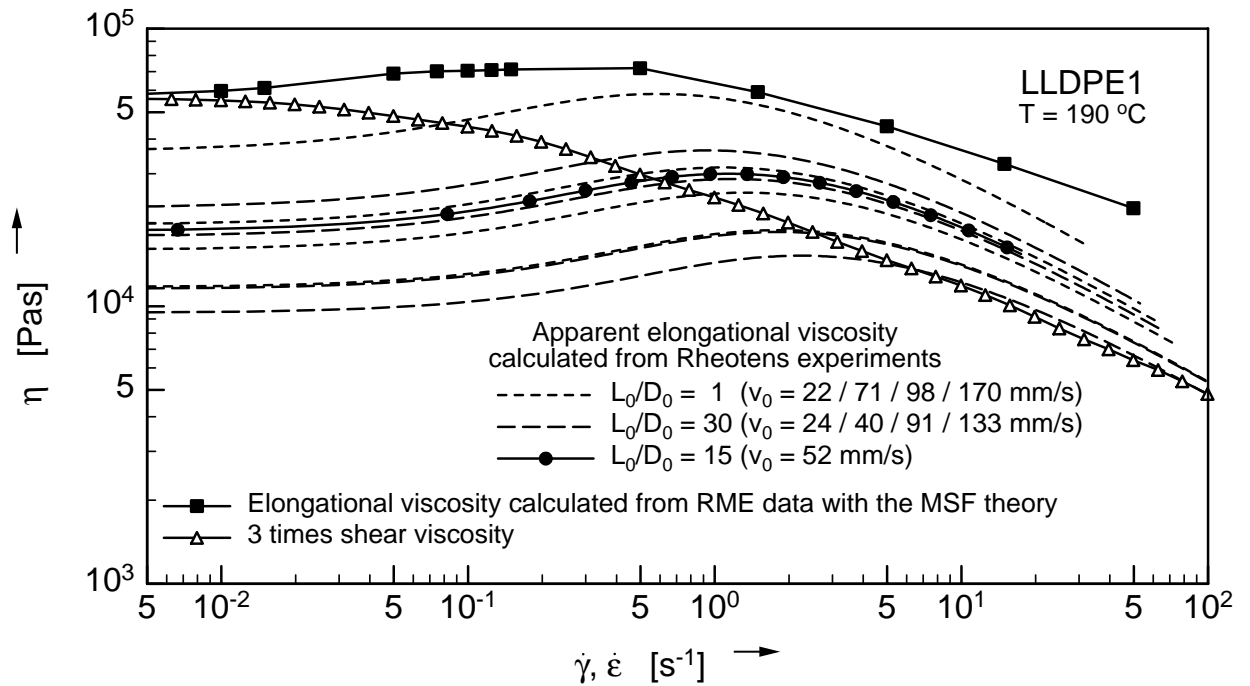


Figure 4.8: Apparent elongational viscosity calculated from Rheotens curves by use of the similarity model for melt LLDPE1. Also shown is the elongational viscosity calculated from RME data [5] as well as 3 times the shear viscosity.

(2) V_s is a function of the drawdown force: $V_s = V_s(F)$

For many polymer melts however, a stronger dependence of the starting velocity on the drawdown force $V_s = V_s(F)$ is found, as is illustrated in fig. 4.9 for LDPE2. If this is the case, neither the analytical model nor the version of the similarity model given above are valid any more. However, the similarity model can be extended in such a way, that a nin-constant value of V_s for different drawdown forces can be handled.

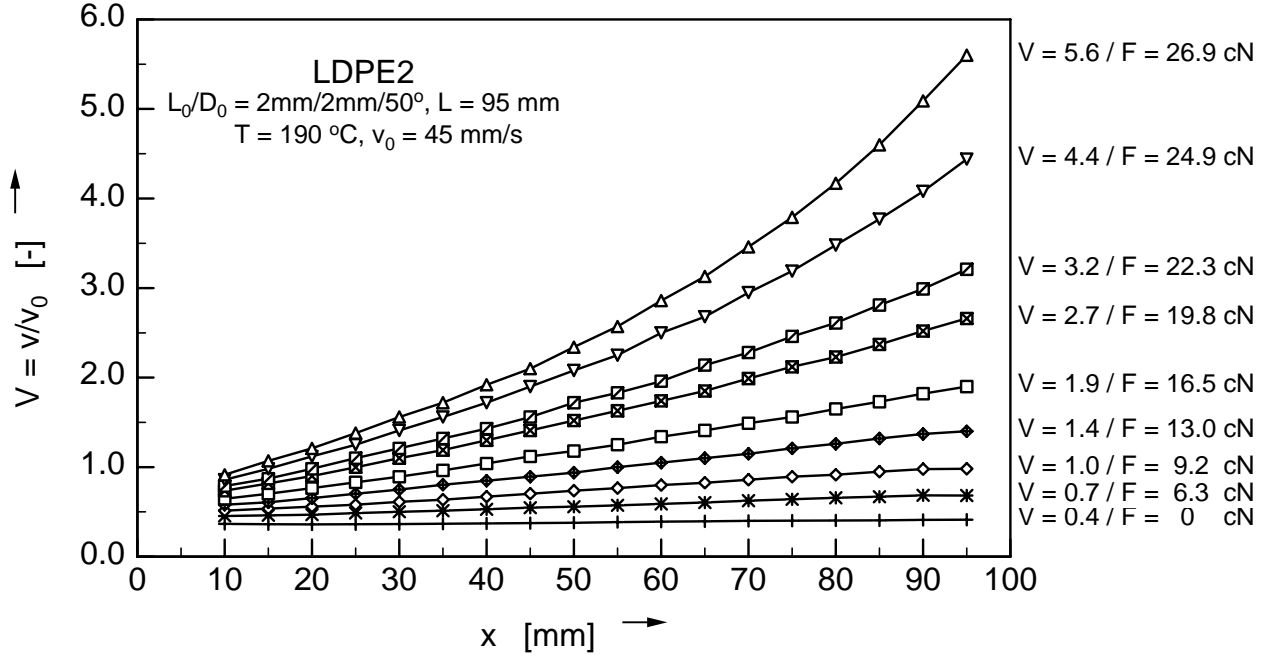


Figure 4.9: Filament velocity v along the length x of the spinline for melt LDPE2. Measurements (symbols) by LDV.

Fig. 4.10 gives a sketch of the modified conditions in this case. The stretch ratio $\lambda = V/V_s$ is defined with an individual value of V_s , $V_s(F)$, corresponding to each drawdown force F . A similar argument as in the case of constant V_s is valid under the assumption $\eta = \eta(\lambda)$.

The force F can be calculated as follows:

$$F = A_0 \frac{v_0}{x} \int_1^{\lambda(x)} \eta(\lambda') d \ln \lambda' \quad (4.22)$$

Hence the same analogon as in the case of $V_s = \text{const}$ is found:

$$F_x = F_L \frac{x}{L} \quad \text{or} \quad x = L \frac{F_x}{F_L} \quad (4.23)$$

The conversion of velocity profiles into the original Rheotens curve $F(V)$ is given in fig. 4.11 a) and compared to the conversion as a function of λ according to eq. (4.23) in fig. 4.11 b). Only in the case of fig. 4.11 b) a unique curve is found.

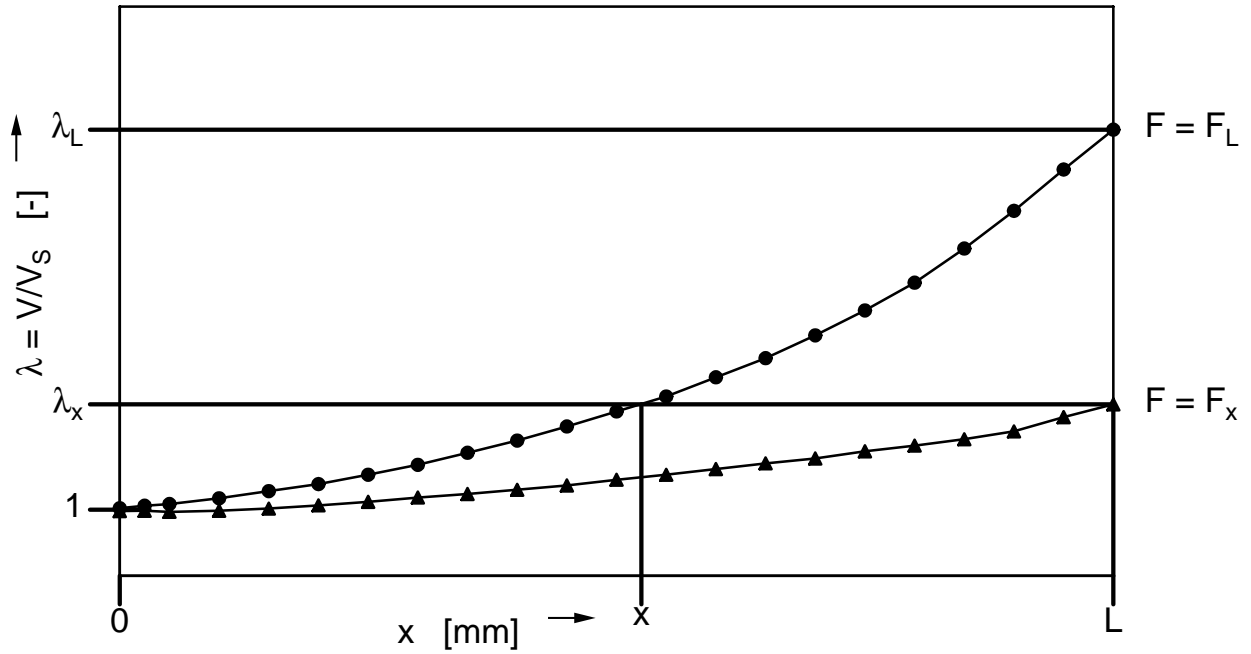


Figure 4.10: LDV measurement of the velocity distribution along the fiber in case $V_s = V_s(F)$

It is important to note that also the original Rheotens curve needs to be replotted as a function of λ , with each value of the draw ratio V being divided by the corresponding starting draw ratio V_s , which is given in the table inserted in fig. 4.11 b).

The apparent elongational viscosity $\eta(\lambda)$ and the corresponding strain rate $\dot{\epsilon}$ can be calculated according to

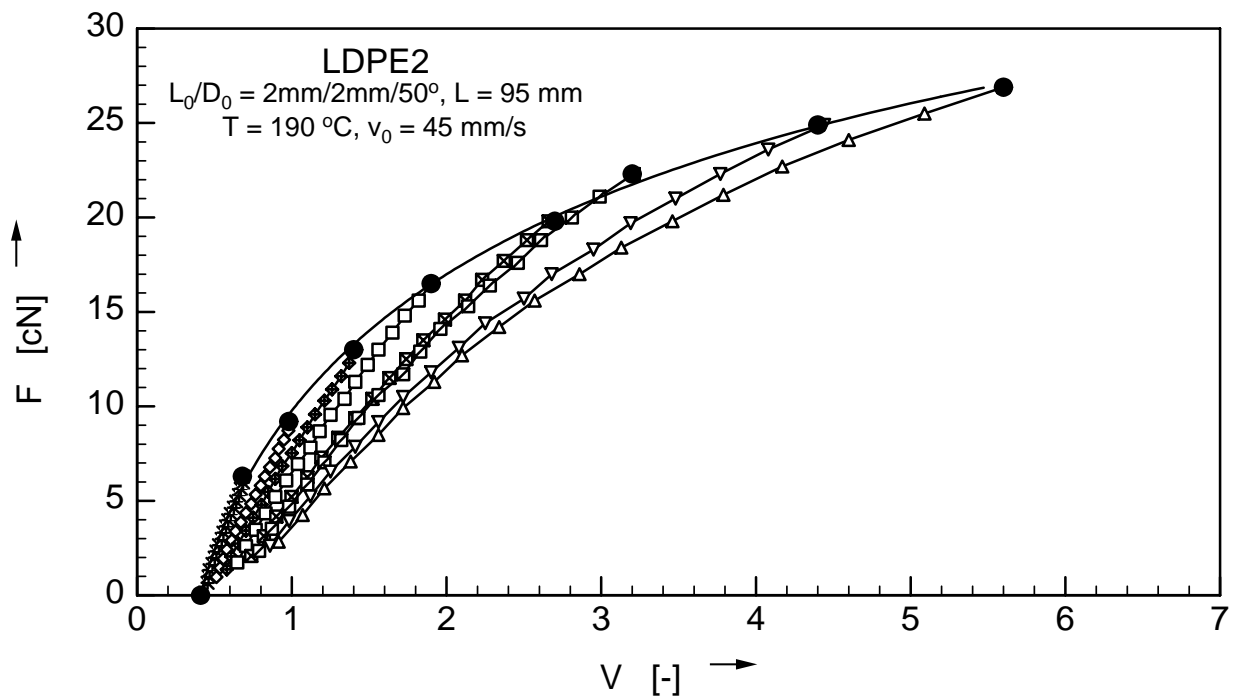
$$\eta(\lambda) = \frac{1}{A_0} \frac{L}{v_0} \frac{dF}{d \ln \lambda} \quad (4.24)$$

and

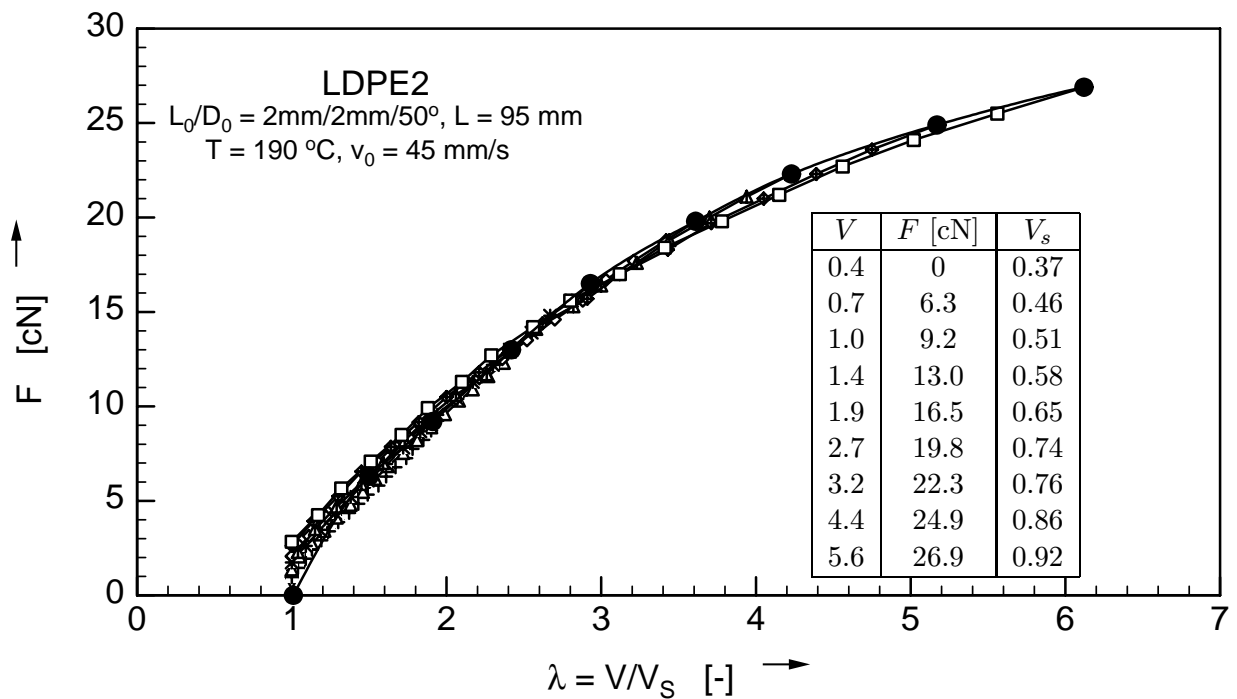
$$\dot{\epsilon} = \dot{\epsilon}(x = L) = \frac{v_0}{L} \left(\frac{d \ln F}{d \lambda} \right)^{-1} \quad (4.25)$$

In fig. 4.12 the results are compared of converting the Rheotens curve for melt LDPE2 as a function of V according to eqs. (4.18) and (4.20), and as a function of λ according to eqs. (4.24) and (4.25). A difference in the level of the elongational viscosity is visible, but the shape of the curves is similar. However, the influence of V_s varying with the pulling force F cannot be neglected.

From a practical point of view, this additional shifting procedure is unfavourable, as the information on the reduction of swelling by the drawdown force and thus the variation of V_s with F is not available from the standard Rheotens test. Therefore the Rheotens the experimental



a) as a function of V



b) as a function of λ

Figure 4.11: Force curve resulting from the conversion of velocity profiles according to the similarity solution (4.23) for melt LDPE2. Values $V_s(F)$ necessary for the conversion are indicated.

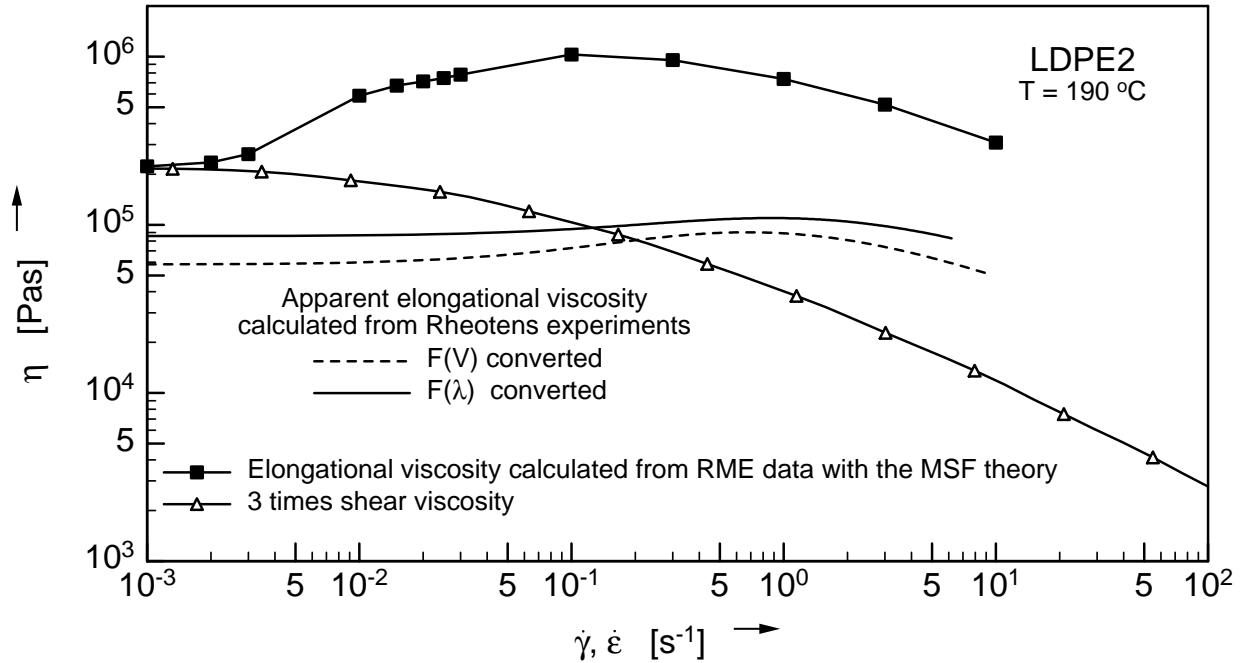


Figure 4.12: Apparent elongational viscosity calculated from Rheotens curves by use of the general solution as a function of V and λ for melt LDPE2. Also shown is the elongational viscosity calculated from RME data [5] as well as 3 times the shear viscosity.

conditions are investigated under which the similarity solution for constant V_s is valid. These should be applied, if the main interest of the Rheotens measurement is to extract elongational viscosities.

For the following melts, velocity profiles have been measured by LDV and are reported in appendix B: LDPE1, LDPE2, HDPE1, HDPE2, LLDPE1. For the same materials, and additionally for PP1 and PS1, elongational viscosities have been measured with the extensional rheometer RME by Bastian [5] (for LDPE1 experimental results of a slightly different material, Lupolen 1810H from BASF, are used). The normalised elongational viscosity (steady-state values calculated from the MSF theory) are compared in fig. 4.13 to illustrate the amount of strain hardening exhibited by the different melts. Also included into fig. 4.13 are data on melt PP2, which was investigated by Kurzbeck with a Muenstedt type elongational rheometer [24], [25]. Both LDPE melts (due to long chain branching), as well as melt HDPE1 (presumably due to a high molecular weight tail) show pronounced strain hardening. Melt PP2 is an example for a branched polypropylene which also shows significant strain hardening. On the contrary, the other, linear materials hardly show any strain hardening effect.

Tab. 4.1 illustrates for which materials and which die geometries the similarity assumption is valid either for constant V_s (case (1)) or for increasing V_s as a function of the drawdown force (case(2)). Obviously, the similarity assumption is only valid under certain experimental conditions. Only for LLDPE1, a constant V_s is found for all die geometries. For the strain hardening materials, the similarity assumption is not valid for all the dies, increasing discrepancy with increasing L/D ratio of the die is found. To distinguish between LDPE1 and LDPE2, the swelling behaviour is also taken into account, as the amount of strain hardening is

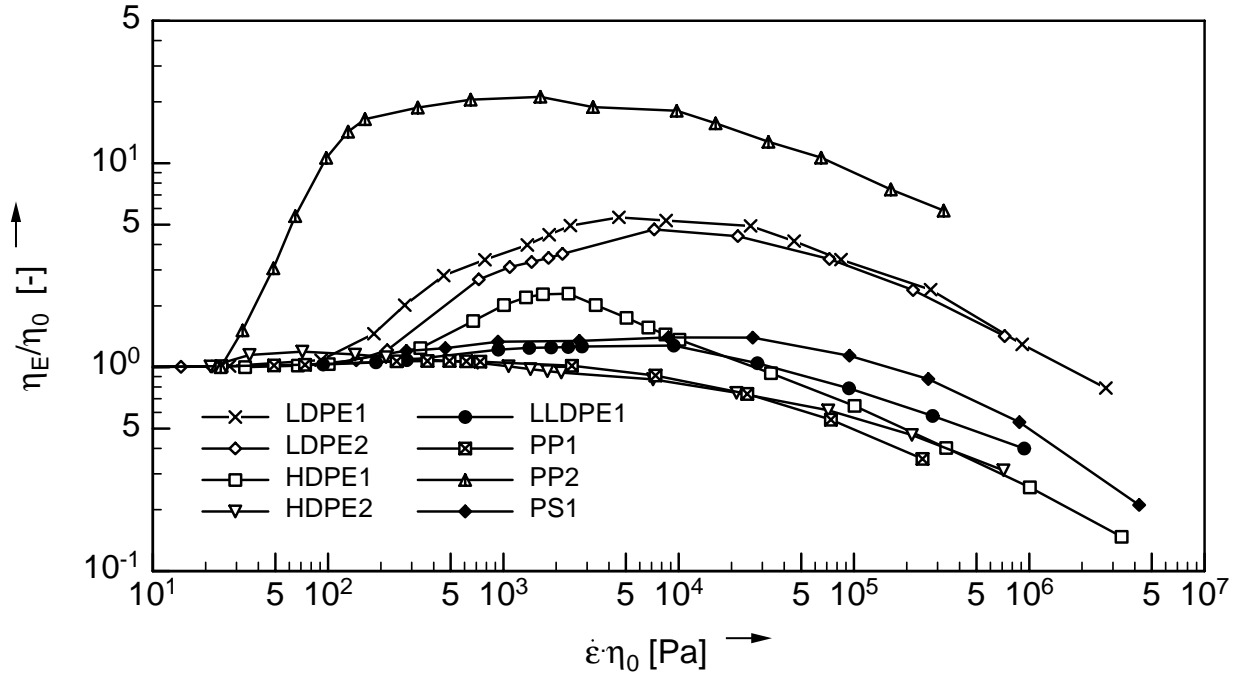


Figure 4.13: Normalised steady-state elongational viscosity of different polymer melts.

similar. From experiments at constant extrusion pressure it can be seen that LDPE1 exhibits more extrudate swell than LDPE2. Hence for the material with higher elasticity, the influence of the drawdown force on V_s is less pronounced.

In conclusion, either high extrudate swell (caused by high elasticity) or low strain hardening minimises the influence of the drawdown force on the velocity close to the exit of the extrusion die. Therefore to calculate elongational viscosities from Rheotens experiments, it is advantageous to perform measurements by use of short dies which cause a high level of extrudate swell.

| Material | $L_0/D_0 = 1$ | $L_0/D_0 = 15$ | $L_0/D_0 = 30$ |
|----------|----------------|----------------|----------------|
| LDPE1 | $V_s = \phi$ | $V_s = V_s(F)$ | $V_s = V_s(F)$ |
| LDPE2 | $V_s = V_s(F)$ | - | - |
| HDPE1 | $V_s = V_s(F)$ | - | - |
| HDPE2 | $V_s = V_s(F)$ | $V_s = V_s(F)$ | $V_s = V_s(F)$ |
| LLDPE1 | $V_s = \phi$ | $V_s = \phi$ | $V_s = \phi$ |
| PP1 | $V_s = V_s(F)$ | - | - |

Table 4.1: Validity of the similarity assumption for different materials and die geometries.

4.3 Comparison of apparent and true elongational viscosity

For comparison of apparent and true elongational viscosities [4], the true steady-state elongational viscosity is obtained from experimental data of Bastian [5] (with the exception of melt PP2, where experimental data and material were provided by Kurzbeck [24]). Startup experiments in uniaxial elongation with the elongational rheometer RME result in transient elongational viscosity data. These are described by the MSF theory [50], [44], and the plateau of the steady-state viscosity is fitted to the measurements. Hence the steady-state elongational viscosity is known and can be compared to the analysis of Rheotens experiments. For some of the materials it was necessary to shift the steady-state viscosity to the temperature of the Rheotens experiment by use of the Arrhenius relation.

The comparison is presented for LLDPE1 (fig. 4.8), LDPE1 (fig. 4.14), LDPE2 (figs. 4.12 and 4.15), HDPE1 (fig. 4.16), HDPE2 (fig. 4.17), PP1 (fig. 4.18), PP2 (fig. 4.19), and PS1 (fig. 4.20). For simplicity, the conversion of Rheotens curves to elongational viscosities was made under the assumption that V_s is a constant, independent of the drawdown force. Additionally, Appendix C contains examples for several other LDPE melts, where the comparison to the analytical model is given (figs. C.1 - C.4). For all examples, the apparent elongational viscosity calculated from Rheotens experiments shows first a viscoelastic startup behaviour turning into a viscous power-law behaviour after a critical tension is reached. The power-law index is similar to the one found in steady-state extension and in shear.

The apparent elongational viscosities extracted from the Rheotens curves obviously do not match the steady-state viscosity obtained or extrapolated from the RME experiments. This is caused by the preshear of the material in the extrusion die. High preshear (corresponding to a high extrusion velocity v_0) leads to a lower level of elongational viscosity, which was also found by the analytical model. The different polymer grades differ in the amount of strain hardening and also in the amount of reduction of the apparent viscosity due to preshear.

The LDPE melts (figs. 4.14 and 4.15), which have a high degree of long-chain branching, show pronounced strain hardening, i.e. the true steady-state elongational viscosity shows a pronounced maximum, before it decreases with increasing deformation rate, in line with the shear viscosity. The apparent elongational viscosities extracted from the Rheotens curves also show this strain hardening effect clearly: for low extrusion velocities, the steady-state level is nearly reached and the shape of the curves is very similar (except for the start-up, which is much influenced by the absolute value of V_s). For high extrusion velocities the level of the apparent elongational viscosity is still considerably higher than three times the shear viscosity. This means that close to typical industrial processing conditions, the strain hardening effect of LDPE melts remains significant, even after extrusion. This is also true for the long-chain branched melt PP2 (fig. 4.19). In this case, however, the steady-state elongational viscosity level is not reached, even at small extrusion velocities. A possible explanation is that the long-chain branches of this melt are parallelised to the backbone of the macromolecule, which causes the apparent viscosity to drop considerably.

Concerning the linear materials, HDPE1 (fig. 4.16) is a melt which shows some strain hardening of the true steady-state elongational viscosity. This is drastically reduced by extrusion, and at higher strain rates, the apparent elongational viscosity derived from Rheotens measurements is close to three times the shear viscosity, which is also true for HDPE2 (fig. 4.17). For the other linear materials, LLDPE1, PP1, and PS1 (figs. 4.8, 4.18, 4.20), the apparent viscosities are found to be inbetween steady-state elongational viscosity and three times the shear viscosity.

For none of these melts the apparent viscosity is found to be above the steady-state elongational viscosity, nor is a level below three times the shear viscosity reached within the accuracy of the model. Hence the steady-state viscosities in elongation and shear limit the polymer rheology which is found under processing conditions by use of the Rheotens test. This is in agreement with an earlier statement of Laun and Schuch [32]: "There is evidence that uniaxial elongation represents the upper limit of strain hardening, whereas simple shear seems to characterize the lower limit of strain softening".

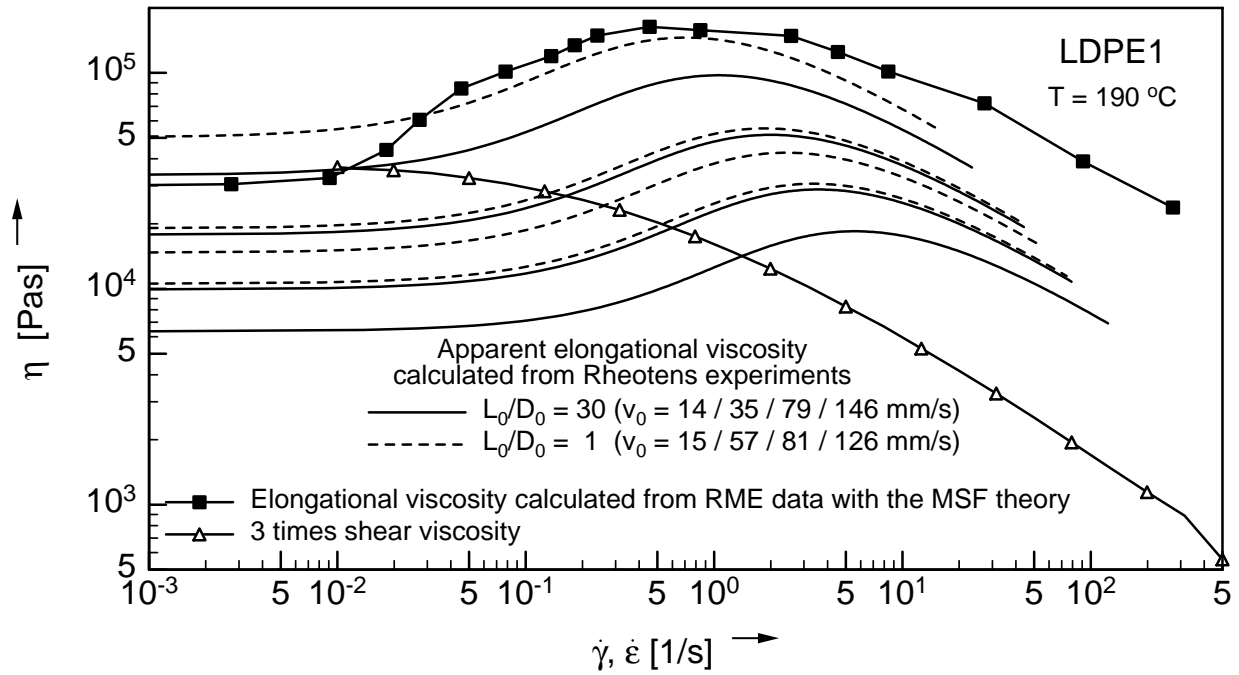


Figure 4.14: Comparison of the steady-state shear and elongational viscosity to the apparent elongational viscosity calculated from Rheotens curves for melt LDPE1.

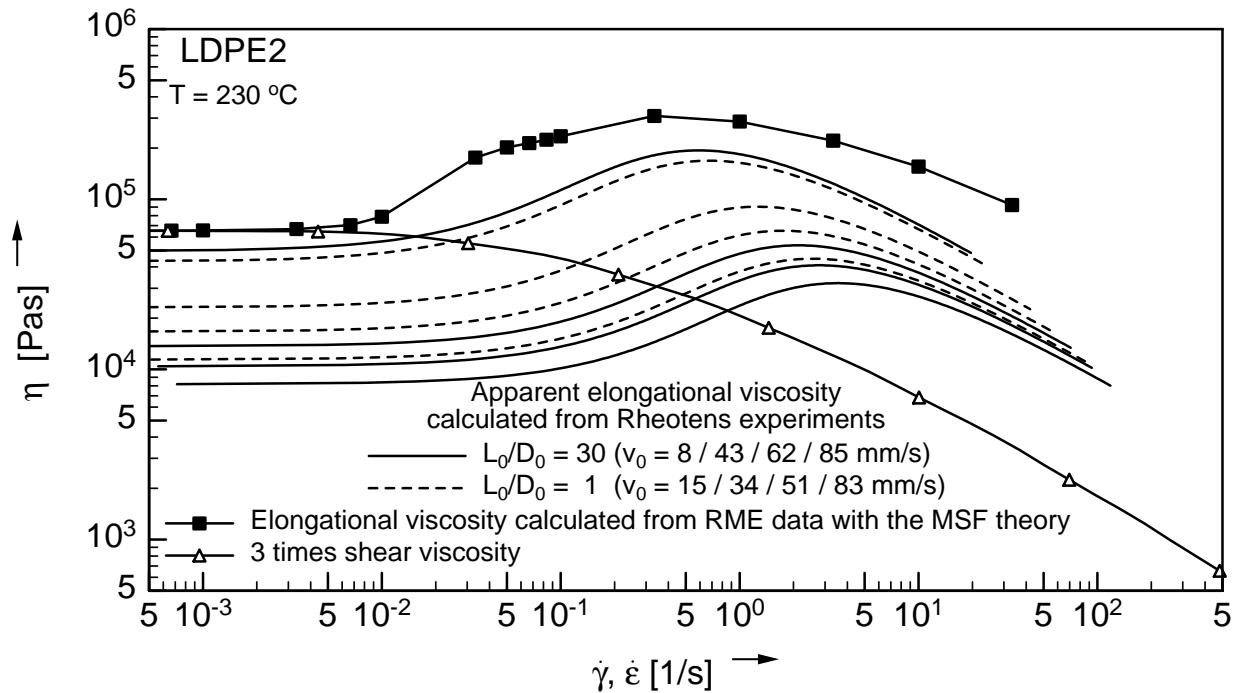


Figure 4.15: Comparison of the steady-state shear and elongational viscosity to the apparent elongational viscosity calculated from Rheotens curves for melt LDPE2.

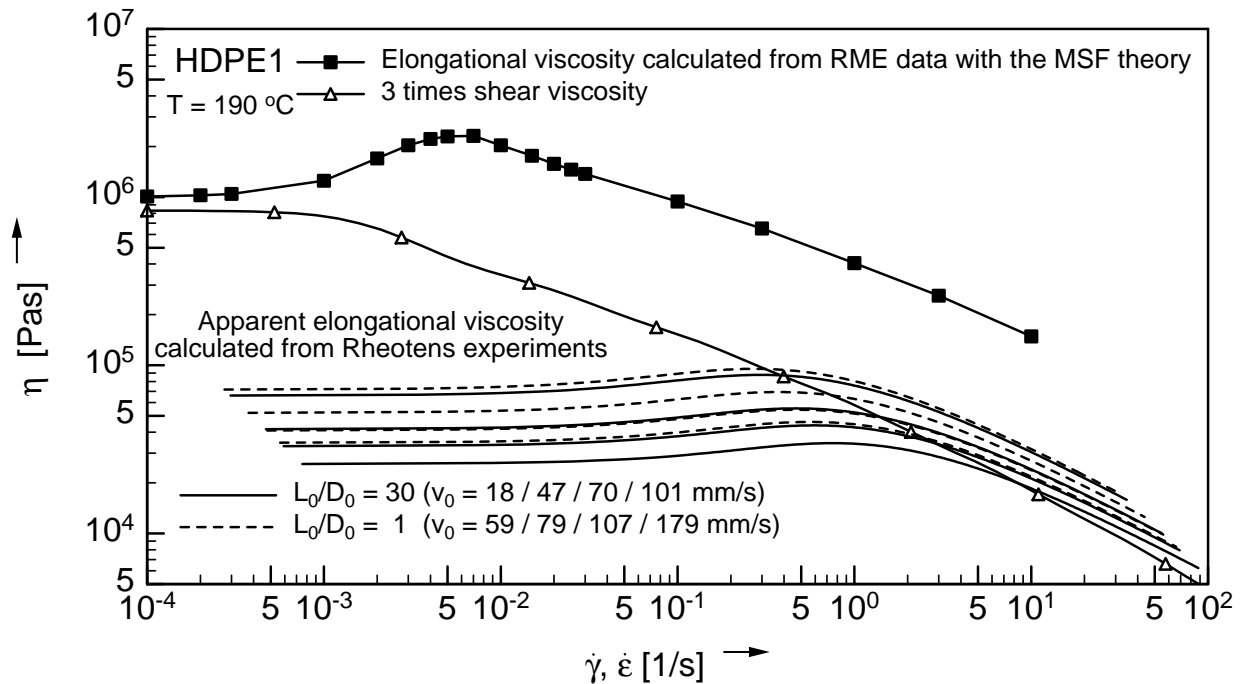


Figure 4.16: Comparison of the steady-state shear and elongational viscosity to the apparent elongational viscosity calculated from Rheotens curves for melt HDPE1.

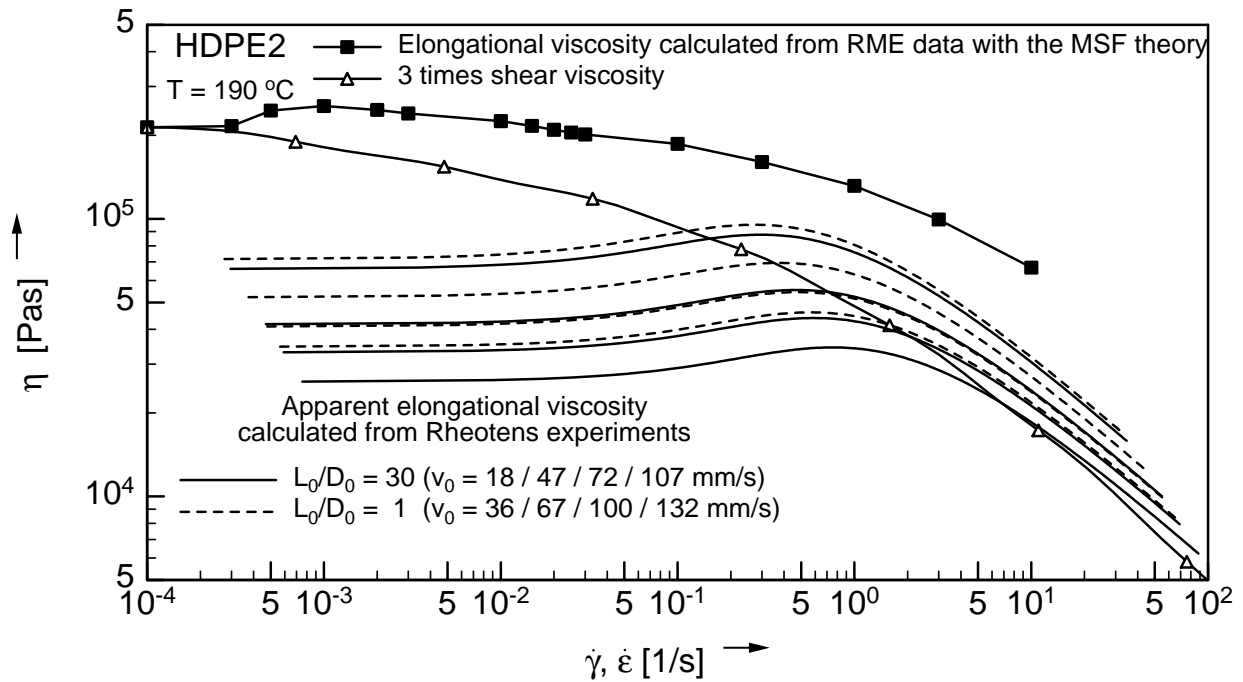


Figure 4.17: Comparison of the steady-state shear and elongational viscosity to the apparent elongational viscosity calculated from Rheotens curves for melt HDPE2.

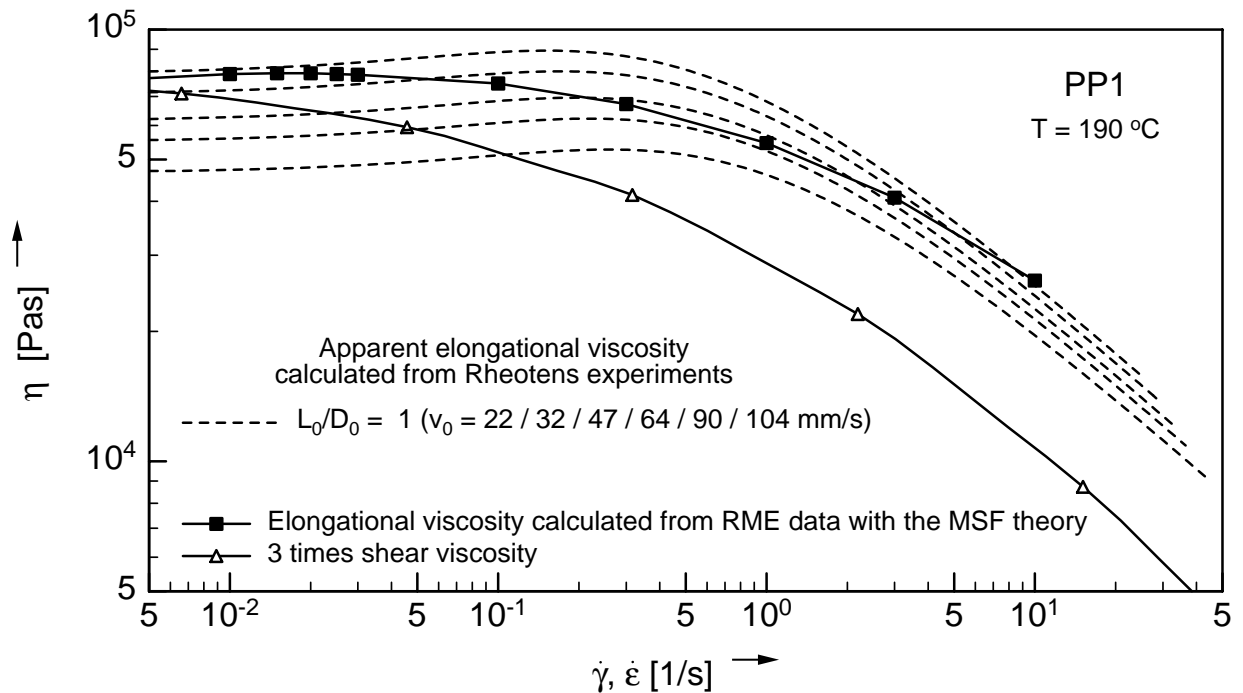


Figure 4.18: Comparison of the steady-state shear and elongational viscosity to the apparent elongational viscosity calculated from Rheotens curves for melt PP1.

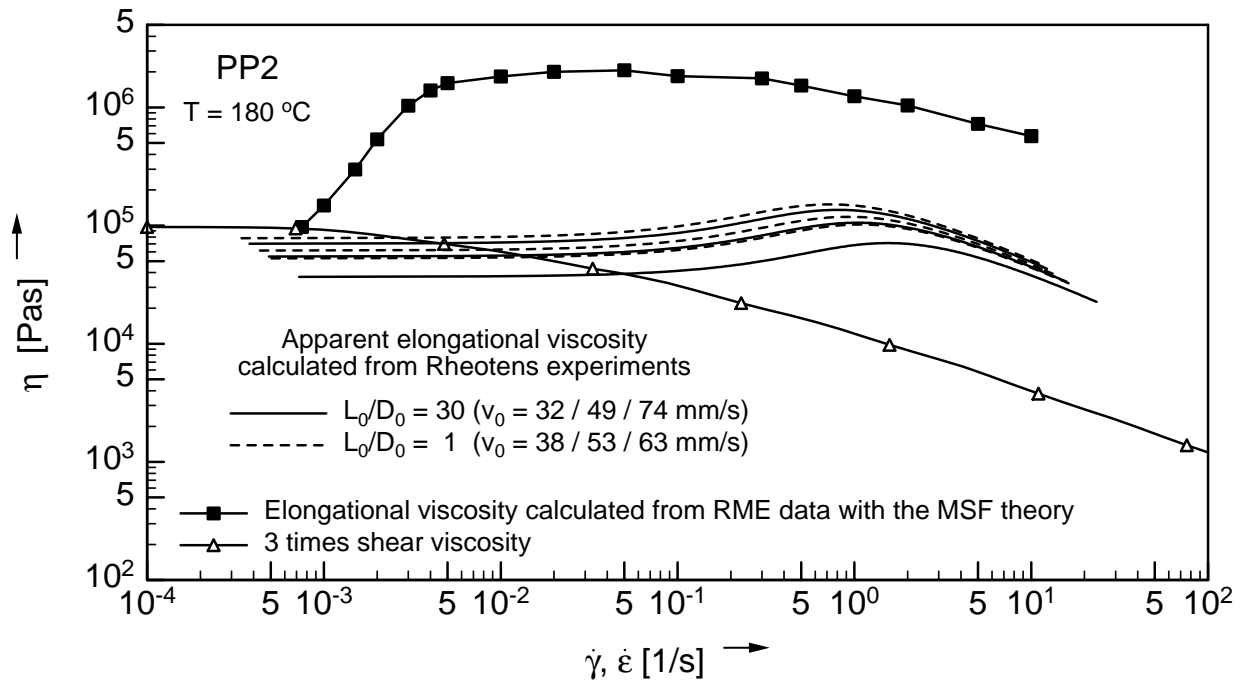


Figure 4.19: Comparison of the steady-state shear and elongational viscosity to the apparent elongational viscosity calculated from Rheotens curves for melt PP2.

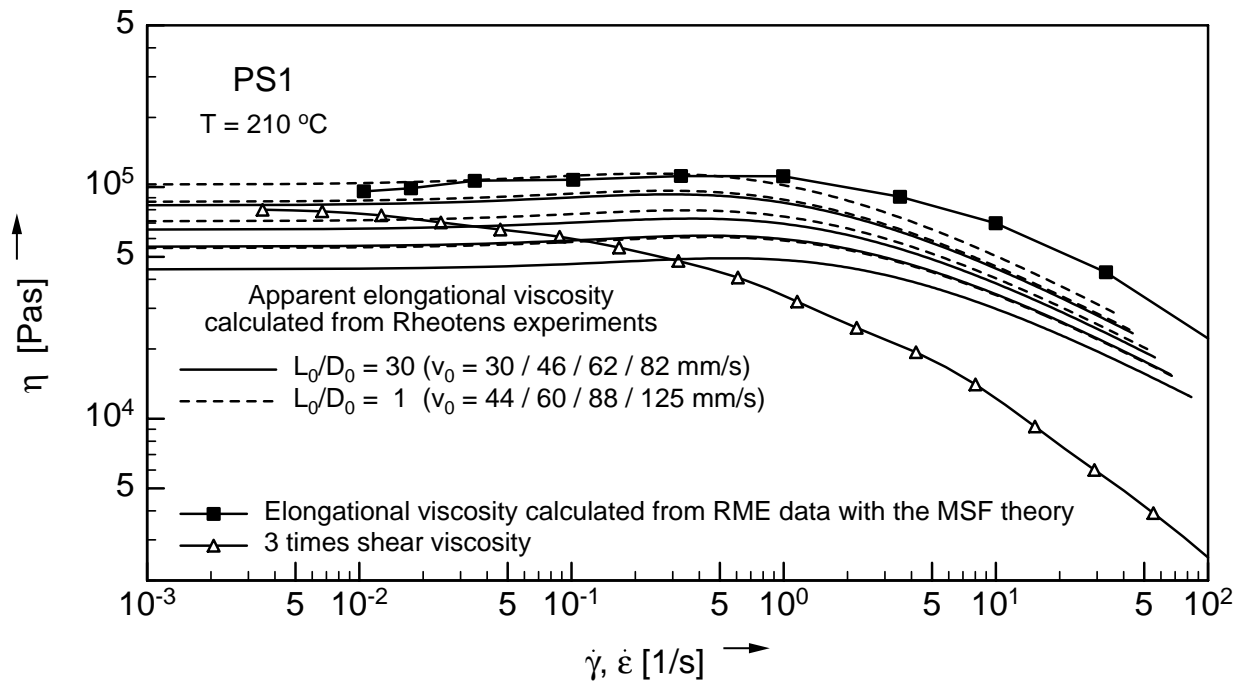


Figure 4.20: Comparison of the steady-state shear and elongational viscosity to the apparent elongational viscosity calculated from Rheotens curves for melt PS1.

4.4 Relevant Processing Conditions for the Approximation of Elongational Viscosities

Finally, the aim is to find test conditions for Rheotens measurements, which result in a good approximation of the steady-state elongational viscosity. This is done for those melts where the similarity model was found to be valid for the short die ($L_0/D_0 = 1$), LDPE1, LLDPE1, and also for LDPE2 and HDPE1, where it is only an approximation. It is also attempted for a selection of LDPE melts (and the results are given in Appendix C), for which a sufficient amount of experimental data at constant processing conditions (long die $L_0/D_0 = 30$) is available.

The following procedure was used and is shown for the example of LDPE1 in detail. A set of Rheotens curves measured at different flowrates and constant die ($L_0/D_0 = 1$) and spinline geometry is fitted by the similarity model (fig. 4.21). Obviously, the apparent elongational viscosity calculated from the Rheotens curve with $v_0 = 15$ mm/s is already close to the steady-state elongational viscosity, but slightly too low. Therefore, the dependence of the shift factor b on the extrusion velocity v_0 is extrapolated to lower flowrates (fig. 4.22). A processing condition (v_0, b) is selected in such a way, that the resulting apparent elongational viscosity matches the maximum of the steady-state elongational viscosity approximately (fig. 4.23). This can only be achieved by an iterative procedure. The final result is already included into figs. 4.21 - 4.23, with a shift factor of $b = 1.46$ leading to a corresponding extrusion velocity of $v_0 = 13$ mm/s. This means that a Rheotens curve can be calculated from the supermastercurve, which results in an apparent elongational viscosity approximating the steady-state viscosity.

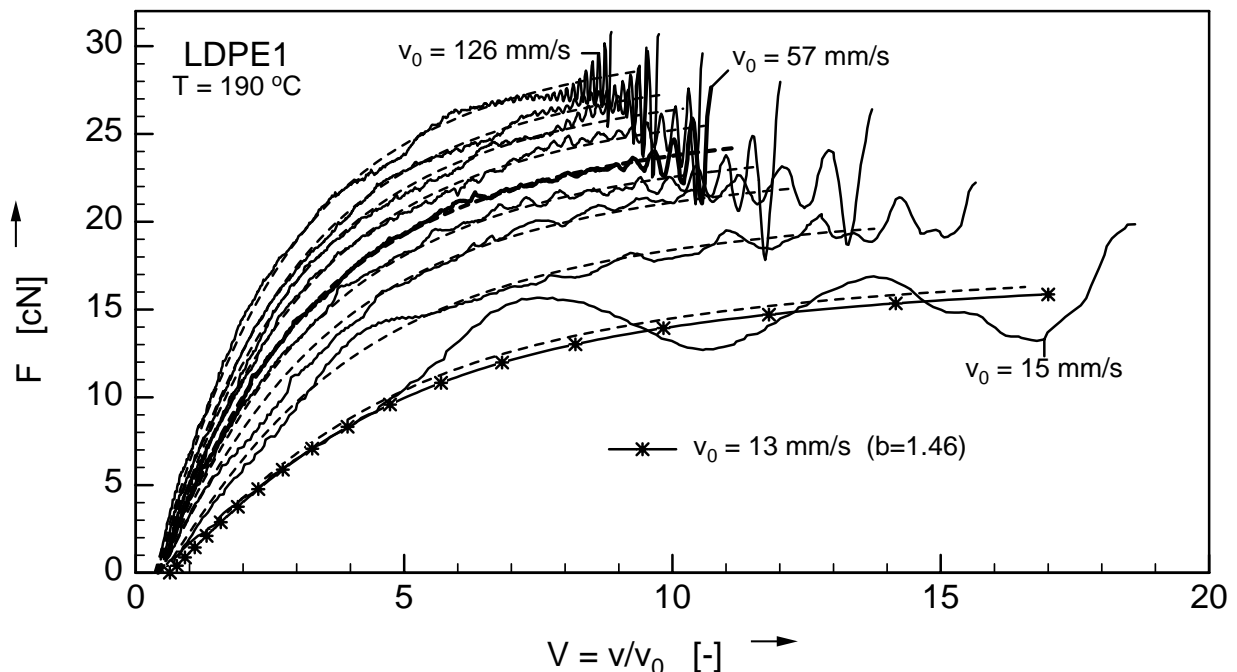


Figure 4.21: Comparison of experimental Rheotens curves for melt LDPE1 and fit by the similarity model. Also shown is the Rheotens curve (*) from which an approximation of the elongational viscosity is calculated and shown in fig. 4.23.

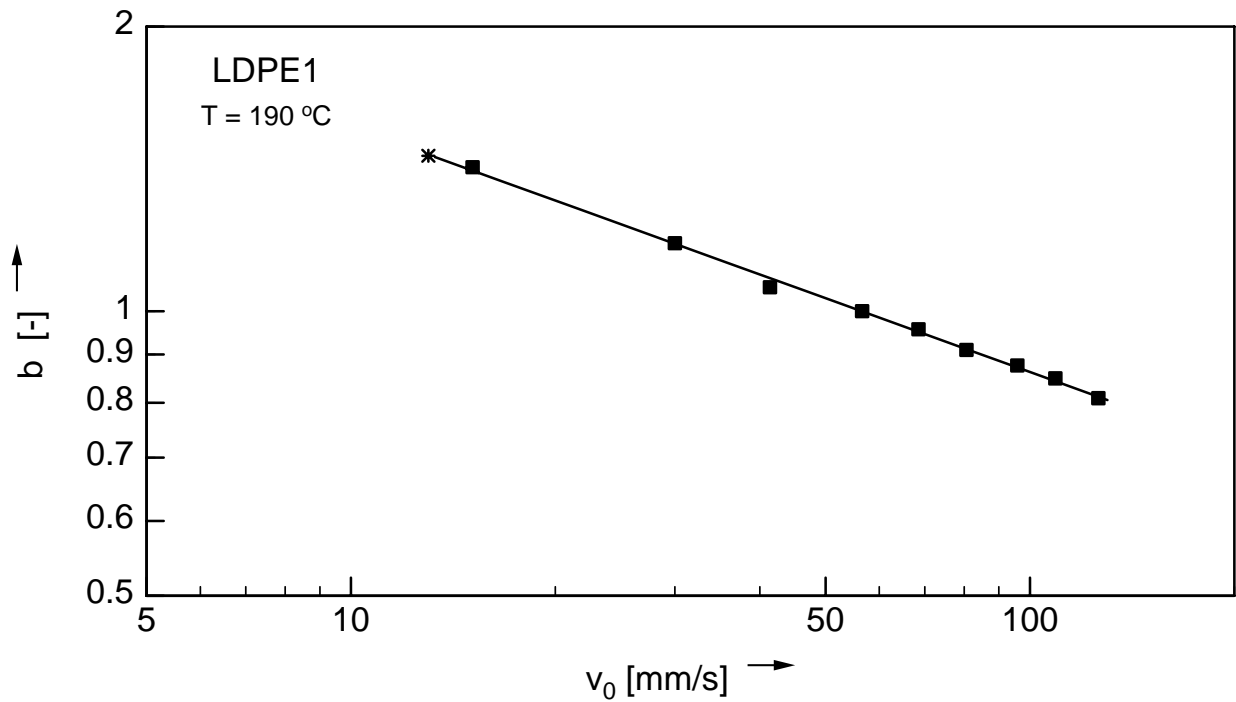


Figure 4.22: Dependence of shift factor b on extrusion velocity v_0 , needed for shifting of Rheotens curves onto the grandmastercurve for melt LDPE1.

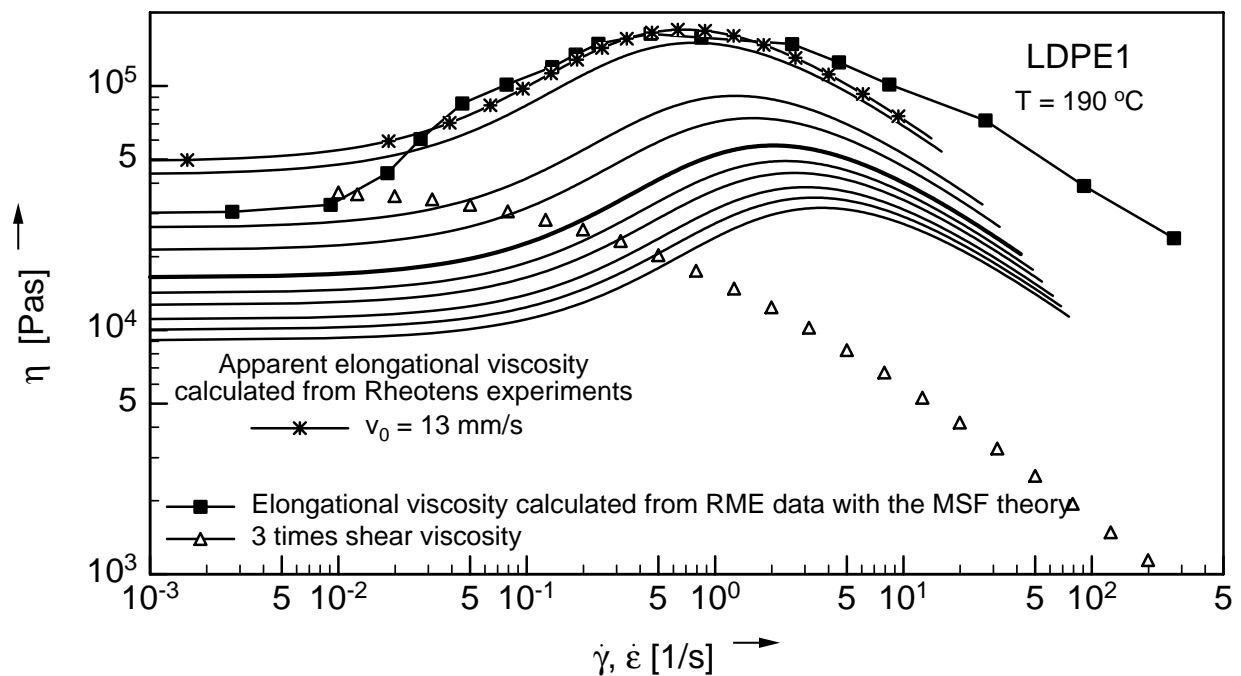


Figure 4.23: Comparison of the steady-state shear and elongational viscosity to the apparent elongational viscosity calculated from Rheotens curves for melt LDPE1. Also shown is the approximation of the steady-state elongational viscosity (*) calculated from Rheotens curve (*) shown in fig. 4.21.

Closer analysis of fig. 4.23 reveals that in the viscoelastic startup region, a viscosity higher than three times the shear viscosity is predicted. But if shear viscosity data are available, the Trouton viscosity could be used instead. Although the decrease of viscosity at higher elongation rates according to the power law is somewhat steeper than the original steady-state elongational viscosity curve, a combination of three times the shear viscosity (in the range of linear material behaviour) and the apparent elongational viscosity calculated from the Rheotens curve with $v_0 = 13$ mm/s (in the range of nonlinear material behaviour) results in a good approximation of the steady-state elongational viscosity.

Figs. 4.24 - 4.26 present similar results for melts LLDPE1, LDPE2, and HDPE1, where also Rheotens curves measured by use of the short die with $L_0/D_0 = 1$ were the basis of the calculation. For LLDPE1, no extrapolation to a lower flowrate was necessary, the data for $v_0 = 14$ mm/s already match the steady-state elongational viscosity. For melts LDPE2 and HDPE1, extrapolation to lower extrusion velocities was carried out.

Investigation of the processing conditions leading to the Rheotens curve from which the steady-state elongational viscosity is estimated is necessary, as the main interest certainly is not to fit the steady-state elongational viscosity but to predict it. For melts LDPE1, LLDPE1, and LDPE2, a value of v_0 around 10 mm/s ($\pm 50\%$) for the particular die and spinline geometry ($L_0/D_0 = 1$, $L = 100$ mm) leads to an approximation of the steady-state elongational viscosity. However, for melt HDPE1 extrapolation to a much smaller flowrate ($v_0 = 1$ mm/s) is necessary.

From figs. C.5 - C.9 in Appendix C where the steady-state elongational viscosities for several LDPE melts are compared to those calculated from Rheotens measurements, the same magnitude of the extrusion flowrate (keeping all other parameters of the experiment constant) leads to an approximation of the steady-state elongational viscosities. For the long die with $L_0/D_0 = 30$ a value of v_0 in the order of 8 mm/s ($\pm 50\%$) is found.

In conclusion this means that it is possible to approximate the steady-state elongational viscosity by analysis of Rheotens experiments. It is recommended to use measurements with a short die and a wide variation in flowrate. As it is easier to compare the apparent elongational viscosity of different materials than to predict absolute values of the elongational viscosity, all other parameters of the experiment, like the barrel before the die, must be kept constant. It was not possible to define exact processing conditions, which for all materials lead to an approximation of the steady-state elongational viscosity, but it certainly must be a low flowrate avoiding high preshear. For LDPE melts, a processing condition can be specified by measuring a well characterised melt like melt I and by comparing the apparent elongational viscosity to the steady-state elongational viscosity from the literature [36]. Performing Rheotens experiments with other LDPE melts at the same conditions (or, to avoid cooling at low flowrates, rather extrapolating the measurements to this conditions), will then lead to a prediction of elongational viscosity in the right order of magnitude.

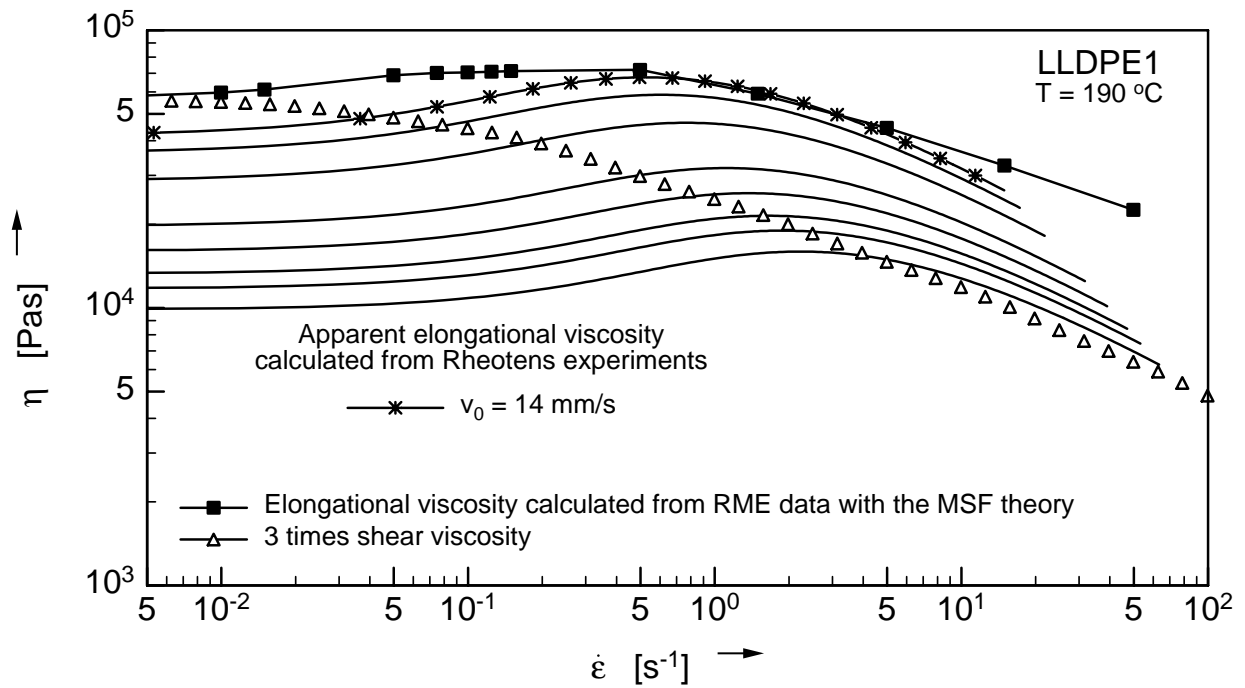


Figure 4.24: Comparison of the steady-state shear and elongational viscosity to the apparent elongational viscosity calculated from Rheotens curves for melt LLDPE1. Also shown is the approximation of the steady-state elongational viscosity (*).

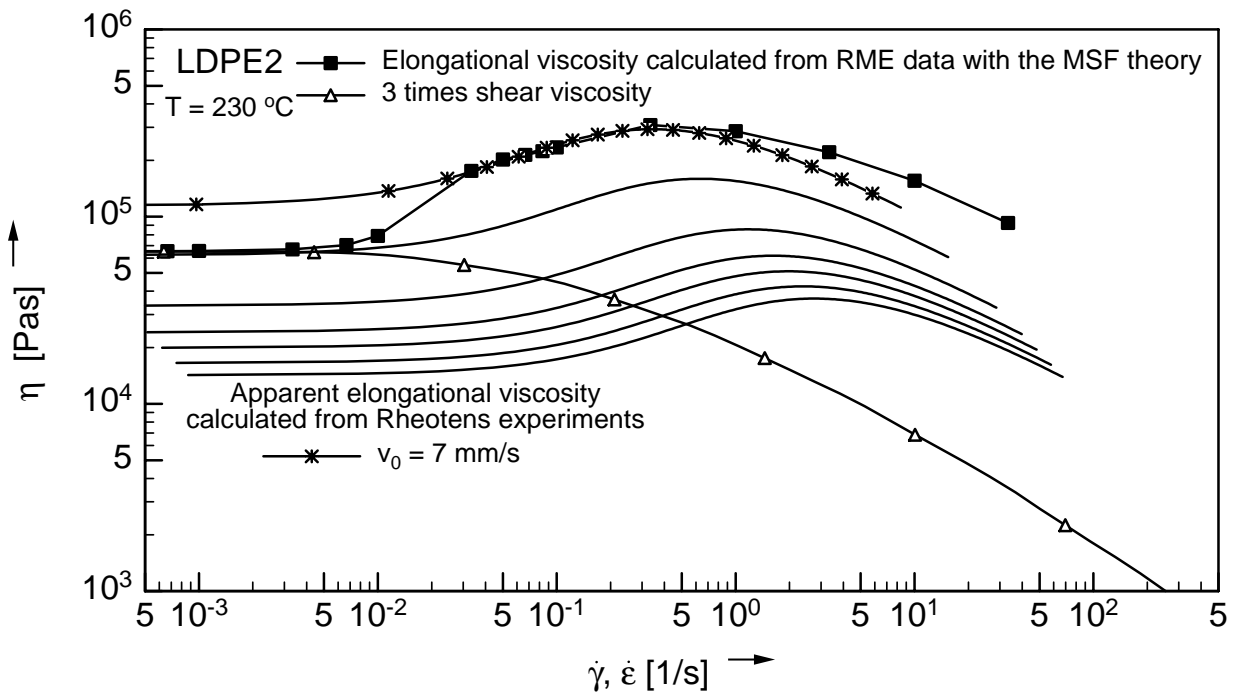


Figure 4.25: Comparison of the steady-state shear and elongational viscosity to the apparent elongational viscosity calculated from Rheotens curves for melt LDPE2. Also shown is the approximation of the steady-state elongational viscosity (*).

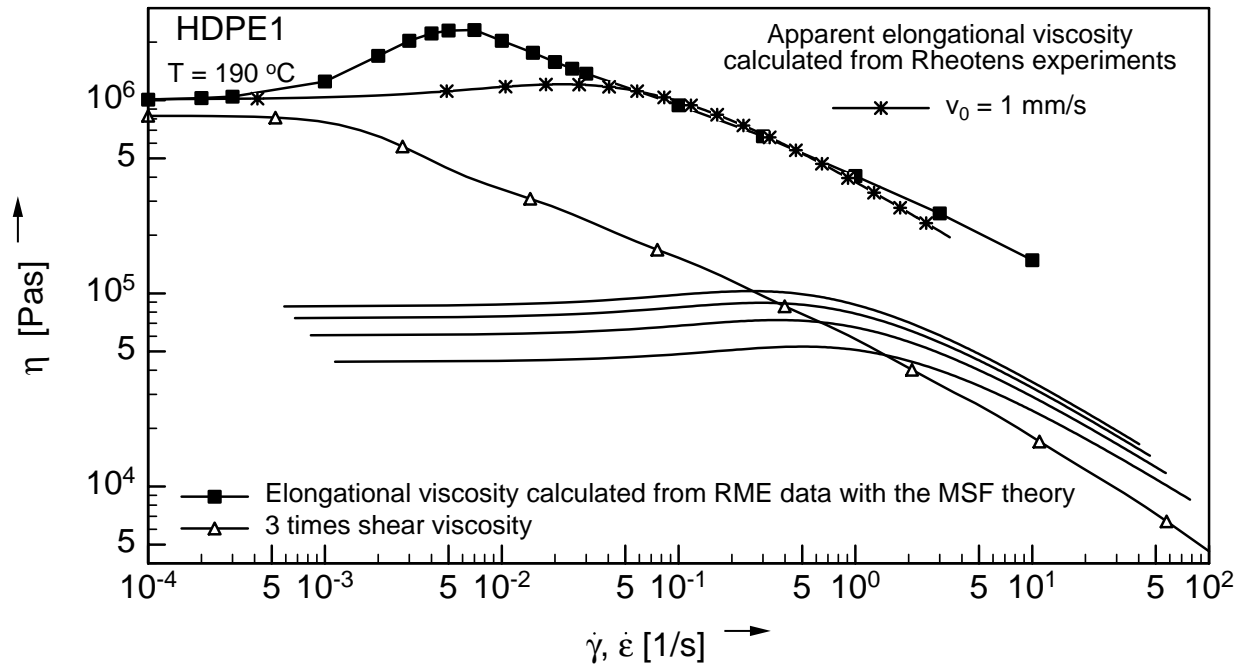


Figure 4.26: Comparison of the steady-state shear and elongational viscosity to the apparent elongational viscosity calculated from Rheotens curves for melt HDPE1. Also shown is the approximation of the steady-state elongational viscosity (*).

5 Numerical Simulation of the Rheotens Test

In this chapter, the detailed knowledge of the velocity distribution along the spinline of the fibre measured by LDV is used to evaluate the quality of numerical simulation. To do so it is important to select a constitutive equation which is capable to model the viscoelastic behaviour of the polymer melt, as elasticity certainly plays a dominant role for the simulation of extrudate swell. Also, mixed shear and elongational flow has to be taken into account. Therefore the integral constitutive equation suggested by Wagner [49] has been selected for this analysis, as it was tested widely for complex flows. It has been used by many researchers to model polymer melt flow behaviour. For example, Goublomme and Crochet used it to calculate extrudate swell [19], [11], and Mitsoulis reported results for fibre spinning, film blowing, and film casting applications [39], [6], [38].

5.1 Integral Constitutive Equation

According to the integral constitutive equation as suggested by Wagner [49], the extra stress tensor can be expressed as

$$\underline{\underline{\sigma}}(t) = -p\underline{\underline{E}} + \int_{-\infty}^t m^0(t-t') H(t,t') \underline{\underline{C}}^{-1}(t') dt', \quad (5.1)$$

where p is the isotropic pressure, $\underline{\underline{E}}$ the unit tensor, $\underline{\underline{C}}^{-1}(t')$ the relative Finger strain tensor, $m^0(t-t')$ the memory function, and $H(t,t')$ the nonlinear damping functional.

The memory function is obtained from linear viscoelastic measurements and described by a discrete relaxation spectrum with n components,

$$m^0(t-t') = \frac{\partial}{\partial t'} G^0(t-t') = \sum_{i=1}^n \frac{g_i}{\lambda_i} e^{-\frac{(t-t')}{\lambda_i}}. \quad (5.2)$$

The damping functional $H(t)$ is derived from the damping function $h(t)$, describing the nonlinear behaviour of the polymer melt. Different empirical expressions for the damping function have been found. The expression of Papanastasiou et. al (PSM) [42] is a function of the generalised invariant I of the Finger strain tensor,

$$h(I) = \frac{\alpha}{\alpha + I - 3}, \quad (5.3)$$

$$\text{with } I = \beta I_1 + (1 - \beta) I_2, \quad (5.4)$$

where

$$I_1 = I_2 = 3 + \gamma^2 \quad (5.5)$$

in simple shear flow, and

$$I_1 = e^{2\varepsilon} + 2e^{-\varepsilon} \quad \text{and} \quad I_2 = e^{-2\varepsilon} + 2e^{\varepsilon} \quad (5.6)$$

in uniaxial elongational flow.

From the assumption of the irreversibility of network disentanglement [57], it follows that the damping functional $H(I)$ can only decrease, therefore

$$H(I) = \text{Min}[h(I)]. \quad (5.7)$$

Another formulation of the damping function, the double exponential damping function suggested by Laun [27] is also used,

$$h = f e^{-n_1 \sqrt{I-3}} + (1-f) e^{-n_2 \sqrt{I-3}}. \quad (5.8)$$

The integral constitutive equation (5.1) is capable to describe shear and uniaxial elongational deformation correctly, but shows deficiencies in biaxial elongation and does not predict a second normal stress difference [54]. But as the deformation in a spinning experiment is mainly uniaxial, eq. (5.1) can be used to model the Rheotens test.

As an example, the linear and nonlinear material characterisation of melt HDPE1 is given in detail. The linear relaxation time spectrum g_i , λ_i (eq. (5.2)) is fitted to mastercurves of the storage and loss moduli, G' , G'' (fig. 5.1). These were measured by use of a Rheometrics DSR 200.

The nonlinear material characterisation is a more complicated task. The damping function in shear was measured directly by step-strain measurements, performed on a RMS 800 in cone-and-plate geometry at 230 °C, resulting in the relaxation modulus $G(t, \gamma)$ (fig. 5.2), which is independent of the shear deformation γ in the range of linear viscoelasticity, i.e. $G(t, \gamma) = G^0(t)$, and decreases with increasing γ in the nonlinear range. The damping function h_γ (fig. 5.3) is calculated as

$$h_\gamma(\gamma) = \frac{G(t, \gamma)}{G^0(t)}. \quad (5.9)$$

Eq. (5.8) represents the damping function expression which best fits the experimental data. In shear, the first and the second invariant of the finger tensor, I_1 and I_2 are the same, and the parameters $f = 0.134$, $n_1 = 0.095$, and $n_2 = 0.39$ are obtained by fitting the experimental damping function in fig. 5.3. The parameters are confirmed by the agreement of the prediction of eq. (5.1) with the steady-state shear viscosity (fig. 5.4). Finally, the parameter β is varied in such a way that transient elongational viscosity data (fig. 5.5) are well described without changing the shear parameters. The best fit is obtained by a value of $\beta = 0.2$.

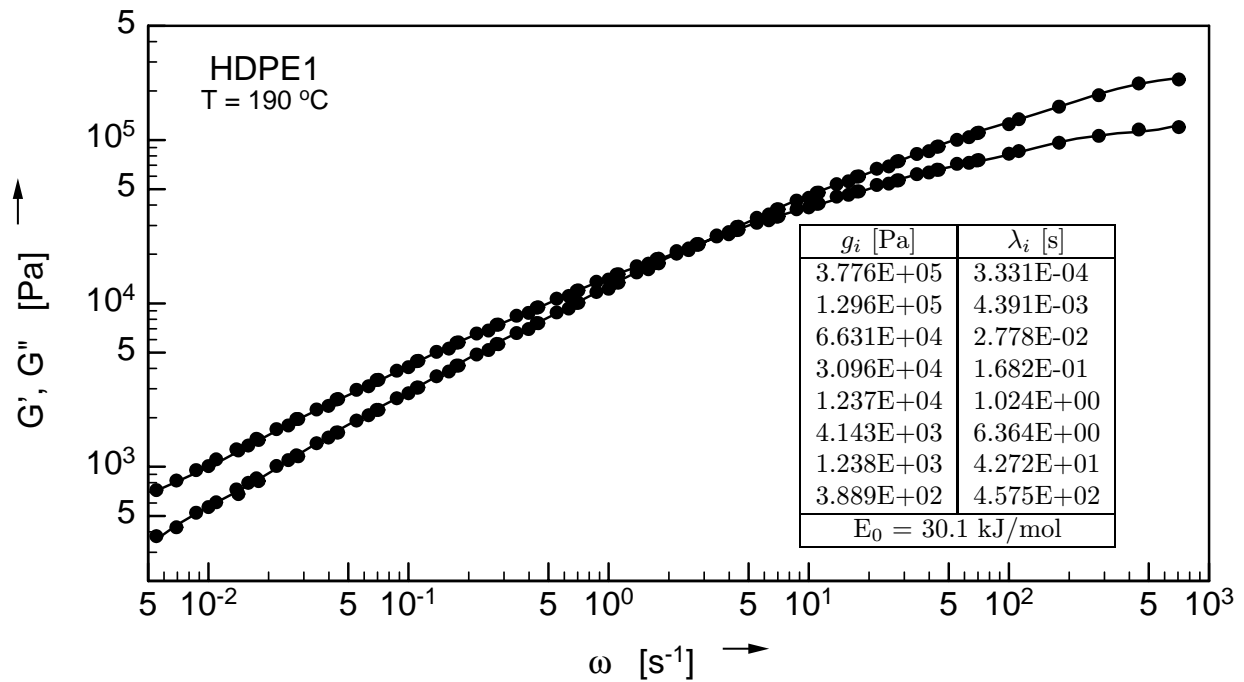


Figure 5.1: Mastercurve of storage and loss modulus, G' and G'' , for melt HDPE1 at 190°C. Experimental data (symbols) and fit by the relaxation time spectrum, g_i and λ_i (lines).

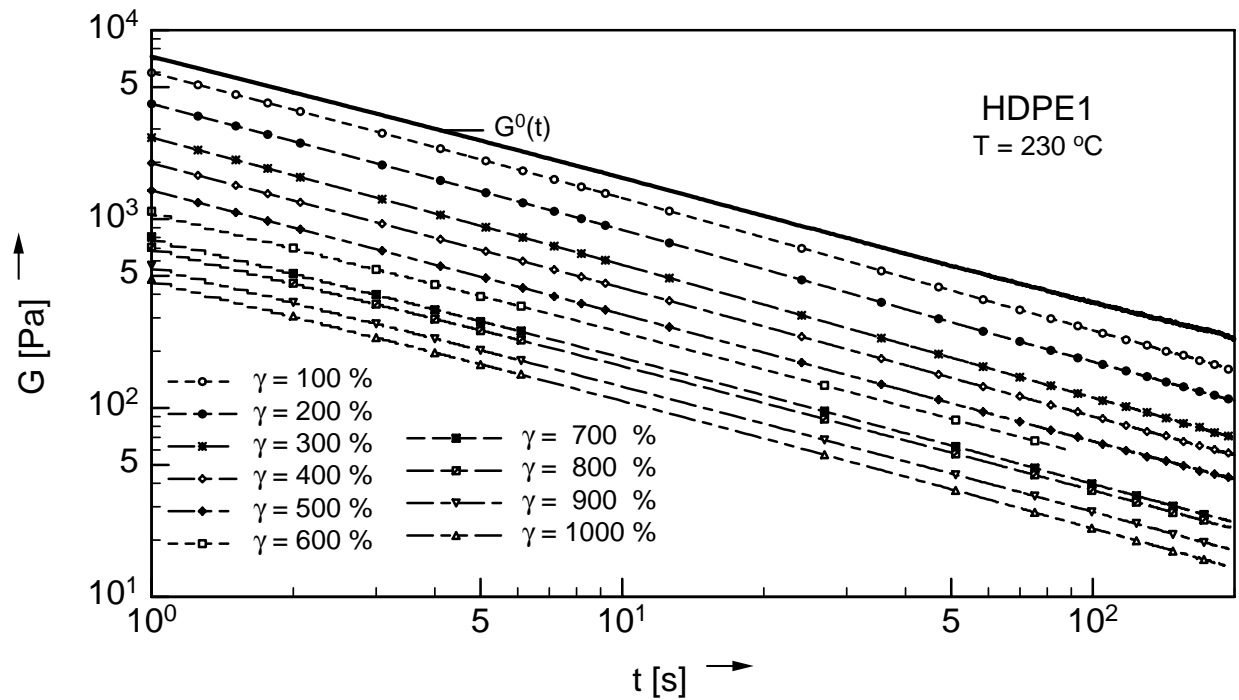


Figure 5.2: Shear modulus $G(t)$ as a function of shear deformation γ at $T = 230^\circ\text{C}$ for melt HDPE1.

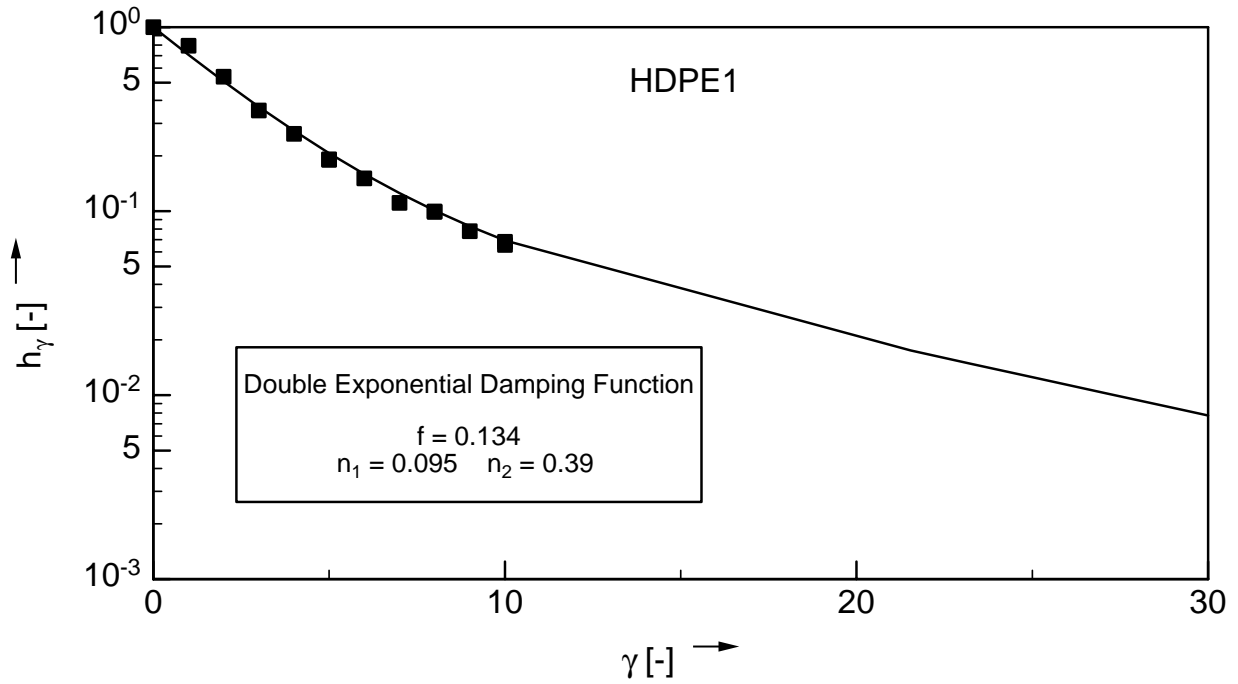


Figure 5.3: Damping function h_γ for simple shear flow of melt HDPE1. Experimental data (symbols) and fit by eq. (5.8) (line).

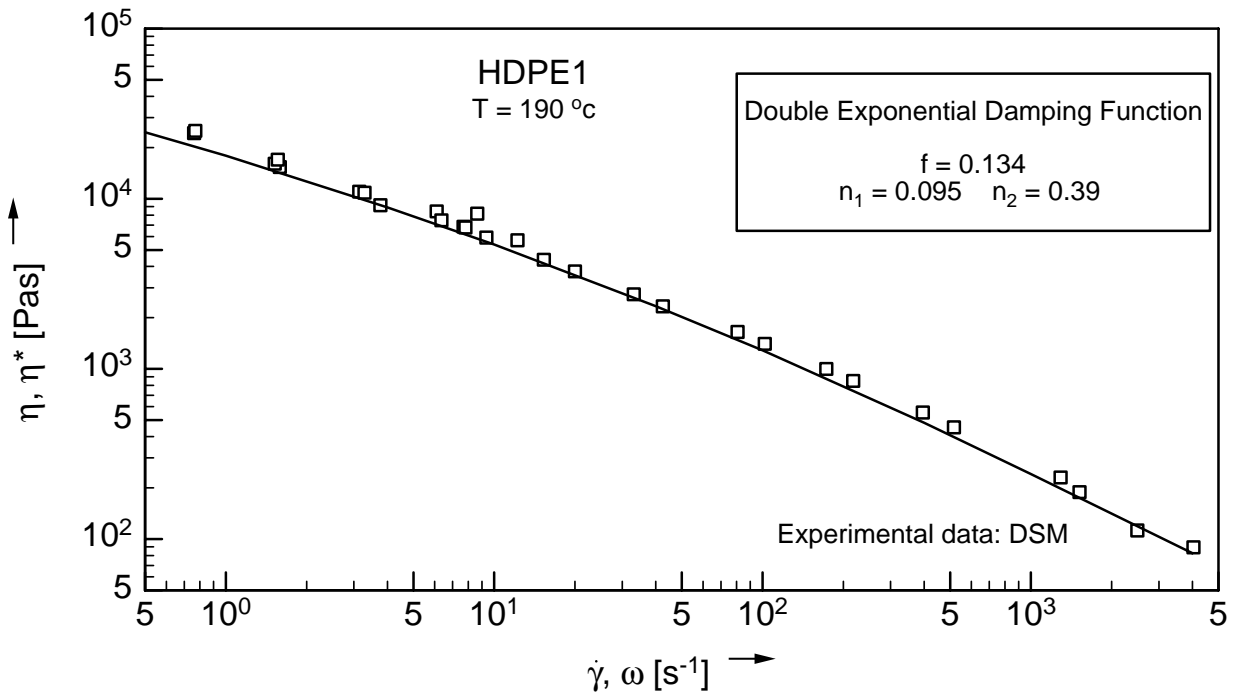


Figure 5.4: Steady-state shear viscosity for melt HDPE1 at $190^\circ C$. Experimental data (symbols) and description by integral constitutive equation (5.1) (line).

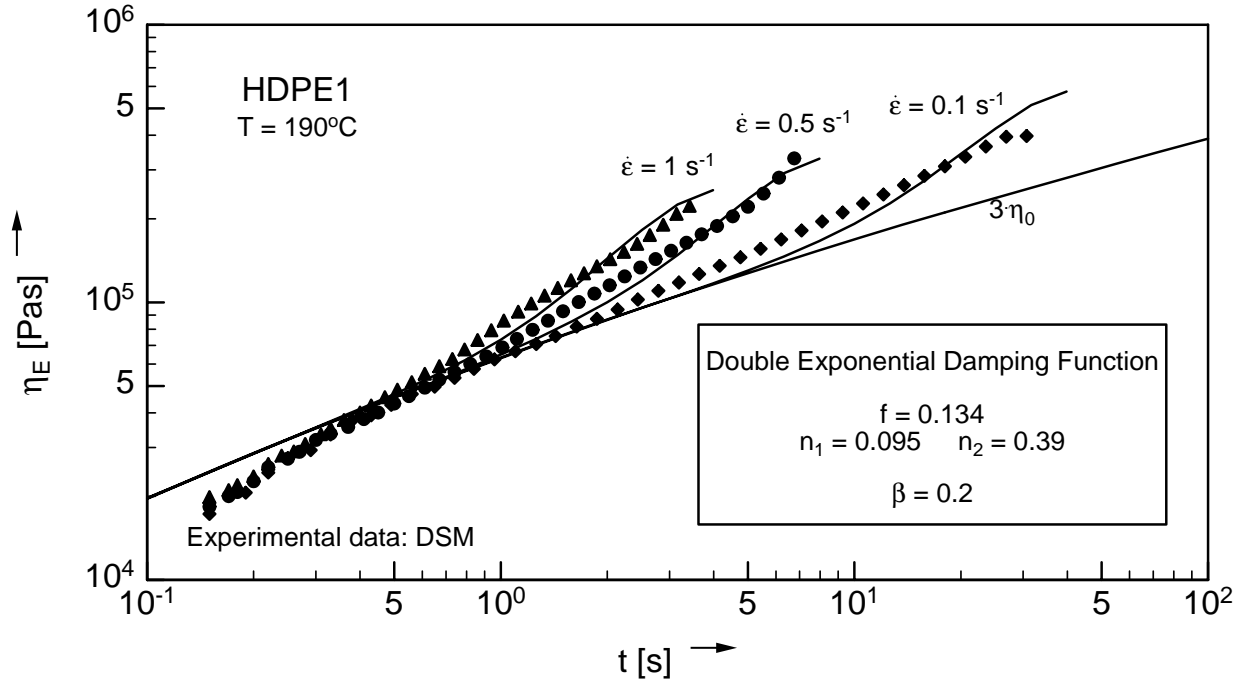


Figure 5.5: Transient elongational viscosity for melt HDPE1 at 190°C. Experimental data (symbols) and description by integral constitutive equation (5.1) (lines).

5.2 The Simulation Program

In principle it is possible to solve a viscoelastic flow problem by a finite element approach, where the viscoelastic material behaviour is described by an integral constitutive equation. However, the integral nature of the constitutive equation coupled with the free surface calculation of the extrudate swell is likely to cause convergence problems. Also, the calculation is very time consuming.

Instead, the simulation of the Rheotens test is done here on the basis of a semi-analytical approach published by Fulchiron et. al. [14] using the program *filage* developed at the University of St. Etienne, France, by Fulchiron and Carrot. The simulation is done stepwise, for a constant drawdown velocity, in analogy to the experiments by LDV.

For a realistic material description, not only the drawdown of the fibre, but also the deformation history in the extrusion die and the barrel need to be taken into account for the evaluation of the Finger strain tensor. Hence the velocity field in front of the die exit must be known. In the work of Fulchiron et. al., this velocity field does not result from a viscoelastic flow simulation, but is assumed to be a Poiseuille tube flow of a power law fluid, an assumption, which can be considered to be a realistic assumption. The second kinematic assumption is a constant axial velocity after the die exit, which certainly is valid after a short distance from the die. The velocity field description is shown in fig. 5.6. The influence of inertia and air drag are neglected, gravitational forces are taken into account.

The calculation of the Finger tensor components is done using a procedure presented by Adachi [1], [2] which is based on the Protean coordinate system described by Duda and Vrentas [13].

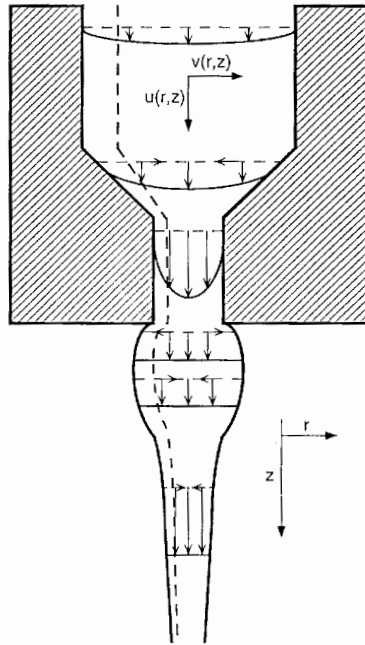


Figure 5.6: Velocity field description for the simulation of isothermal melt spinning (Fulchiron et. al. [14]).

This method is suited well for the description of steady, axisymmetric flow. Fast convergence of the simulation is achieved by using a Newton iteration scheme. The program *filage* of Fulchiron and Carrot runs on a personal computer without difficulties. The known parameters of the problem are the volumetric flowrate, the geometrical data, the draw ratio, and the material parameters for the integral constitutive equation (and additionally the pseudoplasticity index n of the power law). From this set of data the corresponding drawdown force as well as the velocity distribution along the spinline are calculated.

5.3 Modelling Results

Figs. 5.7 and 5.8 compare the predicted Rheotens curves for melt HDPE1 to experimental results for two different dies with $L_0/D_0 = 1$ and $L_0/D_0 = 30$. It can be seen that for all flowrates investigated, the simulation matches the experiments qualitatively well, especially the force level at high draw ratios. However, the starting point of the predicted curves deviates considerably from the experimental data, indicating that extrudate swell is highly overpredicted by the integral model.

This is demonstrated in more detail in the following example for melt HDPE1: Fig. 5.9 shows a) the experimental Rheotens curve measured by step-wise increasing drawdown, and b) the resulting velocity profile along the spinline from LDV measurements. Fig. 5.10 presents the corresponding simulation results, and fig. 5.11 a direct comparison of experiment and simulation for the velocity profile at two point of the Rheotens curve, one with a small ($V = 0.6$), the other with a high ($V = 5.5$) draw ratio. The numerical simulation predicts a higher extrudate swell, corresponding to a lower draw ratio at drawdown force $F = 0$, than observed experimentally. Also, the shape of the predicted Rheotens curve is too steep at low draw ratios and too flat at

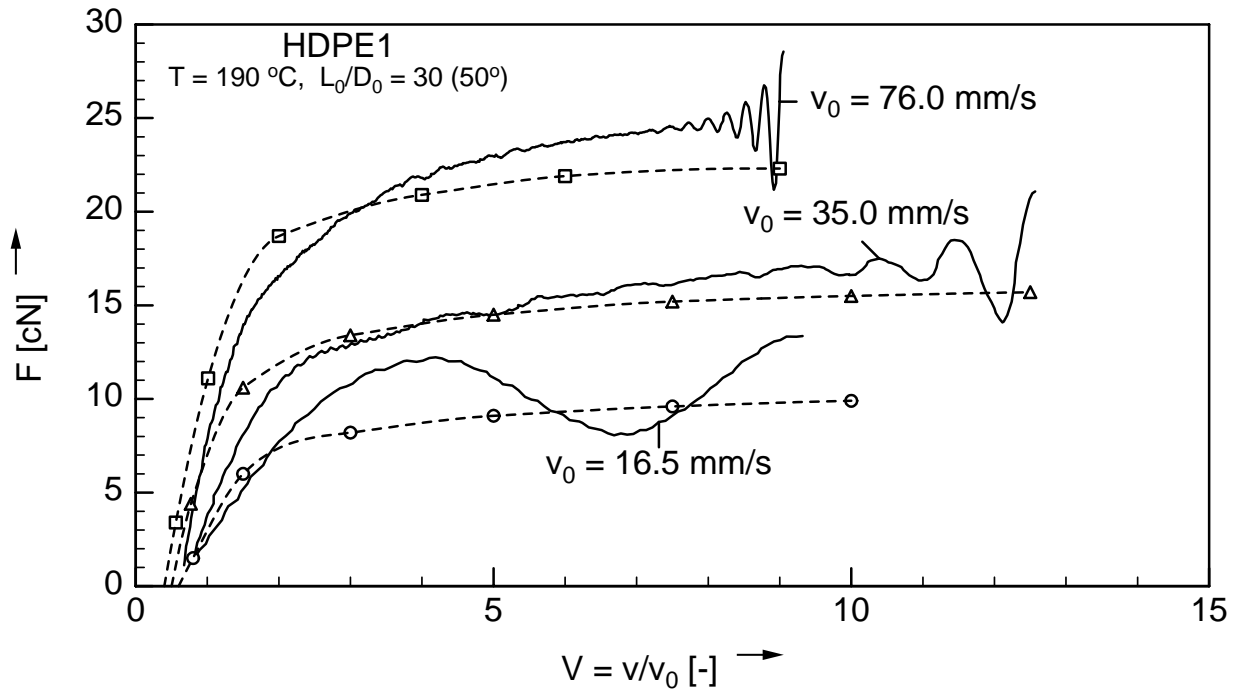


Figure 5.7: Rheotens curves of melt HDPE1 for various flow rates, die $L/D = 30$. Comparison of experimental (lines) and simulation (lines with symbols) results.

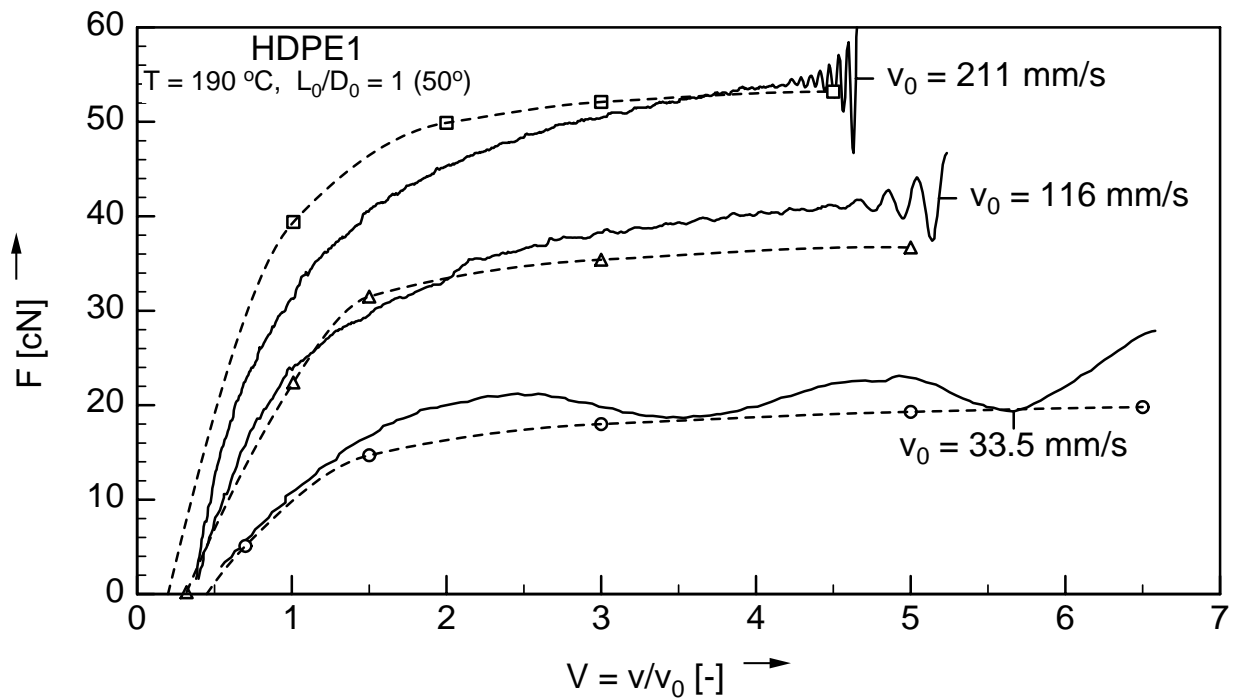


Figure 5.8: Rheotens curves of melt HDPE1 for various flow rates, die $L/D = 1$. Comparison of experimental (lines) and simulation (lines with symbols) results.

high draw ratios. This is reflected in the velocity profiles: In the experiment, an influence of the drawdown force on the extrudate swell observed is clearly visible, but this is not predicted by the simulation. This means that during the experiment swelling is partly compensated by the drawdown force, while the simulation does hardly show an influence of the drawdown force on the velocity shortly after the die exit. This is overcompensated at the end of the spinline length by a fast change of the draw ratio shortly before the take-up wheels.

The results of the numerical simulation of the Rheotens test can be summarised as follows: The simulation predicts a higher degree of melt elasticity at the die exit than observed experimentally, resulting in an overprediction of extrudate swell. This is compensated at high draw ratios by a material response which is more viscous than found by experiments. There is strong indication that the discrepancies seen between simulation and experimental evidence have their origin in the formulation of the constitutive equation. A possible reason is that the integral constitutive equation (5.1) used does not describe biaxial extension correctly, and extrudate swell represents an equibiaxial extension. Another reason might be that the formulation of irreversibility used (eq. (5.7)) does not describe the effect of irreversible network disentanglement correctly, and extrudate swell represents a reversible deformation, where irreversibility plays a significant role [19], [11]. The result of modelling the Rheotens test clearly demonstrates the necessity to improve the constitutive modelling of the rheological behaviour of polymer melts.

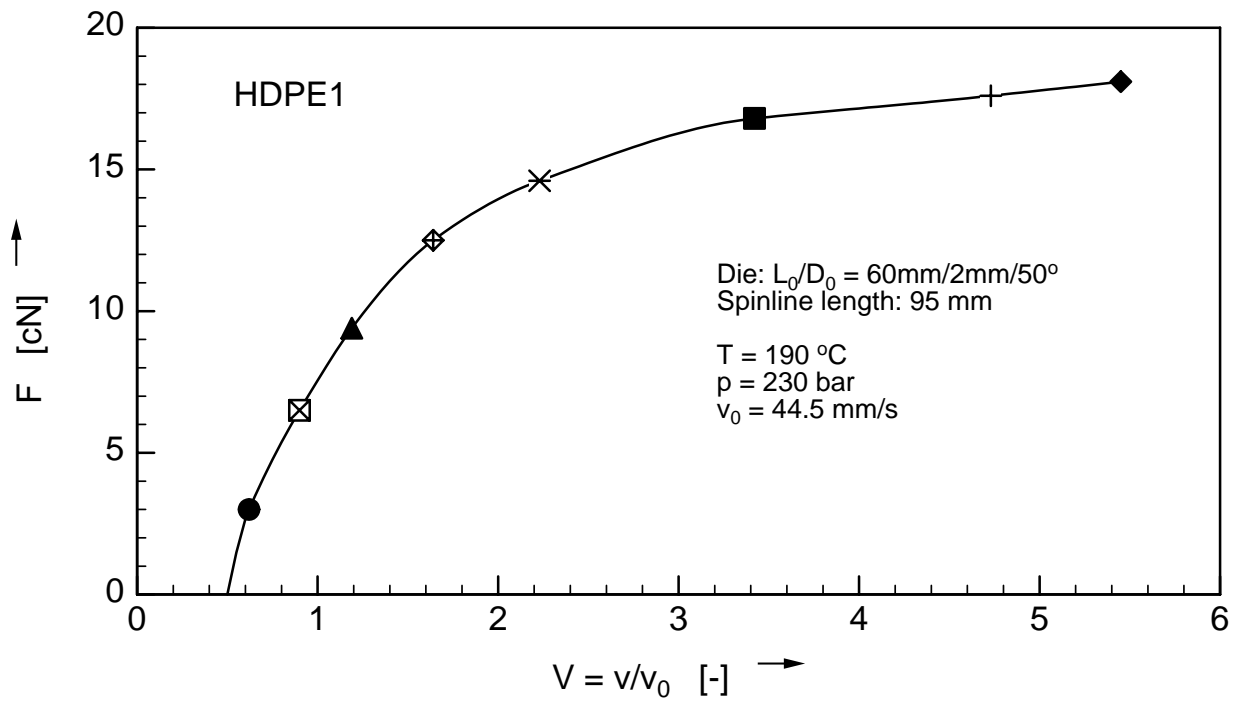


Figure 5.9: a) Rheotens curve for melt HDPE1, experimental data.

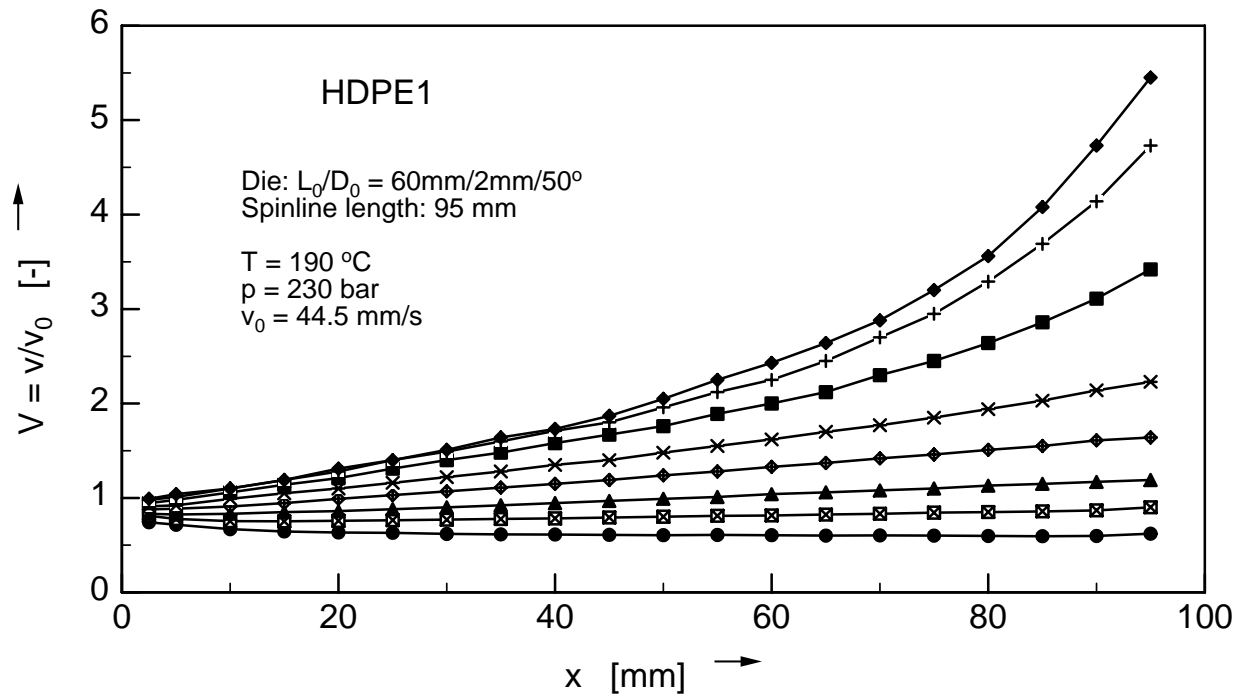


Figure 5.9: b) Velocity profile along Rheotens spinline corresponding to fig. 5.9 a), measurements by LDV.

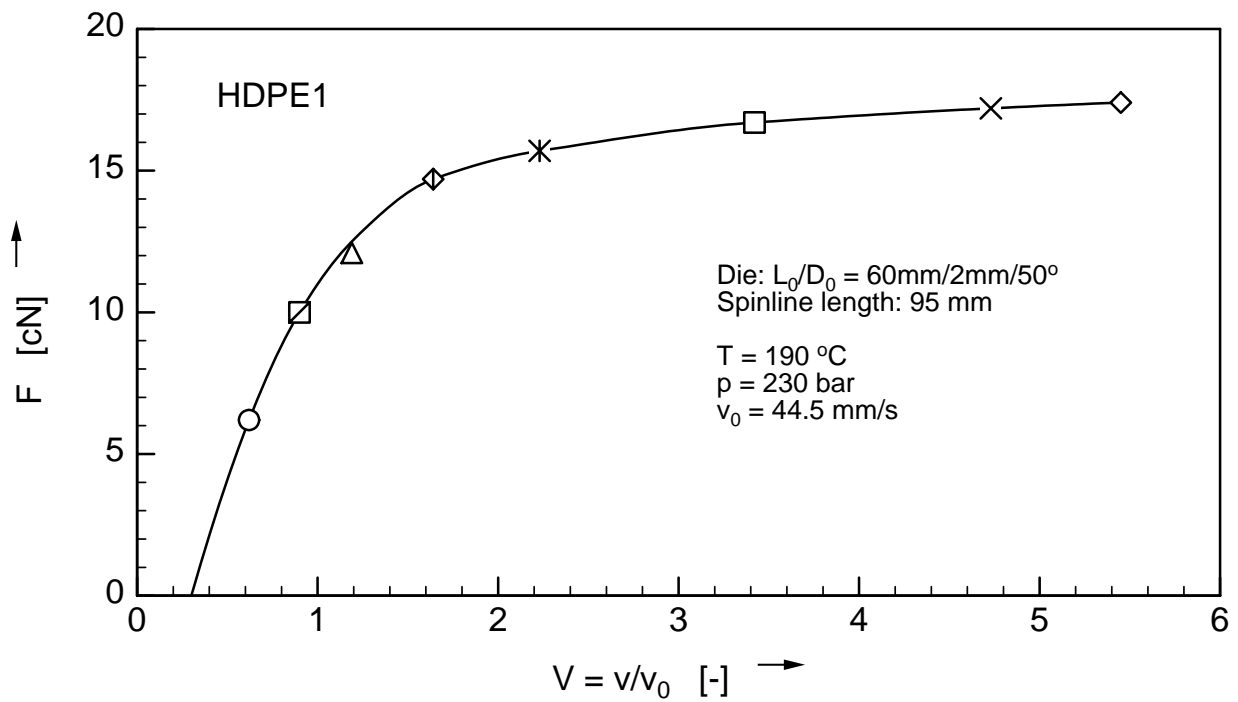


Figure 5.10: a) Rheotens curve for melt HDPE1, result of numerical simulation.

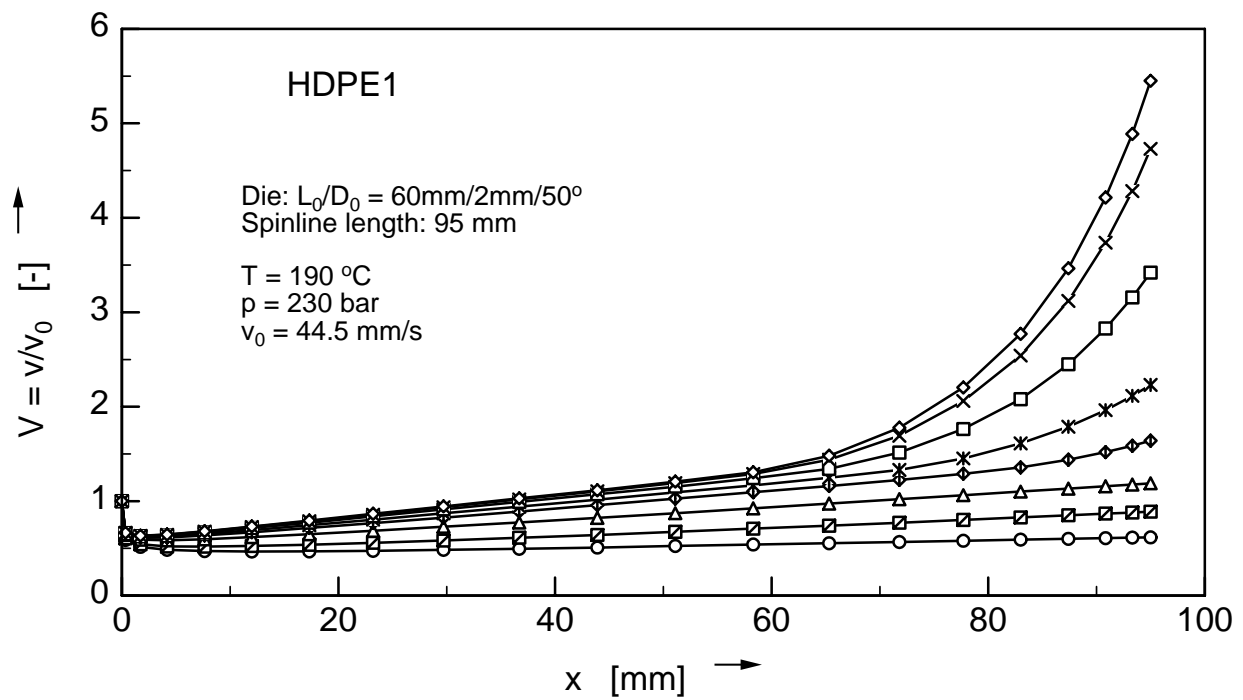


Figure 5.10: b) Velocity profile along Rheotens spinline corresponding to fig. 5.10 a), result of numerical simulation.

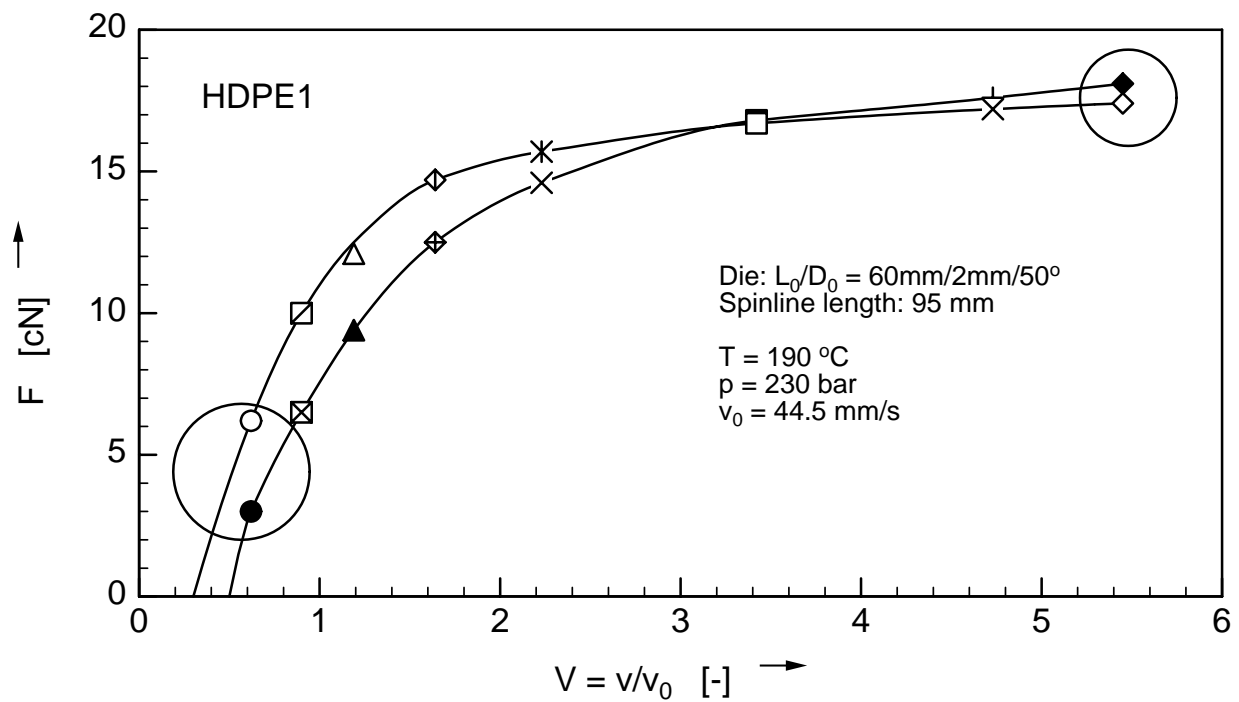


Figure 5.11: a) Direct comparison of experiment and numerical simulation: Rheotens curve for melt HDPE1.

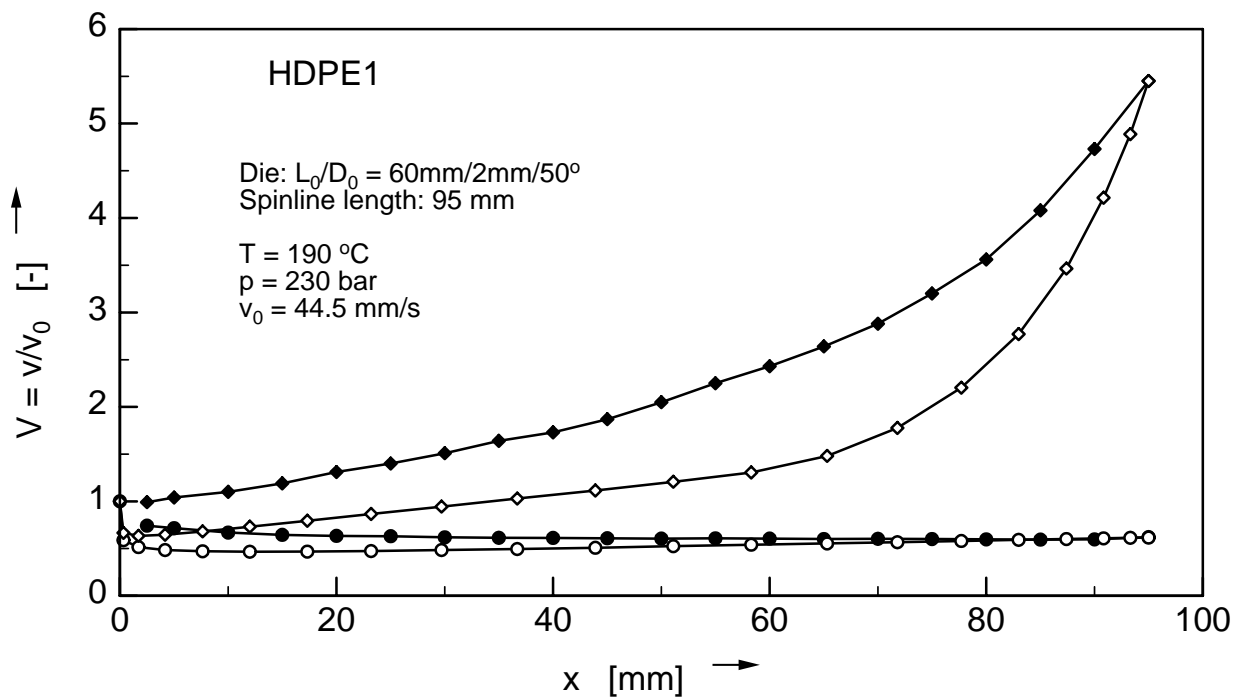


Figure 5.11: b) Direct comparison of experiment and numerical simulation: Velocity distribution along the spinline for two draw ratios indicated in fig. 5.11 a) by circles.

6 Conclusions

The drawability of polymer melts is of great importance for many polymer processing applications. The Rheotens test assesses the elongational properties of polymer melts and results in an extension diagram, which presents the drawdown force of an extruded filament as a function of the drawdown velocity. The experiment is fast and easy to perform with good reproducibility and therefore is widely used in industry. It is known to be very sensitive, even to small changes in the structure of polymer melts. In this work, the Rheotens test was used to investigate the elongational behaviour of a wide variety of polymers with a special emphasis on long-chain branched low density polyethylene.

The Rheotens experiment was extended in this work by means of a Laser-Doppler Velocimeter (LDA) for a direct measurement of the local velocity of the polymer melt along the spinline between the extrusion die and the take-up device of the Rheotens. This enabled us to verify the measured drawdown velocity and could be used to derive the shape of the deformed filament. This additional information was the basis of a model we suggested to calculate the apparent elongational viscosity from Rheotens curves. It also allows a more detailed comparison between experimental and simulation results.

The Rheotens test is very often used in a qualitative way: melt strength and drawability of different polymer melts are compared at a standard processing condition (constant temperature and flowrate in the extrusion die, and constant die and spinline geometry). However, this procedure does not fully take into account the complex rheological prehistory in the extrusion die. It also fails if materials with strongly different melting points or melt flow rates are to be compared.

The existence of Rheotens mastercurves, shown by Wagner and co-workers [53], [56], [55], can be used to overcome this problem. If Rheotens curves are compared on the basis of constant pressure in front of the extrusion die, invariance with respect to temperature and average molar mass is found. This was verified for a broad range of materials in this work. Furthermore, exceptions from temperature invariance caused by (temperature-dependent) wall slip in the capillary die as well as by flow induced crystallisation were found.

Rheotens mastercurves thus allow a direct and quantitative comparison of the elongational behaviour of different polymer melts under the action of an imposed drawdown force. This can be used to investigate how structural differences of the macromolecular chains influence the material properties of a polymer. For example, we found that different production technologies (tubular versus autoclave reactor) for the polymerisation of low density polyethylene result in changes of the tensile force/drawdown speed diagram. Also, influences of the structure of the macromolecular network can be reported on the rupture stress of polymer melts, which is calculated from the force and draw ratio at rupture. The rupture stress is found to be lower for linear polymers than for branched ones. The rupture stress measured by Rheotens experiments is relevant for processing applications.

In general, the drawdown force measured in a Rheotens experiment is a complex function of polymer melt properties, die and spinline geometry, as well as processing conditions (flowrate and drawdown velocity). We proved that a simple scaling law exists, which quantifies the influence of geometry and flowrate modifications on the Rheotens curves. This allows to separate material behaviour from processing conditions. While the Rheotens Grandmastercurve describes the polymer properties in a quasi-isothermal spinning experiment, the scaling factor

gives the information about the processing dependence of the Rheotens curve. In this work, the validity of this scaling law was demonstrated for linear and branched polyethylene melts, as well as for polypropylene, polystyrene and polycarbonate. This enabled us to compare melt strength and drawability of these melts quantitatively.

The calculation of the elongational viscosity from Rheotens experiments was an important objective of this work, as experiments with elongational rheometers are time-consuming and more difficult to perform. Two different models to extract elongational viscosities from Rheotens curves were developed: the analytical model and the similarity model. They are based on the assumption that the extensional viscosity in an experiment under constant force elongation is a function of the draw ratio only. The validity of the assumptions on which the analytical and the similarity model are based could be proved experimentally by LDA measurements.

The apparent elongational viscosity calculated from Rheotens curves strongly depends on the rheological prehistory in the extrusion die. The viscosity curve is shifted to lower viscosities and higher extension rates with increasing extrusion velocity. A large amount of preshear lowers the apparent elongational viscosity to the level of three times the shear viscosity. Low preshear on the other hand results in an apparent elongational viscosity of the same order of magnitude as the steady-state elongational viscosity. The processing conditions resulting in a good approximation of the steady-state elongational viscosity were identified, which enabled us to predict the elongational viscosity.

The apparent elongational viscosity calculated from Rheotens curves depends on the prehistory and therefore on processing conditions, while the steady-state uniaxial elongational viscosity is measured starting from isotropic samples. A comparison of the two viscosities clearly shows that preshear reduces the level of elongational viscosity considerably. This is of importance for many processing applications, which are dominated by elongational flows, and links polymer melt rheology to industrial practice.

Isothermal melt spinning is a prototype industrial flow: the polymer melt is first subjected to shear flow in the extrusion die, which is followed by uniaxial extension under constant force in the spinline. This coupling of shear and elongational flow in combination with the a priori unknown free surface of the filament makes the Rheotens experiment a rather sophisticated test for numerical simulation. It is necessary to use a viscoelastic constitutive equation for a realistic flow description.

The calculations were carried out using the integral Wagner constitutive equation assuming irreversibility of network disentanglement, and the simulation program *filage* of Fulchiron and co-workers with simplifications regarding the velocity profile inside the extrusion die. This allowed fast simulation with good convergence.

Comparison between simulated and measured Rheotens curves showed qualitative agreement of force/drawdown speed diagrams. However, extrudate swell was quantitatively overpredicted. This is caused by the formulation of the integral constitutive equation, which needs further development.

In conclusion, we found the Rheotens experiment to be an appropriate and rather simple means to assess the elongational behaviour of polymer melts under conditions which are relevant for typical industrial processing applications. The existence of Rheotens mastercurves simplifies the description of material behaviour in the spinline: simple scaling laws govern the relationship between drawdown force and elongation and allow to separate polymer melt properties from

processing conditions. Furthermore, the theoretical basis of the rheology of the Rheotens test was extended leading to models by which apparent elongational viscosities can be extracted from Rheotens measurements.

References

- [1] K. Adachi. Calculation of strain histories in Protean coordinate systems. *Rheol. Acta*, 22:336 – 335, 1983.
- [2] K. Adachi. A note on the calculation of strain histories in orthogonal streamline coordinate systems. *Rheol. Acta*, 25:555 – 563, 1986.
- [3] Richard L. Ballman and Jae Chun Hyun. Isothermal melt spinning - Lagrangian and Eulerian viewpoints. *J. Rheol.*, 22(4):349 – 380, 1978.
- [4] H. Bastian, A. Bernnat, and M.H. Wagner. Determination of elongational viscosity of polymer melts by RME and Rheotens experiments. *Proceedings 17. Stuttgarter Kunststoffkolloquium, Germany*, 2001.
- [5] H. Bastian and M.H. Wagner. The strain hardening of linear and branched polyolefin melts. *Proceedings XIII International Congress on Rheology, Cambridge, UK*, 1:309 – 311, 2000.
- [6] M. Beaulne and E. Mitsoulis. Numerical simulation of the film-blowing process. *Int. J. Forming Proc.*, 1(4):451 – 484, 1998.
- [7] A. Bernnat and M.H. Wagner. Rheotens experiments and elongational behaviour of polymer melts. *Proceedings Fifth European Rheology Conference, Portoroz, Slovenia*, pages 375 – 376, 1998.
- [8] A. Bernnat and M.H. Wagner. Effect of wall slip on Rheotens mastercurves for linear PE melts. *Int. Polymer Proc.*, 14:336 – 341, 1999.
- [9] A. Bernnat, M.H. Wagner, and C.K. Chai. Assessment of LDPE melt strength by use of Rheotens mastercurves. *Int. Polymer Proc.*, 15:268 – 272, 2000.
- [10] C.K. Chai. Melt rheology and processability of conventional and metallocene polyethylenes. *Proceedings SPE/Antec'99 New York*, pages 1200 – 1204, 1999.
- [11] M.J. Crochet and A. Goublomme. Numerical prediction of extrudate swell of a high-density polyethylene: further results. *Journal of Non-Newtonian Fluid Mechanics*, 47:281 – 287, 1993.
- [12] M. Denn. Continuous drawing of liquids to form fibers. *Ann Rev Fluid Mech*, 12:365 – 387, 1980.
- [13] J.L. Duda and J.S. Vrentas. *Chem. Eng. Sci.*, 22:855, 1967.
- [14] R. Fulchiron, P. Revenu, B.S. Kim, C. Carrot, and J. Guillet. Extrudate swell and isothermal melt spinning analysis of linear low density polyethylene using the Wagner constitutive equation. *J. Non-Newtonian Fluid Mech.*, 69:113 – 136, 1997.
- [15] A. Ghijssels, Massardier C.H.C., and Bradley R.M. Brittle melt rupture phenomena in polymer processing. *Int. Polymer Proc.*, 12:147 – 154, 1997.
- [16] A. Ghijssels and J. De Clippeleir. Melt strength behaviour of polypropylenes. *Int. Polymer Proc.*, 9:252 – 257, 1994.

- [17] A. Ghijsels, J.J.S.M. Ente, and J. Raadsen. Melt strength behaviour of PE and its relation to bubble stability in film blowing. *Int. Polymer Proc.*, 5:284 – 286, 1990.
- [18] A. Ghijsels, J.J.S.M. Ente, and J. Raadsen. Melt strength behaviour of polyethylene blends. *Int. Polymer Proc.*, 7:44 – 50, 1992.
- [19] A. Goublomme, B. Draily, and M.J. Crochet. Numerical prediction of extrudate swell of a high-density polyethylene. *J. Non-Newtonian Fluid Mech.*, 44:171 – 195, 1992.
- [20] C.D. Han. *Rheology in Polymer Processing*. Academic Press, 1976.
- [21] C. Krohmer and H.G. Fritz. Extrusion of honeycomb profiles for insulation: Stretching, cooling, and specific structural irregularities. *Proceedings 3rd ESAForm Conference on Material Forming, Stuttgart, Germany, 2000*.
- [22] C. Krohmer and H.G. Fritz. Insulation sheets with honeycomb structures: Aspects of the extrusion process and product properties. *Proceedings 16th annual PPS meeting, Shanghai, China, 2000*.
- [23] R. Kuhn and H. Kroemer. Structures and properties of different low density polyethylenes. *Colloid & Polymer Sci.*, 260:1083 – 1092, 1982.
- [24] S. Kurzbeck. *Dehnrheologische Eigenschaften von Polyolefinschmelzen und Korrelation mit ihrem Verarbeitungsverhalten beim Folienblasen und Thermoformen*. PhD thesis, Universität Erlangen, Germany, 1999.
- [25] S. Kurzbeck, F. Oster, H. Münstedt, T.Q. Nguyen, and R. Gensler. Rheological characterisation of two polypropylenes with different molecular structure. *J. Rheol.*, 43:359 – 374, 1999.
- [26] F.P. La Mantia and D. Acierno. Influence of the molecular structure on the melt strength and extensibility of polyethylenes. *Polym. Eng. Sci.*, 25:279 – 283, 1985.
- [27] H.M. Laun. Description of the non-linear shear behaviour of a low density polyethylene melt by means of an experimentally determined strain dependent memory function. *Rheol. Acta*, 17:1 – 15, 1978.
- [28] H.M. Laun. Wall slip of polymer melts from squeeze flow and capillary rheometry. *Proceedings Fifth European Rheology Conference, Portoroz, Slovenia*, pages 26 – 29, 1998.
- [29] H.M. Laun. Elongational flow of polymer melts subsequent to extrusion. *Proceedings XIII International Congress on Rheology, Cambridge, UK*, 1:55 – 56, 2000.
- [30] H.M. Laun and V. Rauschenberger. A recursive model for Rheotens tests. *J. Rheol.*, 41:719 – 737, 1997.
- [31] H.M. Laun and W. Reuther. *to appear in Rheol. Acta*, 1999.
- [32] H.M. Laun and H. Schuch. Transient elongational viscosities and drawability of polymer melts. *J. Rheol.*, 33:119 – 175, 1989.
- [33] K. Lee and M.R. Mackley. The significance of slip in matching polyethylene processing data with numerical simulation. *J. Non-Newtonian Fluid Mech.*, 94:159 – 177, 2000.

- [34] M.R. Mackley, R.P.G. Rutgers, and D.G. Gilbert. Surface instabilities during the extrusion of linear low density polyethylene. *Journal of Non-Newtonian Fluid Mechanics*, 76:281 – 297, 1997.
- [35] J. Meissner. Dehnungsverhalten von Polyethylen- Schmelzen. *Rheol. Acta*, 10:230 – 240, 1971.
- [36] J. Meissner. Basic paramters, melt rheology, processing and end - use properties of three similar low density polyethylene samples. *Pure and Applied Chemistry*, 4:553 – 612, 1975.
- [37] J. Meissner and J. Hostettler. A new elongational rheometer for polymer melts and other highly viscoelastic liquids. *Rheol. Acta*, 33:1 – 21, 1994.
- [38] E. Mitsoulis. Quasi two-dimensional simulations of the film-casting process for polymers. *Proceedings 2nd ESAForm Conference on Material Forming, Guimaraes, Portugal*, 1999.
- [39] E. Mitsoulis and M. Beaulne. Some issues arising in the numerical simulation of fibre spinning. *Proceedings 15th annual PPS meeting, s’Hertogenbosch, The Netherlands*, 1999.
- [40] M. Mooney. Explicit formulas for slip and fluidity. *J. Rheol.*, 2:210 – 222, 1931.
- [41] H. Münstedt and H.M. Laun. Elongational properties and molecular structure of polyethylene melts. *Rheol. Acta*, 20:211 – 221, 1981.
- [42] A.C. Papanastasiou, L.E. Scriven, and C.S. Macosko. An integral constitutive equation for mixed flows: Viscoelastic characterization. *J. Rheol.*, 27:387 – 410, 1983.
- [43] Polytec. Laser surface velocimeter lsv-065/lsv-200. *Handbuch*, 1998.
- [44] P. Rubio, H. Bastian, and M.H. Wagner. The molecular stress function model for polymer melts with dissipative constraint release. *in preparation*, 2001.
- [45] R.P.G. Rutgers, M.R. Mackley, L.E. Rodd, and A. Bernnat. Die gap geometry and wall boundary condition effects on the formation of extrusion surface instabilities for polyethylene melts. *Proceedings XIII International Congress on Rheology, Cambridge, UK*, 3:179 – 181, 2000.
- [46] F.R. Schwarzl. *Polymermechanik*. Springer Verlag, 1990.
- [47] T. Sridhar and R.K. Gupta. Material properties of viscoelastic liquids in uniaxial extension. *J. Rheol.*, 35:363 – 377, 1991.
- [48] T. Steffl and H. Muenstedt. Relevance of Rheotens experiments for film blowing. *Proceedings 3rd ESAFORM Conference on Material Forming, Stuttgart, Germany*, 2000.
- [49] M.H. Wagner. A constitutive analysis of uniaxial elongational flow data of a low-density polyethylene melt. *J. Non-Newtonian Fluid Mech.*, 4:39 – 55, 1978.
- [50] M.H. Wagner, H. Bastian, P. Hachmann, J. Meissner, S. Kurzbeck, H. Münstedt, and F. Langouche. The strain-hardening behaviour of linear and long-chain-branched polyolefin melts in extensional flows. *Rheol. Acta*, 39:97 – 109, 2000.
- [51] M.H. Wagner, A. Bernnat, and V. Schulze. Zur Rheologie des Schmelzespinnprozesses. *KGK*, 50:653 – 659, 1997.

- [52] M.H. Wagner, A. Bernnat, and V. Schulze. The rheology of the Rheotens test. *J. Rheol.*, 42:917 – 928, 1998.
- [53] M.H. Wagner, B. Collignon, and J. Verbeke. Rheotens mastercurves and elongational viscosity of polymer melts. *Rheol. Acta*, 35:117 – 126, 1996.
- [54] M.H. Wagner and A. Demarmels. A constitutive analysis of extensional flows of polyisobutylene. *J. Rheol.*, 34:943 – 958, 1990.
- [55] M.H. Wagner, V. Schulze, and A. Göttfert. Beurteilung der Spinnbarkeit von Polymerschmelzen mit Hilfe von Rheotens - Masterkurven. *KGK*, 49:38 – 43, 1996.
- [56] M.H. Wagner, V. Schulze, and A. Göttfert. Rheotens mastercurves and drawability of polymer melts. *Polym. Eng. Sci.*, 36:925 – 935, 1996.
- [57] M.H. Wagner and S.E. Stephenson. The irreversibility assumption of network disentanglement in flowing polymer melts and its effects on elastic recoil prediction. *J. Rheol.*, 23:489 – 504, 1979.
- [58] Shi-Quing Wang and P.A. Drda. Stick-slip transition in capillary flow of linear polyethylene: 2. molecular weight and low temperature anomaly. *Macromolecules*, 29:4115 – 4119, 1996.
- [59] Shi-Quing Wang and P.A. Drda. Superfluid-like stick-slip transition in capillary flow of linear polyethylene: 1. general features. *Macromolecules*, 29:2527 – 2632, 1996.
- [60] J.L. White and H Yamane. A collaborative study of the stability of extrusion, melt spinning and tubular film extrusion of some high-, low- and linear-low density polyethylene samples. *Pure and Applied Chemistry*, 59:193 – 216, 1987.
- [61] R. Wolff. Untersuchung des Rheotensversuchs hinsichtlich seiner Eignung als Wareneingangskontrollverfahren. *Polym. Proc. Eng.*, 4:97 – 123, 1986.

A Linear Material Characterisation

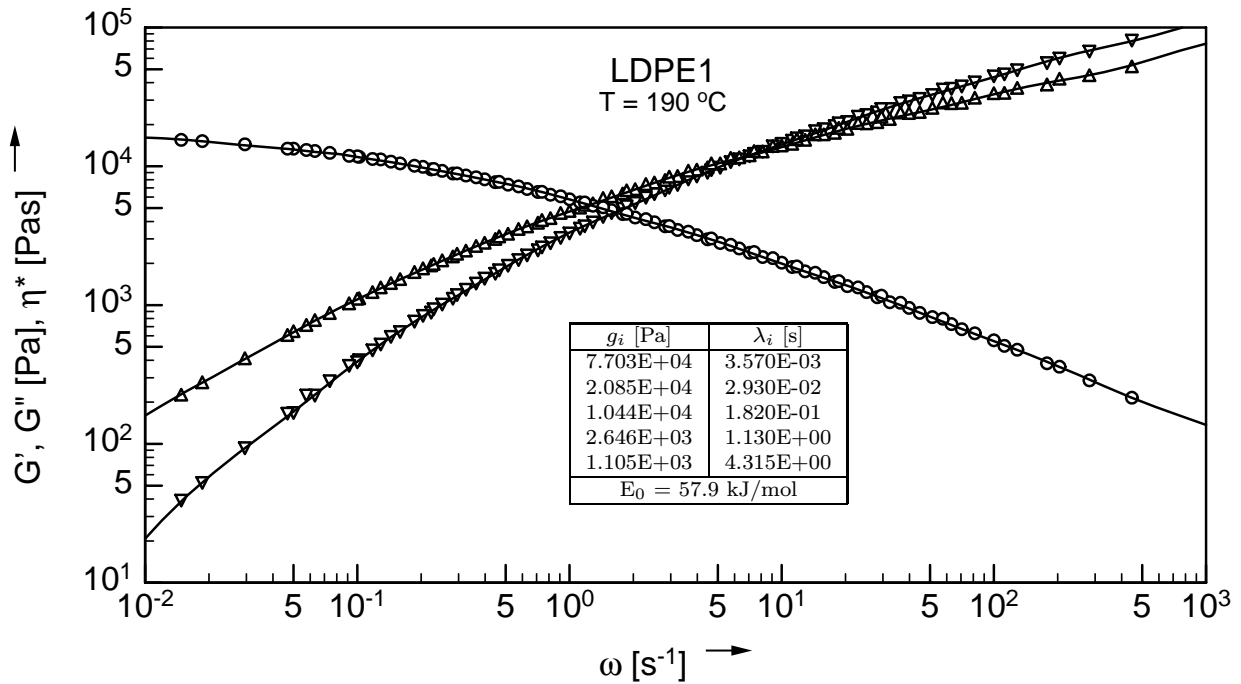


Figure A.1: Mastercurve of storage and loss modulus, G' and G'' , for melt LDPE1 at 190°C. Experimental data (symbols) and fit by the relaxation time spectrum, g_i and λ_i (lines).

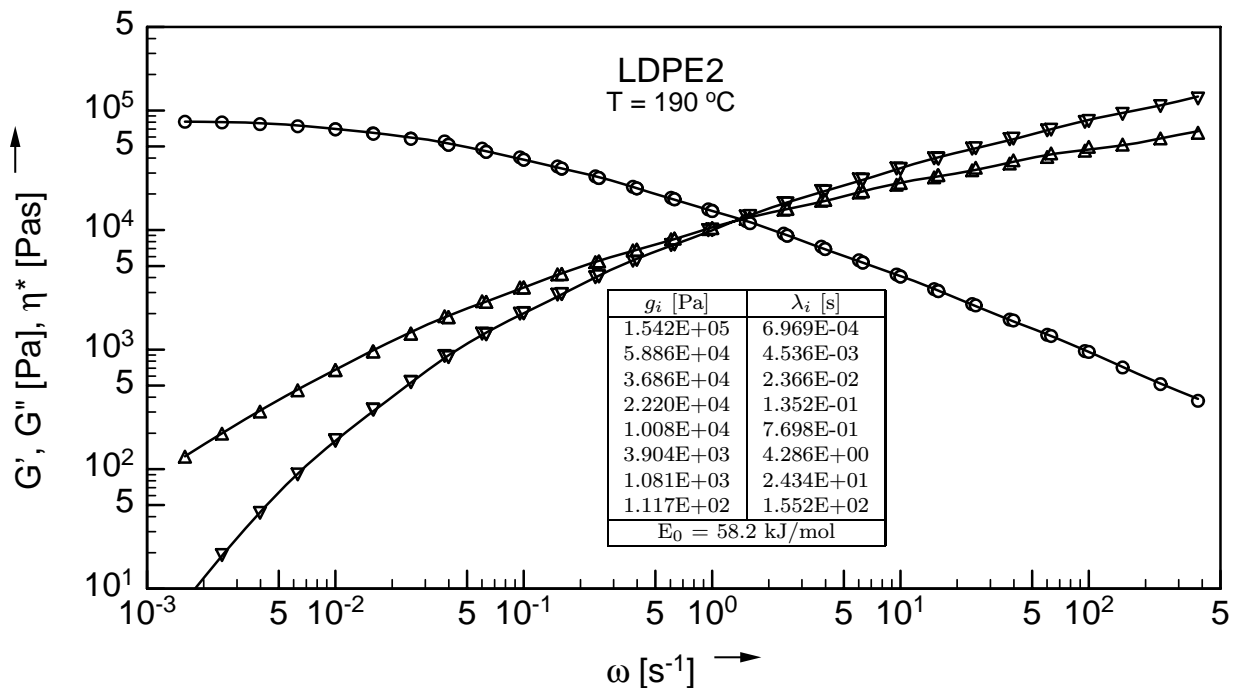


Figure A.2: Mastercurve of storage and loss modulus, G' and G'' , for melt LDPE2 at 190°C. Experimental data (symbols) and fit by the relaxation time spectrum, g_i and λ_i (lines).

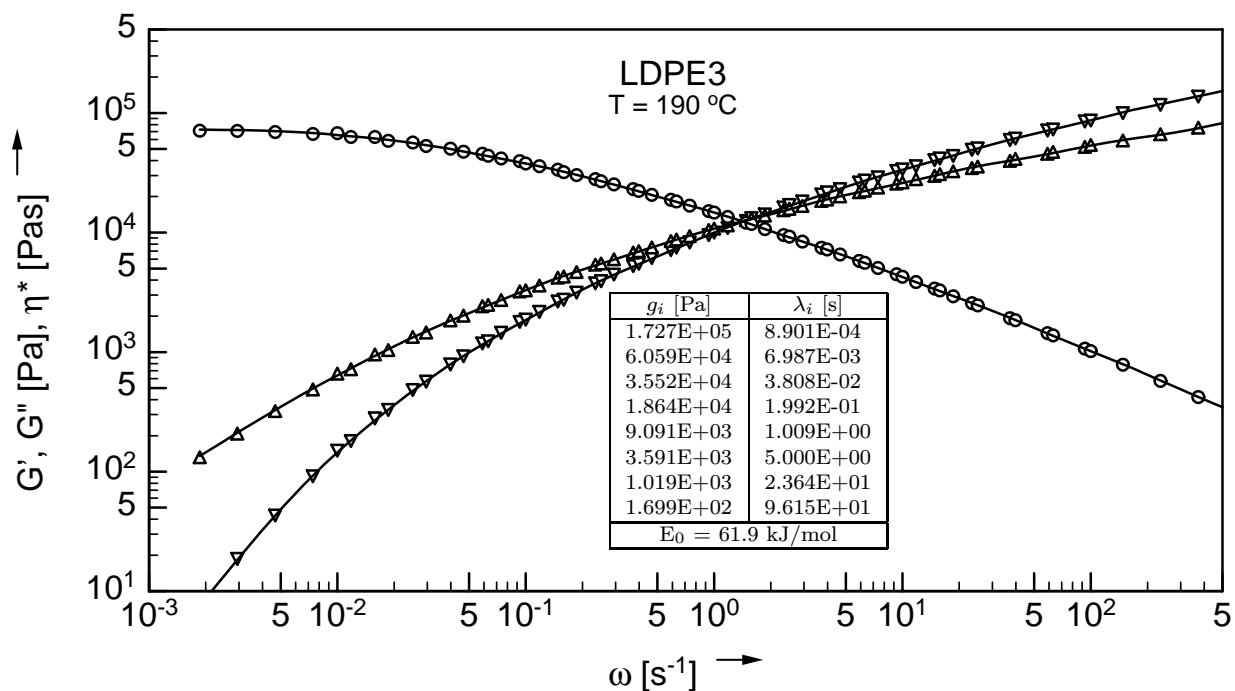


Figure A.3: Mastercurve of storage and loss modulus, G' and G'' , for melt LDPE3 at 190°C. Experimental data (symbols) and fit by the relaxation time spectrum, g_i and λ_i (lines).

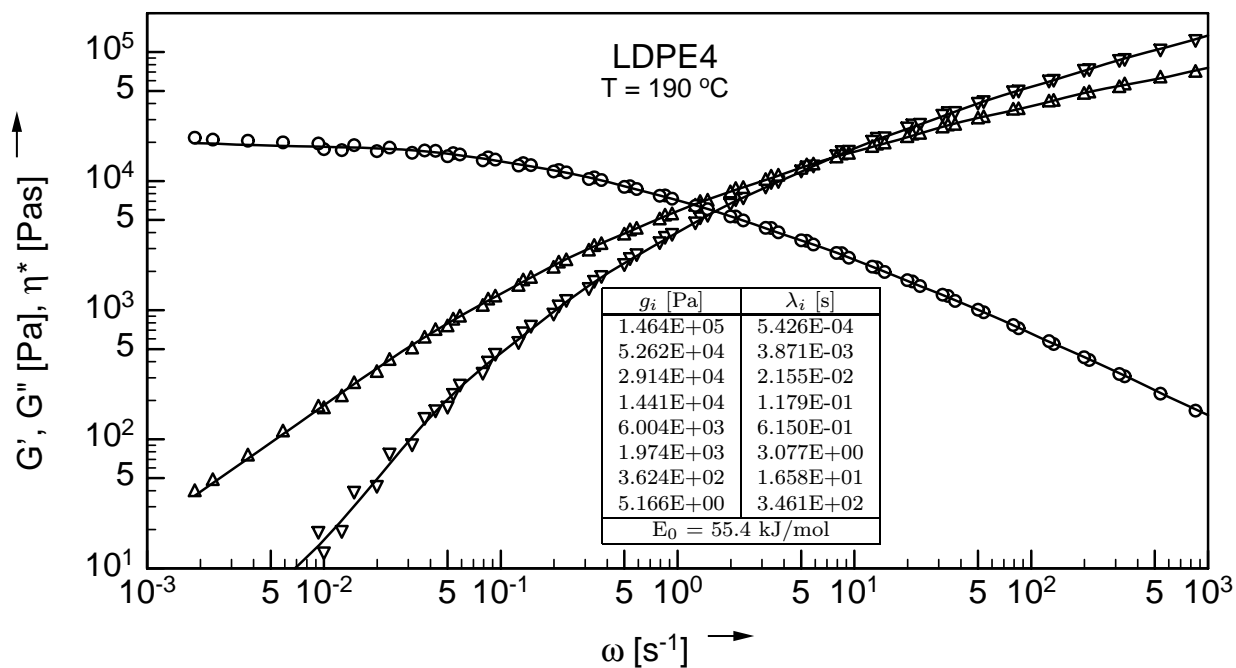


Figure A.4: Mastercurve of storage and loss modulus, G' and G'' , for melt LDPE4 at 190°C. Experimental data (symbols) and fit by the relaxation time spectrum, g_i and λ_i (lines).

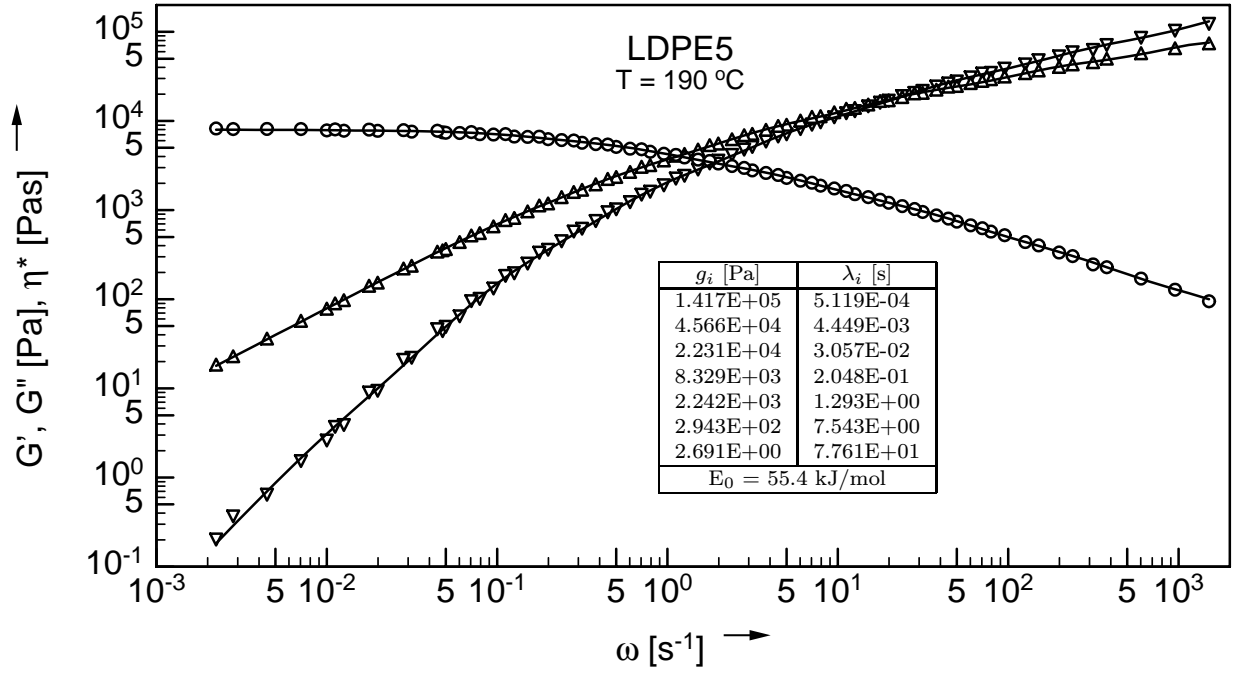


Figure A.5: Mastercurve of storage and loss modulus, G' and G'' , for melt LDPE5 at 190°C. Experimental data (symbols) and fit by the relaxation time spectrum, g_i and λ_i (lines).

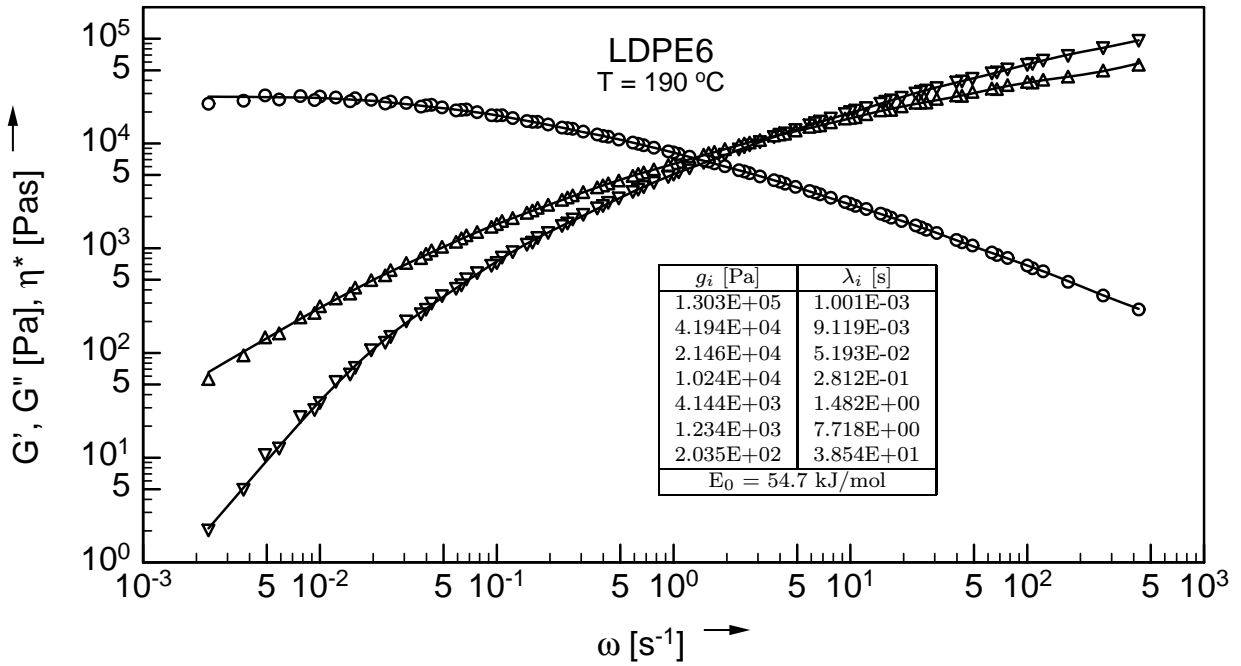


Figure A.6: Mastercurve of storage and loss modulus, G' and G'' , for melt LDPE6 at 190°C. Experimental data (symbols) and fit by the relaxation time spectrum, g_i and λ_i (lines).

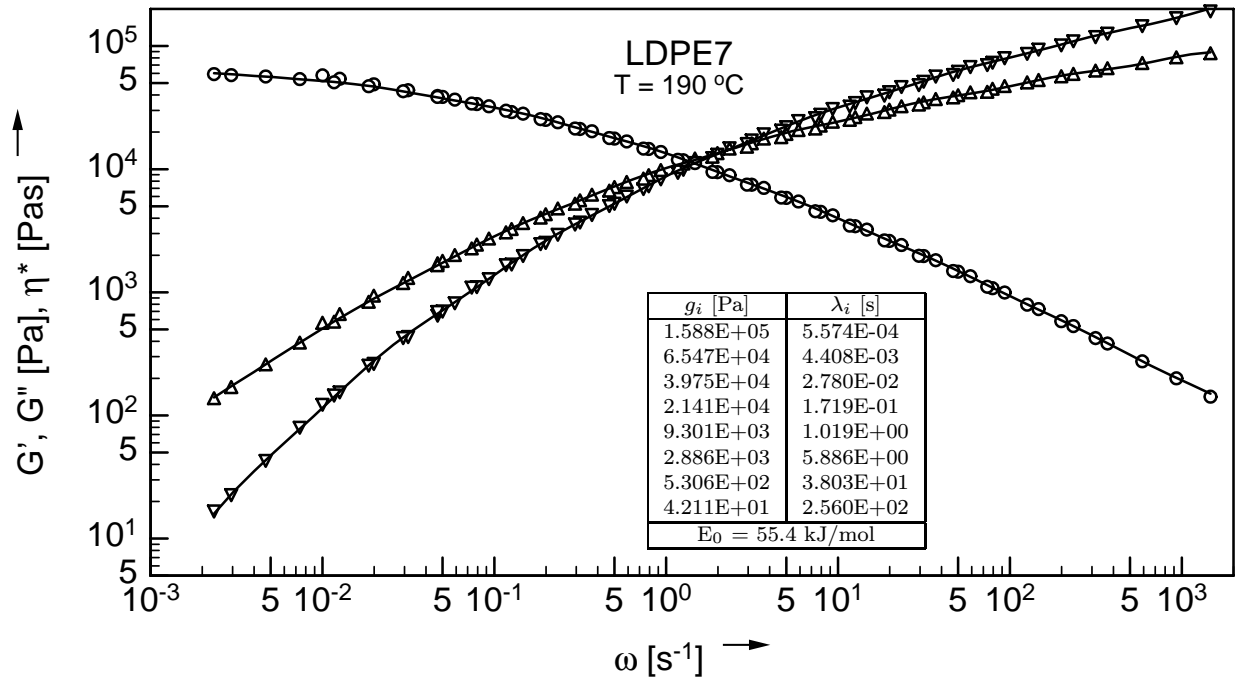


Figure A.7: Mastercurve of storage and loss modulus, G' and G'' , for melt LDPE7 at 190°C. Experimental data (symbols) and fit by the relaxation time spectrum, g_i and λ_i (lines).

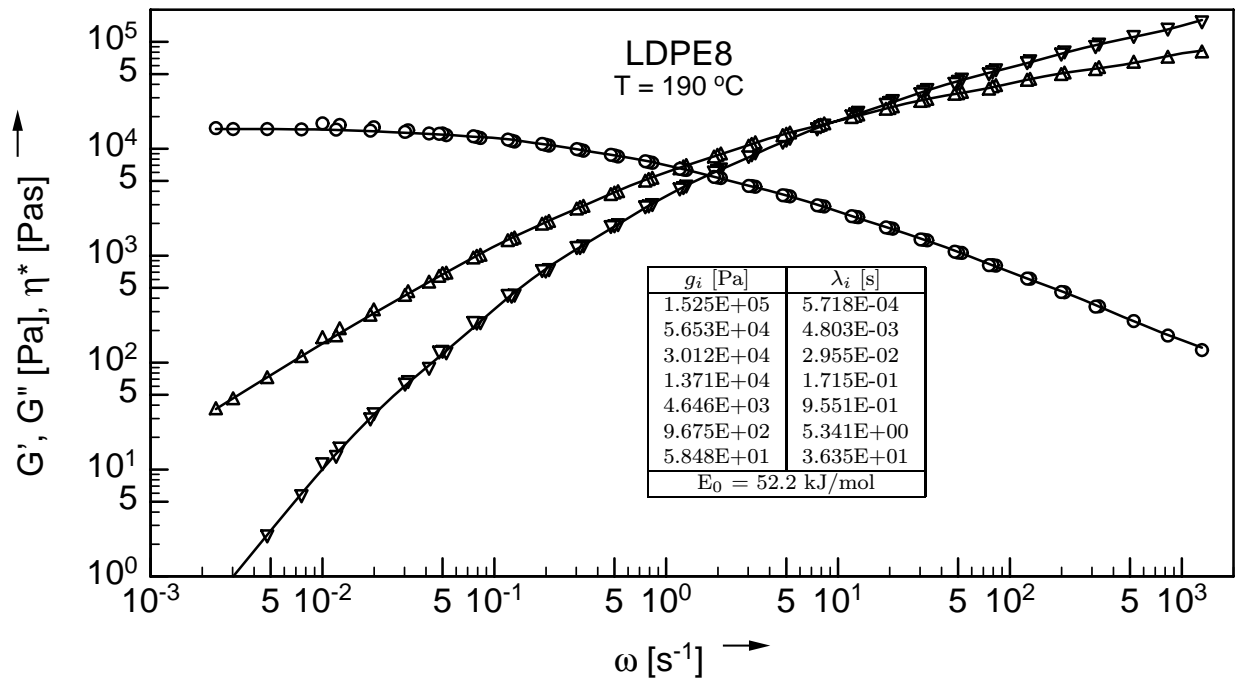


Figure A.8: Mastercurve of storage and loss modulus, G' and G'' , for melt LDPE8 at 190°C. Experimental data (symbols) and fit by the relaxation time spectrum, g_i and λ_i (lines).

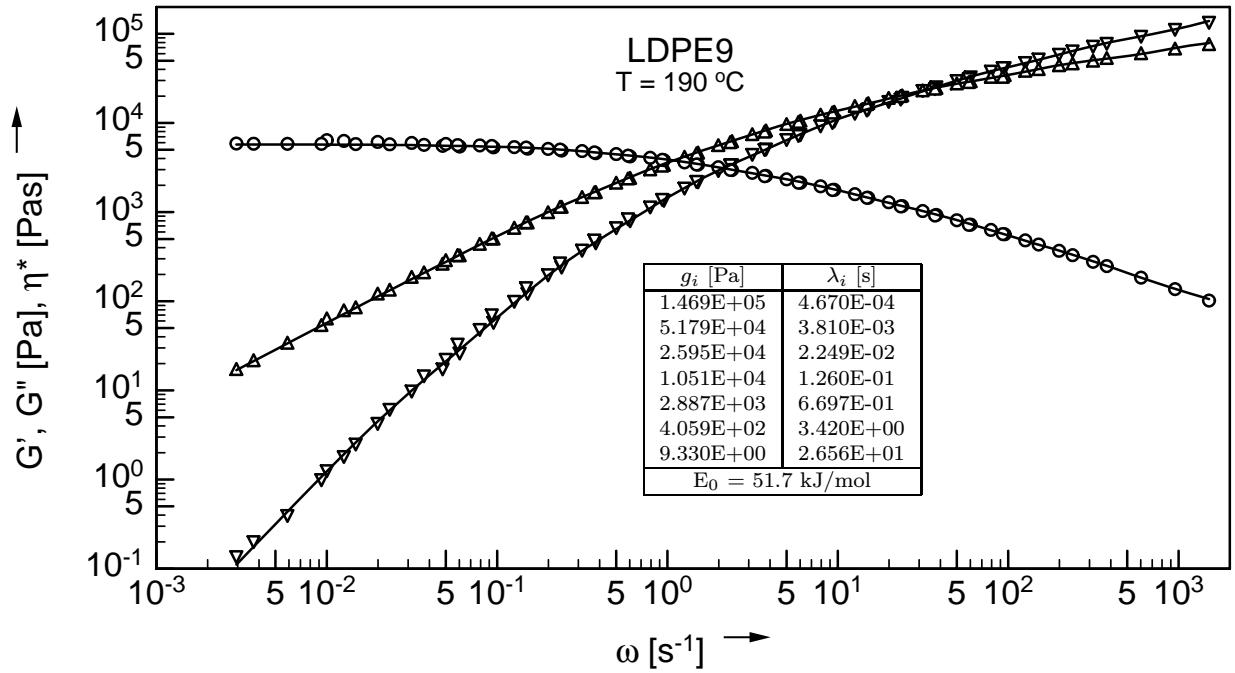


Figure A.9: Mastercurve of storage and loss modulus, G' and G'' , for melt LDPE9 at 190°C. Experimental data (symbols) and fit by the relaxation time spectrum, g_i and λ_i (lines).

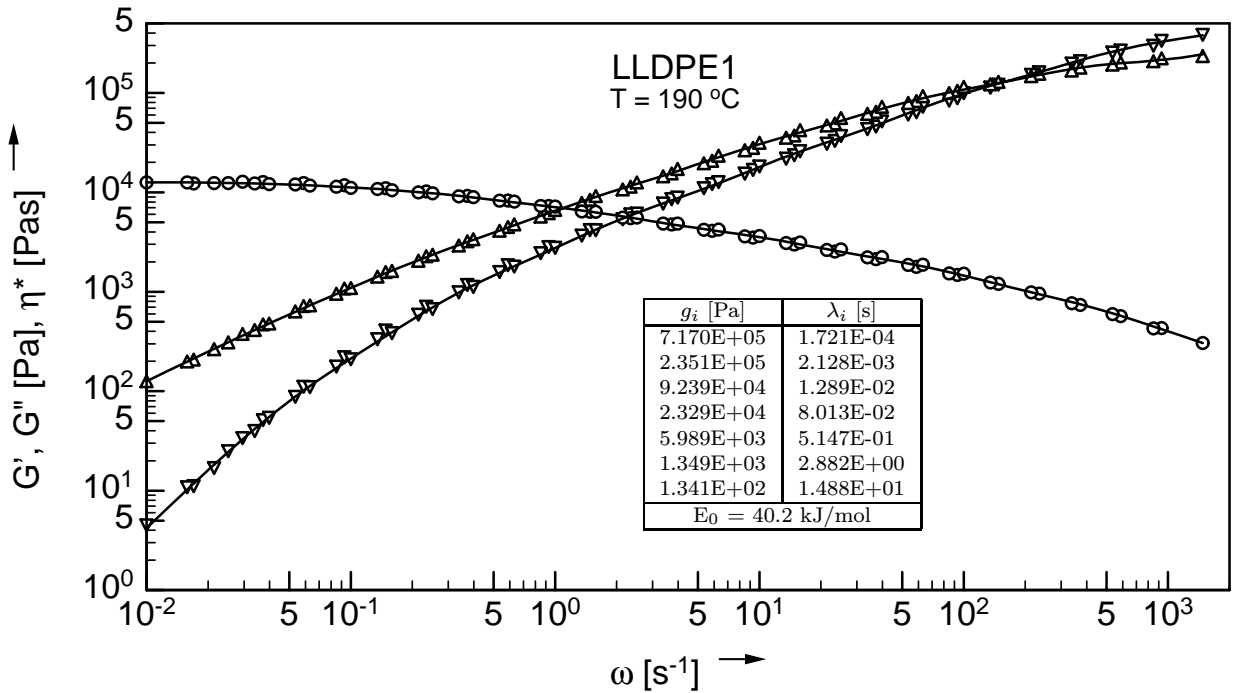


Figure A.10: Mastercurve of storage and loss modulus, G' and G'' , for melt LLDPE1 at 190°C. Experimental data (symbols) and fit by the relaxation time spectrum, g_i and λ_i (lines).

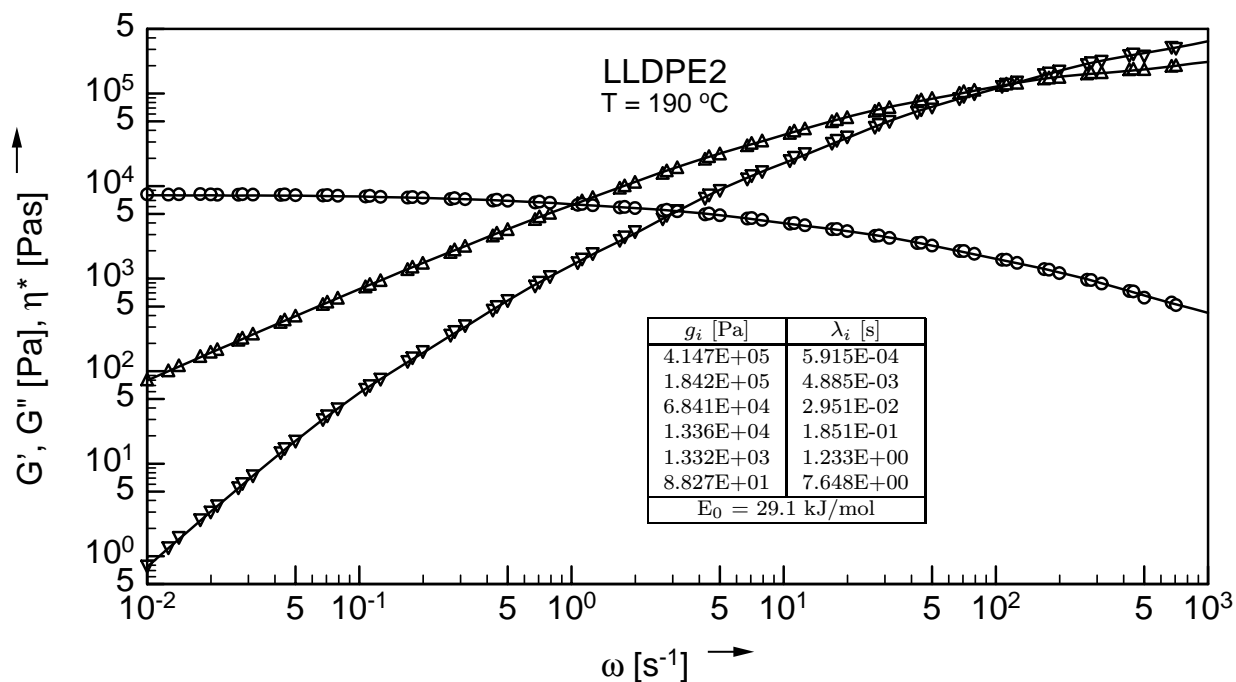


Figure A.11: Mastercurve of storage and loss modulus, G' and G'' , for melt LLDPE2 at 190°C. Experimental data (symbols) and fit by the relaxation time spectrum, g_i and λ_i (lines).

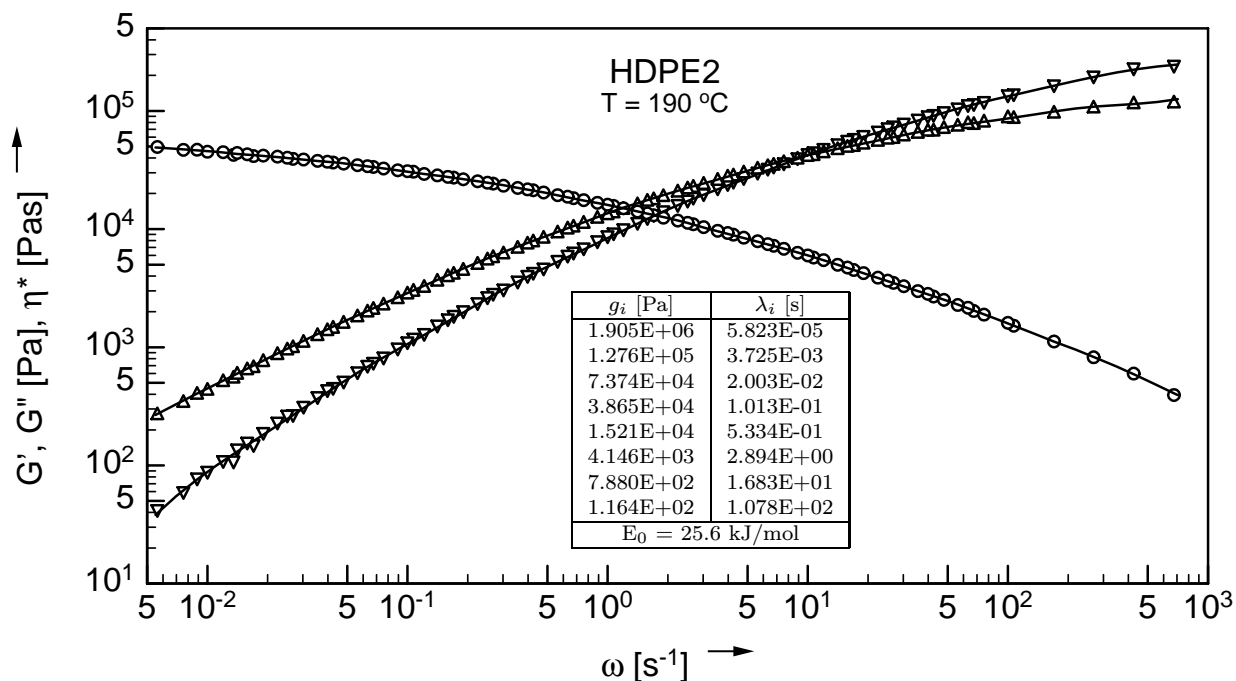


Figure A.12: Mastercurve of storage and loss modulus, G' and G'' , for melt HDPE2 at 190°C. Experimental data (symbols) and fit by the relaxation time spectrum, g_i and λ_i (lines).

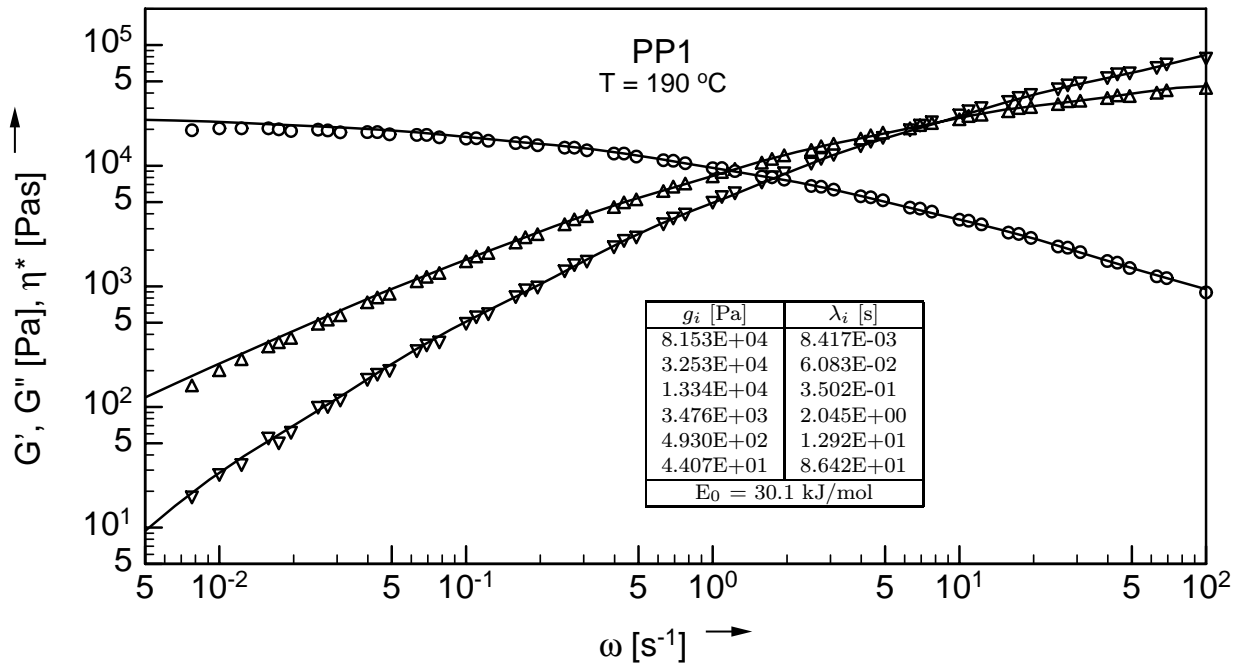


Figure A.13: Mastercurve of storage and loss modulus, G' and G'' , for melt PP1 at 190°C. Experimental data (symbols) and fit by the relaxation time spectrum, g_i and λ_i (lines).

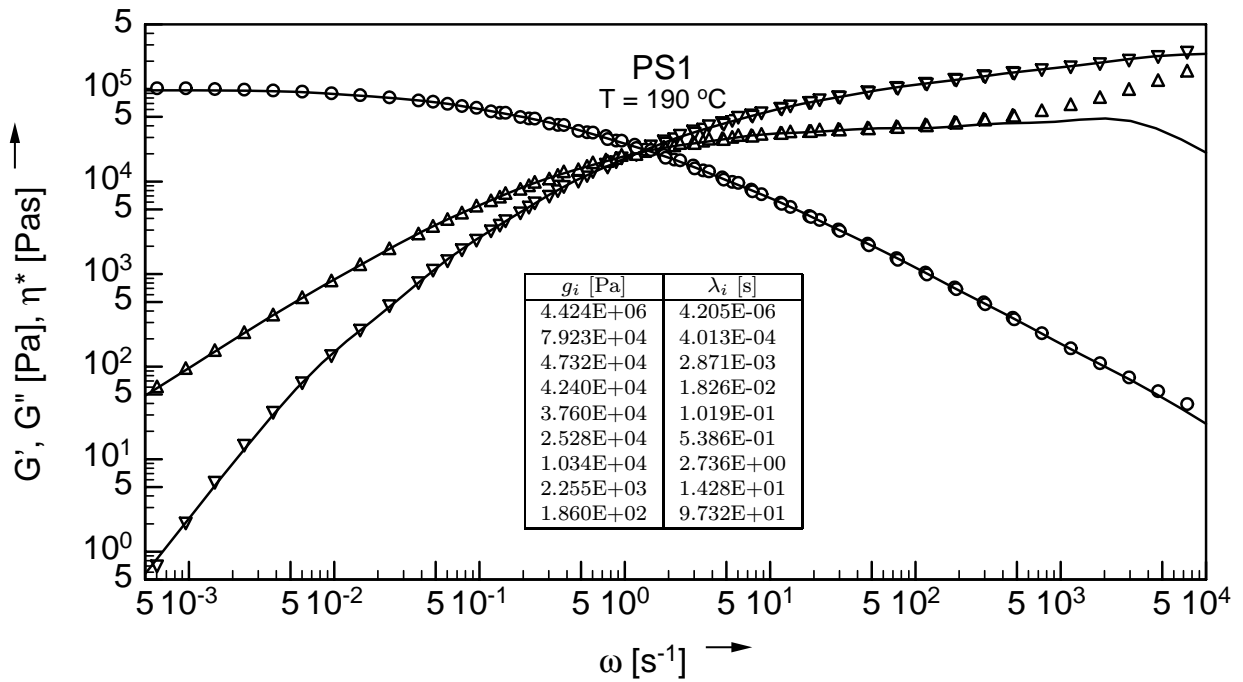


Figure A.14: Mastercurve of storage and loss modulus, G' and G'' , for melt PS1 at 190°C. Experimental data (symbols) and fit by the relaxation time spectrum, g_i and λ_i (lines).

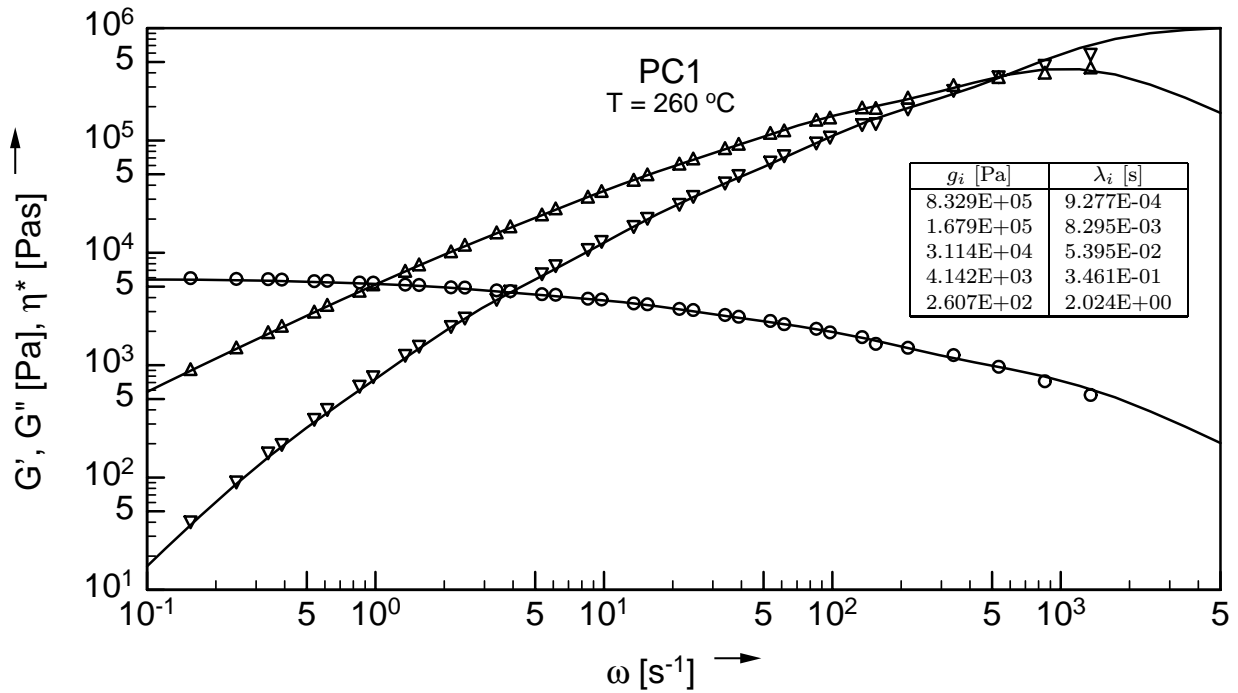


Figure A.15: Mastercurve of storage and loss modulus, G' and G'' , for melt PC1 at 260°C. Experimental data (symbols) and fit by the relaxation time spectrum, g_i and λ_i (lines).

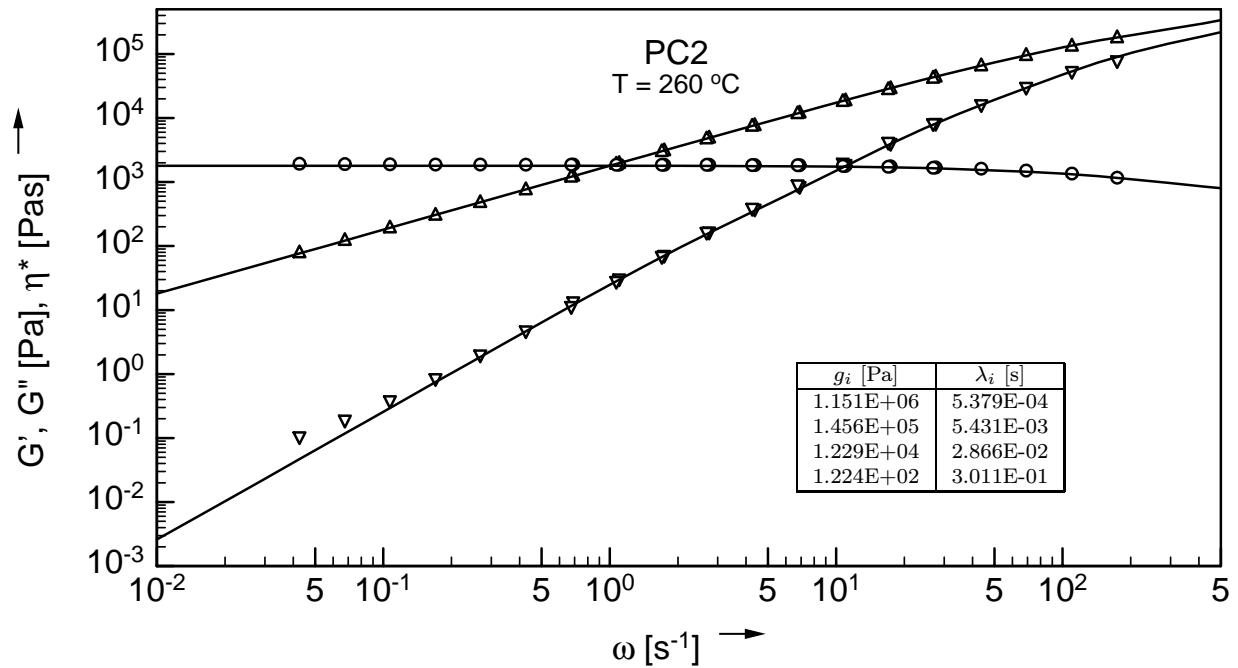


Figure A.16: Mastercurve of storage and loss modulus, G' and G'' , for melt PC2 at 190°C. Experimental data (symbols) and fit by the relaxation time spectrum, g_i and λ_i (lines).

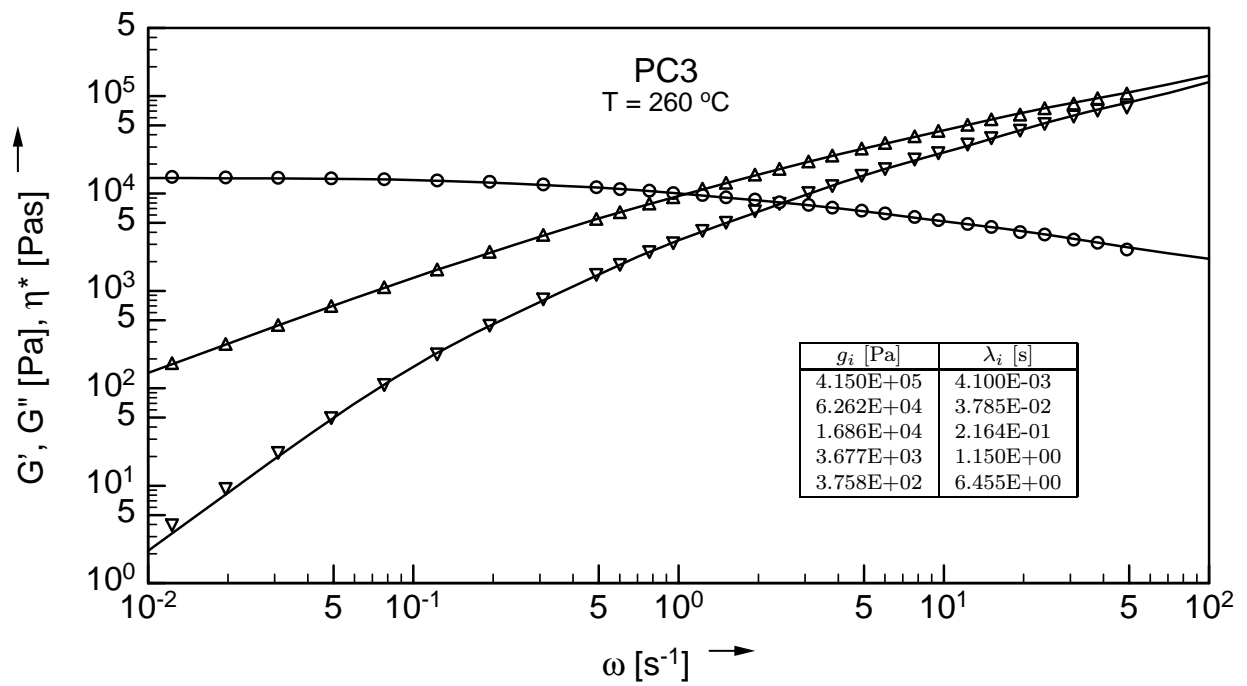


Figure A.17: Mastercurve of storage and loss modulus, G' and G'' , for melt PC3 at 260°C. Experimental data (symbols) and fit by the relaxation time spectrum, g_i and λ_i (lines).

B LDV measurements and the similarity model

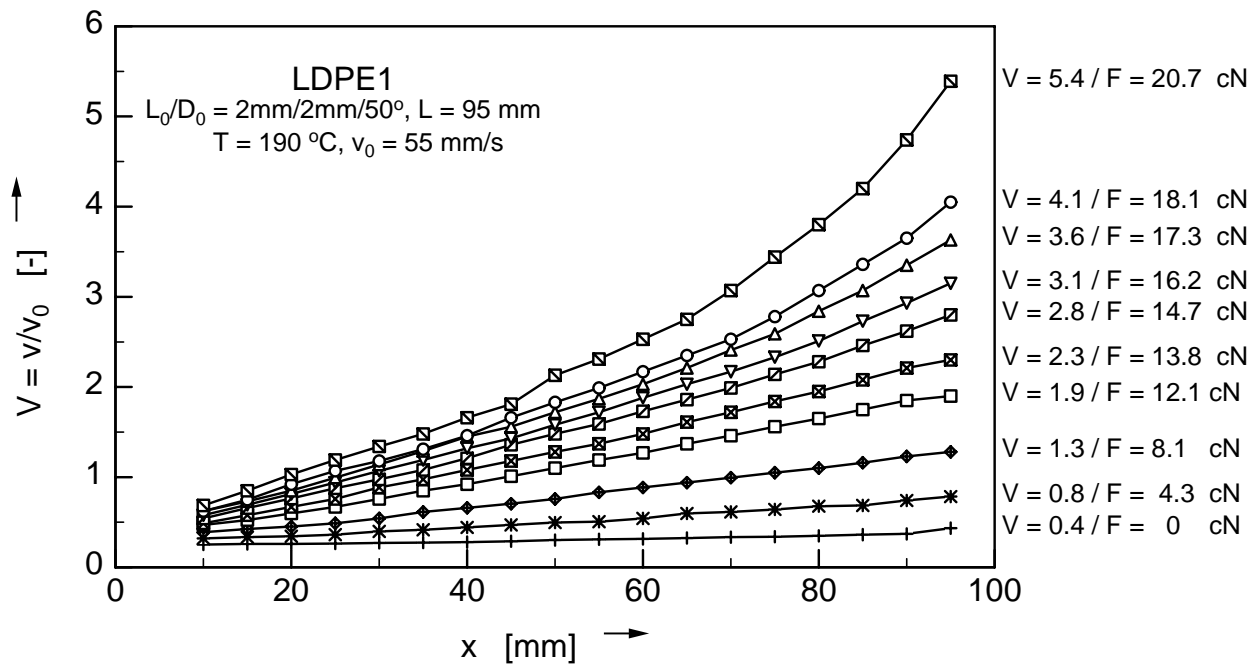


Figure B.1: a) Filament velocity v along the length x of the spinline for melt LDPE1. Measurements (symbols) by LDV.

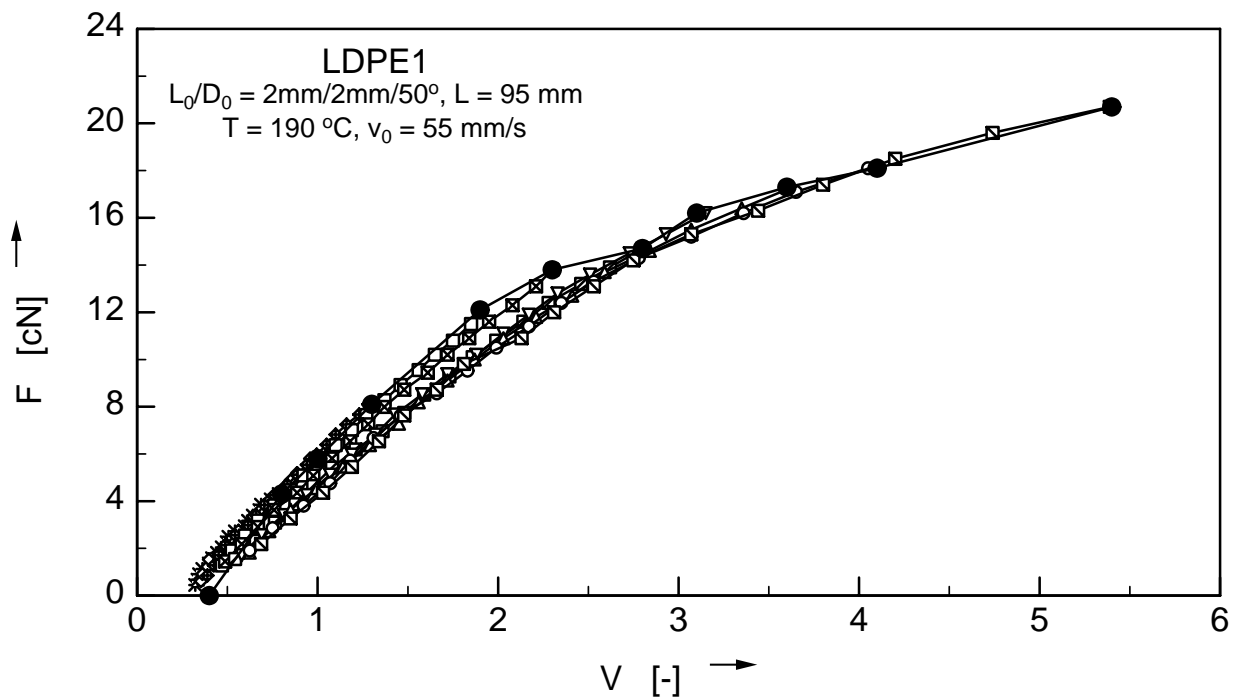


Figure B.1: b) Force curve resulting from the conversion of the velocity profiles from fig. B.1 a) according to the similarity solution for melt LDPE1.

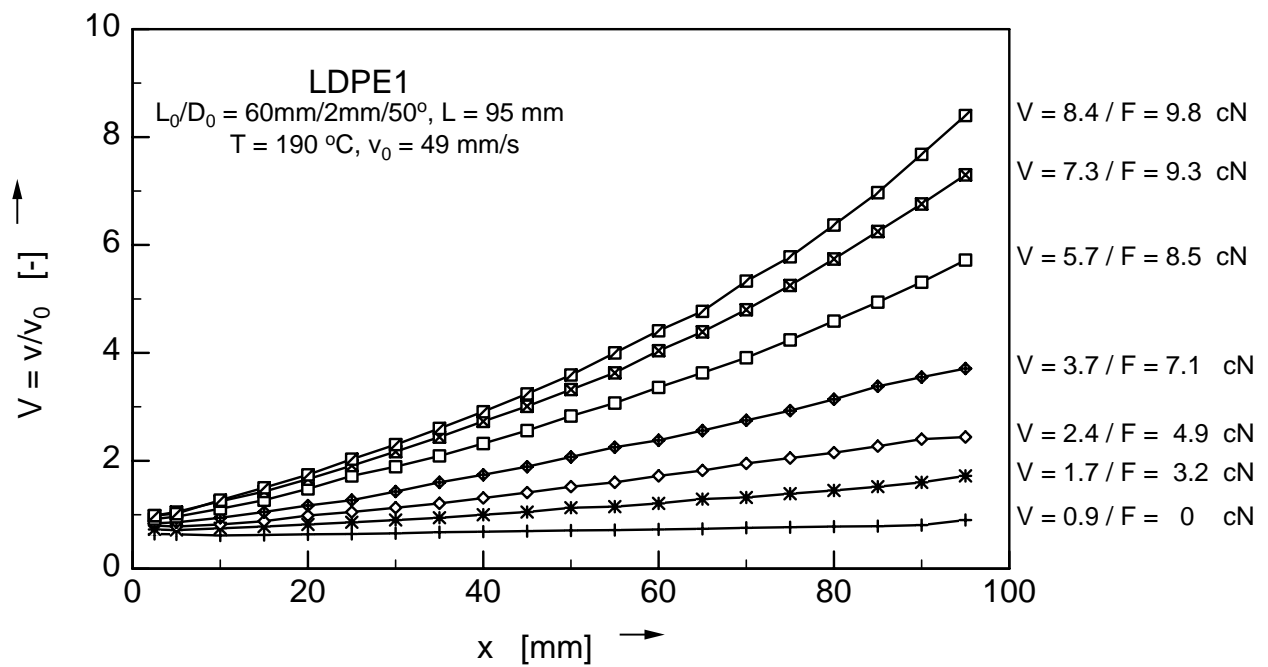


Figure B.2: a) Filament velocity v along the length x of the spinline for melt LDPE1. Measurements (symbols) by LDV.

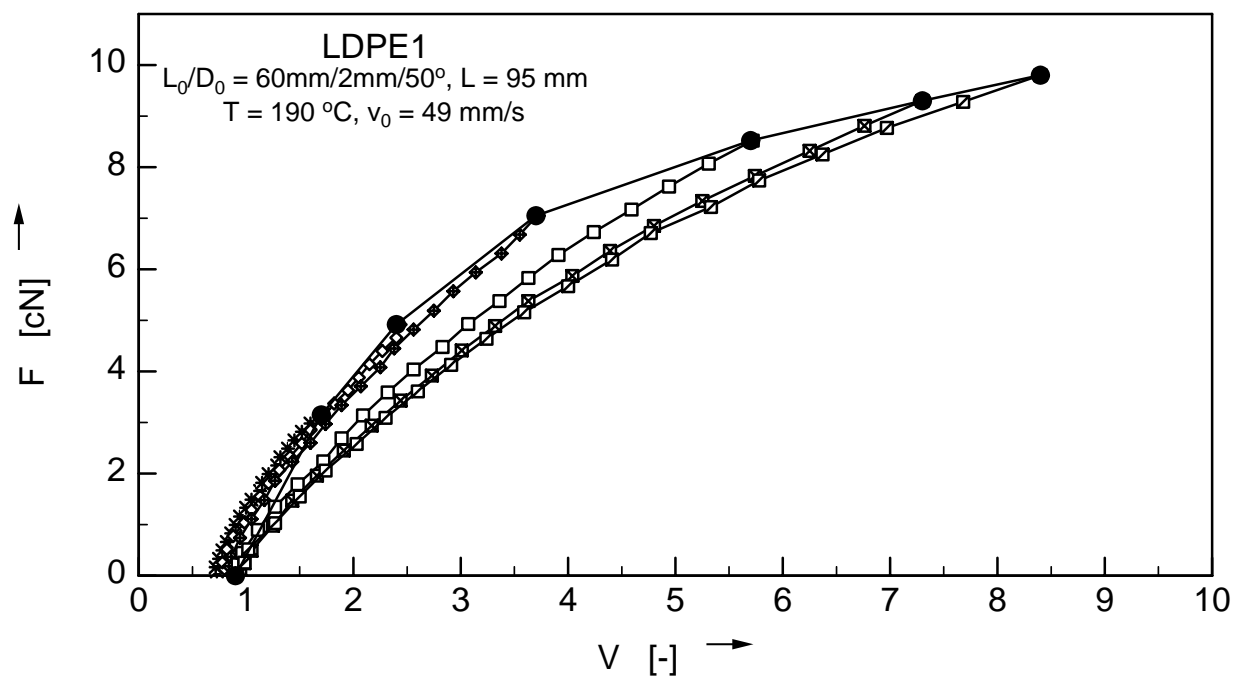


Figure B.2: b) Force curve resulting from the conversion of the velocity profiles from fig. B.2 a) according to the similarity solution for melt LDPE1.

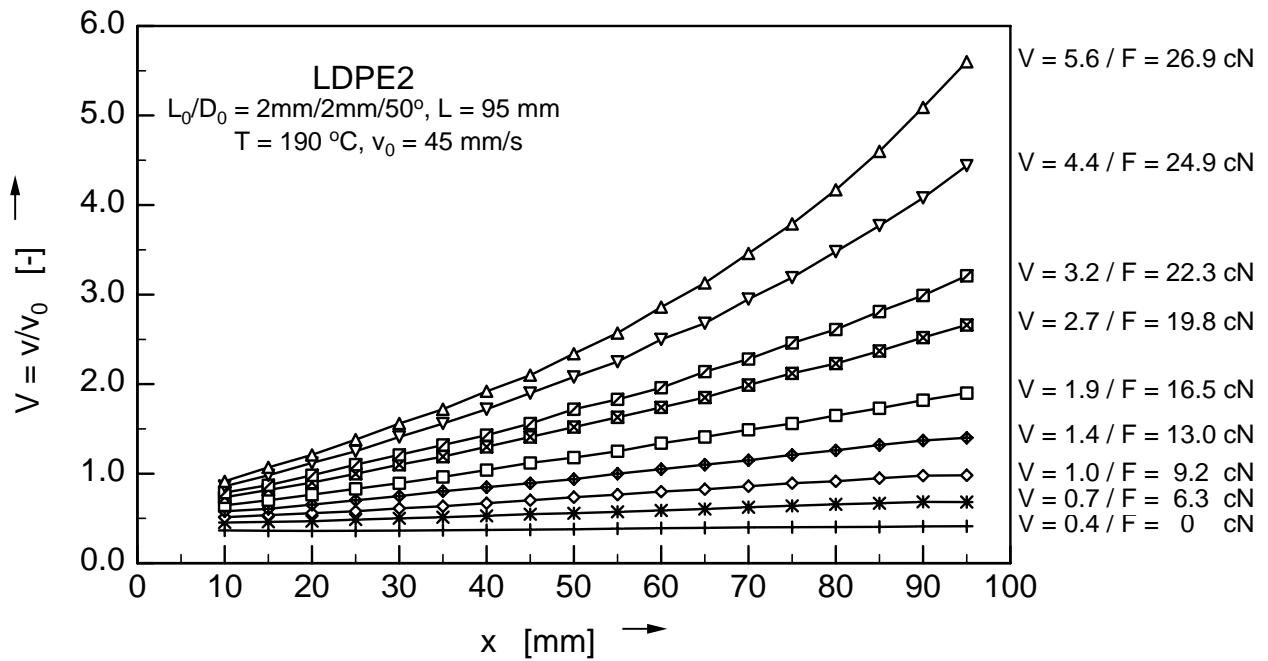


Figure B.3: a) Filament velocity v along the length x of the spinline for melt LDPE2. Measurements (symbols) by LDV.

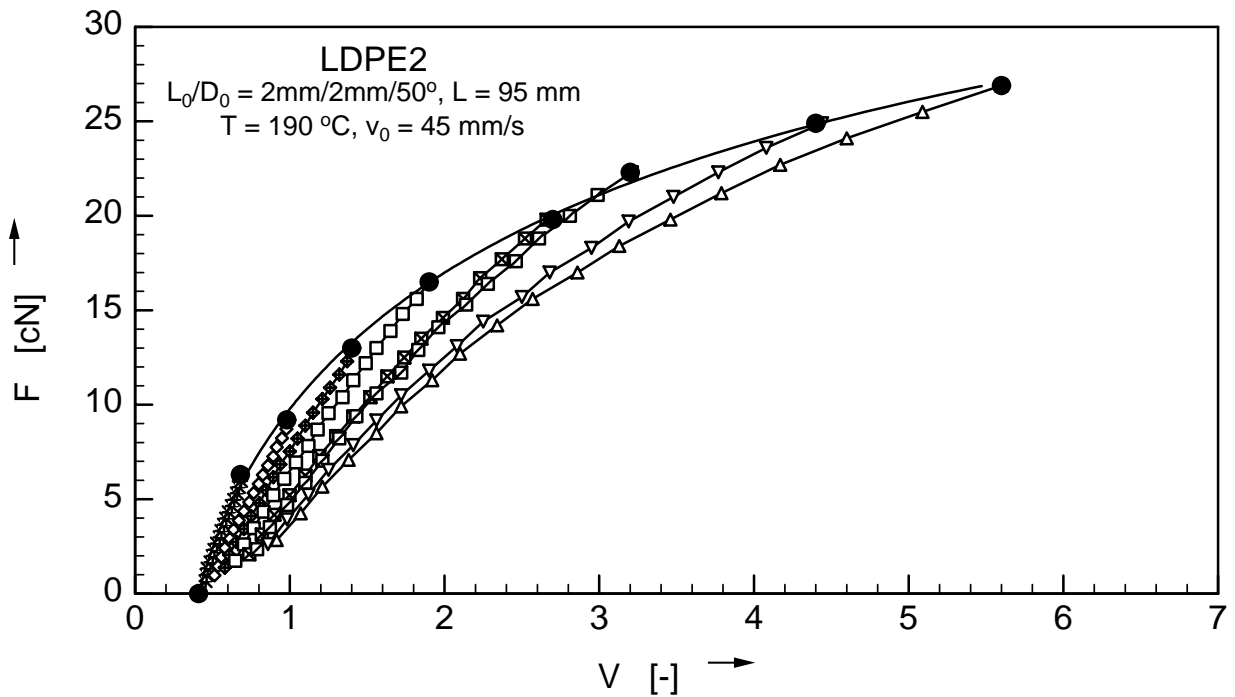


Figure B.3: b) Force curve resulting from the conversion of the velocity profiles from fig. B.3 a) according to the similarity solution for melt LDPE2.

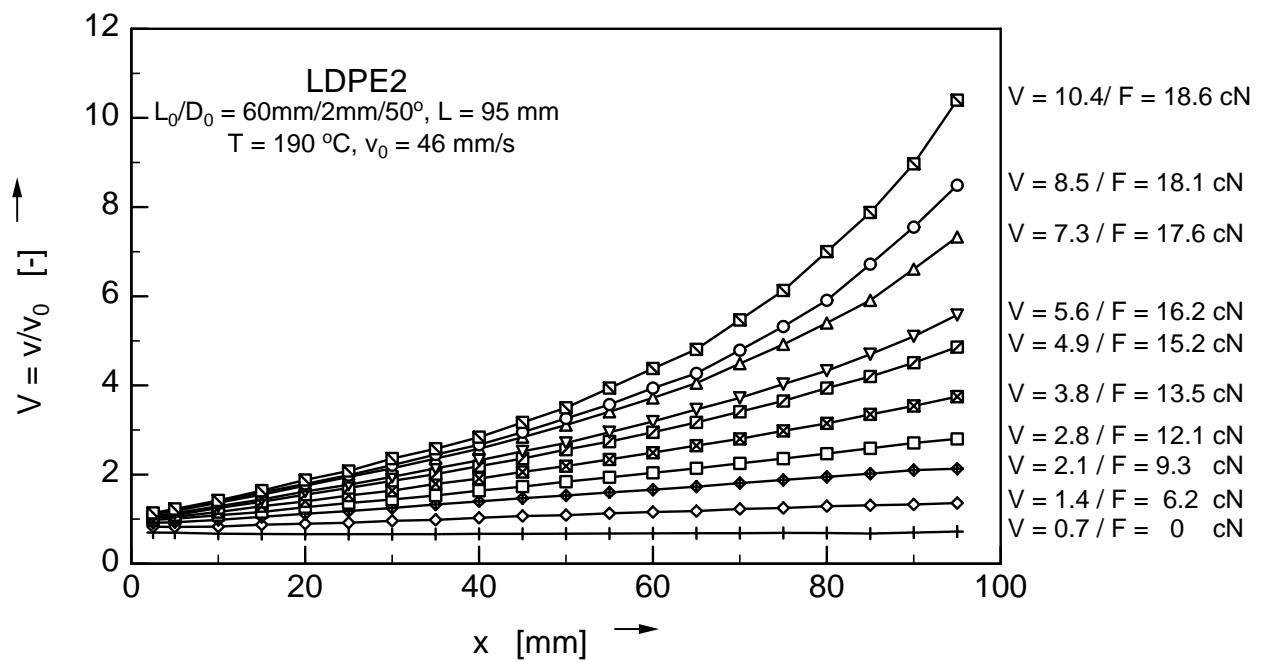


Figure B.4: a) Filament velocity v along the length x of the spinline for melt LDPE2. Measurements (symbols) by LDV.

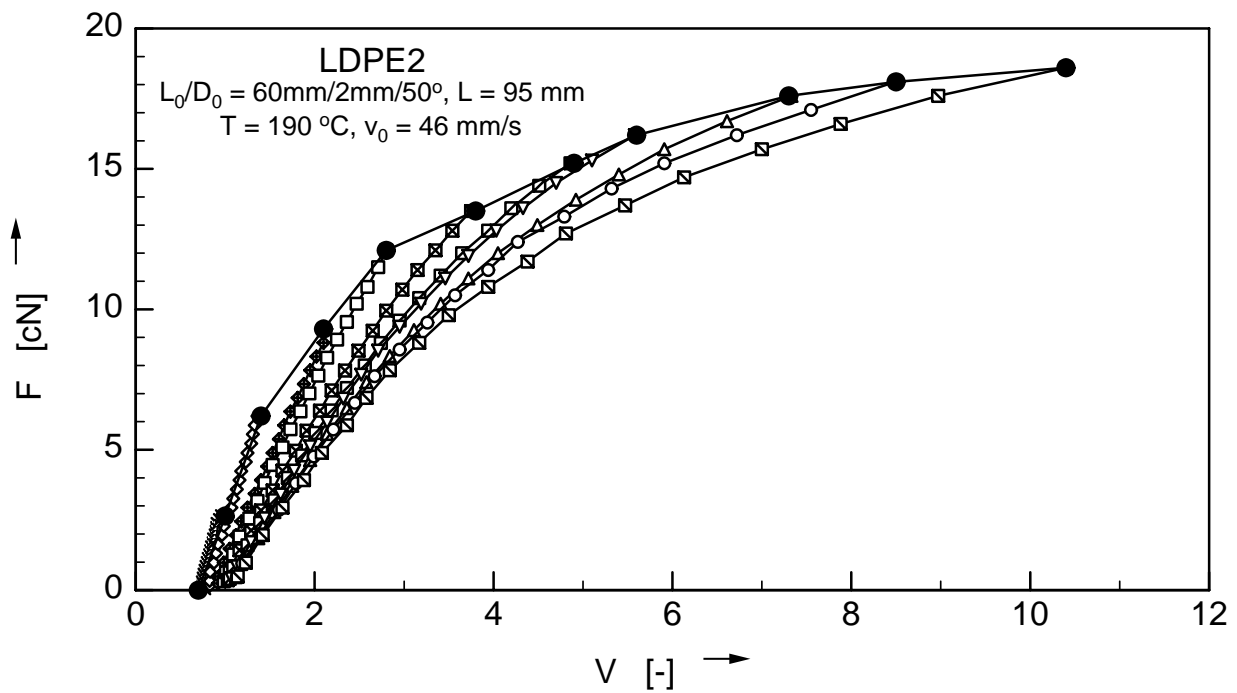


Figure B.4: b) Force curve resulting from the conversion of the velocity profiles from fig. B.4 a) according to the similarity solution for melt LDPE2.

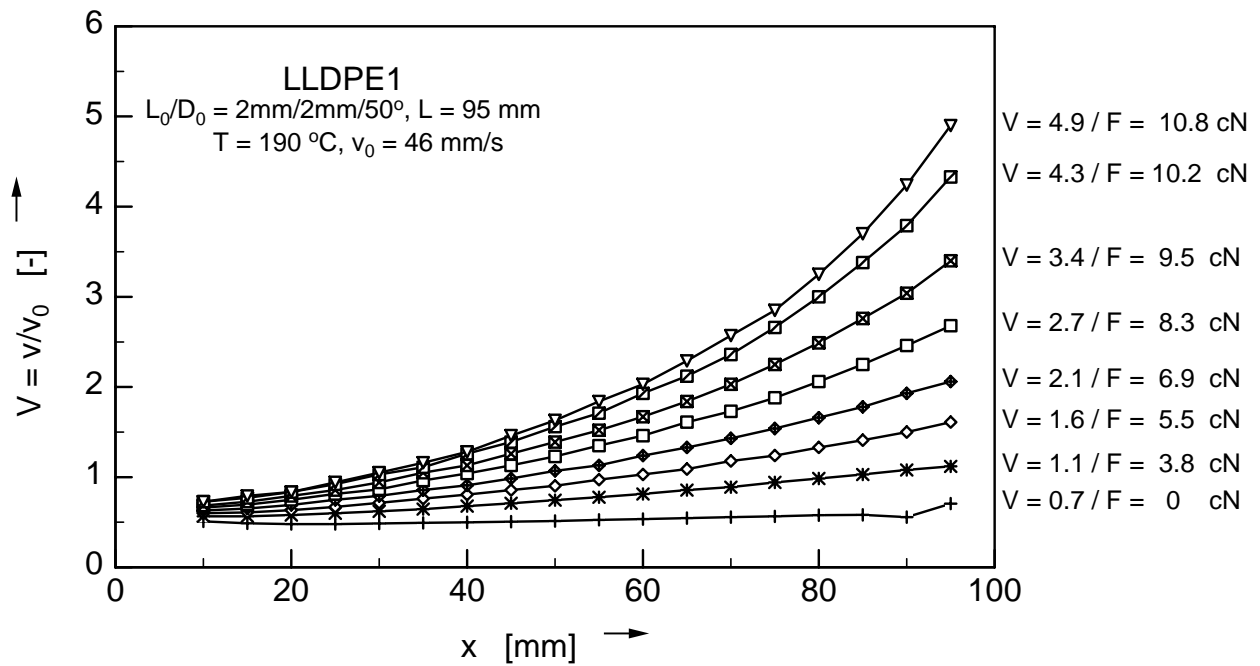


Figure B.5: a) Filament velocity v along the length x of the spinline for melt LLDPE1. Measurements (symbols) by LDV.

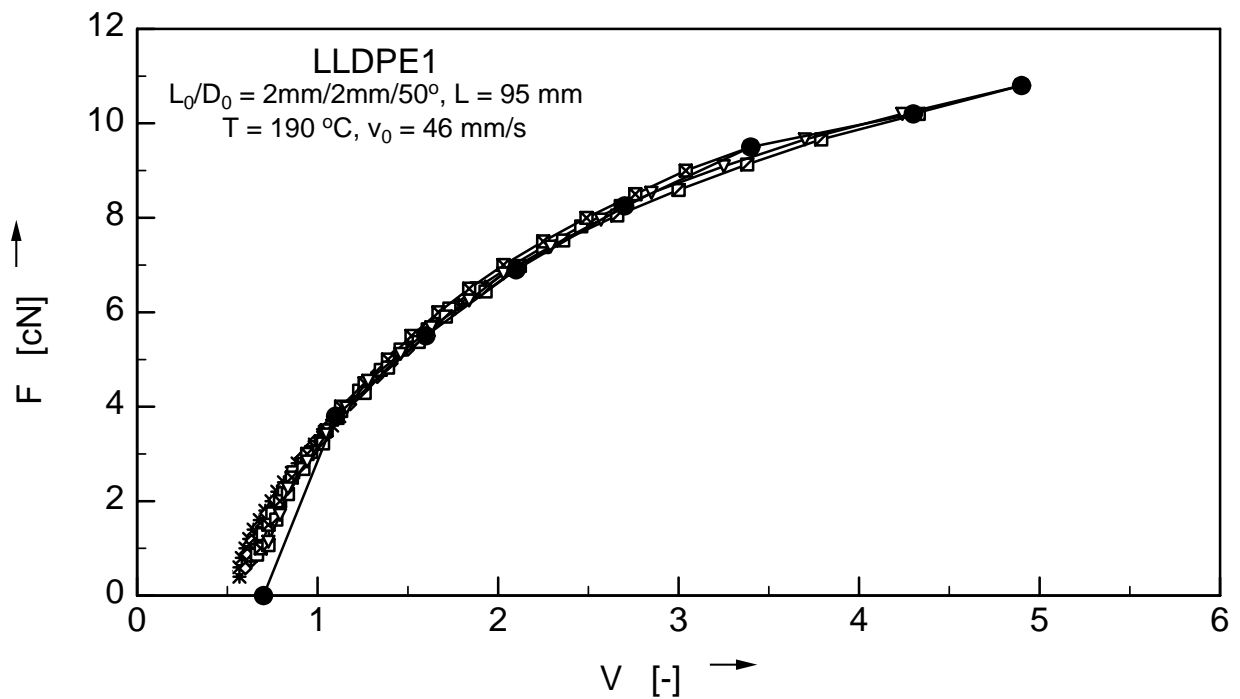


Figure B.5: b) Force curve resulting from the conversion of the velocity profiles from fig. B.5 a) according to the similarity solution for melt LLDPE1.

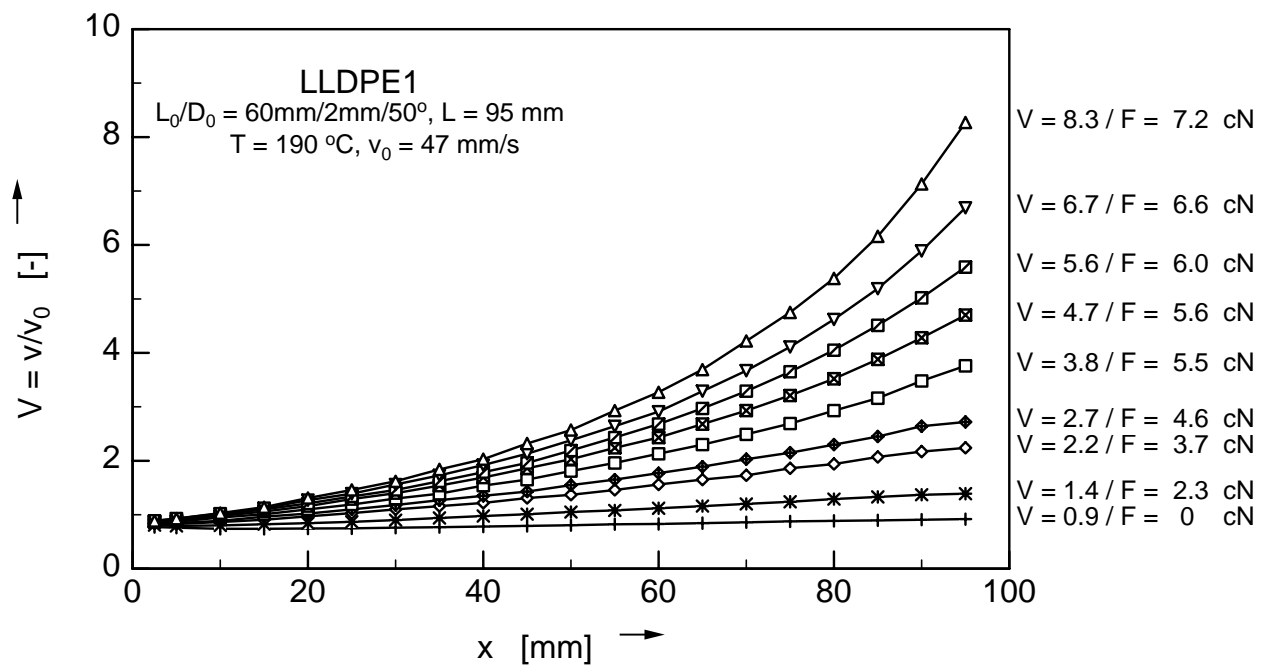


Figure B.6: a) Filament velocity v along the length x of the spinline for melt LLDPE1. Measurements (symbols) by LDV.

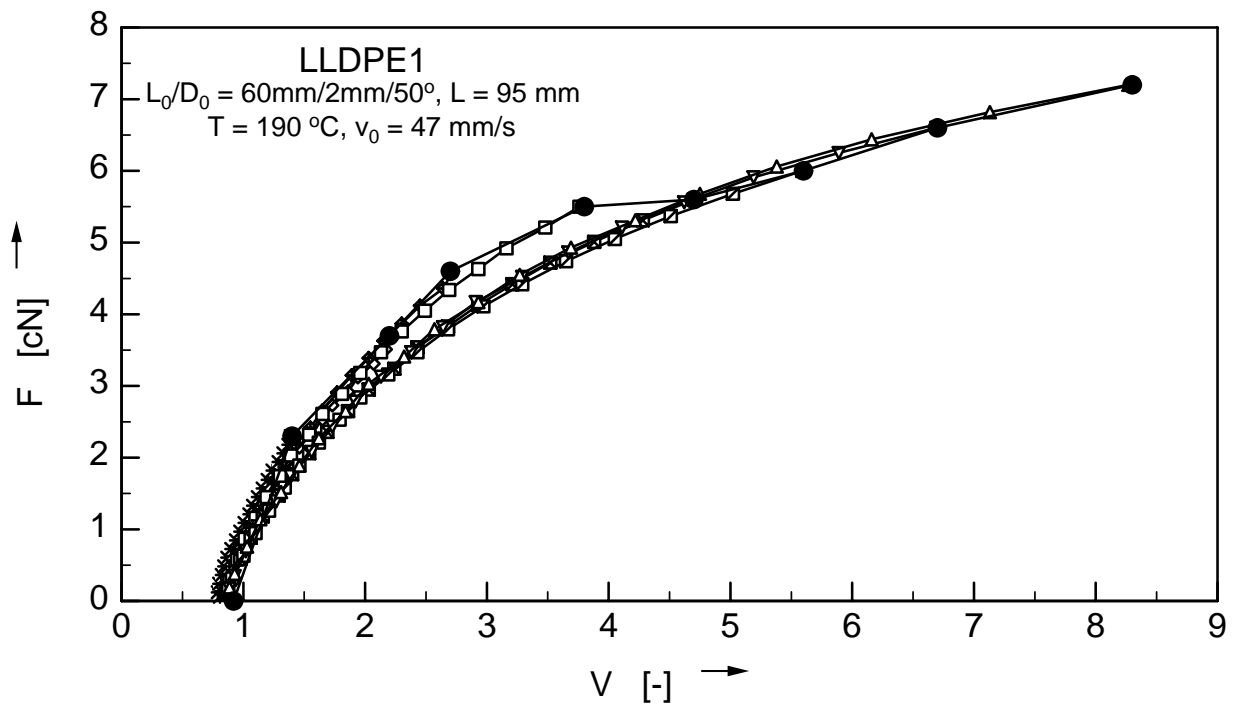


Figure B.6: b) Force curve resulting from the conversion of the velocity profiles from fig. B.6 a) according to the similarity solution for melt LLDPE1.

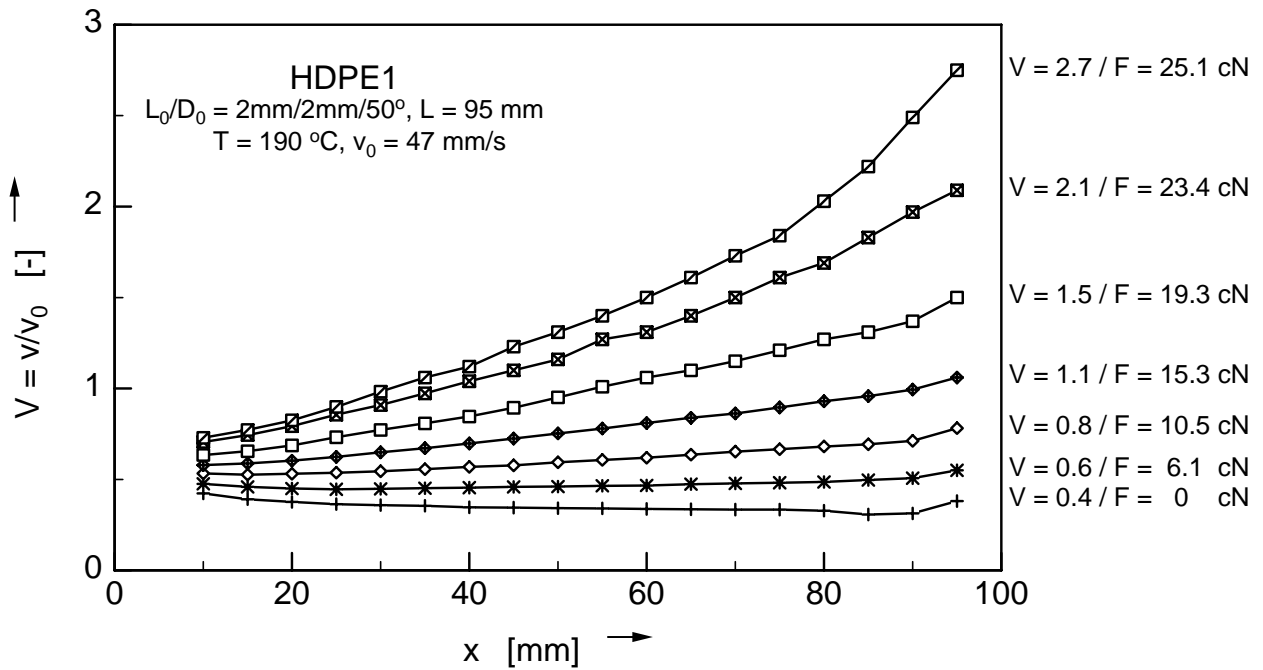


Figure B.7: a) Filament velocity v along the length x of the spinline for melt HDPE1. Measurements (symbols) by LDV.

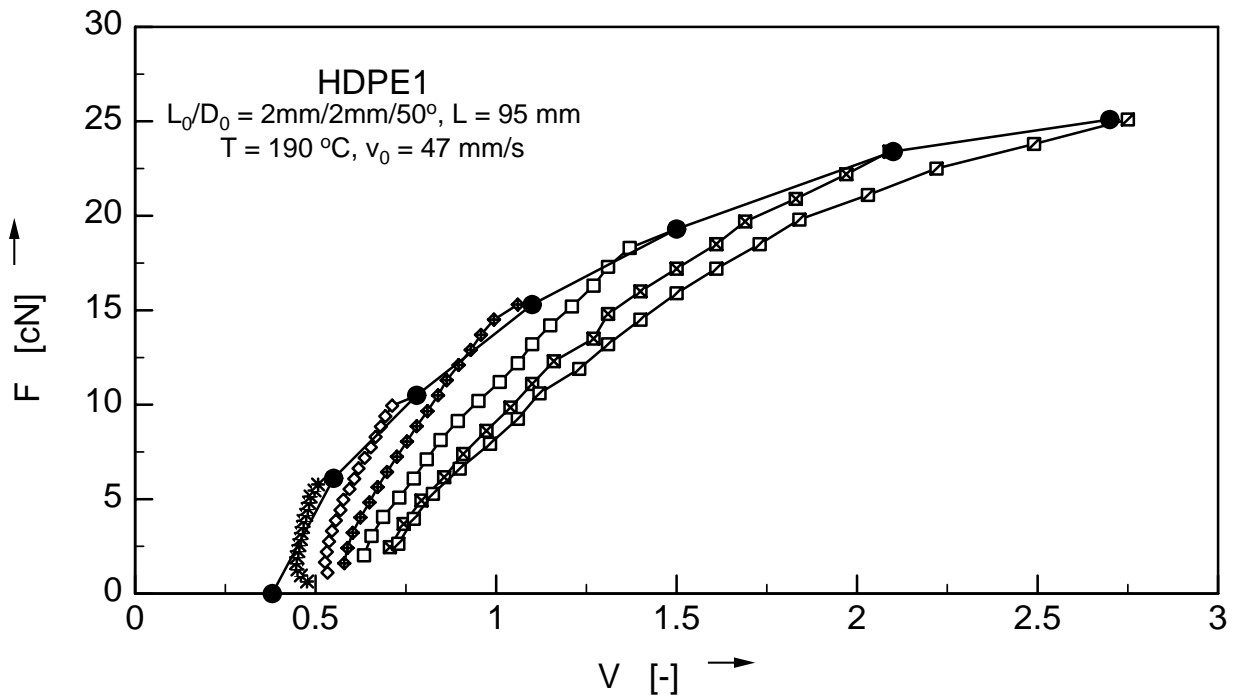


Figure B.7: b) Force curve resulting from the conversion of the velocity profiles from fig. B.7 a) according to the similarity solution for melt HDPE1.

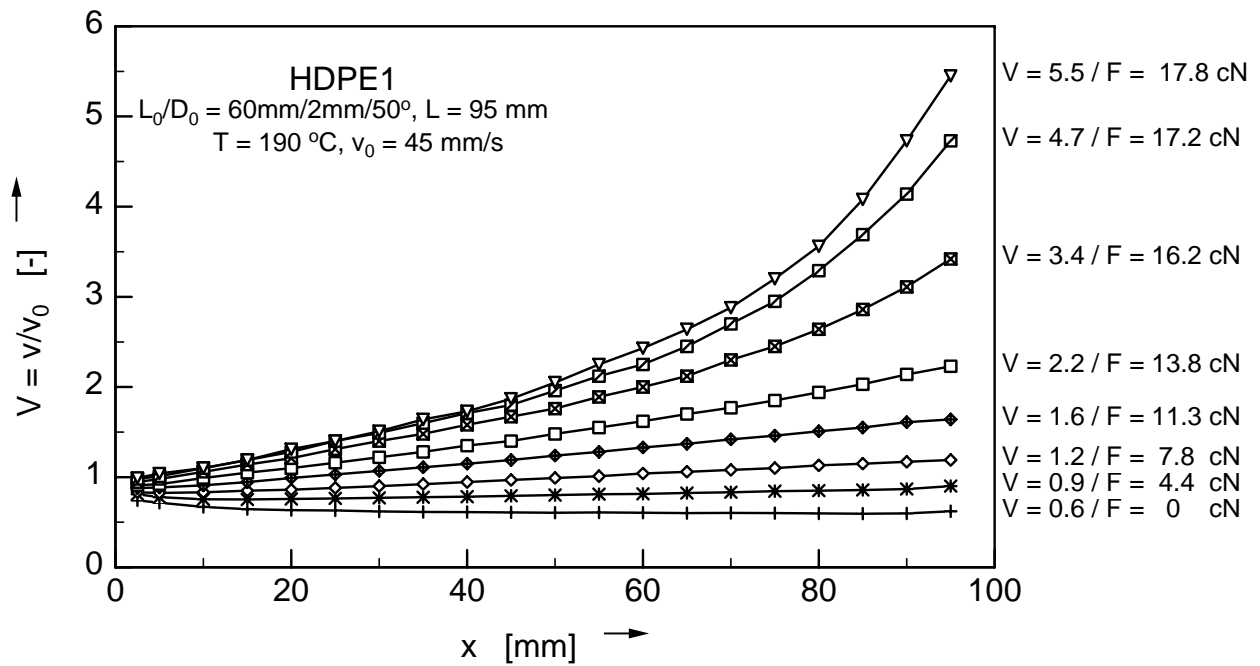


Figure B.8: a) Filament velocity v along the length x of the spinline for melt HDPE1. Measurements (symbols) by LDV.

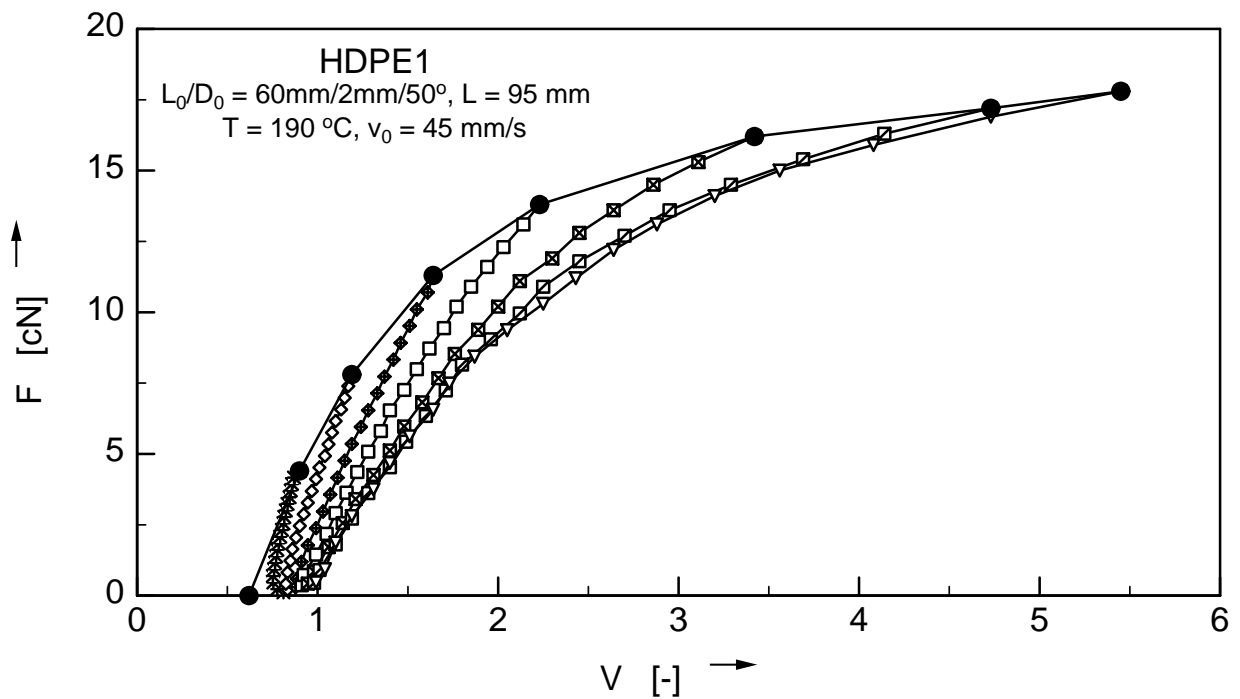


Figure B.8: b) Force curve resulting from the conversion of the velocity profiles from fig. B.8 a) according to the similarity solution for melt HDPE1.

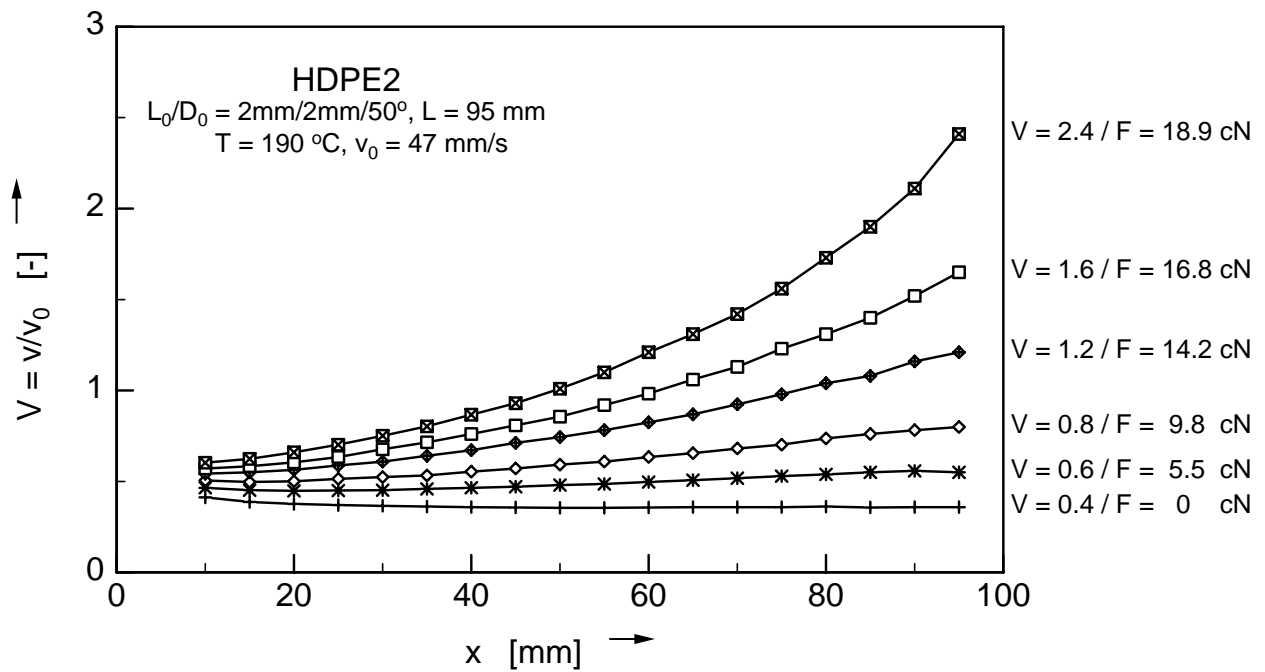


Figure B.9: a) Filament velocity v along the length x of the spinline for melt HDPE2. Measurements (symbols) by LDV.

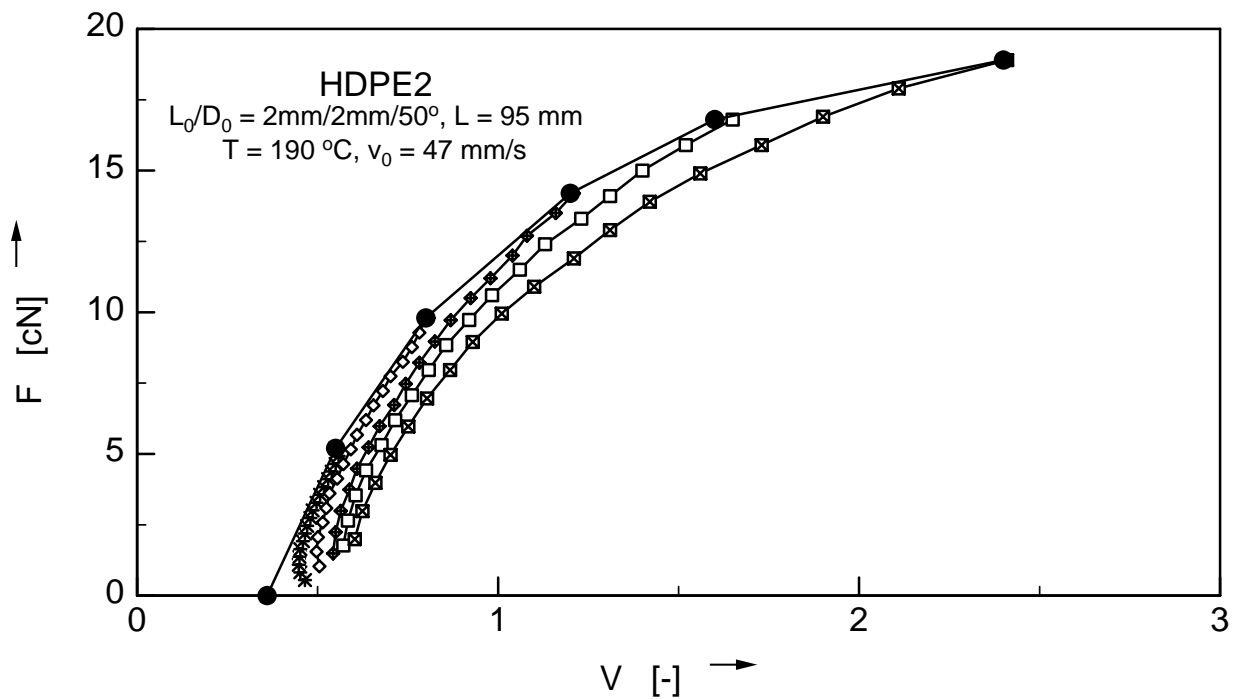


Figure B.9: b) Force curve resulting from the conversion of the velocity profiles from fig. B.9 a) according to the similarity solution for melt HDPE2.

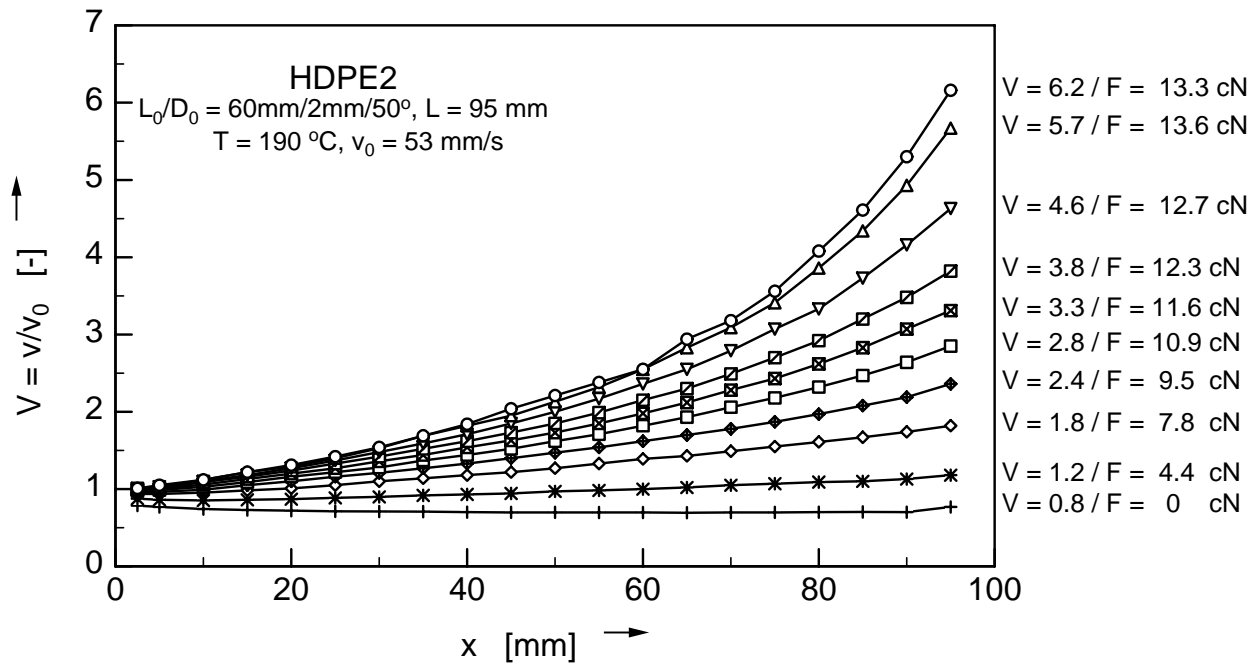


Figure B.10: a) Filament velocity v along the length x of the spinline for melt HDPE2. Measurements (symbols) by LDV.

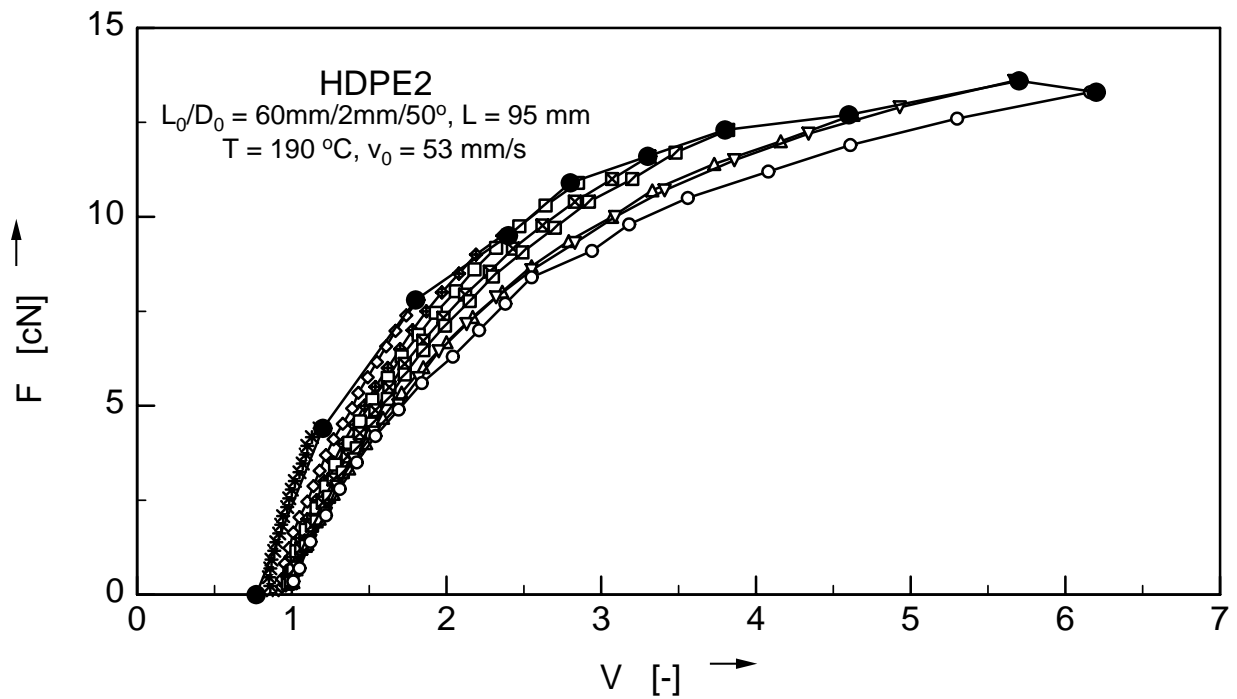


Figure B.10: b) Force curve resulting from the conversion of the velocity profiles from fig. B.10 a) according to the similarity solution for melt HDPE2.

C Results of the analytical model and the similarity model

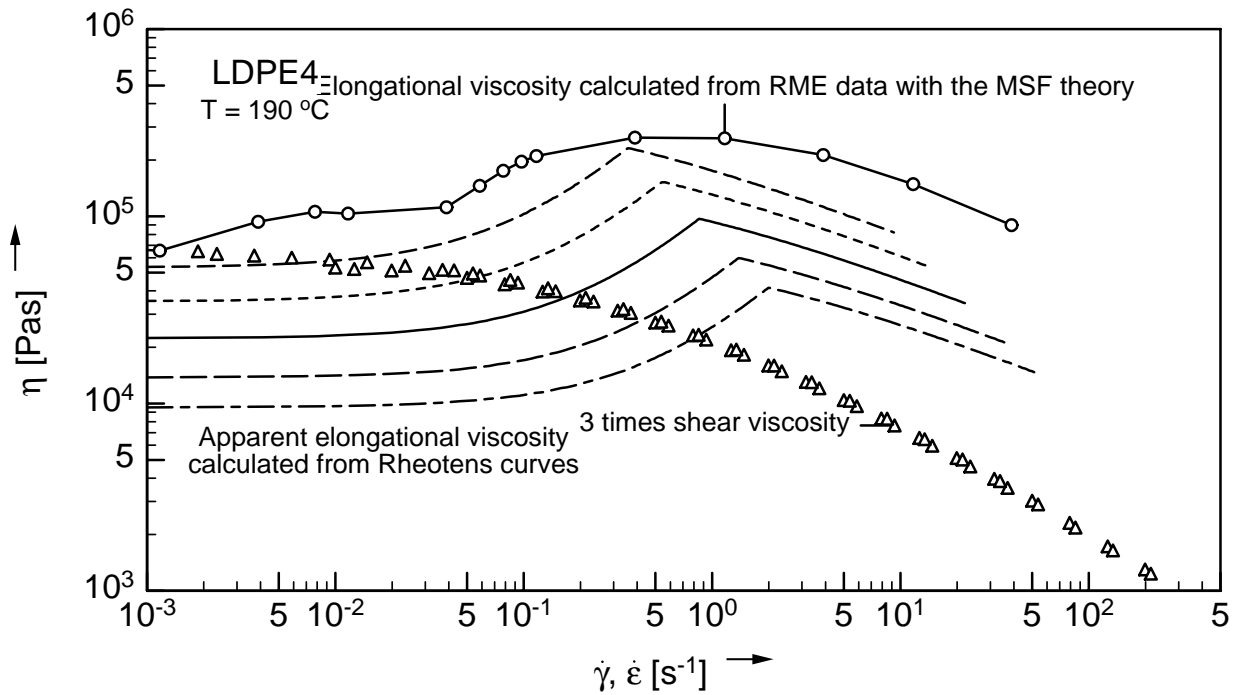


Figure C.1: Apparent elongational viscosity for melt LDPE4 calculated from Rheotens curves by use of the analytical model in comparison to steady-state viscosity.

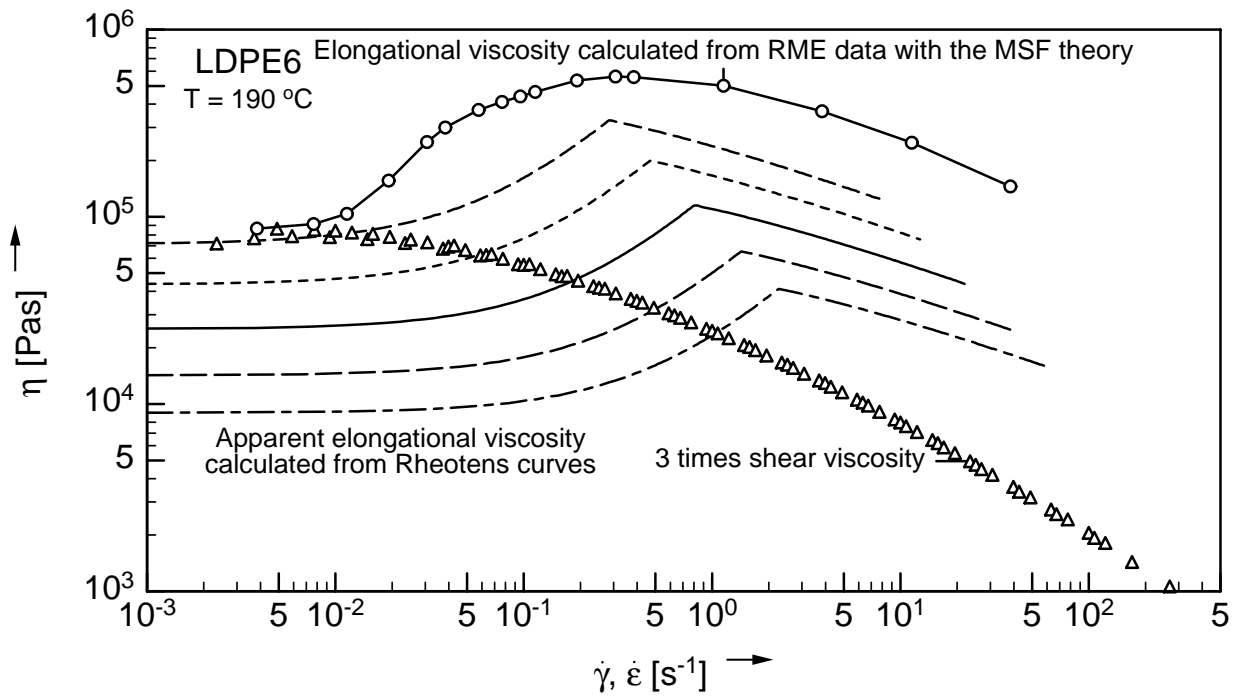


Figure C.2: Apparent elongational viscosity for melt LDPE6 calculated from Rheotens curves by use of the analytical model in comparison to steady-state viscosity.

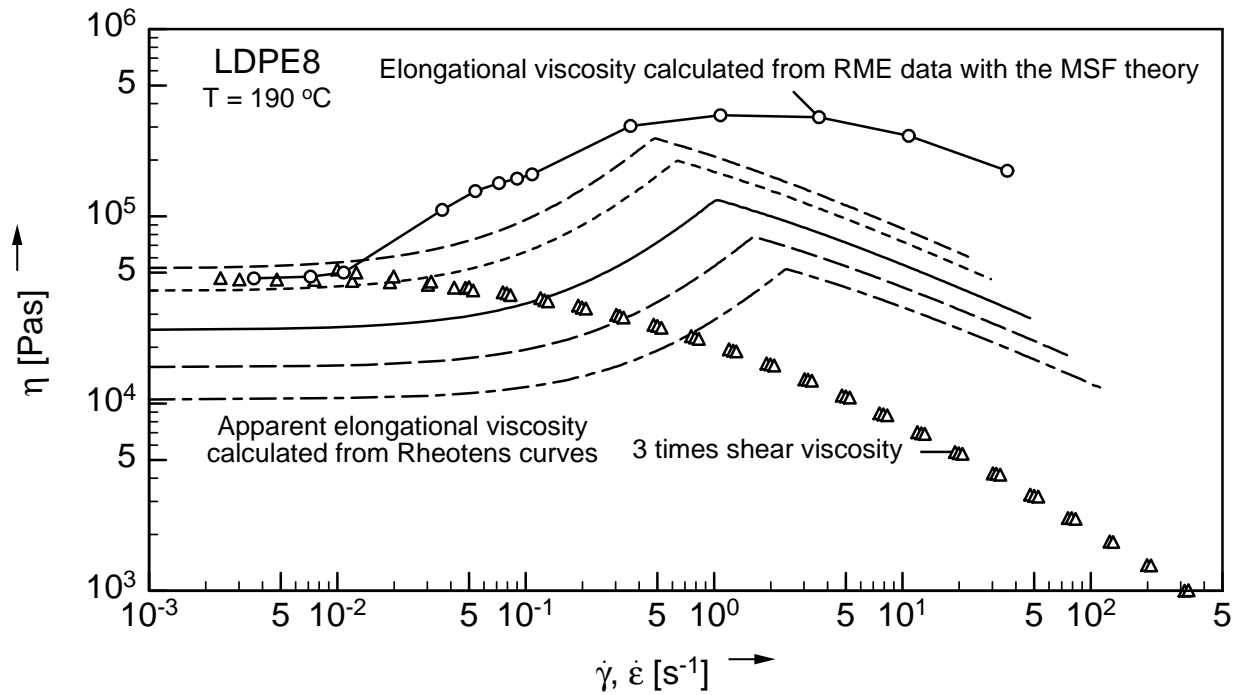


Figure C.3: Apparent elongational viscosity for melt LDPE8 calculated from Rheotens curves by use of the analytical model in comparison to steady-state viscosity.

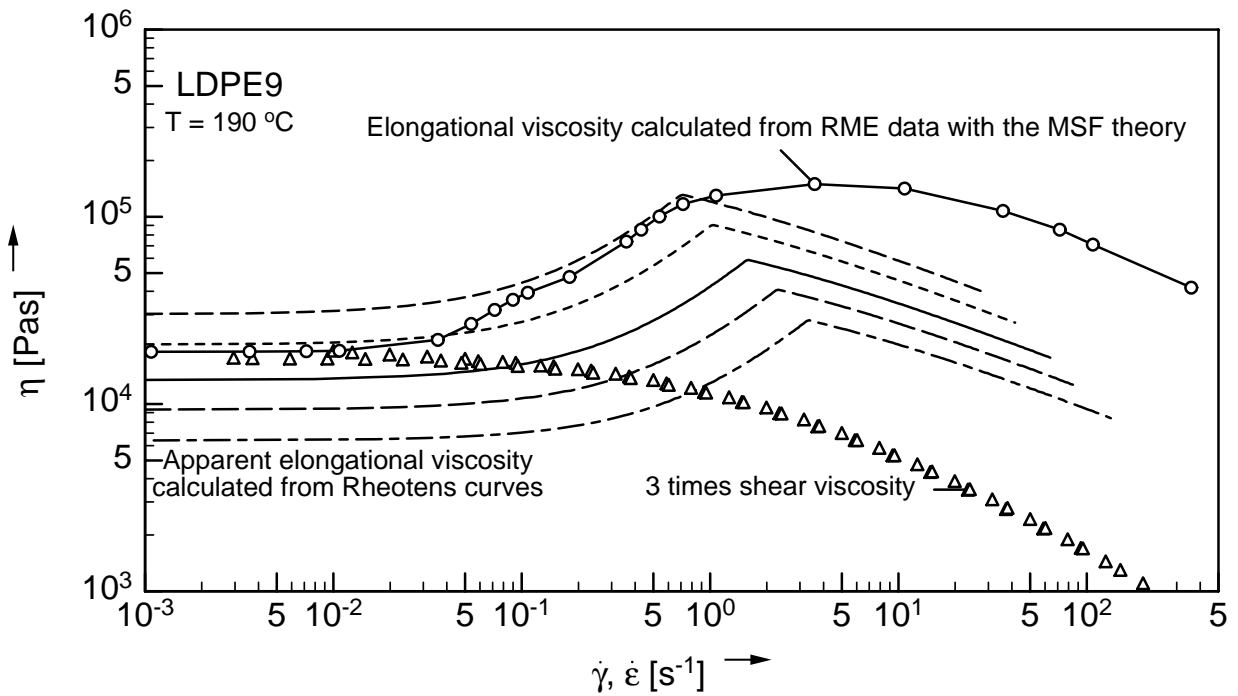


Figure C.4: Apparent elongational viscosity for melt LDPE9 calculated from Rheotens curves by use of the analytical model in comparison to steady-state viscosity.

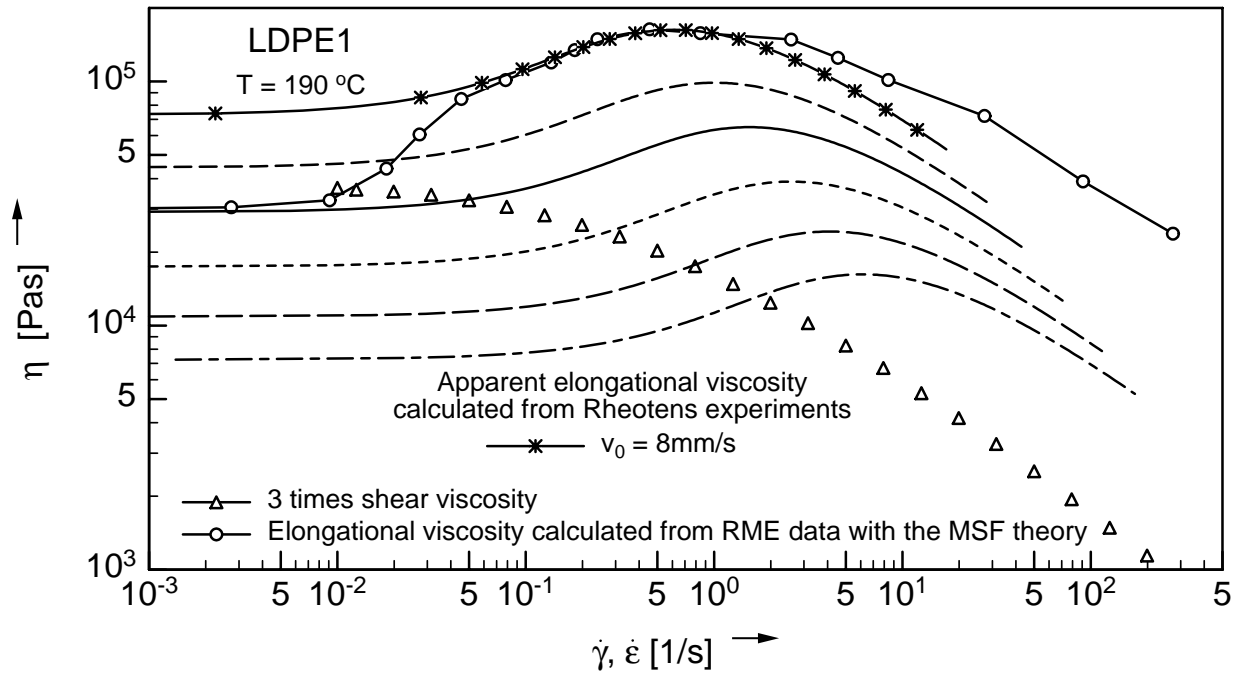


Figure C.5: Estimated elongational viscosity for melt LDPE1 calculated from Rheotens curves by use of the similarity model in comparison to steady-state viscosity.

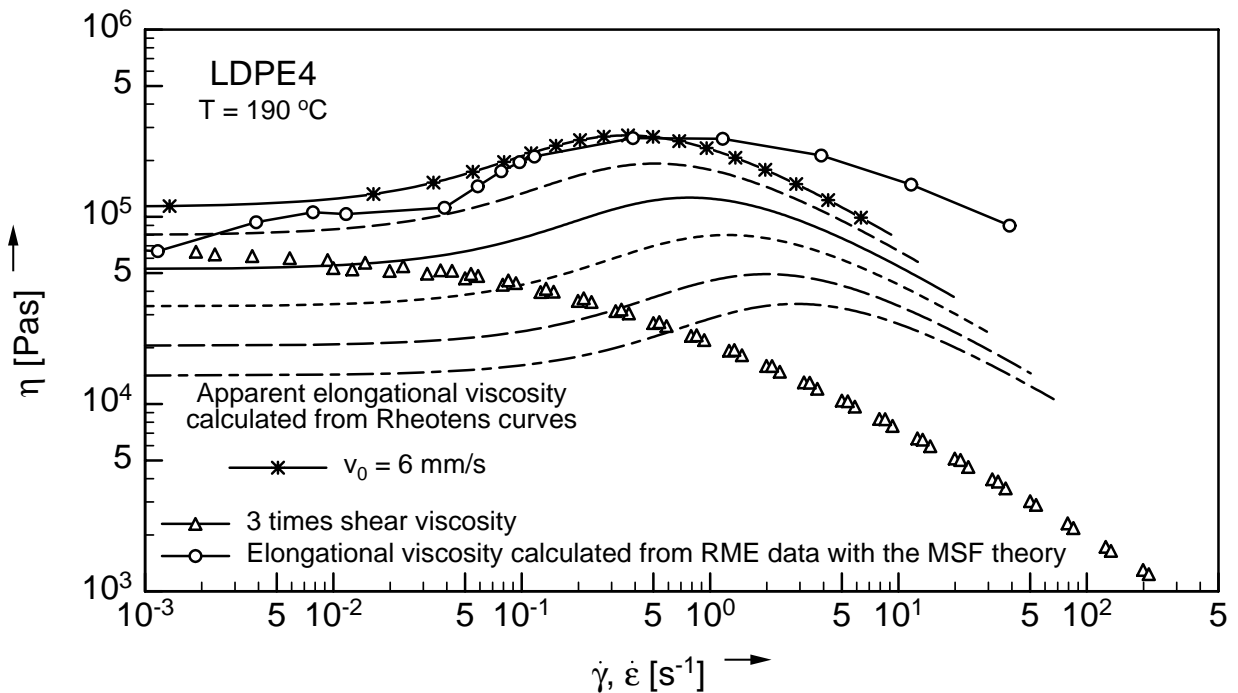


Figure C.6: Estimated elongational viscosity for melt LDPE4 calculated from Rheotens curves by use of the similarity model in comparison to steady-state viscosity.

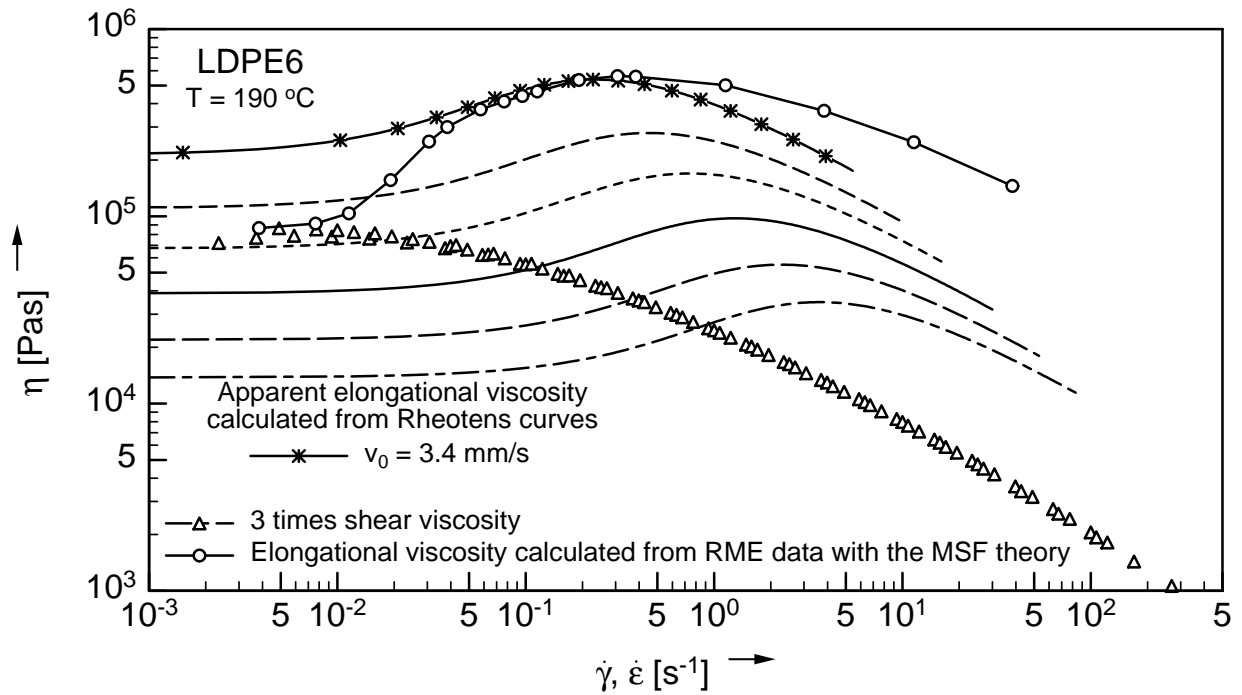


Figure C.7: Estimated elongational viscosity for melt LDPE6 calculated from Rheotens curves by use of the similarity model in comparison to steady-state viscosity.

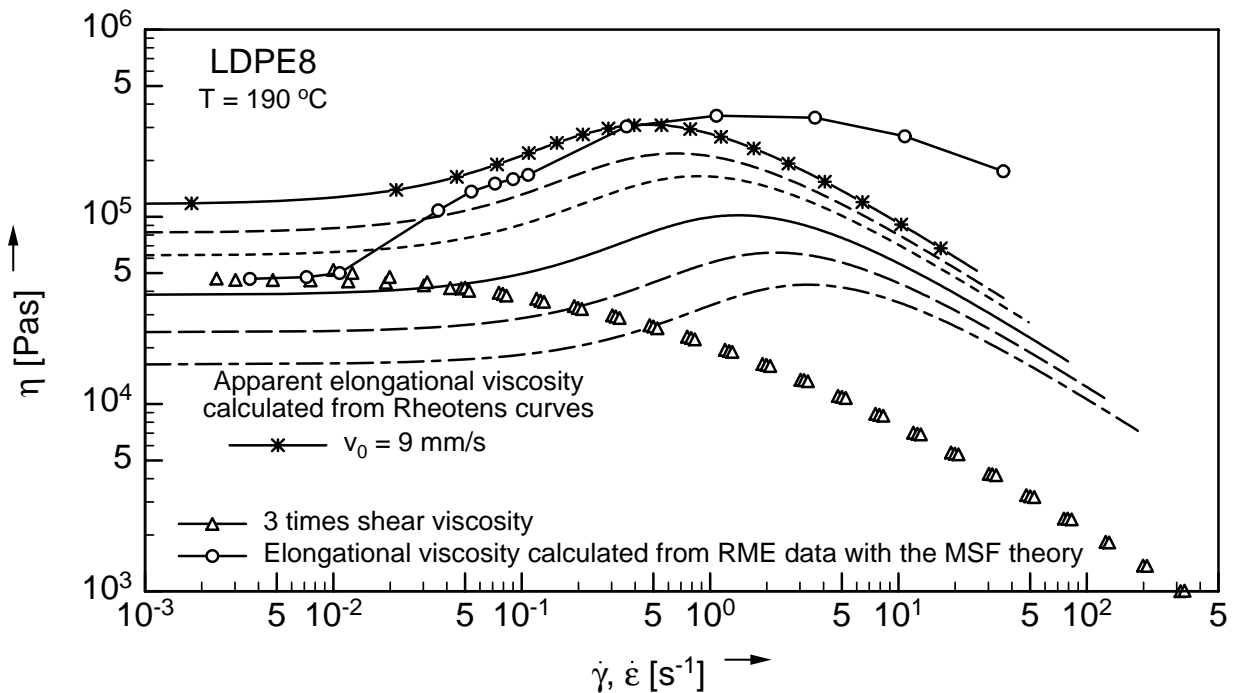


Figure C.8: Estimated elongational viscosity for melt LDPE8 calculated from Rheotens curves by use of the similarity model in comparison to steady-state viscosity.

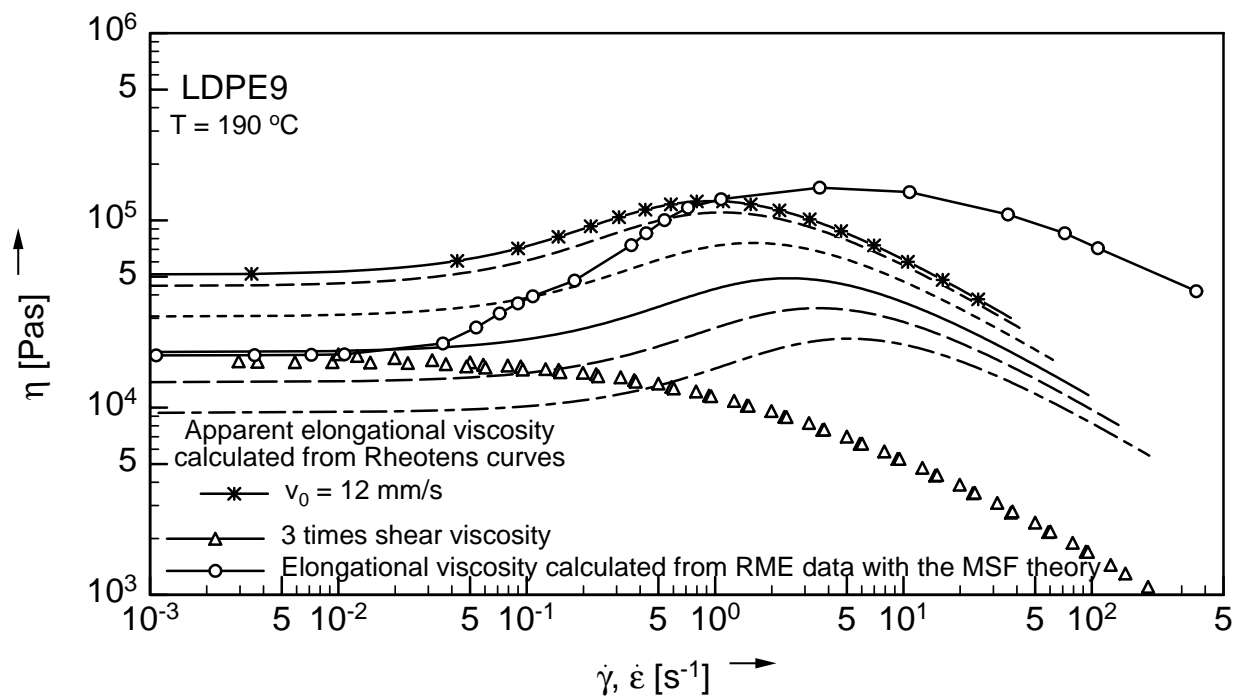


Figure C.9: Estimated elongational viscosity for melt LDPE9 calculated from Rheotens curves by use of the similarity model in comparison to steady-state viscosity.

Lebenslauf

Anka Claudia Bernnat

geb. 1.12.1968, Stuttgart

- | | |
|-------------------|---|
| 1975 - 1979 | Grundschule Stuttgart Degerloch |
| 1979 - 1988 | Philipp - Matthäus - Hahn - Gymnasium, Echterdingen Abschluß: Allgemeine Hochschulreife |
| 1989 - 1992 | Vordiplom Maschinenwesen, Universität Stuttgart |
| 1992 - 1996 | Hauptdiplom Verfahrenstechnik, Universität Stuttgart Abschluß: Diplom-Ingenieur |
| Okt. 94 - Mai 95 | Studienaufenthalt am Imperial College of Science, Technology, and Medicine in London |
| Juli 96 - Dez. 00 | Wissenschaftliche Mitarbeiterin am Institut für Kunststofftechnologie, Abteilung numerische Strömungsmechanik - Rheologie und Rheometrie, Universität Stuttgart |
| seit Jan. 2001 | Mitarbeiterin der BASF AG, Ludwigshafen Anwendungsforschung für Technische Kunststoffe |